

**NUMERICAL MODELING FRAMEWORK
FOR
SOIL-GEOSYNTHETICS INTERACTION PROBLEMS**

By

Mahmoud G. Hussein

Department of Civil Engineering and Applied Mechanics



McGill University
Montréal, Québec, Canada

August 2016

A thesis submitted to McGill University in partial fulfillment of
the requirements for the degree of Doctor of Philosophy

© Mahmoud Hussein, 2016

Dedication

To the spirit of my **Father**
Saad (1947-2002)

To my favourite **Mom**
Aicha

To my adored **Wife**
Basma

To my beloved **Children**
Asal (11 years), *Anas* (4 years) & *Adam* (2 years)

ABSTRACT

Incorporating geosynthetic materials in civil engineering projects is rapidly growing, especially in the design of earth supported structures. Applications include reinforced earth fills, retaining walls, embankments, road pavement, buried structures and shallow foundations. Numerical modeling of soil-structure interaction problems involving flexible or soft geosynthetic inclusions and large deformations is known to be challenging, especially in the presence of nearby rigid structures. This is attributed to the complicated nature of the created soil-geosynthetic-structure system with different material models and interaction behavior. Analyzing the problem using continuum approaches (e.g. finite element method) consists of finding a unique system of displacements for each component that satisfies both force equilibrium and material continuity. Finite element method has proven to be a powerful tool in modelling boundary value problems, particularly those involving soil-structure interaction.

This thesis is devoted to developing a numerical modeling framework for soil-geosynthetics interaction problems. It reports results from 2D and 3D analyses with explicit modeling of the geometry and material details of the geosynthetic structure and the surrounding backfill. The results are compared with previously reported experimental data tested under controlled laboratory conditions. The research results have been published in refereed journals and conference proceedings. These papers are compiled to produce 7 chapters and 1 appendix in this manuscript-based thesis. Two types of geosynthetics that are commonly used in geotechnical projects are considered using the proposed numerical framework; EPS geofoam and geogrid.

A numerical procedure for modeling the short-term response of EPS geofoam under uniaxial compression loading is first developed and validated for three different EPS geofoam materials. To examine the performance of such model in analyzing complex interaction problems, a laboratory experiment that involves a rigid structure buried in granular material with EPS geofoam inclusion is simulated in 2D analysis. This analysis aims at investigating

the role of geofoam material and geometrical properties on the reduction of earth loads acting on buried structures. The results showed that the introduction of EPS geofoam block immediately above the structure has a significant effect on the contact pressure distribution particularly on the upper wall that is covered by the geofoam inclusion. The proposed FE modeling approach has proven to be efficient in capturing the behavior of EPS geofoam material under complex interaction soil-structure condition.

To further study the role of EPS configuration on the load reduction on a buried structure, two different conditions of EPS arrangements are examined. The first case involves an EPS block placed directly above the buried structure whereas in the second case three geofoam blocks were placed above the upper wall and next to the side walls of the structure. A comparison between the numerical results of the two examined cases was made. This comparison showed that adding EPS blocks next to the side walls decreases the earth pressure significantly on the lower and side walls while increases the contact pressure on the upper wall of the structure. The calculated pressures on the buried box were compared with the theoretical overburden pressure in addition to the surface loading. Preliminary design charts are proposed with an example to allow for the proper choice of EPS material that satisfies a specific embankment height.

The rest of the thesis is devoted to introduce a numerical framework that is suitable for the three-dimensional analyses of applications involving soil-geogrid interaction. In chapter five, the geogrid response is investigated under unconfined and soil-confined conditions. A numerical model that is capable of simulating the response of the unconfined biaxial geogrid under tensile loading is first introduced and validated using index test results. In developing this model, the three-dimensional details of the geogrid geometrical features are explicitly simulated. To confirm the validity of this unconfined model, and to investigate the soil-geogrid interaction, a reinforced subgrade subjected to a square shaped surface loading is simulated in three dimensions. The FE approach has proven to be efficient in capturing the 3D response of both unconfined and soil-confined geogrid conditions.

The proposed modeling approach for soil-confined geogrid is further adapted and used in another 3D analysis to investigate the behavior of biaxial geogrid embedded in granular

backfill and subjected to pullout loading. Modeling the 3D soil-geogrid interaction under these loading conditions is challenging and requires a special consideration to simulate the different modes of resistance that contribute to the pullout capacity under large deformations. The results of the numerical analysis are compared with experimental data. The detailed behavior of the geogrid, the surrounding backfill, the geogrid displacements and stresses, and the contact surface are investigated.

Finally, conclusions and recommendations are made regarding the suitability of the FE framework to solve the soil-geosynthetics interaction problems.

RÉSUMÉ

L'intégration de matériaux géosynthétiques dans des projets de génie civil se développe rapidement, en particulier dans la conception d'ouvrages de retenue de terre. Les applications comprennent les murs de soutènement, les remblais, la chaussée de la route, les structures enterrées et les fondations peu profondes. La modélisation numérique des problèmes d'interaction sol-structure impliquant des inclusions géosynthétiques flexibles ou souples et de grande déformation est reconnue pour sa complexité, surtout en présence de structures rigides à proximité. Cela est dû à la nature complexe du système sol-géosynthétique structure créée avec des propriétés et modèles de matériaux différents. L'analyse du problème en utilisant une approche des milieux continus (par exemple, la méthode des éléments finis) consiste à trouver un système unique de déplacements pour chaque élément qui satisfait aussi bien l'équilibre des forces et la continuité des matériaux. La méthode par éléments finis est reconnue pour être un outil puissant pour la modélisation des problèmes de valeur limite, en particulier celles impliquant une interaction sol-structure.

Cette thèse a pour objectif majeur l'élaboration d'un concept de modélisation numérique pour les problèmes d'interaction sol-géosynthétiques. Il fait état des résultats des analyse 2D et 3D avec la modélisation explicite de la géométrie et des détails des matériaux de la structure géo synthétique et le remblai environnant. Les résultats sont comparés avec les données expérimentales antérieures précédemment testées dans des conditions de laboratoire contrôlées. Les résultats de la recherche ont été publiés dans des revues à comité de lecture et actes de conférence. Ces documents sont compilés pour produire 7 chapitres et 3 annexes, dans cette thèse sur la base manuscrite. Deux types de géo synthétiques qui sont couramment utilisés dans les projets géotechniques sont considérés en utilisant le cadre numérique proposée; géogrille et Polystyrène expansé (PSE) Geofam.

Une procédure numérique de modélisation du comportement à court terme de Geofam PSE soumis à une charge uni axiale de compression est d'abord développé et validé pour trois matériaux de Geofam PSE différents. Pour examiner les performances de ce modèle dans

l'analyse des problèmes d'interaction complexes, une expérience de laboratoire qui implique une structure rigide enterrée dans un matériau granulaire avec un ajout de Geofom PSE est simulée par analyse 2D. Cette analyse a pour but d'étudier le rôle des matériaux Geofom PSE et des propriétés géométriques sur la réduction des pressions de terre qui agissent sur les structures enfouies. Les résultats ont montré que l'introduction du bloc de Geofom PSE immédiatement au-dessus de la structure a un effet important sur la distribution des pressions de contact, en particulier sur la paroi supérieure qui est couverte par l'ajout de Geofom PSE. L'approche proposée de modélisation par élément fini a prouvé son efficacité dans l'analyse de comportement du matériau Geofom PSE pour des interactions complexes sol-structure.

Pour approfondir l'étude du rôle de la configuration des PSE sur la réduction de pression sur une structure enterrée, deux conditions différentes d'arrangements PSE sont examinés. Le premier cas concerne un bloc de PSE placé directement au-dessus de la structure enterrée alors que dans le second cas, trois blocs de Geofom ont été placés au-dessus de la paroi supérieure et à côté des parois latérales de la structure. Une comparaison entre les résultats numériques des deux cas examinés a été faite. Cette comparaison a montré que l'ajout de blocs de PSE à côté des parois latérales diminue la pression de la terre sensiblement sur les parois latérales inférieures et augmente alors la pression de contact sur la paroi supérieure de la structure. Les pressions calculées sur la zone enterrée ont été comparées à la pression de surcharge théorique en plus de la charge de surface. Des tentatives de conception d'abaques sont proposées, par exemple, pour permettre le bon choix du matériau PSE qui satisfait à une certaine hauteur du remblai.

Le reste de la thèse est consacrée à l'introduction d'un cadre numérique adapté aux analyses en trois dimensions des applications impliquant l'interaction sol-géogrid. Dans le chapitre cinq, le comportement de la géogrid est étudié aussi bien dans des conditions de non-confinement que et de confinement de sol. Un modèle numérique capable de simuler le comportement de la géogrid biaxiale non confinée sous une charge de traction est d'abord introduit et validé en utilisant les résultats des tests d'index. Dans l'élaboration de ce modèle, les détails en trois dimensions des caractéristiques géométriques de la géogrid sont explicitement simulés. Pour confirmer la validité de ce modèle non-confiné, et étudier

l'interaction sol-géogrid, une plate-forme renforcée soumise à une surface de chargement de forme carrée est simulée en trois dimensions. L'approche par Éléments Finis a prouvé son efficacité dans la capture la réponse 3D des deux conditions de géogrid (non-confinée et sol-confinée).

En outre, l'approche de modélisation proposée pour la géogrid sol-confinée est adaptée et utilisée dans le cadre d'une autre analyse 3D pour établir le comportement d'une géogrid biaxiale intégrée dans le remblai granulaire et soumise au chargement par arrachement. Modéliser de l'interaction 3D sol-géogrid dans ces conditions de chargement est difficile et nécessite une attention particulière pour simuler les différents modes de résistance qui contribuent à la résistance à l'arrachement sous de grandes déformations. Les résultats de l'analyse numérique sont comparés aux données expérimentales. Le comportement détaillé de la géogrid, le remblai environnant, les déformations de la géogrid et des contraintes, et la surface de contact sont étudiées.

Enfin, les conclusions et les recommandations sont formulées quant à la pertinence de l'analyse par Éléments Finis pour résoudre les problèmes d'interaction sol-géosynthétiques.

CO-AUTHORSHIP

This thesis contains published materials as well as submitted for publication that are co-authored by M. G. Hussein, and his supervisor, Prof. M. A. Meguid. The finite element analyses were performed by Mahmoud Hussein under the supervision of Prof. Mohamed Meguid. The preparation of the manuscripts has been completed by the candidate, reviewed and approved by his thesis supervisor.

ACKNOWLEDGMENTS

This research is the outcome of an effort where a number of people have been involved. I remain grateful to all of them.

First of all, I wish to express my deepest appreciation and gratitude to my research advisor Prof. Mohamed Meguid for his guidance, encouragement, and support throughout the duration of this research program. His academic insight and deep knowledge in geotechnical engineering and numerical modeling were necessary for the completion of this dissertation.

Many thanks to my colleagues in the geotechnical group at McGill University who directly or indirectly have contributed to the accomplishment of this thesis.

Special thanks are due to the Technical and Administrative Staff of the Department of Civil Engineering at McGill University, notably Mr. Jorge Sayat and Mrs. Franca Della-Rovere.

I would like to express my thanks to the following individuals for their assistance during my studies: Mr. Mohamed Shawki, Dr. Sherif Kamel, Dr. Mostafa El Sayed, Dr. Tamer Elshimi, Dr. Mohamed Feteiha, Dr. Yousry Mowafy, Dr. Ahmed Asran, Dr. Rani Fouad, and Dr. Ahmed Hamdy.

Financial support for this work was provided by: a Collaborative Research and Development grant from Plasti-Fab Company, the Natural Sciences and Engineering Research Council of Canada (NSERC), and McGill University.

I owe deep appreciation and thanks to my parents who have taught me how to be patient, to believe in myself, to be honest with myself and others. Without their love and encouragement for a further education, my achievement so far would not have been possible. Thanks Mom, sisters, and brothers for the love, prayers and support during my study. You have been always available and standing by me whenever needed.

Above all, I am indebted to my wife, Basma, for her love, patience, support and prolonged understanding over the years; to my daughter, Asal and my sons, Anas and Adam, for bringing me a happy life.

LIST OF PUBLICATIONS ARISING FROM THIS THESIS

Refereed Journal Papers

[J1] **Hussein, M.G.** and Meguid, M.A. “A Three-Dimensional Finite Element Approach for Modeling Biaxial Geogrid with Application to Geogrid-Reinforced Soils.” *Geotextiles and Geomembranes*, 44 (3): 295-307, (2016).

<http://dx.doi.org/10.1016/j.geotexmem.2015.12.004>

[J2] **Hussein, M.G.**, Meguid, M.A. “Modeling the Response of Buried Structures Overlain by EPS Geofoam Inclusion.” *Soils and Foundations Journal* (submitted), Manuscript No. SANDF-D-16-00042, (February 2016).

[J3] **Hussein, M.G.** and Meguid, M.A. “Investigation of Soil-Geosynthetic-Structure Interaction Associated with Induced Trench Installation.” *Geotextiles and Geomembranes Journal* (submitted), Manuscript No. G&G 3055, (June 2016).

[J4] **Hussein, M.G.** and Meguid, M.A. “Three-Dimensional Modeling of Soil-Geogrid Interaction Under Pull-out Loading Condition.” *Geotechnical and Geoenvironmental Engineering Journal of ASCE* (to be submitted).

Refereed Conference Papers

[C1] **Hussein, M.G.** and Meguid, M.A. “On the 3D Modeling of Soil-Geogrid Interaction.” *GeoHalifax 2009, the 62nd Canadian Geotechnical Conference*, Halifax, Canada. Paper No. 138 (pp. 986-991), September 2009.

[C2] **Hussein, M.G.** and Meguid, M.A. “Three-Dimensional Finite Element Analysis of Soil-Geogrid Interaction Under Pull-out Condition.” *GeoMontreal 2013, the 66th Canadian Geotechnical Conference*, Montreal, Canada. Paper No. 260 (pp. 452-458), September 2013.

[C3] **Hussein, M.G.** and Meguid, M.A. “On the Numerical Modeling of Buried Structures with Compressible Inclusion.” *GeoQuebec 2015, the 68th Canadian Geotechnical Conference*, Montreal, Canada. Paper No. 577 (8 pages), September 2015.

[C4] **Hussein, M.G.** and Meguid, M.A. "Numerical Modeling of Soil-Structure Interaction with Applications to Geosynthetics." *ICSGE 14, the 14th International Conference on Structural and Geotechnical Engineering – Sustainable Infrastructure: From Research to Practice*, Ain Shams University, Cairo, Egypt. Paper No. 155 (12 pages), December 2015.

Technical Reports

[R1] Meguid, M.A., **Hussein, M.G.**, Ahmed, M. R., Omeman, Z., and Drissi-Kamili, M. "On the Role of EPS Geofoam Inclusion in Reducing Earth Pressure on Buried Structure." *McGill Geo-Group R&D Report No. MGG/PF-11-15-01*, McGill University, Montreal, Canada, November 2015.

Other

[P1] **Hussein, M.G.**, and Meguid, M.A. "Comparative Evaluation of In-Air and In-Soil Geogrid Behavior using 3D Numerical Modelling." *McGill CEGSS Conference*, Montreal, Canada. Paper No. 4, March 2013.

TABLE OF CONTENTS

ABSTRACT	i
RÉSUMÉ	iv
CO-AUTHORSHIP	vii
ACKNOWLEDGMENTS	viii
LIST OF PUBLICATIONS ARISING FROM THIS THESIS	ix
TABLE OF CONTENTS	xi
LIST OF FIGURES	xiv
LIST OF TABLES	xviii
LIST OF SYMBOLS	xix
CHAPTER 1 Introduction	1
1.1. Background.....	1
1.2. Motivation of the Study.....	4
1.3. Objectives and Scope of the Study.....	4
1.4. Format of Thesis.....	5
1.5. Thesis Outline.....	5
CHAPTER 2 Literature Review	8
2.1. Geogrid for Soil Reinforcement Applications.....	8
2.1.1. Soil reinforcement concept	8
2.1.2. Geogrid characterization.....	9
2.1.3. Theoretical considerations of soil-geogrid interaction mechanism	13
2.1.4. Numerical modeling of soil-geogrid interaction.....	19
2.2. EPS Geofoam as Compressible Inclusion	21
2.2.1. The concept of compressible-inclusion function	21
2.2.2. Theory of soil arching in buried conduits.....	22
2.2.3. Techniques of conduit installation.....	24
2.2.4. Imperfect trench installation	27
2.2.5. EPS material characteristics.....	28
2.2.6. ITI design approaches	37
2.2.7. Numerical modeling of soil-structure interaction for box culvert installed using imperfect trench technique.....	40

2.3. Conclusion for the Literature Review	42
CHAPTER 3 Modeling the Response of Buried Structures Overlain by EPS Geofam Inclusion.....	43
3.1. Introduction	44
3.2. EPS Material Model	45
3.2.1. Model components.....	47
3.2.2. Modeling the compression test	52
3.2.3. Effect of lateral confinement	56
3.3. Numerical Analysis of a Buried Structure Installed using ITI Method.....	58
3.3.1. Modeling details	58
3.3.2. Calculated vs. measured earth pressures.....	62
3.3.3. Soil arching mechanism.....	64
3.3.4. Parametric study	66
3.4. Summary and Conclusions.....	75
CHAPTER 4 Numerical Analysis of Buried Structures Installed Using Imperfect Trench Installation.....	77
4.1. Introduction	78
4.2. Description of the Numerical Analysis	81
4.2.1. Models Generation.....	82
4.2.2. Models validation	84
4.2.3. Effect of EPS density.....	88
4.3. Comparison between <i>case-I</i> and <i>case-II</i>	90
4.4. Comparison with theoretical overburden pressure	95
4.5. Design charts for <i>case-I</i> and <i>case-II</i>	99
4.6. Summary and Conclusions.....	102
CHAPTER 5 A Three-Dimensional Finite Element Approach for Modeling Biaxial Geogrid with Application to Geogrid-Reinforced Soils.....	105
5.1. Introduction	106
5.2. Modelling Unconfined Geogrid	108
5.2.1. Tensile tests.....	108
5.2.2. Model development	110
5.2.3. Response to tensile loading.....	120
5.2.4. Exact geometry vs. planer sheet.....	125
5.3. Soil-Confined Geogrid	126

5.3.1. Geogrid-reinforced foundation	126
5.3.2. Numerical modeling of a square footing on geogrid-reinforced soil.....	128
5.3.3. Response of the geogrid.....	135
5.4. Summary and Conclusions	138
CHAPTER 6 Three-Dimensional Modeling of Soil-Geogrid Interaction under Pullout Loading Condition	140
6.1. Introduction	141
6.1.1. Soil-geogrid interface	143
6.1.2. Soil-geogrid interaction under pullout loading.....	144
6.1.3. Background on soil-geogrid pullout modeling	146
6.1.4. Objective of the current study.....	148
6.2. Numerical Modeling of Pullout test	149
6.2.1. Characterization of the simulated pullout setup.....	149
6.2.2. FE-model generation.....	150
6.2.3. Technical details of soil-geogrid interface.....	154
6.2.4. Pullout test modeling	165
6.3. Results and Discussions	167
6.3.1. Validation of the numerical model	167
6.3.2. Response of the geogrid.....	169
6.3.3. Contributions of bearing and frictional resistances	174
6.3.4. Response of the backfill soil.....	182
6.4. Summary and Conclusions	186
CHAPTER 7 Conclusions and Recommendations	188
7.1. Conclusions	188
7.2. Recommendations for future work.....	192
APPENDIX (A) Finite Element Constitutive Models	193
A.1. Introduction	193
A.2. ABAQUS/Extended Mohr-Coulomb Model (EMC)	193
A.3. The Von Mises Isotropic Elasto-Plasticity Model.....	203
REFERENCES	209

LIST OF FIGURES

Figure 1-1	Schematic of soil-geogrid interlocking mechanism.....	2
Figure 1-2	Typical geogrid reinforcement applications	2
Figure 1-3	Applications of geofoam as compressible inclusion.....	3
Figure 2-1	Failure in unreinforced soils, (After Ingold, 1982).....	9
Figure 2-2	Multi-rib tensile test conducted at the current study on biaxial geogrid.....	11
Figure 2-3	Schematic of typical performance tests of geogrid.....	12
Figure 2-4	Definition of reinforcement dimensions (After Jewell et al., 1984)	15
Figure 2-5	Interaction in direct sliding (After Milligan and Palmeira, 1987)	16
Figure 2-6	Interaction in bond resistance (After Milligan and Palmeira, 1987)	17
Figure 2-7	Passive-bearing failure mechanisms on geogrid transverse bars.....	19
Figure 2-8	Soil arching phenomenon in buried conduits	23
Figure 2-9	Pressure transfer within a soil-buried structure system	24
Figure 2-10	Various types of conduit installations.....	26
Figure 2-11	Mechanism of induced trench installation	28
Figure 2-12	EPS uniaxial compression stress-strain curves	33
Figure 3-1	Compression test results for three different EPS geofoam material	46
Figure 3-2	Procedure used to generate ABAQUS input parameters for the EPS geofoam.....	49
Figure 3-3	Decomposition of the total true strain.....	50
Figure 3-4	Hardening rule of the EPS plasticity model.....	50
Figure 3-5	FE model of the compression test.....	53
Figure 3-6	Validation of the EPS material model	54
Figure 3-7	Normal stress distribution (kPa) at 5% strain: a) EPS15, b) EPS22, c) EPS39	55
Figure 3-8	Effect of confining pressure on the stress-strain relationship of EPS material..	57
Figure 3-9	Schematic of the experimental setup	59
Figure 3-10	The finite element mesh used in the buried culvert model	60
Figure 3-11	Model validation for the cases of a) No EPS, b) EPS22 and c) EPS15.....	63

Figure 3-12 In-plane principal stress distribution around the buried structure at applied surface pressure of 140 kPa	65
Figure 3-13 Effect of EPS density on the earth pressure acting on the walls of the structure	68
Figure 3-14 The change in EPS width.....	69
Figure 3-15 Effect of EPS width on the earth pressure acting on the walls of the structure	70
Figure 3-16 The change in EPS thickness	71
Figure 3-17 Effect of EPS thickness on the earth pressure acting on the walls of the structure	72
Figure 3-18 The change in EPS location	73
Figure 3-19 Effect of EPS location on the earth pressure acting on the walls of the structure	74
Figure 4-1 Positive projecting versus induced trench installations	79
Figure 4-2 The finite element mesh used in the model of <i>case-II</i>	83
Figure 4-3 Model validation for <i>case-II</i> : a) No EPS, b) EPS22 and c) EPS15	86
Figure 4-4 Stress distribution around the buried structure for <i>case-II</i>	87
Figure 4-5 Effect of EPS density on the earth pressure acting on the structure (<i>case-II</i>) ...	89
Figure 4-6 Effect of EPS geometric configuration on the change of earth pressure	92
Figure 4-7 Maximum fill height versus pressure reduction (up to 1% EPS strain).....	93
Figure 4-8 Calculated contact pressures around the culvert for three different installations	94
Figure 4-9 Predicted contact pressures vs theoretical overburden pressures for <i>case-I</i>	97
Figure 4-10 Predicted contact pressures vs theoretical overburden pressures for <i>case-II</i> ...	98
Figure 4-11 Proposed design charts for <i>case-I</i> (up to 1% strain)	100
Figure 4-12 Proposed design charts for <i>case-II</i> (up to 1% strain).....	101
Figure 5-1 Multi-rib unconfined tensile test on biaxial geogrid.....	109
Figure 5-2 Experimental axial load-axial strain results in the MD and XMD	110
Figure 5-3 Procedure used to generate ABAQUS input parameters	113
Figure 5-4 Hardening rule of the geogrid plasticity model	114
Figure 5-5 Sample of the geogrid mesh in three-dimensions	119

Figure 5-6 Model performance: experimental versus calculated results	119
Figure 5-7 Geogrid deformation at $U_x = 23$ mm in the XMD:	121
Figure 5-8 Geogrid response at applied displacement of 23 mm: a) Displacement distribution with distance (X) from loaded boundary; b) Stress transfer along the geogrid	122
Figure 5-9 Total displacements in the axial (U_x) and lateral (U_y) directions.....	123
Figure 5-10 Axial and lateral strains at different locations along the geogrid:	124
Figure 5-11 Effect of modeling geogrid as a planer sheet.....	126
Figure 5-12 Plan view of the geogrid mesh for the in-soil model.....	129
Figure 5-13 Complete and partial 3D mesh geometry of the in-soil FE model	130
Figure 5-14 Details of geogrid-soil interaction	133
Figure 5-15 Load-settlement relationships for geogrid-reinforced crushed limestone	134
Figure 5-16 Geogrid deformation at a given footing load (6MPa):.....	136
Figure 5-17 Tensile stresses (S_{xx} & S_{yy}) at footing pressure of 6MPa:	137
Figure 6-1 Pullout failure mechanism: a) reinforced retaining wall and b) reinforced slope	142
Figure 6-2 Pullout and direct sliding mechanisms	143
Figure 6-3 Schematic representation of geogrid pullout components.....	145
Figure 6-4 Plan view of the geogrid mesh and geometry for the pullout model.....	151
Figure 6-5 Details of the 3D mesh geometry for pullout modeling	153
Figure 6-6 Details of soil-geogrid interaction	155
Figure 6-7 surface-to-surface discretization versus node-to-surface discretization	156
Figure 6-8 Coulomb friction model in its basic form.....	157
Figure 6-9 Parameters of direct shear test on soil-geogrid interface	158
Figure 6-10 Coulomb friction model using the penalty contact algorithm	159
Figure 6-11 Contact behavior in the normal direction.....	160
Figure 6-12 Horizontal and vertical interface conditions	163
Figure 6-13 Displacement field of the soil and the geogrid layer at ($\sigma_v = 49$ kPa).....	166
Figure 6-14 Pullout response of the geogrid ($\sigma_v = 49$ kPa).....	168
Figure 6-15 Changes of k_n values on the transverse bars along the geogrid	169

Figure 6-16 Geogrid deformation and relative movements.....	171
Figure 6-17 Geogrid stresses S_{xx} at $U_x = 10$ mm and $\sigma_v = 49$ kPa.....	172
Figure 6-18 Average tensile force T_{xx} in the longitudinal members ($\sigma_v = 49$ kPa)	173
Figure 6-19 Procedure to assess the accumulative contributions of the bearing members	175
Figure 6-20 Cumulative contribution of the bearing members to the total pullout resistance	176
Figure 6-21 Components of the pullout resistance ($\sigma_v = 49$ kPa)	177
Figure 6-22 Contact pressure developed on T-bars versus frontal displacement.....	178
Figure 6-23 Contribution of the transverse members to the total bearing resistance	179
Figure 6-24 Effect of removing transverse bars (reference to Figure 6-19).....	180
Figure 6-25 Change in tensile forces under different conditions at $U_x = 10$ mm (reference to Figure 6-19).....	181
Figure 6-26 Distribution of the vertical stresses (S_{zz}) in the soil specimen	182
Figure 6-27 Displacement field of the soil specimen at $U_x = 10$ mm.....	184
Figure 6-28 Contour plot of AC YIELD in soil at $U_x = 10$ mm.....	185
Figure A-1 Mohr-Coulomb failure criterion.....	194
Figure A-2 Elastic-perfectly plastic assumption of Mohr-Coulomb model	195
Figure A-3 Classical Mohr-Coulomb yield surface in meridional and deviatoric planes .	196
Figure A-4 Mohr-Coulomb yield surface in principal stress space.....	197
Figure A-5 ABAQUS Mohr-Coulomb yield surface in meridional and deviatoric planes	199
Figure A-6 Family of hyperbolic flow potentials in the meridional plane	201
Figure A-7 Menétrey-Willam flow potential in the deviatoric plane	201
Figure A-8 The Von Mises yield criterion in the Π -plane	204
Figure A-9 The Von Mises yield surface	204
Figure A-10 Procedure used to generate ABAQUS input parameters	208

LIST OF TABLES

Table 2-1 Physical property requirements of EPS geofoam (ASTM/D6817-15).....	31
Table 2-2 Interface friction angles between EPS geofoam and dissimilar materials	35
Table 3-1 Properties of the backfill, geofoam and HSS structure used in the model.....	51
Table 5-1 Index properties of the biaxial geogrid.....	109
Table 5-2 Soil input parameters used in the FE analysis of the reinforced-foundation.....	131
Table 6-1 Soil input parameters used in the FE analysis of pullout test.....	152

LIST OF SYMBOLS

Roman Symbols

2D	Two-dimensional analysis
3D	Three-dimensional analysis
EPS	Expanded polystyrene geofoam
FE	Finite element
PET	Polyester type of geogrid
PP	Polypropylene type of geogrid
HDPE	High density polyethylene type of geogrid
P	Interface shear strength
W_r	Width of reinforcement sample
L_r	Length of reinforcement sample
A_r	Grid surface area
f	Interface coefficient
f_{ds}	Interface coefficient due to direct sliding
f_b	Interface coefficient due to bond/pullout
S	Distance between transverse bars of geogrid
B	Thickness of geogrid bearing members
P_{ds}	Direct sliding shear resistance
$P_{s/r}$	Soil-to-reinforcement shear resistance
$P_{s/s}$	Soil-to-soil Shear resistance
P_b	Total pullout (bond) resistance
P_{pb}	Passive-bearing resistance
c	Cohesion of soil
N_c and N_q	Bearing capacity factors

F_v	Vertical frictional forces
H	Height of fill
B_c	Culvert width or diameter
ITI	Induced trench installations
XPS	Extruded polystyrene foam
M-S	Marston-Spangler design method
C_n	Load coefficient
r_{sd}	Settlement ratio
N_A	Arching factor
S_v	Janbu's friction number
K_A	Active earth pressure
HSS	Hollow steel section
V_z	Velocity in z -direction
U_z	Displacement in z -direction
MD	Machine direction test of the geogrid
XMD	Cross machine direction test of the geogrid
U_x	Displacement in x -direction
PEEQ	Equivalent plastic strain
S_{xx}	Stress component in x -direction
U_y	Displacement in y -direction
C3D8	8-noded three-dimensional continuum element
CPE4	4-noded plane strain continuum element
F^*	Pullout resistance factor or coefficient of interaction parameter
L_e	Effective length of reinforcement
TS	Top soil above the geogrid layer
BS	Bottom soil below the geogrid layer
GEO	Geogrid layer embedded in soil

Soil _{OPN}	Soil elements filling the geogrid openings
k_n	Contact/Normal stiffness
k_s	Shear/Tangential stiffness
h	Penetration distance
S_t	Deviatoric stress in uniaxial tension
S_c	Deviatoric stress in uniaxial compression
f_{yt}	Strength of Mohr-Coulomb material in uniaxial tension
f_{yc}	Strength of Mohr-Coulomb material in uniaxial compression
MC	Mohr-Coulomb failure criterion
EMC	Extended Mohr-Coulomb model of ABAQUS
E	Young's modulus
R_{mc}	A measure of the MC yield surface shape in the deviatoric plan
R_{mw}	Polar radius of Menétrey and Willam flow potential function
$c _0$	Initial cohesion yield stress at zero plastic strain

Greek Symbols

σ_1'	Effective vertical stress
σ_3'	Effective lateral stress
ϕ	Internal friction angle (deg)
σ_n	Normal stress
δ	Interface friction angle (deg)
α_s	Solid fraction surface area
α_b	Fraction of grid width available for bearing
σ_{pb}	Passive-bearing stress
γ	Unit weight of soil
σ_n	Vertical earth pressure

ϵ_{c-true}	True compressive strain
σ_{c-true}	True compressive stress
ϵ_{c-nom}	Nominal compressive strain
σ_{c-nom}	Nominal compressive stress
ν	Poisson's ratio
ϵ^{el}	Elastic true strain
ϵ^{pl}	Plastic true strain
ψ	Dilation angle
E_{slip}	Elastic slip
σ_{hx}	Lateral earth pressure in x -direction
σ_{hy}	Lateral earth pressure in y -direction
ϕ_p	Peak friction angle (deg)
ϕ_{cv}	Constant volume (critical state) friction angle (deg)
μ	Coefficient of friction
τ	Shear stress
ϵ_{true}	True tensile strain
σ_{true}	True tensile stress
ϵ_{nom}	Nominal tensile strain
σ_{nom}	Nominal tensile stress
σ_e	Equivalent Von Mises stress
σ_y	One-dimensional yield stress
J_2	The second invariant of the deviatoric stress
ϵ_e	Von Mises effective strain
α	Scale effect correction factor
$\tau_{critical}$	Critical shear stress
Θ	The deviatoric polar angle

CHAPTER 1

Introduction

1.1. Background

Geosynthetics are polymeric materials used in different geotechnical engineering applications to provide one or more of the following functions: separation, filtration, drainage, reinforcement, fluid containment, erosion control, protection, or compressibility (CFEM, 2006). Recent progress on this family of materials has led to a classification which categorizes the geosynthetics based on the manufacturing method. These categories include geotextiles, geogrids, geonets, geomembranes, geocomposites, geosynthetic clay liners, geopipes, geocells, and geofoams (Koerner, 2012). The research work reported in this thesis aims at investigating the potential benefits of using two types of the previously mentioned geosynthetic materials: geogrids and geofoams in geotechnical engineering.

Geogrids are geosynthetic materials that are designed specifically for soil reinforcement. Their three-dimensional open structure, Figure 1-1, which interlocks with the surrounding soil, leads to a cost effective design (Sobhi and Wu, 1996). Geogrids add tensile strength to a soil mass in order to produce — in combination with the soil — a composite that has improved strength and deformation characteristics compared to the unreinforced soil. Geogrid reinforcements are used for various applications in geotechnical engineering such as reinforced earth fills, retaining walls, embankments, road pavement and shallow foundations (Figure 1-2).

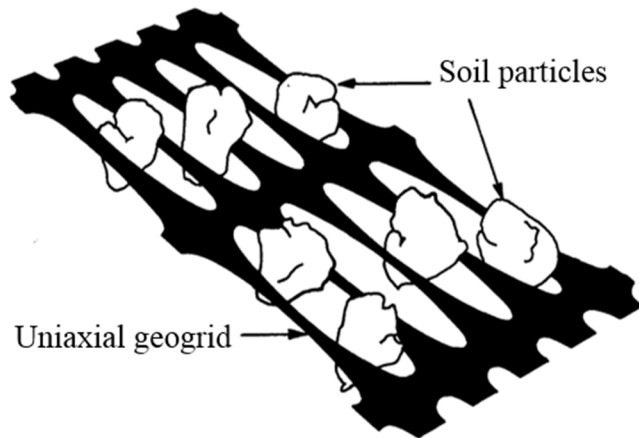


Figure 1-1 Schematic of soil-geogrid interlocking mechanism

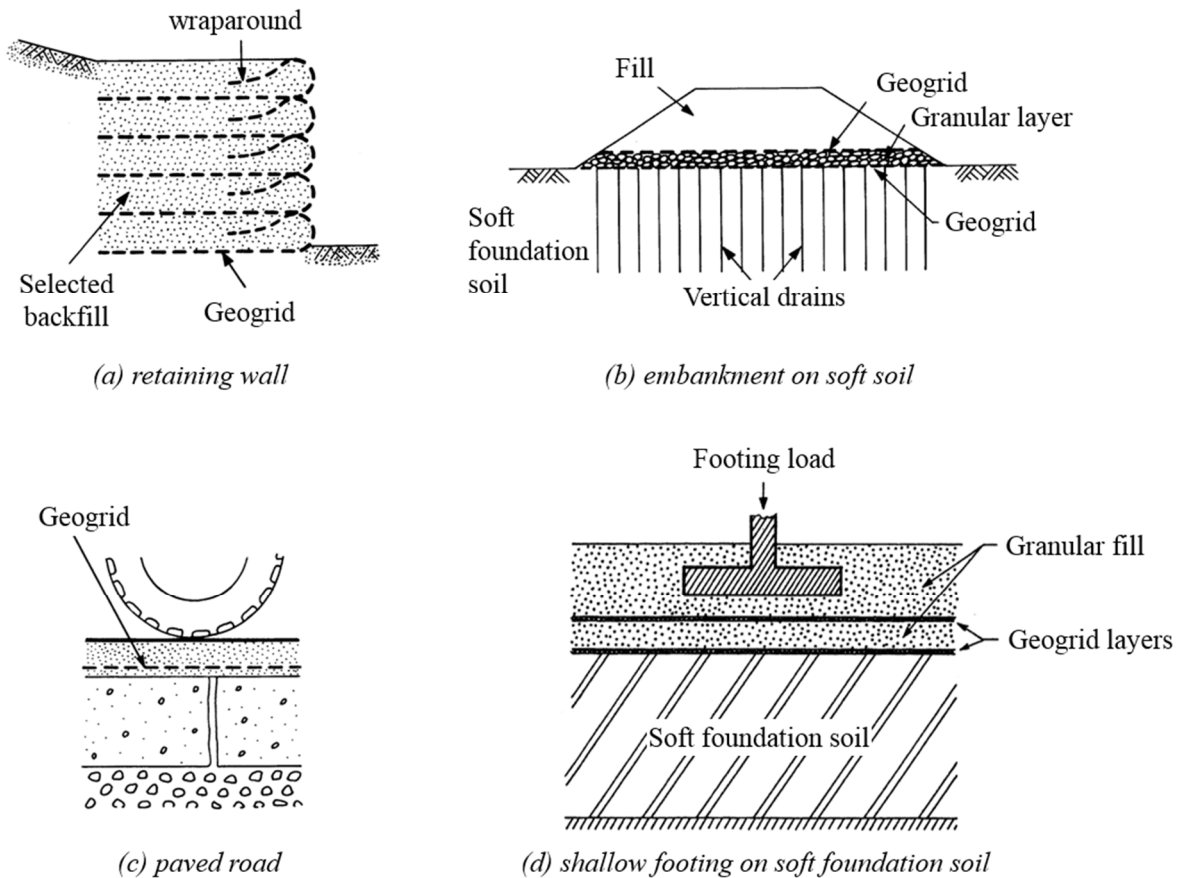


Figure 1-2 Typical geogrid reinforcement applications

Geofoam blocks are geosynthetics that have been created by the expansion of polystyrene foam to form a low-density network of closed, gas-filled cells (Horvath, 1995). Expanded polystyrene (EPS) geofoam is used as a multi-functional key element in a wide variety of geotechnical applications. Among these applications, EPS provides numerous functions, including thermal insulation, as a lightweight fill, as a compressible inclusion, or as a noise, vibration, and seismic buffer to mitigate the effect of dynamic loads on geotechnical structures. The work reported in this thesis investigates a type of application that involves geofoam used primary as a compressible inclusion. Selected examples of geotechnical structures that utilize the EPS compressibility function are shown in Figure 1-3.

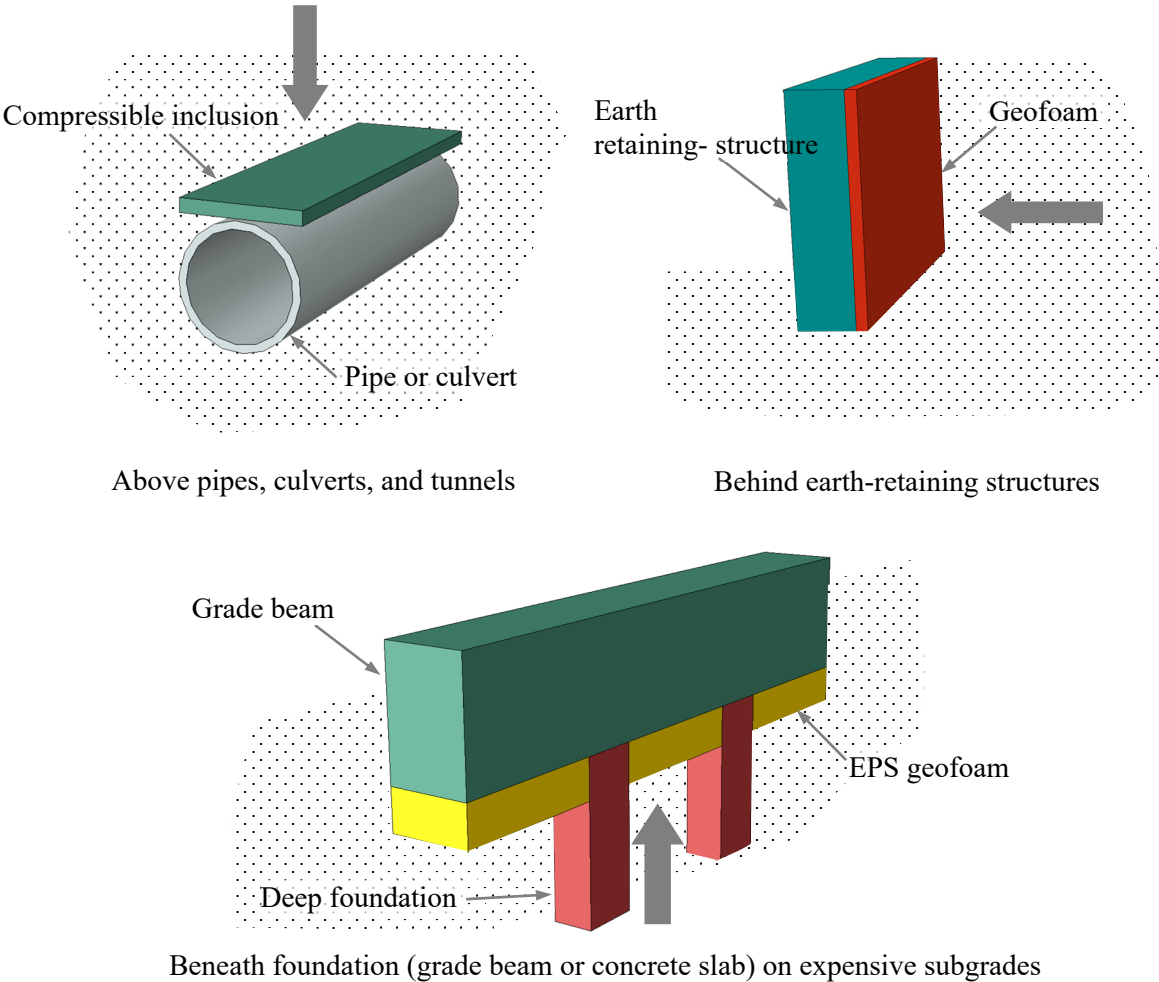


Figure 1-3 Applications of geofoam as compressible inclusion

1.2. Motivation of the Study

Numerical modeling of soil-structure interaction problems involving flexible or soft geosynthetic inclusions is known to be challenging, especially in the presence of rigid structures (e.g. footings, walls, or buried conduits). This is attributed to the complicated nature of the soil-geosynthetic-structure system with different material models and interaction behavior. Analyzing the problem using continuum approaches (e.g. finite element method) involves finding a unique system of displacements for each component that satisfies both force equilibrium and material continuity. Finite element method has proven to be a powerful tool in modelling boundary value problems, particularly those involving soil-structure interaction. In solving this class of problems, modeling issues that need to be carefully addressed include the interaction between the different elements of the composite system, particularly, contact nonlinearity analysis.

Thus, the goal of this study is to develop a FE framework that is appropriate for solving this class of problems. This framework is able to investigate the independent behavior of soil, geosynthetic material, and rigid structure with the capacity of modeling the integrated soil-geosynthetics-structure system. Additionally, the developed FE framework is validated using experimental data and can be adapted to solve different classes of soil-geosynthetics interaction problems.

1.3. Objectives and Scope of the Study

The main objective of this research is to propose a finite element methodology to analyze a particular class of geotechnical problems that involves geosynthetic inclusion. This objective is achieved by addressing the following:

- 1) Develop and validate a material model for EPS geofoam that simulates the true behavior of the geofoam used as a compressible inclusion.
- 2) Quantify and explain the effect of placing an EPS block above and around a buried box culvert on the earth pressure distribution transferred to the walls of the buried structure.

- 3) Develop and validate a geogrid material model used for soil reinforcement. The tensile response of unconfined geogrid is examined by simulating standard tensile tests conducted in the laboratory.
- 4) Analyze a square footing over geogrid-reinforced backfill and understand the behavior of the soil-geogrid interaction system.
- 5) Develop an innovative FE modeling approach to analyze the behavior of a biaxial geogrid embedded in granular material under pullout loading condition.

1.4. Format of Thesis

This thesis has been prepared in a manuscript format in accordance with the regulations and stipulations of the Faculty of Graduate Studies at McGill University. Papers J1, J2, J3, J4, C1, C2, C3, and C4 outlined in the publication list are all the candidate's original work and are included in the thesis. Chapter 3 has been submitted to Soils and Foundations Journal. Chapter 4 will be submitted to Geotextiles and Geomembranes Journal as twin papers. Chapter 5 has been published in Geotextiles and Geomembranes Journal. Chapter 6 is being prepared for publication. An overall conclusion is included in Chapter 7. Additional information is provided in the appendices.

1.5. Thesis Outline

The thesis is organized in seven chapters. After this introduction, Chapter 2 reviews the literature on the numerical modeling of soil-structure interaction problems involving geosynthetic materials. The theoretical background to formulate the behavior of geofoam and geogrid is also outlined. Chapters 3 and 4 are modified versions of journal papers J2 and J3, while Chapters 5 and 6 are versions of journal papers J1 and J4 in the publication list, respectively.

Chapter 3 presents the development of the geofoam material model, its calibration, and validation. A series of plane strain finite element analysis is then performed to investigate the role of EPS density, width, thickness and location on the earth pressure distribution acting

on a rigid buried structure installed using the induced trench method. The numerical results are compared with experimental measurements. The chapter is a modified version of paper J2 in the publication list.

Chapter 4 investigates the efficiency of the FE modeling developed in chapter 3 to further examine the role of EPS configuration on the earth pressure on a buried structure. In this analysis the EPS geofilm inclusion is placed above the upper wall and next to the side walls of the buried box. A comparative study is then performed to evaluate the optimum EPS arrangement by examining the numerical results and compare them with the conventional induced trench method developed in chapter 3 whereas the EPS block was placed on the upper wall only. The calculated pressure on the buried box were also compared to the theoretical overburden pressure. Preliminary design charts that provide a relationship between the pressure reduction ratio and the EPS type for a given fill height were proposed. The chapter presents the work carried out in paper J3 in the publication list.

Chapter 5 presents numerical simulations to investigate the behavior of unconfined and soil-confined geogrid in three-dimensional space. A numerical model that has been developed to simulate the response of the unconfined biaxial geogrid under tensile loading is first introduced and validated using index test results. The details of the geogrid geometrical features are explicitly simulated. The difference between modelling the exact geogrid geometry as opposed to an equivalent sheet is also examined. To confirm the validity of the unconfined geogrid model, and to investigate the soil-geogrid interaction, a 3D analysis is conducted to investigate a reinforced subgrade subjected to a square shaped surface loading. The chapter is a modified version of paper J1 in the publication list.

Chapter 6 investigates the pullout behavior of biaxial geogrid embedded in granular soil using the 3D FE approach that has been developed in chapter 5. In developing this analysis, the geogrid was modeled using an elasto-plastic constitutive material model whereas the backfill soil is simulated using Mohr-Coulomb failure criterion. A detailed procedure of the contact technique used throughout the analysis is described. This includes the contact constitutive models in both the tangential and the normal direction, the contact discretization, and the

constraints evolution. A softened contact pressure-overclosure model is used to simulate the behavior of the transverse members. The results of the analysis were compared with experimental data. The displacements and stresses developing in the geogrid were analyzed and the backfill movements and plastic strains were investigated. The proposed FE approach has proven efficient to model the pullout experiment in three-dimensional space and capturing the response of both the geogrid and the surrounding backfill material. The chapter presents the work carried out in paper J4 in the publication list.

The thesis ends with Chapter 7 that contains a set of conclusions and recommendations for future work.

CHAPTER 2

Literature Review

Literature related to the theoretical, experimental and numerical modeling of geotechnical engineering problems involving geogrids and geofoms is summarized in this chapter. In addition, soil-structure interaction techniques available to simulate this class of problems are reviewed.

2.1. Geogrid for Soil Reinforcement Applications

Geogrid reinforcement has been shown to be an effective method to enhance the performance and service life of different earth structures (e.g. embankments, pavements, foundations and retaining walls). In this section, an extensive literature review has been conducted covering the basic background of soil-geogrid interaction, including, the physical and mechanical properties of the geogrid material, and the laboratory experiments as well as the numerical modeling of the soil-geogrid reinforcement systems.

2.1.1. Soil reinforcement concept

Soil is a material that is, generally, strong in compression and shear, but has virtually no tensile strength. By adding reinforcement — a material exhibiting high tensile strength — to compensate for soil's lack of tensile resistance, a composite material can be formed. This new composite material is analogous to reinforced concrete and has far superior tensile-strength than the unreinforced material. The improved tensile properties are attributed to the interaction between the reinforcement and the soil. It has been suggested by Henri Vidal — the inventor of *Reinforced Earth* in 1963 — that the reinforcement acts to increase the effective confining pressure in the soil. This concept was later investigated by Ingold (1982) as follows:

- Unreinforced soils follow the Mohr-Coulomb failure criterion which for a granular soil may be simply defined by two linear failure envelopes, as shown in Figure 2-1.

If a soil element is loaded by a vertical principal stress (σ_1') then in order for the element not to fail, there must also be a lateral confining stress (σ_3') forming with (σ_1') a Mohr's circle that does not cross the limiting failure envelope.

- If the externally applied confining pressure is reduced to zero, then under the action of (σ_1') the Mohr's circle will cross the failure envelope which represents a condition of shear failure.
- So intuitively, the concept of reinforcing soils can be defined as the introduction of an inclusion that resists tensile stresses and consequently increases the soil confining stresses.

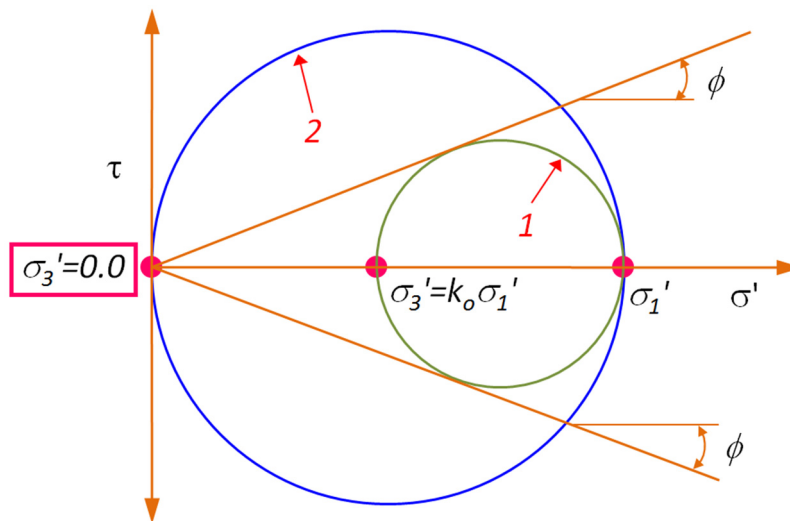


Figure 2-1 Failure in unreinforced soils, (After Ingold, 1982)

2.1.2. Geogrid characterization

According to the ASTM definition, “A geogrid is any planar structure formed by a regular network of tensile elements with apertures of sufficient size to allow interlocking with surrounding soil, rock or any geotechnical material to perform the functions of reinforcement and/or segregation”, (ASTM/D6706-01, 2013).

Material properties of geogrid

The polymers commonly used as raw material for geogrids are usually polyester (PET), polypropylene (PP) and high density polyethylene (HDPE). Geogrids, being polymer-based products, are viscoelastic, which means that, under working conditions, their performance is dependent on the temperature, the stress, the rate and duration of the applied load.

a) Physical properties of geogrid

Many of the physical properties of geogrids can be measured directly and are relatively straightforward. These include the type of structure, junction type, aperture size, and thickness. Other properties that are of interest are mass per unit area, which varies over a wide range from 200 to 1000 g/m², and percent open area, which varies from 40% to 95% (Koerner, 2012).

An additional physical property of geogrids that is of interest is its bending stiffness. This can be measured using ASTM/D1388-14e1 (2014) test for flexural rigidity. The method uses a 1-in. (25 mm) wide strip of geogrid specimen and placed lengthwise over the edge of a horizontal surface. The length of overhang is measured when the tip of the specimen bends under its own weight and just touches an inclined plane making an angle of 41.5 degrees with the horizontal. One half of this length is the bending length of the specimen. The cube of this quantity multiplied by the mass per unit area of the geotextile is its flexural rigidity, or stiffness (Shukla, 2002).

b) Mechanical properties of geogrid

There are several mechanical properties for geogrid, some of them are index tests (in-air), while others are performance related (in-soil).

Index properties and tests

Index tests are carried out under standardized conditions used to compare the basic properties of geogrid tests (e.g. wide-width tensile strength, creep under load, friction properties, etc.).

These are generally used in quality control and quality assurance and reflect design features or applications.

Tensile strength of geogrid is defined as the peak load that can be applied per unit width. Tensile strength is generally determined by a tensile test on a 200 mm wide strip (ASTM/D6637M-15, 2015), to approximate plane strain conditions (Figure 2-2). The test provides parameters such as peak strength, elongation and tensile modulus.

Tensile modulus is the slope of the stress-strain curve, as determined from tensile test procedures. This is equivalent to Young's modulus for other construction materials (e.g. concrete, steel, timber and/or etc.).

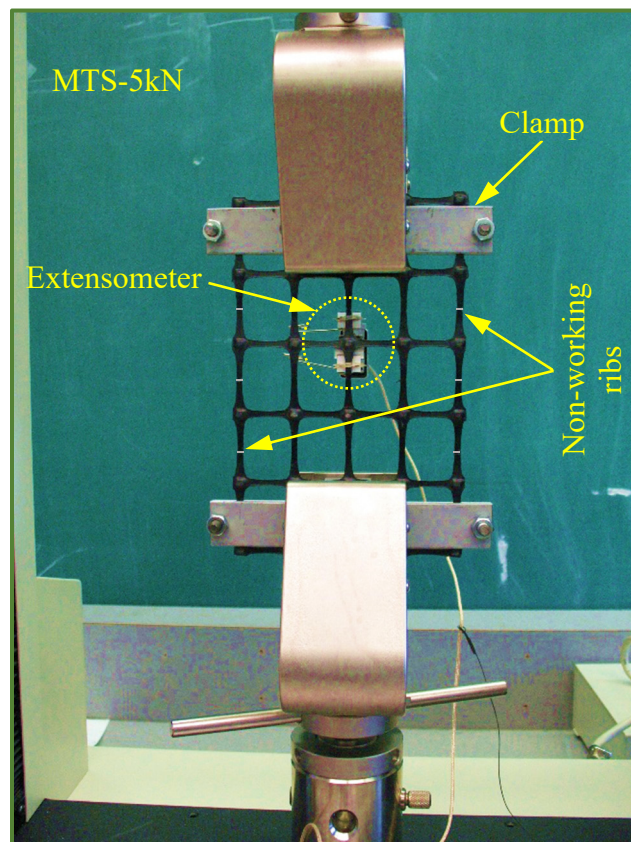


Figure 2-2 Multi-rib tensile test conducted at the current study on biaxial geogrid

Performance properties and tests

Performance tests are carried out by placing the geogrid in contact with soil under standardized conditions in the laboratory. Laboratory investigations of soil-geogrid interaction has generally been restricted to shear box and pullout tests. These two methods model the soil-geogrid bond in different ways. Pullout test is used to model the reinforcement-soil load transfer mechanism in the anchorage zone of slopes and walls, Figure 2-3a. Shear box test is applicable to potential failure mechanisms where failure propagates along the plane of the reinforcement. It can be used to quantify the frictional bond between soils and the solid area of the reinforcement, Figure 2-3b.

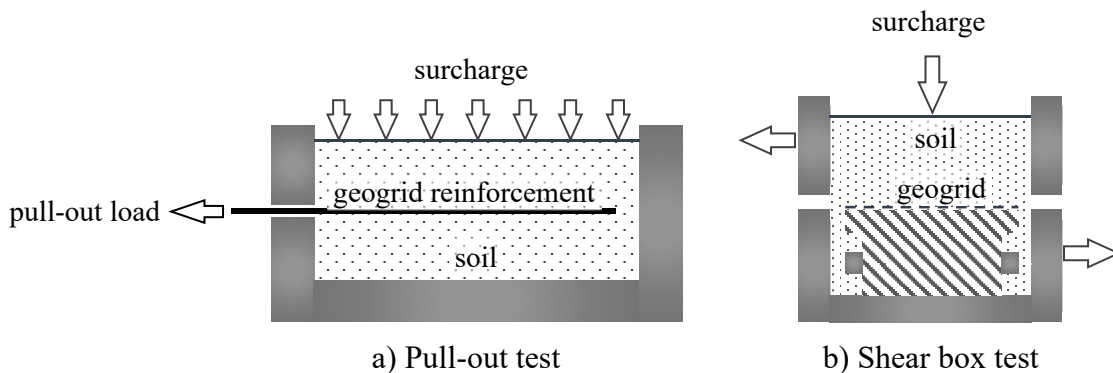


Figure 2-3 Schematic of typical performance tests of geogrid

Pull-out test

Pull-out test is used to study the anchorage capacity of extensible and inextensible reinforcement embedded in soil. The test involves pulling a geogrid reinforcement sample out of a soil filled box, usually at a constant rate of displacement. Surcharge loads are applied at the soil surface to simulate variable depths of overburden. The pull-out test results are affected by many factors, including, equipment boundary condition, testing procedure, the size of the reinforcement sample, and backfill material. The influence of these factors on the pull-out test were reviewed by several researchers (e.g. Palmeira and Milligan, 1989, Lopes and Ladeira, 1996, Moraci and Recalcati, 2006).

Direct shear test

Direct shear tests are commonly used to determine the shear strength parameters of granular soils. Due to their simplicity and consistency of results, direct shear tests remain popular in practice and are preferred over more sophisticated tests. The geosynthetic is placed freely between the two halves of the shear box or is glued to the lower half and the upper half moves under lateral loading. Frictional resistance in the direct shear test is largely a function of the surface roughness of the geosynthetic and the interlocking of the soil particles. In contrast to research on pullout tests on reinforced soil, very few investigations on direct shear tests are available, especially for large samples. The sizes of shear box used to determine the shear strength of composites vary greatly. They range from a conventional (60 x 60 x 32 mm) shear box to (330 x 330 x 330 mm). Again a small shear box may not provide parameters which would be indicative of the shear behaviour of the reinforced earth structures.

2.1.3. Theoretical considerations of soil-geogrid interaction mechanism

Finding the interaction mechanism between soil and geogrids is very essential in the design and analysis of geogrid-reinforced soil structures. Stresses in the reinforcing elements are transferred to the surrounding soil through the bond between the soil and the reinforcement. This bond generally comes from i) friction, ii) passive soil resistance, or iii) a combination of both. To maintain equilibrium, the bond must resist the maximum tensile load carried by the reinforcing element.

In the 1980's and 1990's, researchers developed theoretical approaches to describe the soil-reinforcement interaction. Jewell et al. (1984) and Milligan and Palmeira (1987) classified the different modes in which the reinforcement interacts with soils within a reinforced soil element into three main forms:

- skin friction along the reinforcement
- soil-soil friction
- passive (bearing) resistance on the transverse members of the reinforcement

There are two main mechanisms that are responsible for the mobilization of strength at the soil-reinforcement interface. The first mechanism is a *direct sliding resistance* (when a block

of soil slides across one side of the reinforcement that is linked to the soil on the other side), while the second is a *bond (pull-out) resistance mechanism* (when the reinforcement moves in relation to the surrounding soil).

The reinforcements can be divided into three groups, namely: (i) planer sheet; (ii) strip over planer sheets; (iii) grid. For sheet and strip type reinforcements, the soil-reinforcement interactions are controlled by friction between the soil and the reinforcement (the first mechanism) only. However, for grid reinforcements, the direct sliding resistance mode is controlled not only by the friction between the soil and the grid surface area but also by the friction of the soil itself. The bond (pull-out) resistance mode is governed by the friction between the soil and the grid surface as well as the bearing resistance of the soil on the transverse members of grid. Usually, the bearing resistance is much higher than the friction resistance (Chang et al., 1977, Milligan and Palmeira, 1987).

The general form of the soil-reinforcement interface shear strength can be defined as:

$$P = 2W_r L_r \cdot \sigma_n \cdot f \cdot \tan \phi \quad (2.1)$$

where σ_n is the normal stress at the reinforcement level, ϕ is the soil friction angle, W_r and L_r are defined in Figure 2-4, f is the interface coefficient ($0 < f < 1$), A_r is grid surface area ($A_r = W_r L_r$).

Equation 2.1 is for general application and the main challenge usually lies with the definition of f . In fact f depends on the interaction mobilized on the soil reinforcement interface and on the relative movement that occurs on the same interface.

For the case of planer sheet, such as geotextiles, the resistance mechanism is only skin friction. Hence, f is identical and has the same value for direct sliding and pull-out (bond) movements as:

$$f = f_{ds} = f_b = \frac{\tan \delta}{\tan \phi} \quad (2.2)$$

where f_{ds} is the interface coefficient of skin direct sliding, f_b is the interaction coefficient of bond (pull-out), δ is the skin friction angle between the soil and the reinforcement.

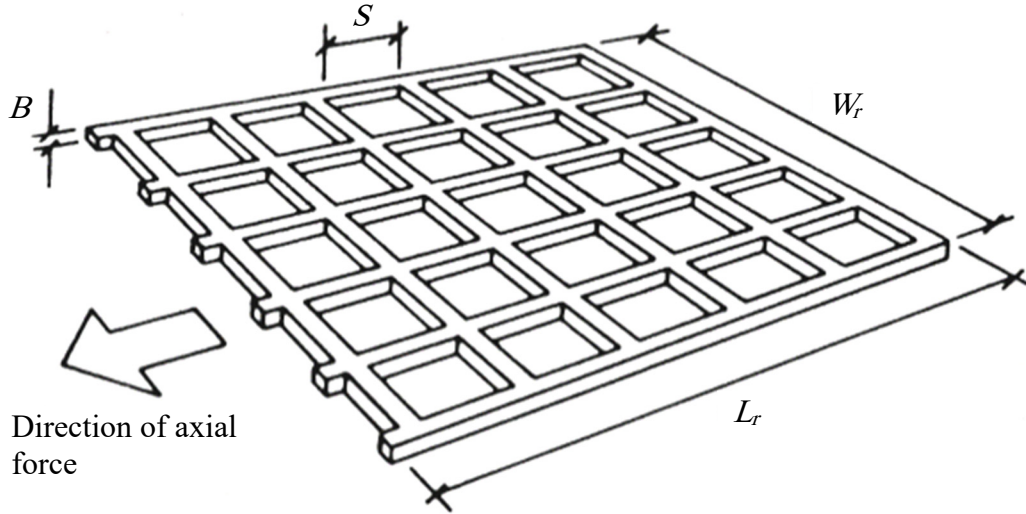


Figure 2-4 Definition of reinforcement dimensions (After Jewell et al., 1984)

For the case of grid reinforcement, such as geogrid, the shear strength of the soil-reinforcement interface is dependent on the mode of movement as described below.

Direct sliding resistance

According to Jewell et al. (1984), the direct sliding resistance between the reinforcement and the soil has two components, namely; the shear resistance between the soil and the reinforcement-plane surface area ($P_{s/r}$), and the soil-to-soil shear resistance at the grid opening ($P_{s/s}$). The direct-shear (sliding) resistance, (P_{ds}), can be expressed as follows:

$$P = P_{ds} = P_{s/r} + P_{s/s} \tag{2.3}$$

where

$$P_{s/r} = 2\alpha_s \cdot W_r \cdot L_r \cdot \sigma_n \cdot \tan\delta \tag{2.4}$$

and

$$P_{s/s} = 2(1 - \alpha_s). W_r. L_r. \sigma_n. \tan\phi \quad (2.5)$$

where α_s is a fraction of grid surface area that is solid (Figure 2-4).

Substitute equations 2.4 and 2.5 in equation 2.3 will result in:

$$P = P_{ds} = 2\alpha_s. W_r. L_r. \sigma_n. \tan\delta + 2(1 - \alpha_s). W_r. L_r. \sigma_n. \tan\phi \quad (2.6)$$

Using equations 2.1 and 2.6:

$$P = 2W_r L_r. \sigma_n. f. \tan\phi = 2\alpha_s. W_r. L_r. \sigma_n. \tan\delta + 2(1 - \alpha_s). W_r. L_r. \sigma_n. \tan\phi$$

Then, the interface (interaction) coefficient of direct sliding (f_{ds}) mode is obtained as:

$$f = f_{ds} = \alpha_s \left(\frac{\tan\delta}{\tan\phi} \right) + (1 - \alpha_s) \quad (2.7)$$

Figure 2-5 shows the different modes of direct sliding mechanisms between soils and three different types of reinforcement.

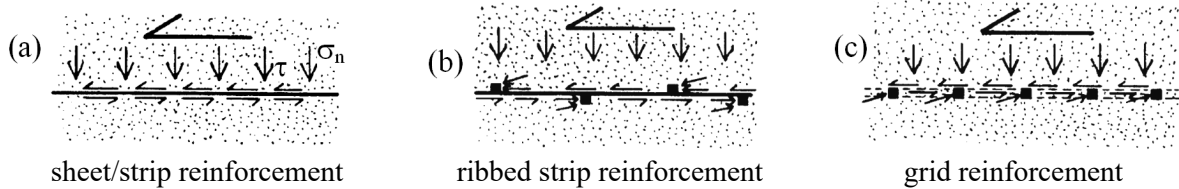


Figure 2-5 Interaction in direct sliding (After Milligan and Palmeira, 1987)

Bond (pull-out) resistance

For the case of pull-out movement, the contribution of a soil-soil ($P_{s/s}$) friction mechanism on soil-reinforcement interface resistance is almost nil as there is no relative movement of the soil on either side of the grid (Milligan and Palmeira, 1987, Lopes, 2002). Generally, the pullout (bond), (P_b), resistance consists of two parts, namely: friction resistance ($P_{s/r}$) and passive-bearing (P_{pb}) resistance on the bearing members.

$$P = P_b = P_{s/r} + P_{pb} \quad (2.8)$$

Where $P_{s/r}$ is expressed by equation 2.4 and P_{pb} is:

$$P_{pb} = \left(\frac{L_r}{S}\right) \alpha_b \cdot W_r \cdot B \cdot \sigma_{pb} \quad (2.9)$$

where L_r is the length of the reinforcement element, S is the distance between bearing (transverse) members, B is the thickness of the bearing members, σ_{pb} is the passive-bearing resistance, and α_b is the fraction of grid width available for bearing. As illustrated in Figure 2-4, L_r/S is the number of bearing surfaces.

Substitute equations 2.4 and 2.9 in equation 2.8 will result in:

$$P = P_b = 2\alpha_s \cdot W_r \cdot L_r \cdot \sigma_n \cdot \tan\delta + \left(\frac{L_r}{S}\right) \alpha_b \cdot W_r \cdot B \cdot \sigma_{pb} \quad (2.10)$$

Using equations 2.1 and 2.10:

$$P = 2W_r L_r \cdot \sigma_n \cdot f \cdot \tan\phi = 2\alpha_s \cdot W_r \cdot L_r \cdot \sigma_n \cdot \tan\delta + \left(\frac{L_r}{S}\right) \alpha_b \cdot W_r \cdot B \cdot \sigma_{pb} \quad (2.11)$$

Then, the interface (interaction) coefficient of bond (f_b) is obtained as:

$$f = f_b = \alpha_s \left(\frac{\tan\delta}{\tan\phi}\right) + \left(\frac{\sigma_{pb}}{\sigma_n}\right) \left(\frac{\alpha_b \cdot B}{S}\right) \left(\frac{1}{2\tan\phi}\right) \quad (2.12)$$

If $\alpha_s = 1$ and $\alpha_b = 0$, equation 2.12 will equal equation 2.2, representing the coefficient of bond of a reinforcement where the only interaction mechanism mobilized is skin friction, as in geotextiles.

Figure 2-6 shows the different modes of bond resistance mechanisms between soils and three different types of reinforcement.

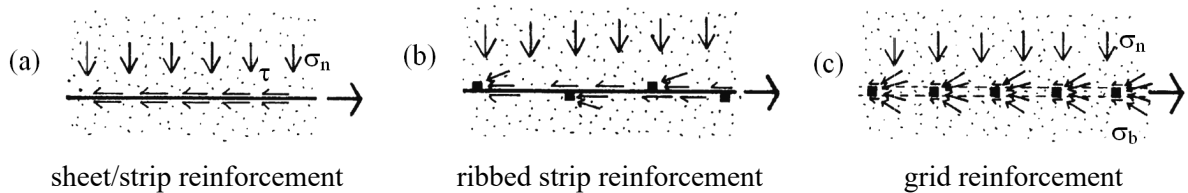


Figure 2-6 Interaction in bond resistance (After Milligan and Palmeira, 1987)

According to Jewell et al. (1984) and Palmeira and Milligan (1989), the passive-bearing resistance (σ_{pb}) in equation 2.12 is evaluated using the bearing-capacity theory and can be expressed as follows:

$$\sigma_{pb} = cN_c + \sigma_n \cdot N_q \quad (2.13)$$

where σ_{pb} is the bearing resistance on grid-bearing members, c is the cohesion of the backfill soil, N_c and N_q are the bearing capacity factors.

Different assumptions have been used for determining the bearing-capacity factors. Peterson and Anderson (1980) assumed a normal characteristic field for a foundation rotated to the horizontal to form a general-failure mode, as shown in

Figure 2-7a. The expressions for N_q and N_c are as follows:

$$N_q = e^{[\pi \tan \phi]} \tan^2\left(\frac{\pi}{4} + \frac{\phi}{2}\right) \quad (2.14)$$

$$N_c = (N_q - 1) \cot \phi \quad (2.15)$$

Jewell et al. (1984) assumed a punching-failure mode for reinforcement passive-bearing resistance. The stress characteristic field is as shown in

Figure 2-7b. The expressions for bearing-capacity factors are:

$$N_q = e^{[\frac{\pi}{2} + \phi] \tan \phi} \tan\left(\frac{\pi}{4} + \frac{\phi}{2}\right) \quad (2.16)$$

$$N_c = (N_q - 1) \cot \phi \quad (2.17)$$

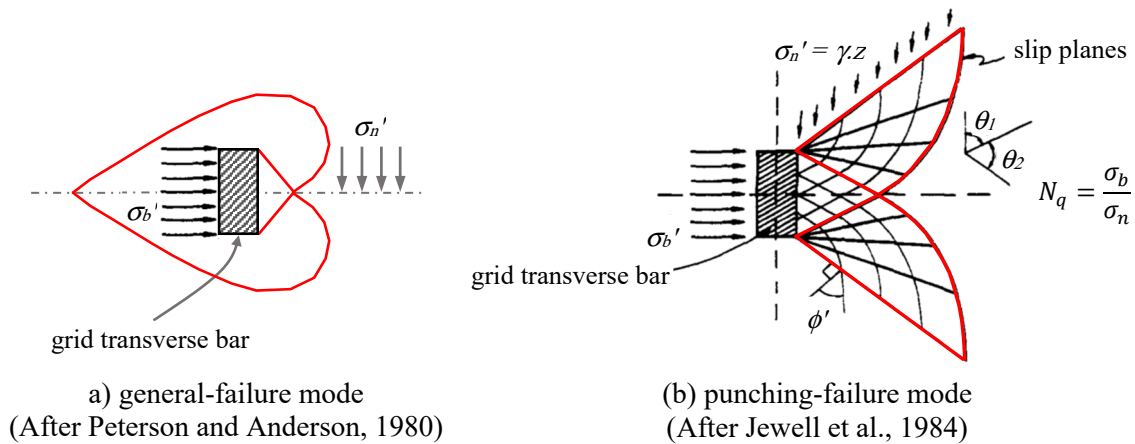


Figure 2-7 Passive-bearing failure mechanisms on geogrid transverse bars

2.1.4. Numerical modeling of soil-geogrid interaction

Modeling soil-geogrid interaction problems is a challenging task particularly in three dimensions. In the past three decades several numerical methods have been used along with laboratory data to develop a better understanding of soil-geogrid interaction. Many of these studies employed the finite element method (e.g. Yogarajah and Yeo, 1994, Hatami and Bathurst, 2005, Prozzi and R., 2007, Hussein and Meguid, 2013), while the others used the discrete element method (e.g. McDowell et al., 2006, Wang et al., 2016) or the coupled finite-discrete element technique (e.g. Tran, 2013).

Yogarajah and Yeo (1994) used the finite-element program CRISP to simulate a pull-out experiment. A two-dimensional model was developed where the geogrid was simulated using bar elements. Joint elements were used to model the interface between the geogrid layer and the soil.

Perkins and Edens (2003) conducted finite-element analysis of a pull-out test using the finite-element software ABAQUS employing the constitutive model suggested by Perkins (2000) for the geogrid layer and the bounding surface plasticity model for the soil. The geogrid was modeled using 4-noded membrane/plane sheet elements. Shear interaction between the geogrid and the aggregate was established using two contact surface pairs employing Coulomb frictional model.

El Sawwaf (2007) studied the potential benefits of reinforcing a replaced layer of sand constructed near a slope crest. The numerical analyses were conducted using the geotechnical finite-element program PLAXIS/2D. In these analyses, the sand was modeled using hardening soil model, which is an elastoplastic hyperbolic stress-strain model. The foundation was treated as elastic beam elements based on Mindlin beam theory with significant flexural rigidity (EI) and normal stiffness (EA). The soil was discretized with six-noded triangle plane strain elements, whereas the footing and the geogrid were simulated with three node beam elements. The interaction between the geogrid and the soil was modeled at both sides by means of interface elements.

Zhuang and Wang (2015) carried out a comparative study to investigate the 3D nature of a biaxial geogrid used in piled embankments. The three-dimensional analyses were performed using the FE software ABAQUS. Even though the analysis was conducted initially to examine the 3D nature of the biaxial geogrid, the geogrid was simulated using three different modeling approaches using membrane and truss elements. Indeed, none of the utilized elements reflect the true geometry of the geogrid structure.

Wang et al. (2016) conducted a two dimensional discrete element (DE) analysis to investigate the soil-geogrid interaction under pull-out loading using PFC^{2d} (Particle Flow Code). The soil was modelled using unbonded particles with linear contact-stiffness model, while the geogrid was modeled using bonded particles using the piecewise linear model (based on parallel bond model).

Although the above studies explained several interesting features of the soil-geogrid interaction under different loading conditions, they were mostly focused on the overall response of the reinforced structure while adopting simplifying assumptions related to either the details of the geogrid geometry or the constitutive model of the geogrid material.

2.2. EPS Geofoam as Compressible Inclusion

Expanded polystyrene (EPS) geofoam has been successfully used as a compressible inclusion in geotechnical engineering projects to induce soil strains and hence reduce earth pressures on the geotechnical structures (e.g. buried structures, retaining walls and structural slabs). In this section, an extensive literature review has been conducted covering the basic knowledge of the geofoam material properties, the benefits of using the geofoam as compressible inclusion around buried structures, and the numerical simulation of the soil-geofoam-culvert system.

2.2.1. The concept of compressible-inclusion function

In geotechnical applications, a compressible inclusion is typically placed between a below-ground structure and the surrounding ground. Because the inclusion is the most compressible component in the system, it will likely to deform more readily than the other system components under an applied load or displacement (Horvath, 1997). The use of a compressible inclusion is a more cost effective alternative than designing the structure to withstand abundant loads. This is especially true in the case of an existing structure that requires upgrading to resist loads larger than those for which it was originally designed.

The concept of using a compressible inclusion in geotechnical applications is not new. Numerous materials have been used since the 20th century as compressible inclusions. For examples, bales of hay or straw, leaves, sawdust, shredded rubber tires, very loose/compressible fill, or expanded polystyrene (EPS) have been previously utilized to induce vertical arching and reduce stresses exerted on the buried structures (e.g. pipes or culverts).

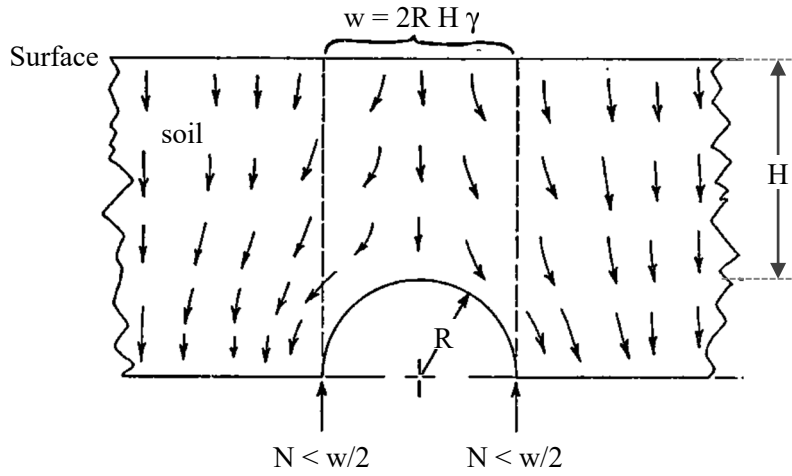
2.2.2. Theory of soil arching in buried conduits

In general, soil arching takes place when a soil prism yields while the remainder soil mass stays stationary. Particularly, in conduits design, the basic concept of soil arching is that a part of the weight of the soil (and any additional surface load) is transferred between the soil prism above the conduit and the adjacent soil prisms. This phenomenon can lead to stresses, on the conduit, that are greater than the total weight of the overlying soil plus the surface loads “*negative arching*”, or it can result in loads that are significantly less “*positive arching*”. Terzaghi (1943) defined this pressure transfer from the yielding soil mass to adjoining stationary parts as *arching effect*. Soil arching theory plays a tremendously important role in calculation of earth loads acting on underground structures.

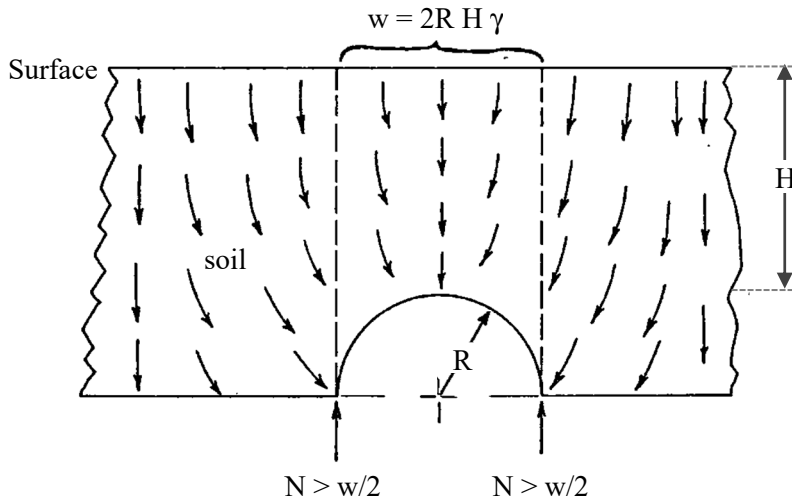
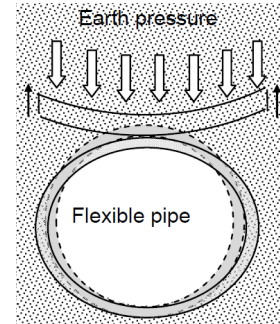
As explained by Katona et al. (1976), positive arching is a favorable condition wherein a portion of the overburden load is diverted around the buried structure in a compression arch. The amount of positive arching is measured by the percent reduction of total springline thrust ($2N$) as compared to the weight (w) of the soil column above the conduit (Figure 2-8a, $N < w/2$). On the other hand, negative arching is unfavorable and implies that the conduit is drawing load in excess of the soil column weight (Figure 2-8b, $N > w/2$).

From the above discussion, it should be noted that positive arching enhances as the soil stiffness increases and/or conduit stiffness decreases. Based on this, conduits are traditionally classified as rigid or flexible structures. Rigid conduits (e.g. reinforced concrete or cast iron) typically have large stiffnesses compared to the surrounding soil and hence likely to induce negative arching unless special construction methods are employed (e.g. induced trench method). In contrast, flexible conduits, generally generate positive arching.

The loading on buried conduits is primarily affected by soil arching, however, soil arching is influenced by the installation technique employed as discussed in the next section.



a) Positive soil arching



b) Negative soil arching

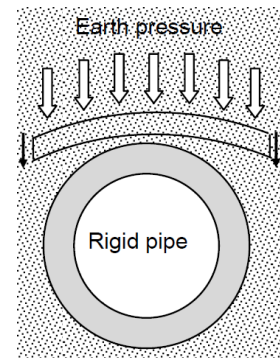


Figure 2-8 Soil arching phenomenon in buried conduits

2.2.3. Techniques of conduit installation

Loads on buried conduits have shown to be dependent upon installation conditions. Due to importance of installation conditions when determining loads, installations of buried structures are classified into two broad categories: trench (ditch) installations and embankment installations (Kim and Yoo, 2002).

Figure 2-9 shows the pressure transfer around a buried conduit due to the relative movements between the soil prisms directly above and adjacent to the conduit. These relative settlements generate frictional stresses that are added to or subtracted from the dead weight of the central prism and affect the resultant load on the conduit. When the relative settlement of the soil prism directly above the structure is less than that of the adjacent soil prisms, as usually found in embankment installations (Figure 2-9a), the layers of soil in the central prism are subjected to an arch shape deformation (*negative*), and the earth load on the structure increases by the downward frictional forces exerted on the central soil prism ($\downarrow F_v$). Likewise, when the relative settlement of the soil prism directly above the structure is greater than that of the adjacent soil prisms, as depicted in the trench installations (Figure 2-9b), the layers of soil in the central prism are subjected to a reverse arch shape deformation (*positive*), and consequently, the earth load on the structure decreases by the amount of the upward frictional forces exerted to the central soil prism ($\uparrow F_v$).

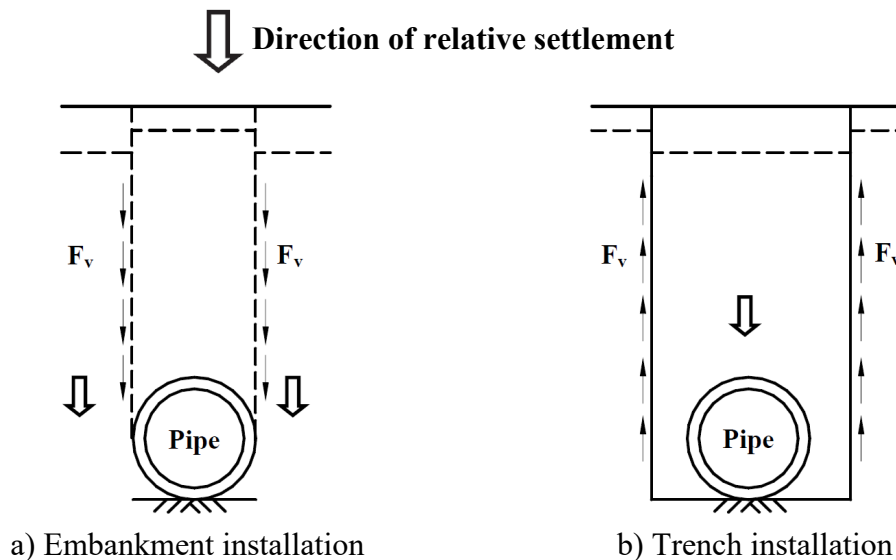


Figure 2-9 Pressure transfer within a soil-buried structure system

Trench (ditch) installation

Conduit installations are called trench installations when the conduit is located completely below the natural ground surface and the backfill over the conduit is placed between vertical or sloping walls of natural (in-situ or undisturbed) soil extending to the surface (ACPA, 1994). Frictional forces between the sides of the trench and the backfill material help to support the weight of the soil overlaying the conduit (Figure 2-10a).

Embankment installation

Embankment installations refer to those installations where soil is placed in layers above the natural ground (ACPA, 1994). Embankment installations are further subdivided based on their location relative to the original ground level. Conduits founded partially or totally above the original ground level are classified as *positive projecting* conduits (Figure 2-10b). While conduits founded in a trench excavated below the original ground level beneath the embankment are classified as *negative projecting* conduits (Figure 2-10c). Negative projecting procedure is a very favorable method of installing a railway or highway conduit, since the load produced by a given height of fill is generally less than it would be in the case of a positive projecting conduit.

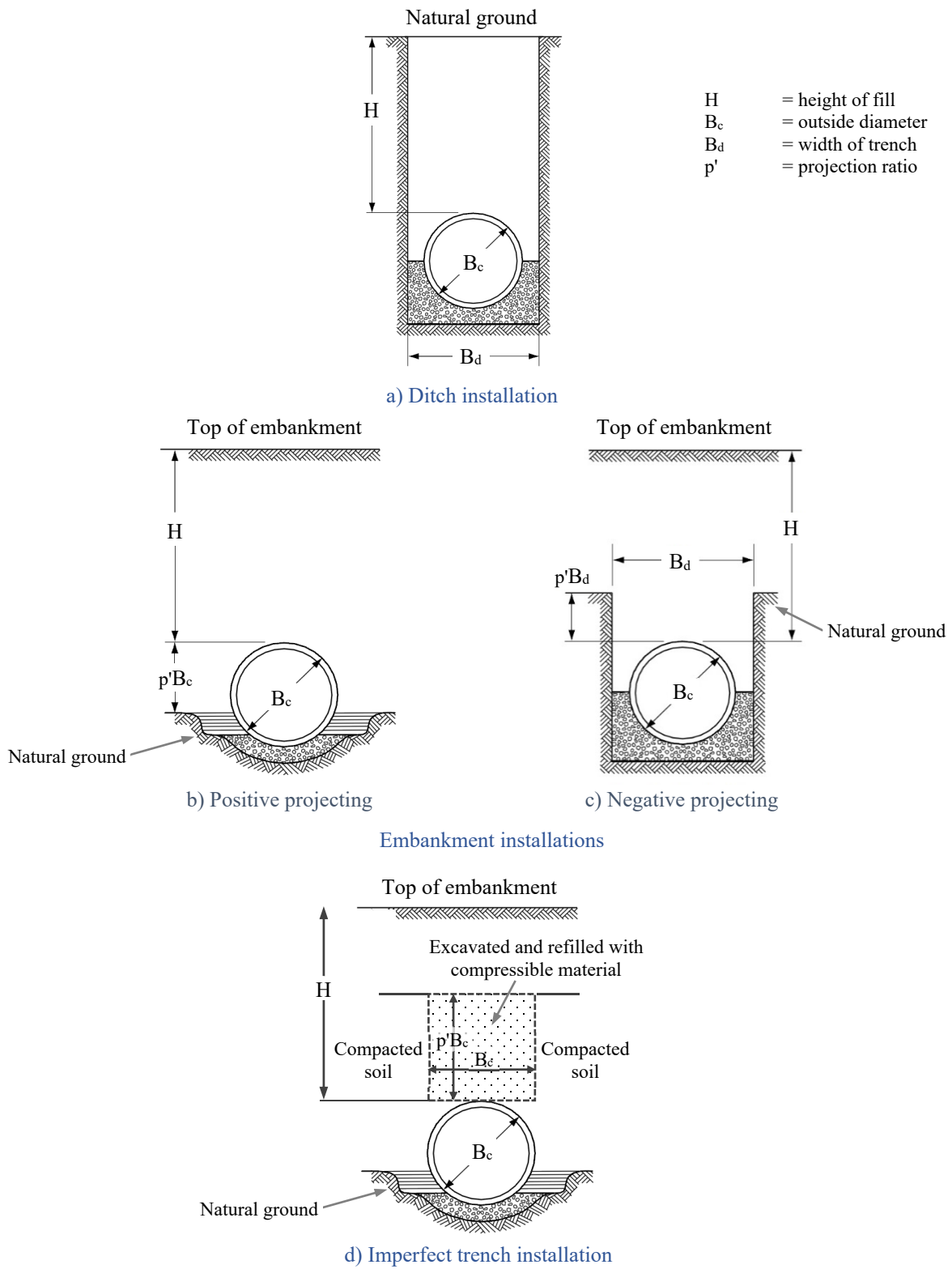


Figure 2-10 Various types of conduit installations

Another important installation condition that is considered a special case of embankment installation, and that is somewhat similar to the negative projecting conduit, is called the *imperfect ditch conduit* (or the induced trench conduit). This method attempts to simulate the condition of a trench installation in an embankment situation (Figure 2-10d). The imperfect trench concept is intended to promote positive arching by constructing a soft inclusion above the buried structure. In this installation method, a conduit is installed first as a positive projecting conduit, then, a fill is constructed above the structure up to an elevation of 1 to 1.5 times the width of the conduit. This fill should be well compacted during construction. Then a trench is dug in the compacted fill down to the top of the conduit. The width of the trench should be the same as that of the conduit. Next, refill the trench with material placed in the loosest possible manner up to the top and then continue construction of the embankment in the ordinary manner (Figure 2-10d). Using this construction technique allows for the interior soil prism to settle relative to the exterior prisms leading to upward shearing forces and consequently the load which the conduit supports will therefore decrease.

2.2.4. Imperfect trench installation

The imperfect trench installation (ITI), sometimes called induced trench installation, attempts to simulate the benefits of a trench installation in an embankment situation. As discussed in the previous section, when using this technique, the soil pressure on the conduit can be significantly reduced by placing loose fill or a soft lightweight compressible material, such as baled hay or straw, or leaves above the conduit. A further refinement of the ITI method is to utilize a synthetic compressible inclusion (expanded polystyrene geofoam, EPS) in place of the loose fill. The ITI is installed with a compressible inclusion (e.g. EPS) between the top of the conduits and the natural ground surface as shown in Figure 2-10d.

Modern design specifications have required buried conduits to be placed under increasing fill heights. In this case, the induced trench installation is used to reduce earth pressures on buried conduits to avoid the failure of the buried structure under these high fill situations. The method involves placing a compressible inclusion directly above the buried structure. This compressible layer induce uplift frictional forces created by differential movements within

the backfill that help support the weight of the soil overlying the conduit. The mechanism of forces induced by the ITI is shown in Figure 2-11.

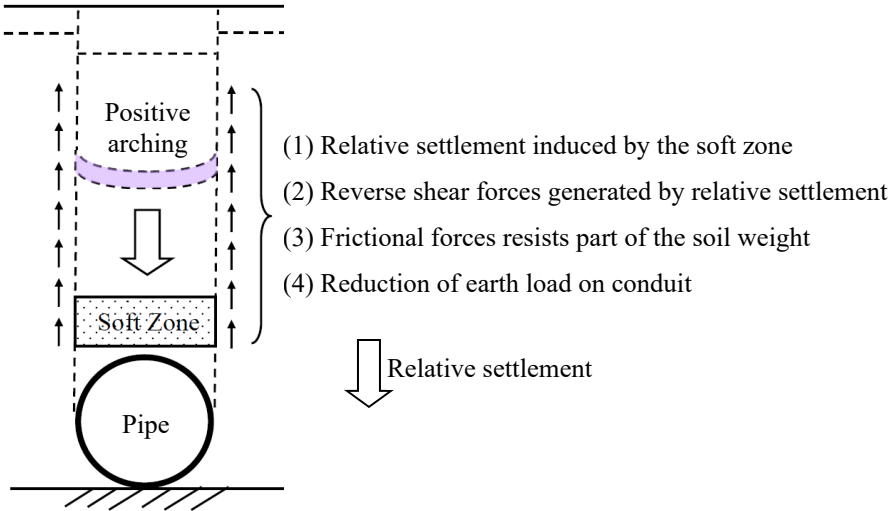


Figure 2-11 Mechanism of induced trench installation

The ITI method was originally proposed by Marston and Anderson (1913), and Marston (1922 and 1930). Significant modifications were made by Spangler (1950 and 1951) to establish what is known as Marston-Spangler theory. Marston-Spangler theory quantified the load on conduits installed by imperfect trench conditions by solving differential equations based on the equilibrium conditions of a simplified free body of prism. The details of the theory is given in the next section.

2.2.5. EPS material characteristics

In the past, organic materials such as leaves, baled hay or straw and sawdust were tried for lightweight materials in the ITI method. However, the properties of these materials are not easily defined due to the variance between samples. In addition, such materials left unanticipated large holes after they rotted away and consequently, the use of ITI methods was perceived to be unreliable despite their theoretical soundness. Another class of compressible material that has been used above conduits comprises old tires, either whole or cut to specific sizes, mixed with soil. The compressibility of tire-soil is considerably less than

those of the organic materials. However, tires can be obtained at a low cost, are easily mixed with soil on site, and are readily available.

Modern non-biodegradable, manufactured materials, such as expanded polystyrene (EPS) are more compressible in comparison to embankment fills. EPS has well defined engineering properties that exhibit less variance than those of organic materials and Tired-soil. EPS is manufactured in large lightweight blocks that can be easily handled, placed and cut on site. However, it is considerably more expensive than other materials due to the costs associated with manufacturing and transportation. Moreover, the use of non-biodegradable lightweight materials such as expanded polystyrene, as opposed to the organic materials, should alleviate concerns for long-term settlement above a conduit.

Composition and manufacturing process of EPS

EPS is mainly constituted from styrene (C₈H₈) which is formed by a reaction between ethylene (C₂H₄) and benzene (C₆H₆), which can be produced from coal or synthesized from petroleum. According to Horvath (1995), geof foam is any manufactured material created by internal expansion process that results in a material with a texture of numerous, closed, gas-filled cells using either a fixed plant or an in situ expansion process.

There are two types of polystyrene foam: expanded polystyrene (EPS) and extruded polystyrene (XPS). This study will focus only on the properties of EPS material. EPS is manufactured by a two-stage process (Arellano, 2005). The first stage consists of pre-expansion of the polystyrene solid resin beads (pre-puff) into a cellular sphere with numerous closed cells by heating with steam. The second stage consists of further expansion of the pre-puff by heating with steam within a fixed-wall mold. The pre-puff fuses during this additional expansion process. The final EPS has the appearance of individual, fused particles. EPS is typically molded as prismatic blocks. Thus, the preferred or more representative name is EPS-block geof foam.

Engineering properties of EPS

The knowledge of the engineering properties of EPS is required to understand the design basis for geotechnical applications. EPS geofoam properties can be grouped into four categories including physical properties, mechanical properties, thermal properties, and endurance properties (Koerner, 2012). This section will shed some light only on the physical and mechanical behaviors of the EPS.

a) Physical properties of EPS

Density and fusion are two key index properties of EPS geofoam. However, other physical properties, such as block dimensions, color, flammability, durability, and environmental effects, can also affect cost, design, or construction. Also, Experience and testing indicates that fusion does not have so much influence on the mechanical and thermal properties of the EPS geofoam. Thus, the EPS density and block dimensions will be discussed in this section.

EPS density

EPS geofoam density appears to be the main parameter that correlate with most of its mechanical properties. Indeed, all the mechanical (e.g. compressive strength, shear strength, tension and flexural strength, stiffness as well as creep behavior) and non-mechanical (e.g. insulation coefficients) properties depend on the density of EPS. The cost of manufacturing an EPS geofoam block is generally linearly proportional to its density (Elragi, 2000). The property requirements of EPS geofoam as per the ASTM/D6817-15 (2015) standard are presented in Table 2-1.

According to the data given in Table 2-1, the densities of EPS for civil engineering applications ranges from 11 to 46 kg/m³, which is about 0.6 to 2.4 percent of the weight of a typical sand at a density of 1940 kg/m³. Because of its lightweight properties (1% of traditional earth materials), geofoam blocks are easy to handle after manufacturing, during transportation or placement on site. The density of the EPS geofoam specimen can be determined in accordance with the standard test method for apparent density of rigid cellular plastics (ASTM/D1622-14).

Table 2-1 Physical property requirements of EPS geof foam (ASTM/D6817-15)

Type	EPS12	EPS15	EPS19	EPS22	EPS29	EPS39	EPS46
Density (kg/m ³)	11.2	14.4	18.4	21.6	28.8	38.4	45.7
Compressive resistance at 1% (kPa)	15	25	40	50	75	103	128
Compressive resistance at 5% (kPa)	35	55	90	115	170	241	300
Compressive resistance at 10% (kPa)	40	70	110	135	200	276	345
Flexural strength (kPa)	69	172	207	276	345	414	517
Oxygen index, volume %	24	24	24	24	24	24	24

Block dimensions

Typical dimensions of the EPS-block geof foam commonly available in North America vary from 305 to 1219 mm (12 to 48 in) in width, 1219 to 4877 mm (48 to 192 in) in length, and 25 to 1219 mm (1 to 48 in) in thickness (ASTM/D6817-15). The block dimensions do not affect other EPS properties.

b) Mechanical properties of EPS

The mechanical properties of EPS geof foam used as a geotechnical element are important for design as they affect the stability of the geotechnical structure (Stark et al., 2004a). The mechanical properties of EPS primarily involve its stress-strain response under various modes and duration of loading. The temperature of the EPS can also affect the mechanical behavior but is generally a secondary issue.

In geotechnical applications, there are two distinct mechanical parameters that need a special attention, the compressive strength of the EPS and the interface shear properties. Some other parameters (e.g. tension, flexure or creep) will also briefly discussed in this section.

Compressive strength

Loading in unconfined uniaxial compression has been and remains the primary mode of loading for tests performed on EPS geofoam. This is because compression is by far the predominant mode of loading for EPS in load-bearing applications. Thus, the most important properties of EPS to test for are those related to the overall mechanical (stress-strain-time-temperature) behavior of an entire EPS block in compression which is the conventional loading encountered in geotechnical applications.

Short-term behavior of EPS using unconfined compression test

Short-term strength of EPS is essential in determining the capacity of the EPS to carry the immediate applied loads and its ability to distribute such loads to the surrounding soil. Thus, the most commonly performed test (ASTM/D1621-10) on EPS specimens involves strain-controlled compression loading at a relatively rapid rate, typically 10 percent per minute, with the load applied in a monotonically increasing fashion until a desired strain level is reached. In this test, a cube with dimensions of 50 mm or a cylinder with 2.8-in. diameter is used with a height that can vary from 1 in. to the diameter of the specimen. The minimum values of compressive resistance at 1%, 5%, and 10% strains, as given in Table 2-1, need to be reached for the EPS-block geofoam.

Stress-strain curve of EPS

An example of the uniaxial compression stress-strain curve of EPS geofoam used for two different densities (12 kg/m^3 and 33 kg/m^3) on 50mm cubic samples is shown in Figure 2-12. From this figure, the stress-strain curve can be split into two straight lines connected with a curved portion. The curve starts with an initial linear response, followed by a curved portion that represent the yielding of the material, and eventually another linear-work hardening response develops. Researchers found that the stress, at any strain level, increases with the increase in material density.

In terms of rupture modes under compressive loadings, there is no defined shear rupture for EPS geofoam. Instead, the EPS behaves more like particulate materials where inter-particle slippage occurs and a steady state or residual strength develops at large strains.

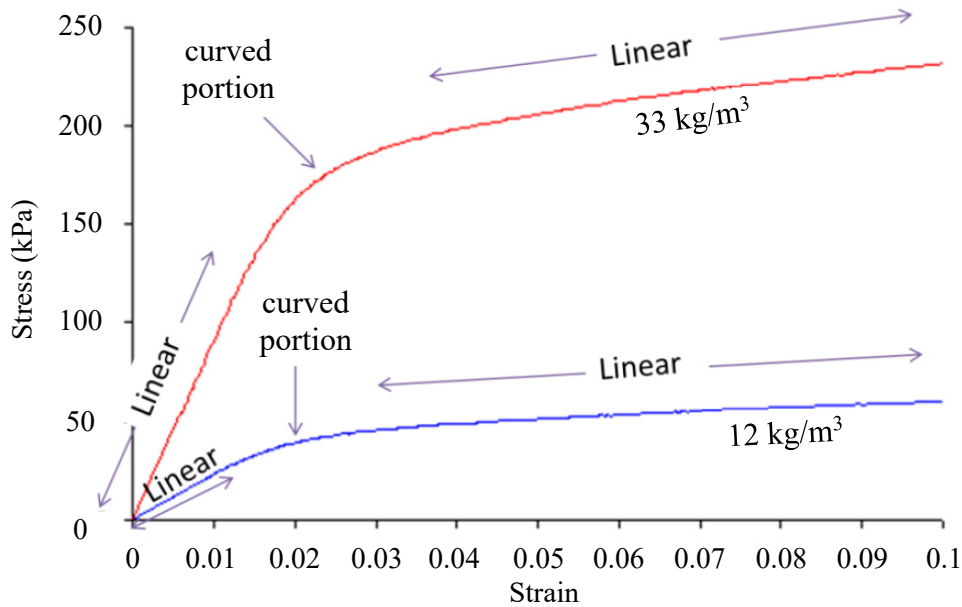


Figure 2-12 EPS uniaxial compression stress-strain curves
(After Negusse and Elragi, 2000)

In summary, the stress-strain behavior of EPS geofoam is both linear and elastic up to a compressive strain of 1%. As a result, a new material parameter for EPS geofoam, called the elastic stress limit, is introduced by Horvath in 1995 (Horvath, 1995). This is defined as the compressive stress at 1% strain as measured in a standard rapid-loading compression test. The 1%, the 5% and the 10% strains are common reference strain levels, at which the stress is considered as the strength of the material.

Elastic modulus of EPS

The strain-stress curve of EPS geofoam shows an initial linear portion before reaching the curved part. The slope of this initial linear portion is defined as the initial tangent modulus or better known as the modulus of elasticity. Previous studies show that the modulus of

elasticity of EPS geofoam is a function of the density however there's no consensus amongst researchers about a constant value for each density.

Poisson's ratio of EPS

Poisson's ratio is an index of the lateral pressure of EPS geofoam in contact with adjacent structural elements for a certain applied vertical load. Determining this ratio for EPS geofoam can be problematic since it varies depending on the degree of loading. Nonetheless, based on the different laboratory tests, the Poisson's ratio value ranges from 0.05 to 0.5, while there is a common agreement between practitioners and designers to consider 0.1 as an adequate value.

Shear strength

There are two modes of shear that are of interest; internal and external shear strengths. The internal shear strength takes place within the specimen of the EPS itself, while the external shear strength (sliding resistance) occurs between EPS blocks (as of EPS embankments) or between an EPS block and the surrounding soil, in other geotechnical applications.

Internal shear strength

The internal shear strength of EPS is measured by loading a test specimen fairly rapidly until the maximum shear stress is reached, whether or not this stress produces a physical rupture of the test specimen. Because the shear strength of EPS is correlated with compressive strength, experience indicates that shear strength test is rarely performed in practice for engineering design (Arellano, 2005).

External shear strength (interface friction properties)

Interface friction is an important consideration in external and internal stability assessments under tangential loads. Thus, tests to assess interface friction between the surface of EPS blocks and a variety of other materials is of interest in projects where significant tangential design loads or internal sliding can occur. Two types of interfaces that are of interest for EPS geofoam in geotechnical applications include an EPS-EPS interface, and an EPS-dissimilar

materials interface (e.g. soil or culvert material). Only the EPS-dissimilar materials interface is discussed here. The test for external shear strength can be conducted similar to the direct shear testing performed to evaluate soil-geosynthetics interfaces (ASTM/D5321-14).

A significant gap in the published literature exists for interface friction values between EPS block and other materials likely to be encountered in EPS geotechnical applications. In 2000, Bartlett et al. conducted a research that involves EPS-sand interfaces and the results indicated that the interface friction angle ($\delta_{EPS-sand}$) equals the Mohr-Coulomb angle of internal friction ($\phi_{sand} = 33$ degrees) of the sand. The study, however, did not indicate whether to use the peak (ϕ_p) or constant-volume (critical state, ϕ_{cv}) value for the sand. It appears reasonable that the choice would depend on the relative magnitude of shear strain, with a peak value (stress dependent) appropriate for small strains and a constant-volume value (usually assumed to be stress independent) for large strains. A friction coefficient, μ , of 0.5 was reported for an EPS-sand interface (Jutkofsky et al., 2000). This is equivalent to an interface friction angle of 27 degrees. An average interface friction angle of 33 degrees was obtained from interface shear strength tests performed between EPS and bedding sand tested over a stress range of 25 kPa to 40 kPa (Bartlett et al. 2000). In summary, the EPS-sand interface friction appears to range from 27 degrees to 33 degrees which is typical for the (ϕ) of the sand. Based on the results obtained from previous studies (Elragi, 2000, Stark et al., 2004a and 2004b), the interface friction angles between the EPS block and various dissimilar materials are summarized in Table 2-2.

Table 2-2 Interface friction angles between EPS geofoam and dissimilar materials

Materials		Interface friction angle (δ°)
EPS	Sand	33
EPS	Non-woven geotextile	25
EPS	Geomembrane	52

Tension (tensile strength)

Although tensile loading is unlikely to develop when using EPS geofabric in geotechnical applications, tensile strength is often used as an indicator of the quality of EPS fusion. Previous studies show that the tensile strength is proportional to the material density as there is an increase in tensile strength when the density increases. Tensile strength is defined as the tensile stress at which material rupture occurs.

Flexure strength

Flexural strength is the stress at which the EPS fractures when it is loaded under a compressive load. Flexural tests are widely used as a quality control test during the manufacturing process of EPS geofabric to examine the tensile strength of the EPS. The material fails in tension as a crack on the tension side appears at the moment of failure. The flexural strength increases with the density. The test is carried out on a beam-shaped specimen to produce maximum bending moment and, therefore, maximum tension in the extreme bottom fiber of the EPS beam. The flexural strength is defined as the calculated maximum-fiber stress at the time of rupture of the specimen.

Deformation

Immediate deformation (short-term)

Several laboratory tests have been carried out to determine the EPS geofabric deformation. The results showed that different variables including sample size, shape, density, confinement, ambient temperature in the laboratory and applied stress level, have an effect on both immediate and long-term deformation (Stark et al., 2004a and 2004b). In general, for a compressive load less than 25% of the compressive strength an immediate strain of $\epsilon < 1\%$ is expected. However, when the loading stress exceeds 50% of the compressive strength, then the resulting strain will be higher than 1% (Gnip et al., 2005).

Creep deformation (long-term)

EPS geof foam can be prone to deformations related to the application of a constant stress level for a long-term period. This time-dependant behavior is called the creep behavior of EPS geof foam. A number of parameters can affect the creep behavior of EPS, among which density, sample size, temperature and degree of loading. Creep deformations decrease with the increase of density (Sun, 1997).

The general time-dependent behavior of EPS is similar to other engineering materials and exhibits primary, secondary, and tertiary creep. Experience indicates that the most useful way to portray creep-test data is by constructing a family of isochronous stress-strain relations for tests performed on EPS specimens of the same density. An isochronous curve is the estimated stress-strain behavior for a range of applied stresses for a specific duration of time. Isochronous stress-strain curves for different durations of loading are useful in geotechnical applications where sustained loads are typically involved (Horvath, 1995).

2.2.6. ITI design approaches

The analytical design approaches that are used for the design of the culverts constructed using ITI installation are summarized in this section.

Marston-Spangler Theory

The Marston-Spangler (M-S) design method is based predominantly on the work presented by Marston over 100 years ago. The design approach of this method quantifies the load on conduits installed by the ITI as follows:

$$W = C_n \gamma B_c^2 \quad (2.18)$$

where C_n is load coefficient, γ is the unit weight of fill material, and B_c is the out-to-out horizontal span of the conduit. Although graphic illustrations are provided for the computation of coefficient, C_n , there are many practical difficulties as the parameters used to determine the coefficient cannot be evaluated readily. These parameters include the settlement ratio and the height of the plane of equal settlement to be determined by a graphical

method as summarized in Kang (2007). In order to use the M-S equation, it is essential to determine the settlement ratio, r_{sd} , which is defined as follows:

$$r_{sd} = \frac{s_g - (s_d + s_f + d_c)}{s_d} \quad (2.19)$$

where r_{sd} is settlement ratio, s_g is settlement of surface of compacted soil, s_d is compression of fill in ditch within height ($p'B_c$), s_f is the settlement of flow line of conduit, d_c is deflection of conduit (i.e. shortening of its vertical dimension), and $(s_d + s_f + d_c)$ is settlement of critical plane. Although the settlement ratio, r_{sd} , is a rational quantity used in the development of the load formula, it is very difficult to determine the actual value that will be developed in a specific case. However, Spangler and Handy (1982) presented some recommended values of the settlement ratio for various culvert types and foundation deformation characteristics based on field observations on actual culverts under embankments. C_n values may be determined graphically using settlement ratio, r_{sd} and projection ratio, p' , which is depth/width ratio of the ditch.

For several years the M-S theory was considered the basis for the design of induced trench installations in many international design standards (e.g. CSA, 2006, AASHTO, 2007) and no significant update is made since the publication of the original work.

The ITI construction method has been an option used by designers to reduce earth pressures on rigid conduits buried under high embankments. Despite its obvious benefits, a number of researchers identified various shortcomings of M-S approach such as the effect of geometry and stiffness of the compressible zone, the mechanical properties of the backfill material, the shape of buried structure and the magnitude of lateral loads (Sladen and Oswell, 1988, Scarino, 2003, Handy, 2004). In addition to the previous shortcomings, limitations of the method have been reported and questions were raised regarding the long-term sustainability of the load reduction process. As a consequence, the American Concrete Pipe Association Handbook (ACPA, 2004) has deleted the induced trench method of design.

AASHTO LRFD bridge design specifications (AASHTO, 2012) has recognized the ITI method as one of the acceptable methods of installation. However, the standards provide

guidelines for estimating earth loads on positive projecting culverts, but not for culverts installed using induced trench technique. Instead of relying on the M-S theory, AASHTO suggested the use of accepted test methods, soil-structure interaction analyses, or past experience to determine the earth load on the culvert (Oshati et al., 2012).

Vaslestad method

The details of this method are outlined in Vaslestad (1991) and Vaslestad et al. (1993). In this method, the earth loads acting on the buried culverts are calculated by applying an arching factor to the overburden pressure. This arching factor is based on the friction number, S_v , used by Janbu to determine friction on piles (Janbu, 1976). Vaslestad's equation for estimating vertical earth pressures (σ_v) on an induced trench culvert is given as follows:

$$\sigma_v = N_A \gamma H \quad (2.20)$$

where N_A is the arching factor, γ is the unit weight of soil, and H is the height of fill cover above the culvert. The arching factor is calculated as follows:

$$N_A = \frac{1 - e^{-2S_v \frac{H}{B}}}{2S_v \frac{H}{B}} \quad (2.21)$$

where S_v is Janbu's friction number, and B is the width of the conduit.

The friction number, S_v , is calculated as follows:

$$S_v = |r| \tan \rho K_A \quad (2.22)$$

where $\tan \rho$ is the mobilized soil friction ($\tan \rho = f \tan \phi$), f is the degree of mobilization ($0 < f < 1$), $\tan \phi$ is the soil friction, r is the roughness ratio ($r = \frac{\tan \delta}{\tan \rho} \leq 1$), $\tan \delta$ is the mobilized friction between the soil and the culvert walls, and K_A is the active earth pressure coefficient that can be calculated using the following formula:

$$K_A = \frac{1}{\left[\sqrt{1 + \tan^2 \rho} + \sqrt{1 - |r|} \right]^2} \quad (2.23)$$

Vaslestad reported that the design method shows good agreement between the earth pressure measured on a full-scale induced trench installation and the results from the finite element analysis program CANDE-89 (Katona et al., 1976, Musser, 1989).

2.2.7. Numerical modeling of soil-structure interaction for box culvert installed using imperfect trench technique

The imperfect trench method has traditionally been used for circular culverts, thus, the majority of induced trench research has been focused on circular culverts and very little work has been done to evaluate the effectiveness of the method for box culverts (i.e. Vaslestad et al., 1993, MacLeod, 2003, Kang et al., 2008, McGuigan and Valsangkar, 2010). Understanding the complex soil-structure interaction issues related to the design of induced trench box culverts is required. Several researchers studied the relevant soil-structure interaction using numerical modeling to address the uncertainties and empirical nurture of the current design methods.

Bourque (2002) developed a numerical analysis, using FLAC (a finite difference software), to study the vertical and horizontal soil pressures acting on twin induced trench box culverts. Bourque performed a parametric study to address the effect of culvert spacing, width of the compressible layer, culvert geometry, and backfill type. The analysis showed that the horizontal pressure for the induced trench was higher than vertical pressure for both single and twin culvert installation. However, this study did not address pressures at the culvert base.

MacLeod (2003) investigated earth pressures around induced trench conduits using centrifuge testing and numerical modelling, and compared the results with prototype results reported in the literature. This analysis examined the effect of variables such as conduit shape (circular and box), backfill material, and compressible zone features on the performance of induced trench installation.

Li and Qubain (2004) used the two-dimensional finite program SIGMA/W to simulate a concrete box culvert to evaluate the effects of foundation yielding on design loads. Yielding, partial yielding, and unyielding foundations were analyzed and compared with classical and

conventional methods. In this analysis a plane strain FEM was used to analyze a 3.35 m wide by 3.81 m high precast concrete box culvert under 11.58 m of embankment fill. They reported that the vertical earth pressure measured from the unyielding foundation was 1.30 times the nominal earth load on average, while for the yielding foundation, measured vertical earth pressure was approximately equal to the nominal earth load.

Kim and Yoo (2005) used finite element modelling to analyse different geometric configurations and backfill material properties for a concrete box culvert installed using the ITI method. The study reported that the preferred width of the compressible layer should not exceed $1.5B_c$ (where B_c is the box culvert width) and that the ratio of the thickness of the compressible layer to the height of the culvert should not be greater than 1.5. They observed that the maximum load reduction rate is achieved when the compressible layer is placed directly on top of the culvert and concluded that the ITI method could reduce the soil–structure interaction factor. The study focused on the beneficial load reduction that can be achieved from the ITI method, and did not address lateral earth pressure or base contact pressure.

Kang et al. (2008) reported on the results from numerical analysis of a box culvert under high fill, and highlighted the effects of frictional forces developed on the sidewalls of box culverts on the base contact pressure. The analysis proposed a preferred compressible zone geometry, formulas for earth load reduction rate for the proposed compressible zone geometry, and a PPI soil–structure interaction factor accounting for downward drag forces developed on the sidewalls of the box culvert.

McGuigan and Valsangkar (2010) presented the results of parametric studies on a single box culvert using centrifuge tests and numerical modelling (with FLAC) to evaluate the pressures acting on the top, sides, and base of a box culvert. They recommend practical optimal preferred compressible zone geometry, along with physical evidence for the increased base pressure caused by downward drag forces developed on the sidewalls of box culverts. The study was limited to a fill height of 12 m and a ratio $B_c/H_c = 1$.

The above soil-structure interaction simulations, of EPS-culvert system, examined several aspects of the problem, however, none of them provides technically design guides (e.g. charts or equations) that can be readily used by designers to correlate the pressures reduction to the embankment height and the EPS stiffness. Moreover, the constitutive model that represent the true response of the EPS material was often simplified either as a linear elastic material or an elastic-plastic which will not help to predict the stress-strain behavior of the geofoam in the short-term.

2.3. Conclusion for the Literature Review

Based on the previous literature review and the review presented in other chapters, it can be seen that modeling the soil-structure interaction problems which involve geosynthetic inclusion is a very complex exercise. Although several soil-geogrid interaction models have been developed, the available 3D analysis is very limited. The induced trench technique is a promising method to reduce the earth pressures on buried culverts beneath high embankments. The effectiveness of the method still needs further examination using an extensive understanding of the nature of EPS-soil-culvert system. Therefore, there is a need to simulate and validate the problem using robust numerical simulations that involve the true behavior of the integrated system. It is necessary to develop an efficient numerical framework that would be capable to simulate such complicated soil-structure interactions. Such development will be presented in this thesis along with experiments and numerical simulations of geotechnical engineering problems.

CHAPTER 3

Modeling the Response of Buried Structures Overlain by EPS Geofoam Inclusion*

Abstract

Expanded Polystyrene (EPS) geofoam is a light weight material used in a wide range of geotechnical engineering applications including embankment construction and bridge approaches to reduce earth loads imposed on the adjacent or underlying soils and structures. EPS is also used as a compressible material above deeply buried culverts to promote positive arching and reduce the load transferred to the walls of the structure. An important step towards understanding the soil-geofoam-structure interaction and accurately model the load transfer mechanism is choosing a suitable material model for the EPS geofoam that is capable of simulating the material response to compressive loading for various ranges of strains. In this study, a material model that is able to capture the response of EPS geofoam is first established and validated using index test results for three different geofoam materials. To examine the performance of the model in analyzing complex interaction problems, a laboratory experiment that involves a rigid structure buried in granular material with EPS geofoam inclusion is simulated. The contact pressures acting on the walls of the structure are calculated and compared with measured data for three different geofoam materials. The developed numerical model is then used to study the role of geofoam density, width, thickness and location on the reduction of earth loads acting on the buried structure.

Keywords: Finite element method, EPS geofoam, Buried structures, Soil-structure interaction, Soil arching.

* A version of this chapter has been submitted to *Soils and Foundations Journal*, February 2016 (Manuscript No. SANDF-D-16-00042).

3.1. Introduction

Earth loads on buried conduits are known to be dependent on the installation conditions. A conduit installed in a trench is usually located completely below the natural ground surface and frictional forces between the sides of the trench and the backfill material help to partially support the weight of the overlaying soil. Embankment installation, however, refers to the condition when soil is placed in layers above the natural ground. The vertical earth pressure on a rigid conduit installed using embankment construction method is generally greater than the weight of the soil above the structure because of negative arching. The induced trench installation (also called imperfect ditch or ITI method) has been often used to reduce vertical earth pressure on rigid conduits. The method involves installing a compressible layer immediately above the conduit to generate positive arching in the overlying soil. The Canadian highway bridge design code (CSA, 2006) and the AASHTO LRFD bridge design specifications (AASHTO, 2012) provide guidelines for estimating earth loads on positive projecting culverts, but not for culverts installed using induced trench technique. This construction method has been an option used by designers to reduce earth pressures on rigid conduits buried under high embankments. Despite its obvious benefits, recent doubts have left many designers uncertain as to the viability of induced trench construction (McAfee and Valsangkar, 2008).

The ITI method of installing rigid conduits under high embankments dates back to the early 1900s. Researchers studied the relevant soil-structure interaction using experimental testing or field instrumentation (Sladen and Oswell, 1988, Vaslestad et al., 1993, Liedberg, 1997, McGuigan and Valsangkar, 2010 and 2011, Sun et al., 2011, Oshati et al., 2012), as well as numerical modelling (Kim and Yoo, 2002, Kang et al., 2008, Sun et al., 2009, McGuigan and Valsangkar, 2010 and 2011) to help understand the method and address uncertainties associated with this design approach.

EPS geofoam material is known to compress in response to uniaxial compression loading without apparent shear failure and, therefore, it is difficult to establish the failure state of the material (Horvath, 2001). It has been accepted in design to use parameters (e.g. elastic limit and initial tangent modulus) that are obtained from the linear elastic stress–strain behavior at

1% strain measured in a monotonic compression load test. Significant efforts have been made by researchers to model the short-term behavior of EPS geofoam used in geotechnical engineering projects. The material is often approximated as linear elastic-perfectly plastic (e.g. Takahara and Miura, 1998) or nonlinear elasto-plastic material (e.g. Hazarika, 2006). Other nonlinear models have been proposed to capture the material response under triaxial loading (e.g. Chun et al., 2004, Leo et al., 2008, Ekanayake et al., 2015).

It is often desired to use index test data (e.g. ASTM/D1621-10), routinely conducted by the manufacturer, to create a representative material model that can be implemented directly into a finite element analysis and used to simulate the compressive behavior of EPS geofoam in a given application. The objective of this study is to propose a numerical modeling approach that can be used to investigate soil arching associated with induced trench installation of rigid conduits overlain by EPS geofoam inclusions. A nonlinear elastic-plastic hardening model is first established for three different EPS geofoam densities. The model is then used to examine the role of EPS properties in reducing earth pressures acting on the buried structure.

The finite element (FE) analyses presented throughout this investigation have been performed using the general finite element software ABAQUS/Standard, version 6.13 (ABAQUS, 2013). It should be noted that the rheological and anisotropic aspects of EPS geofoam were not addressed in this study.

3.2. EPS Material Model

Three types of EPS geofoam materials, namely: i) EPS15; ii) EPS22; and iii) EPS39, are modeled in this study. Index test results obtained from a series of uniaxial unconfined compression tests, carried out by the manufacturer, are presented in Figure 3-1. The tests were performed on 125 mm cubes under monotonic loading for the three different EPS types. Results show that the tested EPS geofoam generally behaves as a nonlinear elasto-plastic hardening material. A constitutive model that is capable of describing the details of material behavior, including the nonlinearity, elasticity, isotropic hardening and plasticity, is needed. These components have been combined using the commercial finite element software ABAQUS and used to represent the EPS geofoam material throughout this study. The

approach used to combine these model features is based on the conversion of the measured strains and stresses into the appropriate input parameters in ABAQUS. This is achieved by decomposing the total strain values into elastic and plastic strains to cover the entire range of the EPS response.

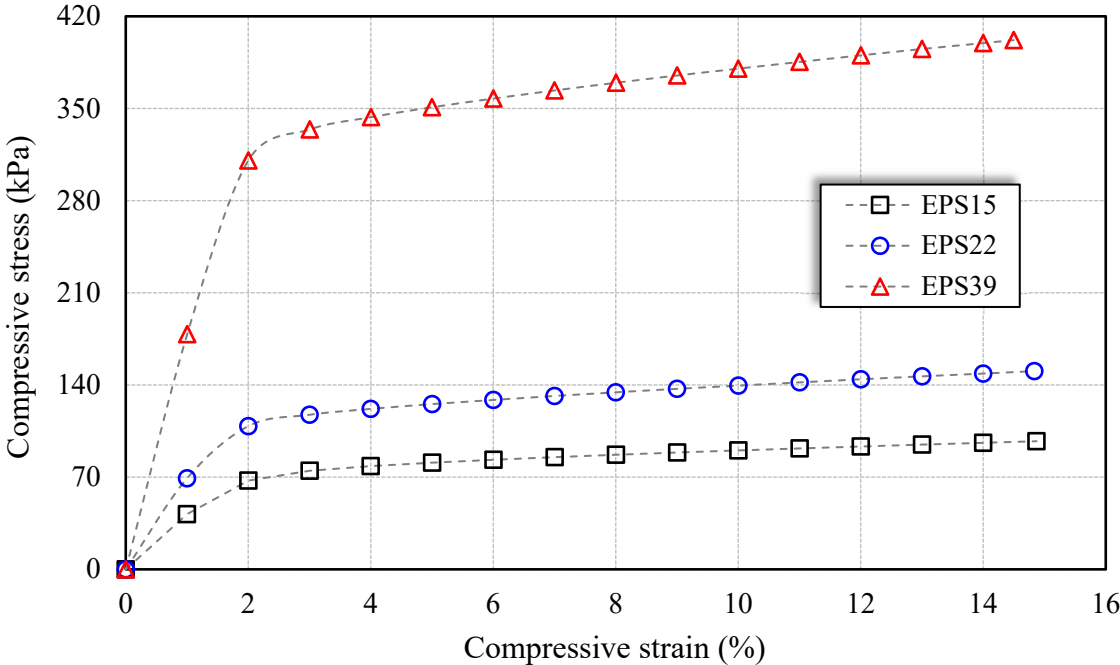


Figure 3-1 Compression test results for three different EPS geofoam material (reported by the EPS manufacturer)

3.2.1. Model components

The elasticity component of the EPS model is described by an elastic isotropic model where the total stress and the total strain are related using the elasticity matrix. The plasticity is modeled using Mises yield criterion with isotropic hardening and associated flow rule. More details about the formulations of the Mises yield criterion can be found in Appendix (A). The isotropic yielding is defined by expressing the uniaxial compressive yield stress as a function of the equivalent uniaxial plastic strain. The isotropic hardening rule is expressed in ABAQUS using a tabular data of compressive yield stress as a function of plastic strains.

The plasticity data has to be specified in terms of true stresses and true strains despite the fact that test data provides nominal (engineering) values of total stresses and total strains (ABAQUS, 2013). A procedure is, therefore, needed to first convert the nominal test data into its true values and then decompose the total strain values into elastic and plastic strain components to allow for direct data input into ABAQUS. A flow chart that illustrates the procedure adopted to determine the numerical input data based on the experimental results is given in Figure 3-2 and summarized in the following steps:

1. Converting the test data (stresses and strains) from nominal to true values using:

$$\varepsilon_{c-true} = \ln(1 + \varepsilon_{c-nom}) \quad (3.1)$$

where ε_{c-true} is the true compressive strain, ε_{c-nom} is the engineering compressive strain.

$$\sigma_{c-true} = \frac{\sigma_{c-nom}}{(1 - \nu \cdot \varepsilon_{c-nom})^2} \quad (3.2)$$

where σ_{c-true} is the true compressive stress, σ_{c-nom} is the engineering compressive stress, ν is Poisson's ratio.

Then, decomposing the total true strain (ε_{c-true}) into elastic and plastic components as illustrated in Figure 3-3:

$$\varepsilon_{c-true} = \varepsilon^{el} + \varepsilon^{pl} \quad (3.3)$$

where ε^{el} is the elastic true strain component, ε^{pl} is the plastic true strain.

2. Using the true stress (σ_{c-true}) and Young's modulus (E) to obtain the elastic strain component:

$$\varepsilon^{el} = \frac{\sigma_{c-true}}{E} \quad (3.4)$$

3. Subtracting the elastic strain values (ε^{el}) from the total true strains (σ_{c-true}) to determine plastic strains (ε^{pl}).

The final EPS plasticity properties are introduced into ABAQUS input module in terms of true stresses versus plastic strains. It should be noted that the compressive stresses and strains used in the above procedure are negative values.

The Young's modulus used to describe the EPS elasticity model is determined using the *initial* true stress and strain values. Discrepancy of the Poisson's ratio value for EPS geofoam was found in the literature. Most frequently, values range between 0.05 and 0.2 were used. Recent research conducted by Negussey (2007) concluded that a Poisson's ratio value of 0.1 is appropriate. The elastic properties for the three EPS types used in the numerical study are summarized in Table 3-1. The hardening rule data used to describe the EPS plasticity model is shown in Figure 3-4.

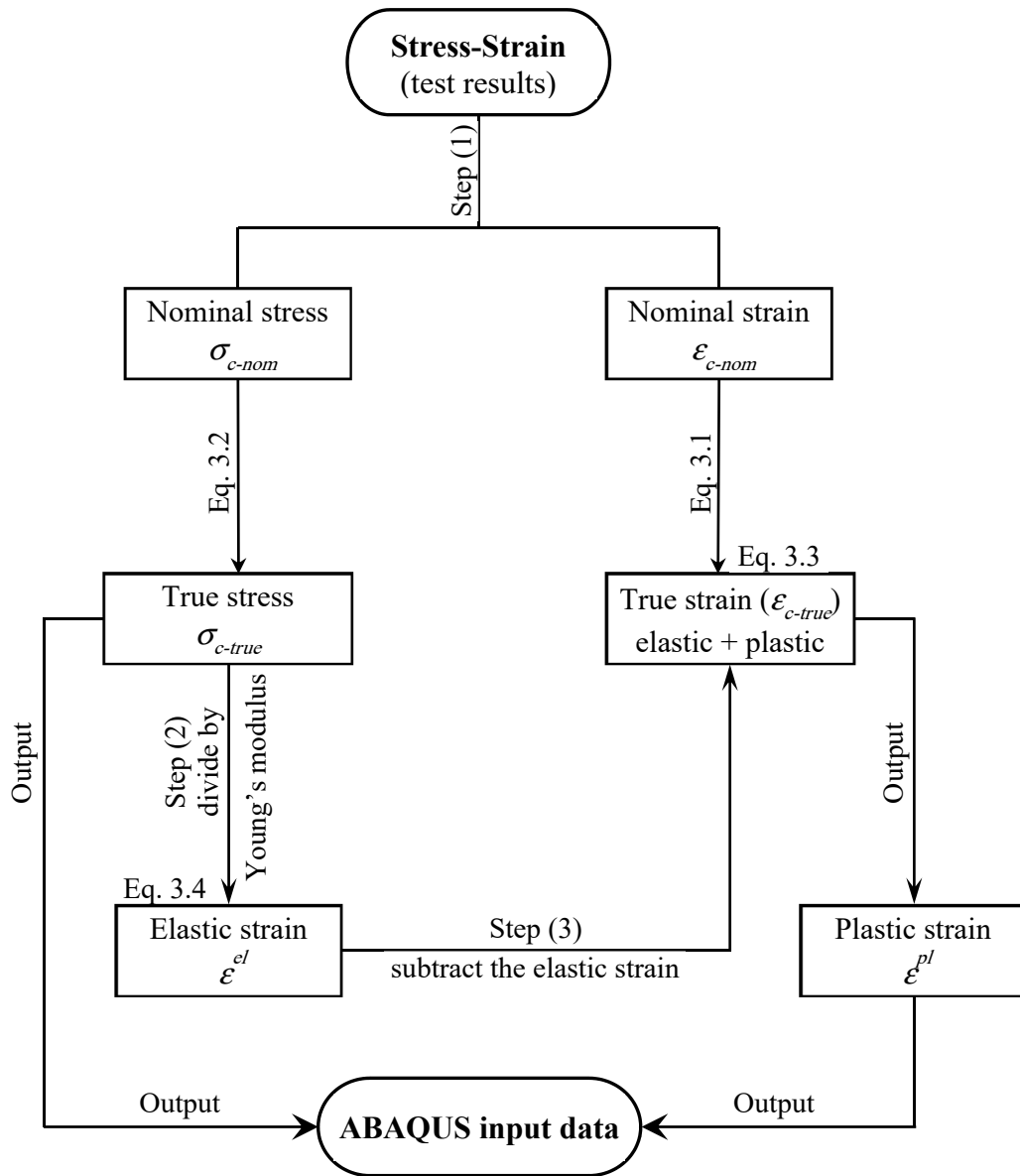


Figure 3-2 Procedure used to generate ABAQUS input parameters for the EPS geofoam

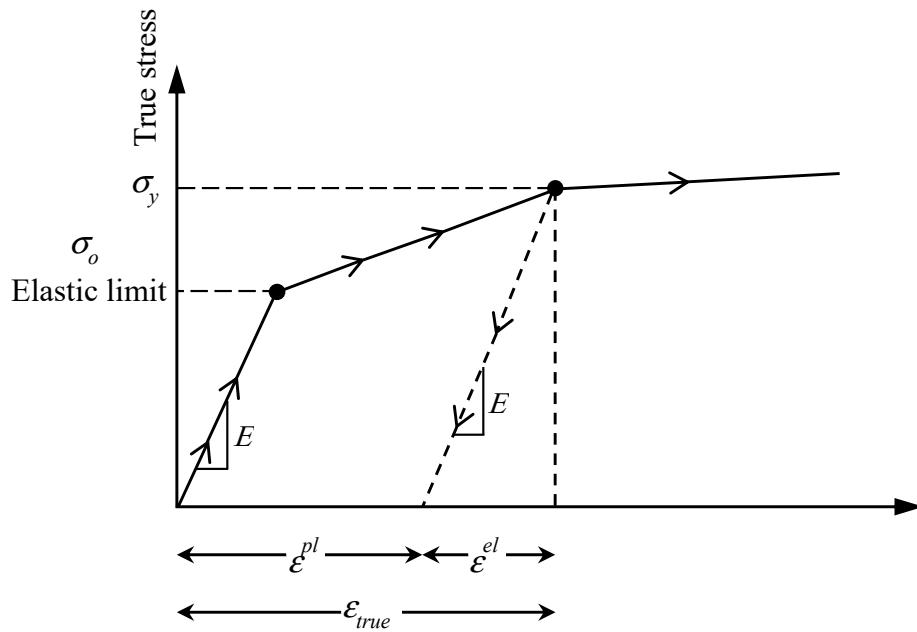


Figure 3-3 Decomposition of the total true strain
(adapted from ABAQUS 6.13 manual)

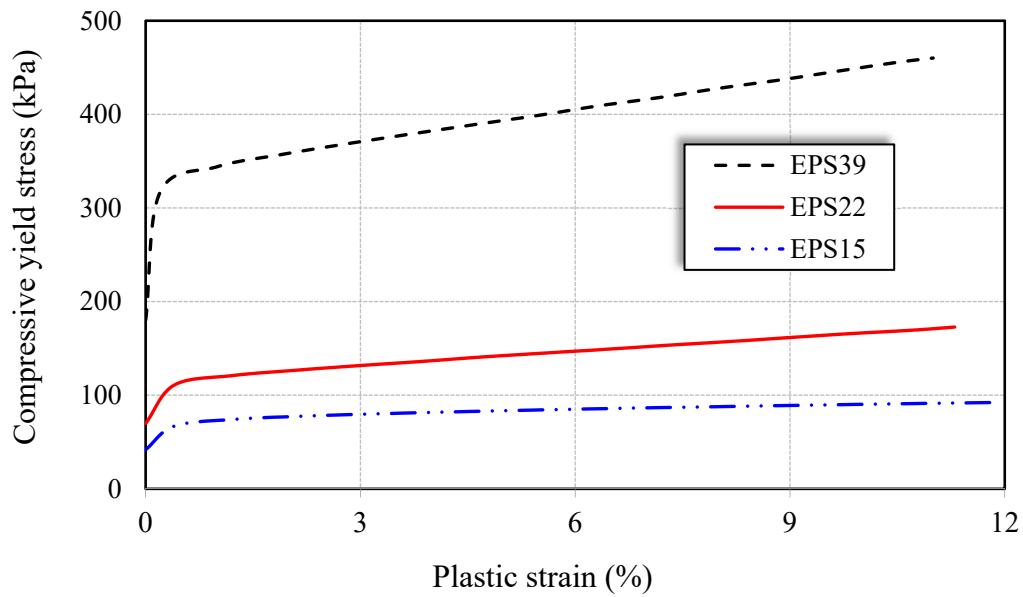


Figure 3-4 Hardening rule of the EPS plasticity model

Table 3-1 Properties of the backfill, geofoam and HSS structure used in the model

Backfill soil properties					
Density (kg/m ³)	<i>E</i> (MPa)	(<i>ν</i>) Poisson's ratio	$\phi^\circ/\phi_{cv}^\circ$	ψ°	Cohesion (MPa)
1628	150	0.3	47/35	15	1E-5
EPS geofoam properties (reported by the EPS manufacturer)					
EPS material type			Density (kg/m ³)	<i>E</i> (MPa)	(<i>ν</i>) Poisson's ratio
EPS39			38.4	17.8	0.15
EPS22			21.6	6.91	0.10
EPS15			14.4	4.20	0.10
Box material properties					
Hollow square section (HSS) 250 x 250 x 10 mm			Density (kg/m ³)	<i>E</i> (GPa)	(<i>ν</i>) Poisson's ratio
			7850	200	0.3
Interface parameters					
Interface type			Friction coefficient (μ)		<i>E_{slip}</i> - tolerance
Soil-EPS			0.60		0.005
Soil-Culvert			0.45		
EPS-Culvert			0.30		

ϕ° = peak friction angle

ϕ_{cv}° = critical state friction angle

ψ° = dilatancy angle (determined using Bolton's equation, 1986)

3.2.2. Modeling the compression test

Three-dimensional FE analyses are conducted to simulate the EPS compressive tests on 125 mm cubes. The elasto-plastic constitutive model, described above, is used to simulate the measured behavior of the EPS. The cube geometry is discretized using 8-node linear brick elements (C3D8) with eight integration points. To simulate the uniaxial compressive test, the EPS model is restrained in the vertical direction ($U_z = 0$) along the base and a compressive load is applied at the top using a prescribed velocity (V_z). The cube movements are constrained in X and Y directions at both ends (top and bottom) to simulate the friction between the grips of the loading machine and the EPS cube. The 3D FE mesh used in the analysis, with over 74,000 elements, is shown in Figure 3-5. Several mesh sizes were tested to determine a suitable mesh that brings a balance between accuracy and computing cost. An average element size of 3 mm was found to satisfy the balance and produce accurate results.

To validate the numerical model, the calculated and measured load-strain relationships are compared in Figure 3-6. It can be seen that the calculated responses for EPS15 and EPS22 agree well with the measured data. For EPS39, the model slightly overestimated the compressive resistance beyond the yield point. In general, the proposed elasto-plastic constitutive model was found to reasonably represent the response of the material in both the elastic and plastic regions.

The results also confirm that there is no obvious shear failure of the material up to 18% strain. For design purposes, the 1 %, 5 %, and 10 % strains are often used to limit the applied pressure, depending on the nature of the project.

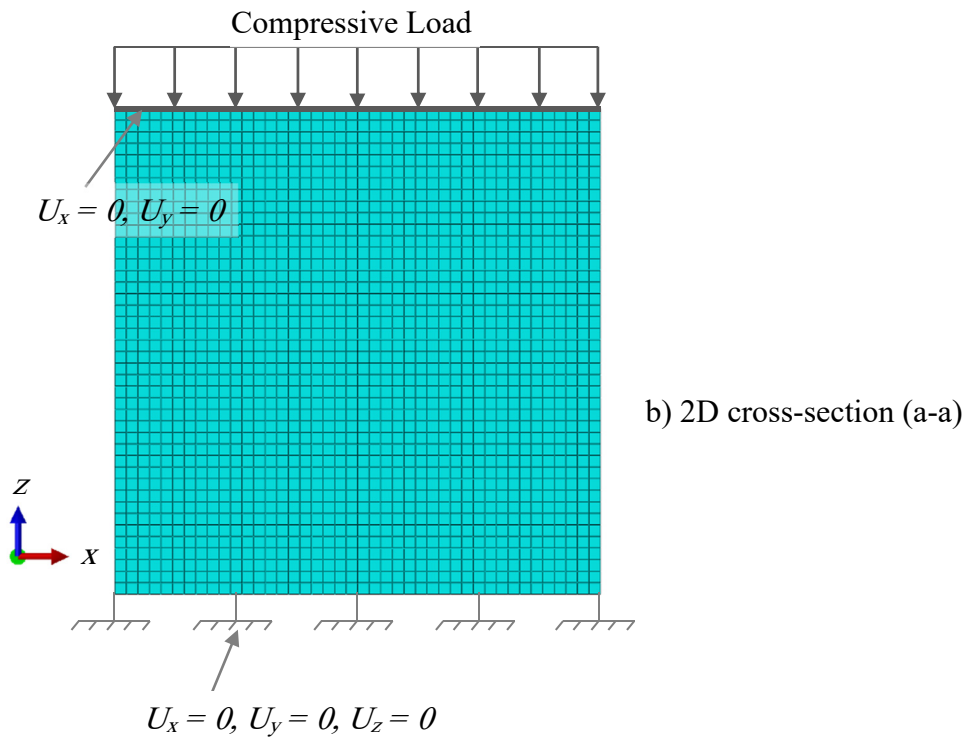
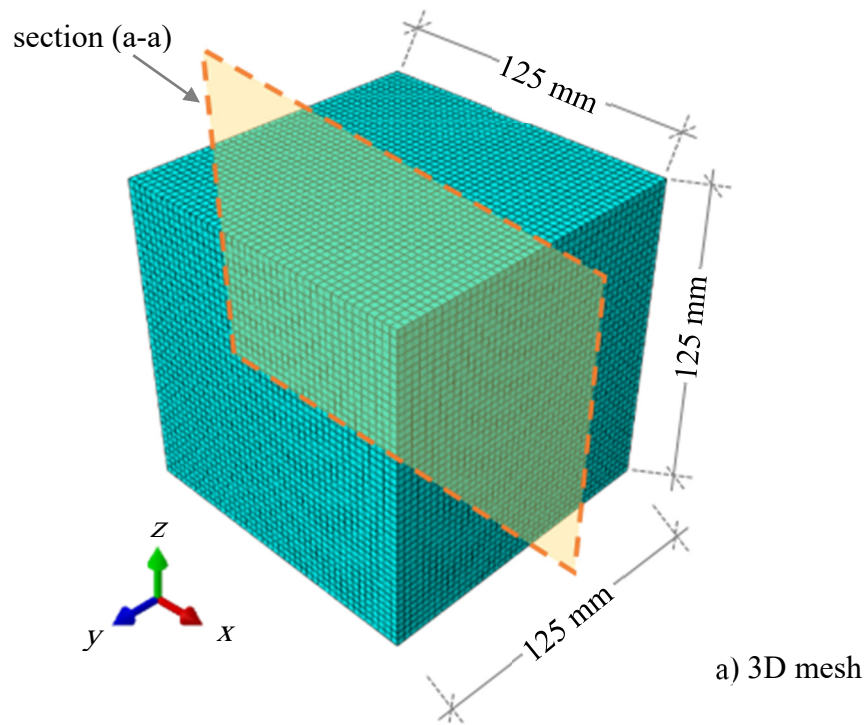


Figure 3-5 FE model of the compression test

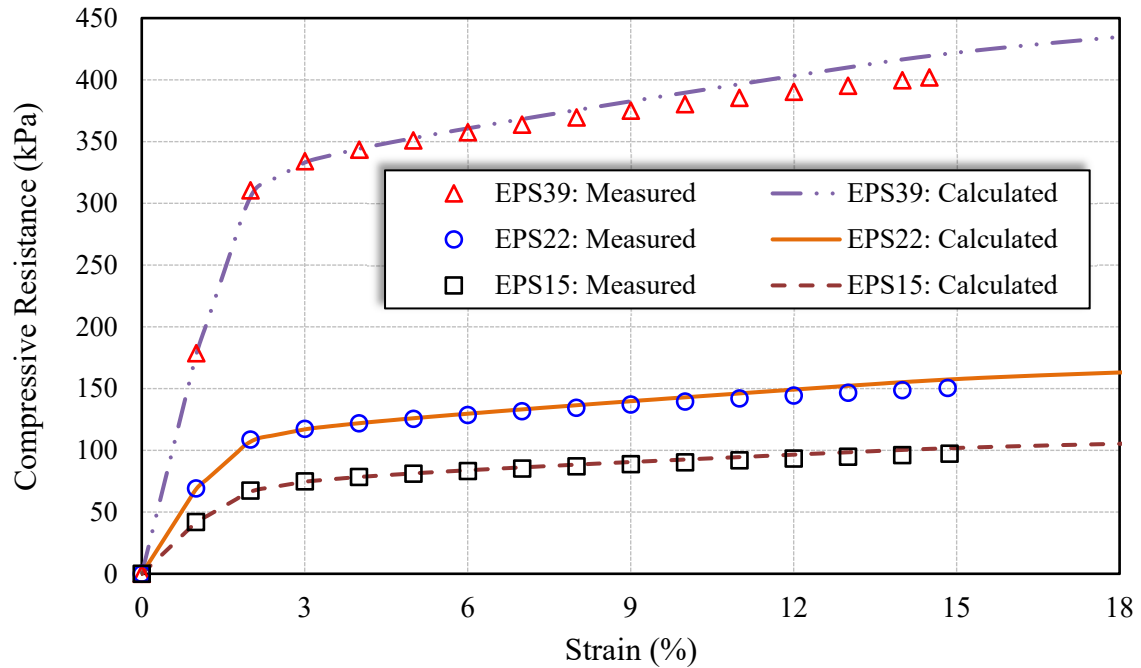


Figure 3-6 Validation of the EPS material model

Figure 3-7 illustrate the normal stress distributions within the EPS cube at 5 % strain level for the three densities used in this study. It is noted that the maximum compressive stress was found to be located near the top and bottom sides of the cube and the stress decreased towards the middle. At 5 % strain, stresses developing at the center of the blocks increased from 70 kPa for EPS15 (Figure 3-7) to 100 kPa for EPS22 (Figure 3-7b) and reached about 300 kPa for EPS39 (Figure 3-7c). The stresses developing in EPS15 and EPS22 were found to be about 20 % and 35%, respectively, of that calculated for EPS39.

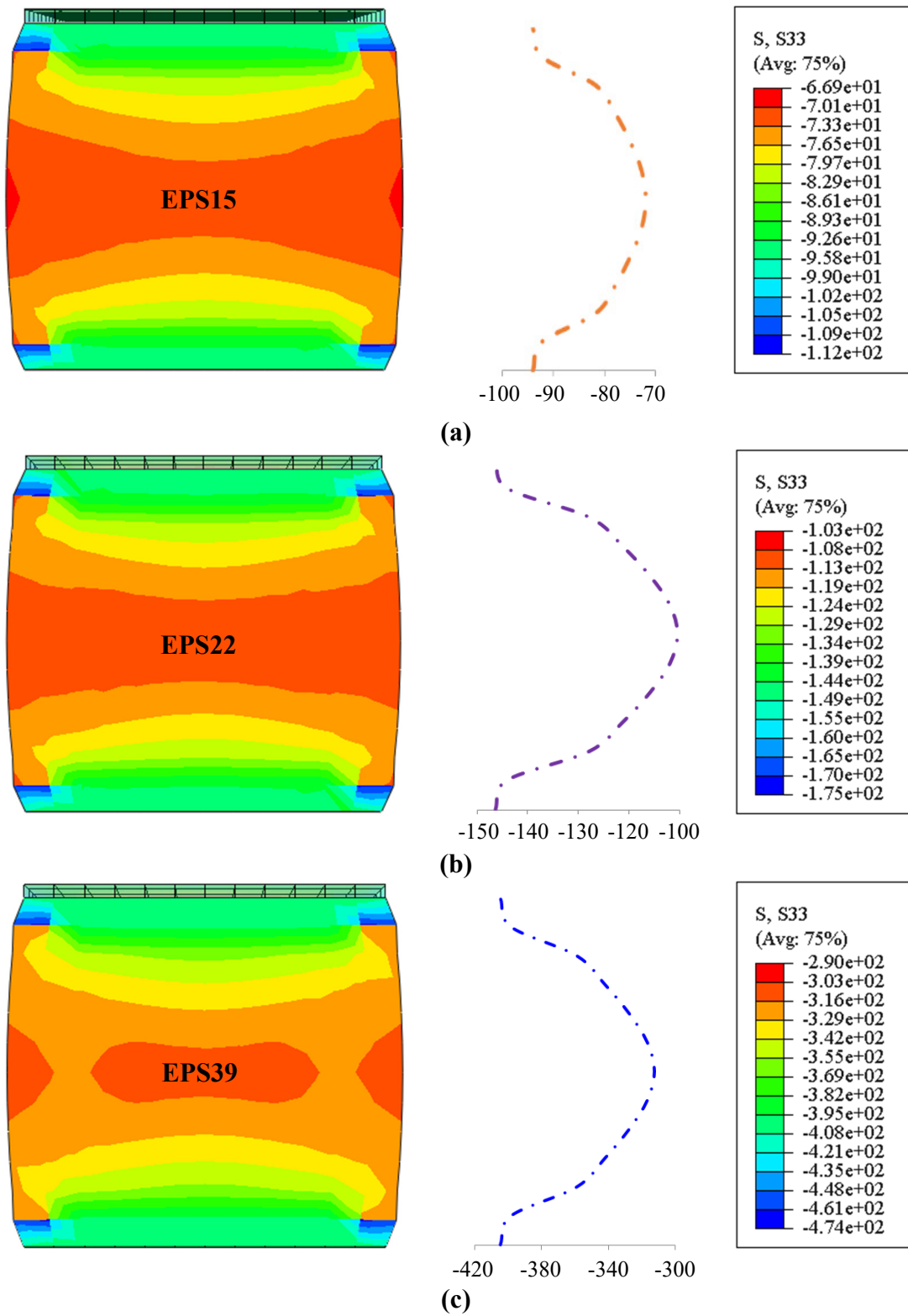


Figure 3-7 Normal stress distribution (kPa) at 5% strain: a) EPS15, b) EPS22, c) EPS39

3.2.3. Effect of lateral confinement

The effect of confinement pressure on the stress-strain behavior of the different EPS materials is investigated by introducing all-around pressure on the EPS blocks that is equal to 50% of the vertical pressure (σ_v). This pressure level was chosen to represent a typical at-rest condition that exists in granular material. The results of the analysis performed using the above material model are presented in Figure 3-8. It can be seen that the EPS response is insensitive to confinement pressure up to about 2% strain. At high strain levels, the presence of confinement resulted in an increase in resistance to the applied axial load. For example, at 5% strain the confined EPS blocks (EPS15, EPS22 and EPS39) experienced an average increase in stress of about 12% as compared to the unconfined samples. It is therefore concluded that for the range of axial strains typically used in subsurface EPS geofoam application (1% to 5%), the confining pressure does not have a significant effect on the material response to axial loading.

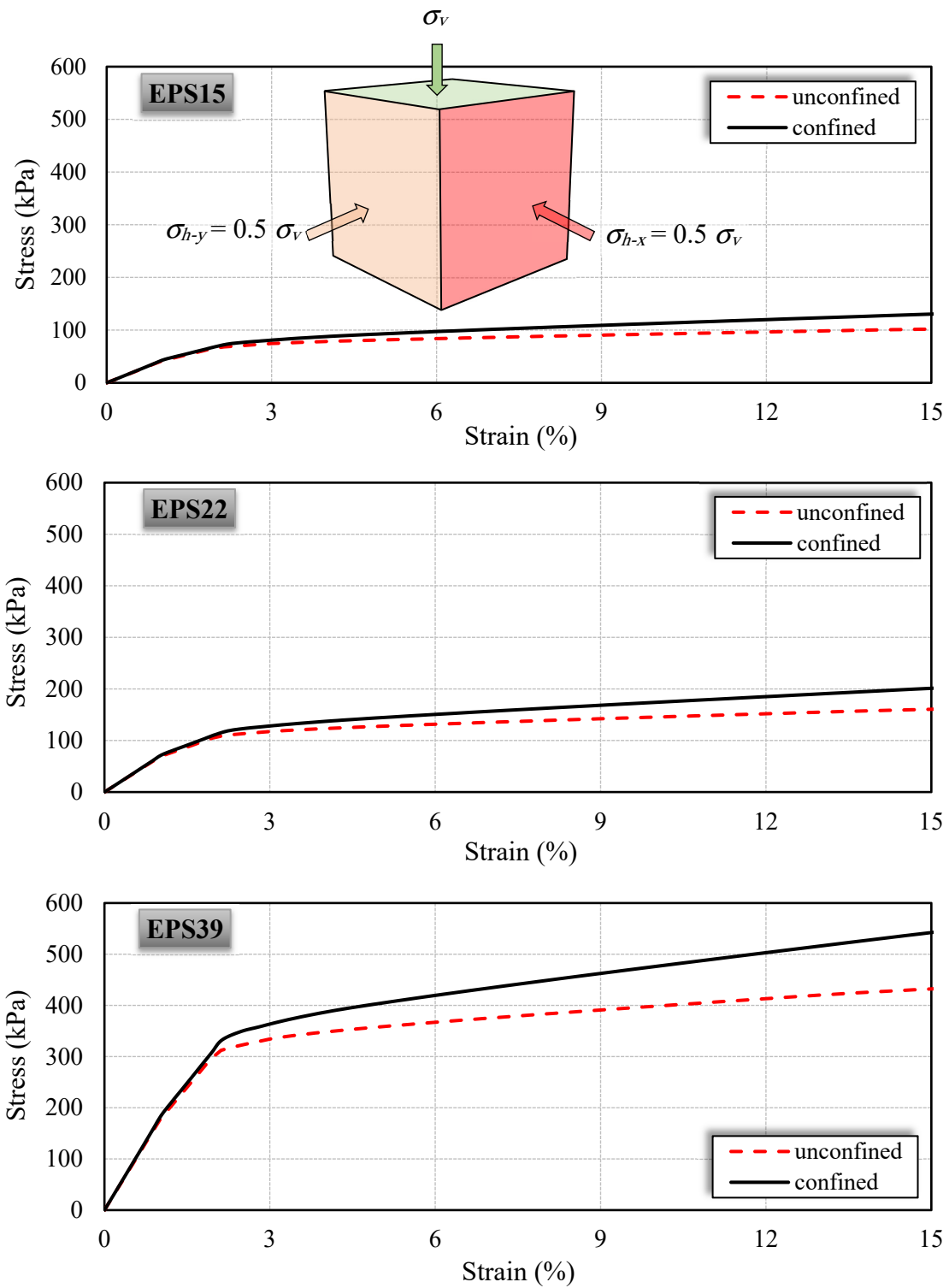


Figure 3-8 Effect of confining pressure on the stress-strain relationship of EPS material ($\sigma_h = 0.5 \sigma_v$)

3.3. Numerical Analysis of a Buried Structure Installed using ITI Method

A two-dimensional finite element model has been developed to simulate the test setup shown in Figure 3-9 and examine the role of EPS geofom on the changes in earth pressure acting on a rigid buried structure. The setup consisted of a hollow structural section of 100 mm wall thickness instrumented using tactile pressure sensors (Hussein and Meguid, 2015, Hussein et al., 2015). A block of EPS geofom, 2 inch in thickness, is used as a compressible material and placed directly above the structure. The chamber dimensions (1.4 x 1.2 x 0.45 m) are selected such that they represent two-dimensional loading condition. The use of air bag ensures uniform distribution of pressure on the surface of the soil. Dry sandy gravel with average unit weight of 16.3 kN/m³ and friction angle of 47° is used as backfill material. A benchmark test is first conducted to measure the contact pressure on the walls of the structure due to the increase in surface pressure in the absence of geofom. EPS geofom blocks, 2 inch in thickness, are then introduced immediately above the structure and the changes in contact pressure are measured for different geofom densities. The details of the experimental investigation is beyond the scope of this study.

3.3.1. Modeling details

FE mesh and boundary conditions

The finite element (FE) mesh that represents the geometry of the experiment, the boundary conditions, and the different soil zones around the HSS section is shown in Figure 3-10. The mesh size was adjusted around the structure to provide sufficient resolution and accuracy within the studied area. The complete mesh comprises a total of 1962 quadratic plane strain elements (CPE8) and 6449 nodes. Boundary conditions were defined such that nodes along the vertical boundaries may translate freely in the vertical direction but are fixed against displacements normal to the boundaries (smooth rigid). The nodes at the base are fixed against displacements in both directions (rough rigid).

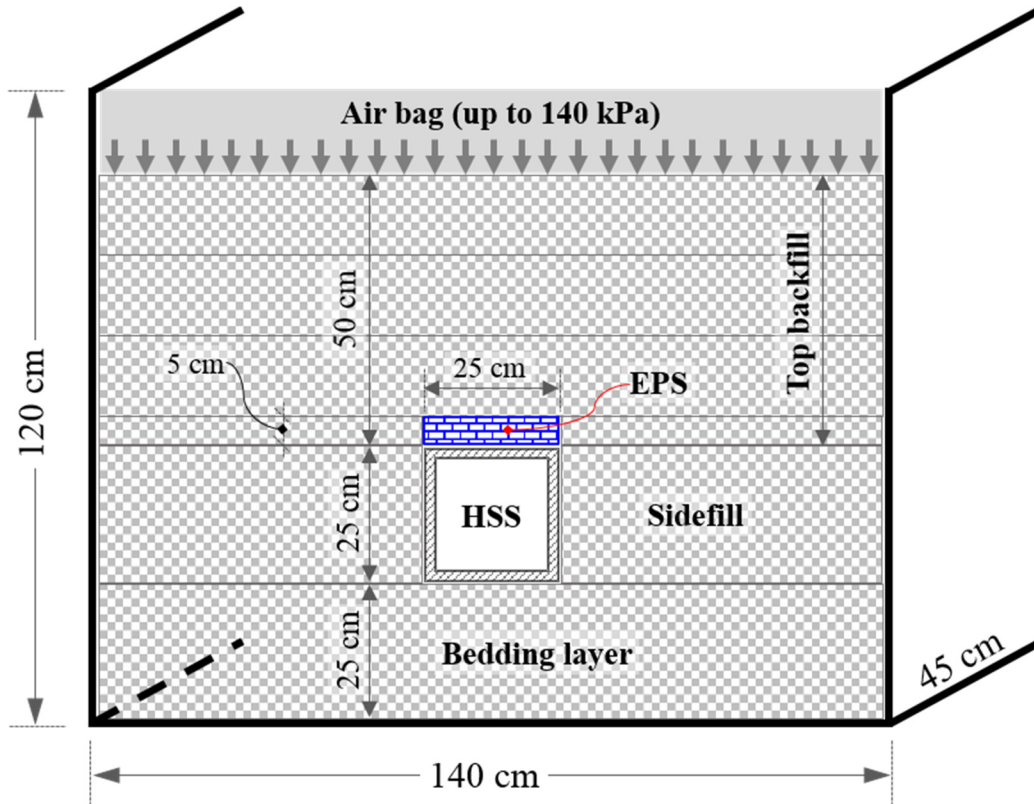


Figure 3-9 Schematic of the experimental setup

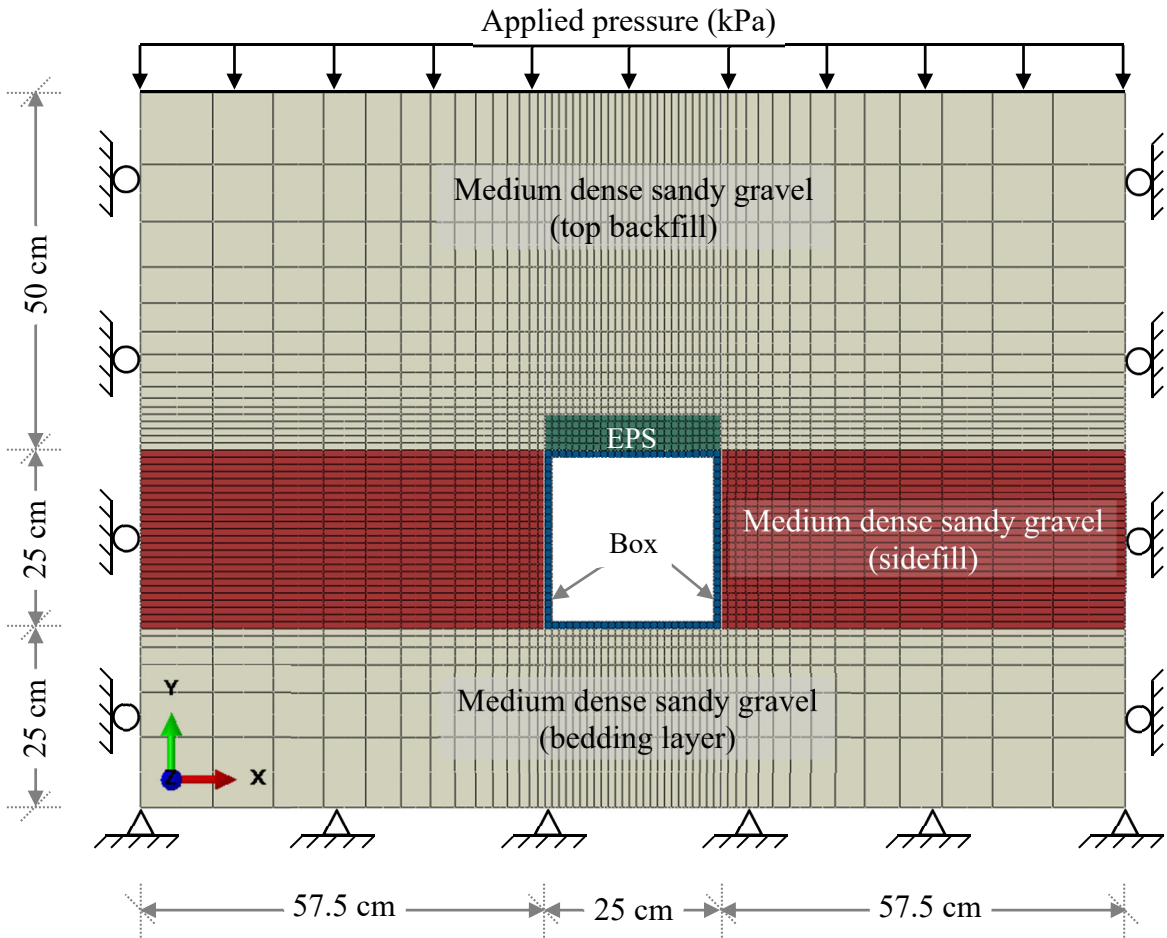


Figure 3-10 The finite element mesh used in the buried culvert model

Materials modeling

The backfill soil is modeled using elasto-plastic Mohr-Coulomb failure criteria with non-associated flow rule, Appendix (A). The input parameters as listed in Table 3-1. The dilatancy angle was determined using Bolton's equation (Bolton, 1986), which relates the mobilized frictional angle (ϕ_p) to the critical state friction angle (ϕ_{cv}). The HSS section is treated as linear elastic material with density of 7850 kg/m³, Poisson's ratio of 0.3, and Young's modulus of 200 GPa. The EPS material model developed in the previous section is used to simulate the geofoam inclusion.

Interface shear strength

Three different contact conditions are considered in this study; namely, i) Soil-EPS interaction, ii) Soil-Culvert interaction and iii) EPS-Culvert interaction. These interactions are simulated using the surface-to-surface, master-slave contact technique available in ABAQUS. The master-slave contact pair approach is a surface-based contact simulation in which we define surfaces for the bodies that could potentially be in contact throughout the analysis. Then, assign the mechanical contact property models that will control the relationship between the contacting bodies. In doing so, one surface in the contact pair is designated to be the slave surface and the other is the master surface. It is suggested that the body with the finer mesh be treated as the slave and the body with the coarser mesh be the master. In the current study, the mesh was matched between the different elements of the system (Soil-EPS-Culvert system) at the interfaces and the assignment of master and slave roles was arbitrary.

Contact formulation in 2D space covers both tangential and normal directions. In the tangential direction, Coulomb friction model is used to describe the shear interaction between the geofoam, the structure, and the surrounding soil. This model involves two materials parameters- a friction coefficient (μ), and a tolerance parameter (E_{slip} - tolerance). The shearing resistance (τ) is considered as a function of the shear displacement that represents the relative movement between the two contacted parties. On the other hand, a 'hard' contact model is used to simulate the contact pressure in the normal direction. The parameters used to describe these interface conditions are given in Table 3-1.

3.3.2. Calculated vs. measured earth pressures

The numerical modeling results are first validated by comparing the calculated pressures on the walls of the buried structure with the measured values for the three cases a) the benchmark test with no geofoam, b) using EPS15, and c) using EPS22. As shown in Figure 3-11, the numerical model is able to capture the pressure changes, at the upper wall of the structure, with a reasonable accuracy for the benchmark test as well as for the induced trench cases. Significant reduction in earth pressure was found due to the addition of EPS geofoam above the structure. For example, at surface pressure of 140 kPa, the earth pressure on the upper wall decreased by 60% (from 149 kPa for the benchmark case to 60 kPa) for the induced trench installation using EPS22 and the reduction in pressure reached about 70% (43 kPa) when EPS15 inclusion was introduced.

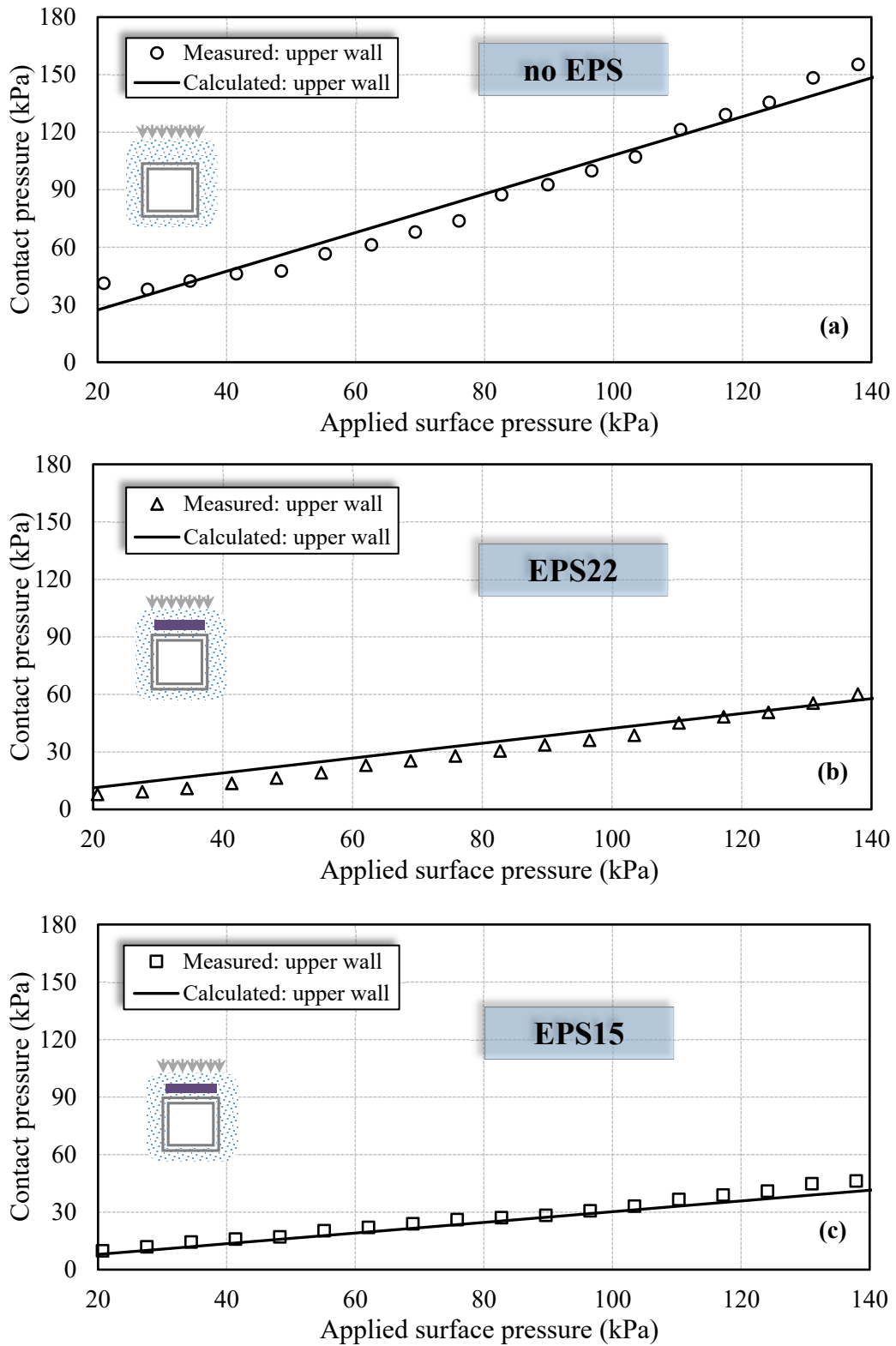
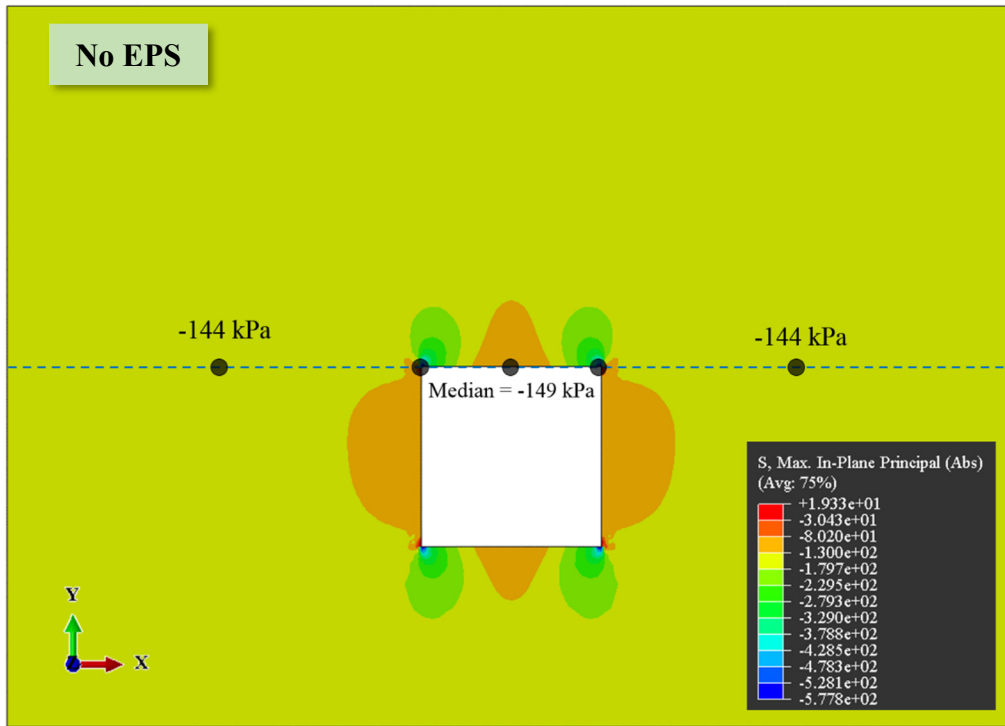


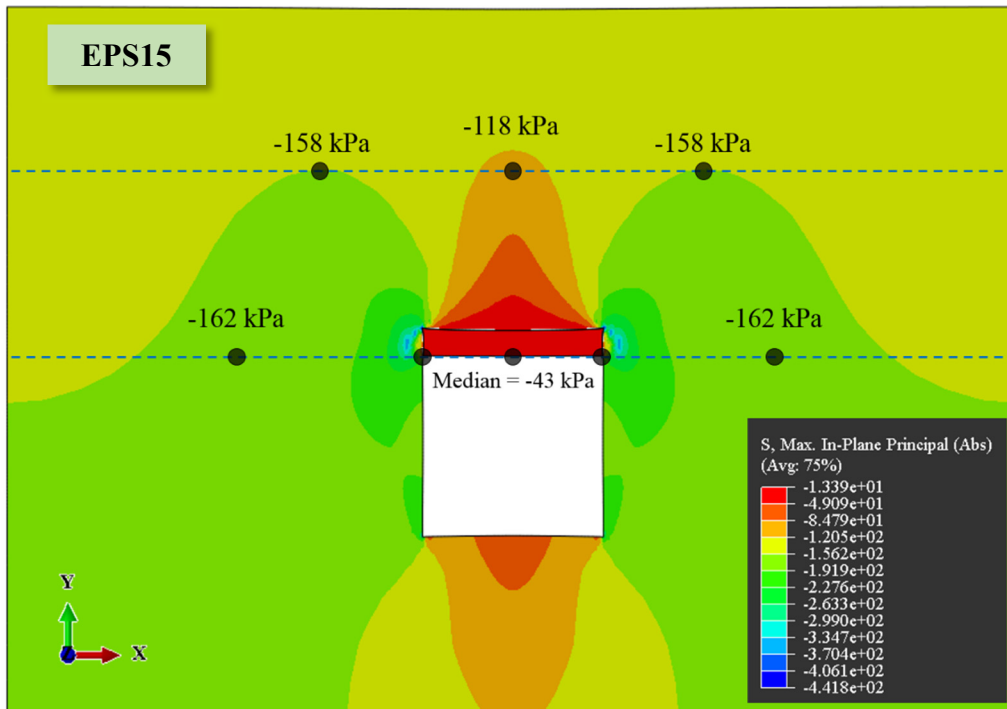
Figure 3-11 Model validation for the cases of a) No EPS, b) EPS22 and c) EPS15

3.3.3. Soil arching mechanism

To demonstrate the changes in pressure distribution on the walls of the buried structure, the in-plane principal stresses are presented in Figure 3-12 at applied surface pressure of 140 kPa. When the box structure is buried in the backfill without geofoam inclusion (Figure 3-12a), negative arching developed where the rigid box attracted more earth load compared to the surrounding soil. By examining the earth pressure distribution on a horizontal plane located along the top of the upper wall (Figure 3-12a), it was found that the average pressure away from the influence zone of the buried structure is 144 kPa which increased to 149 kPa on the upper wall of the box. This represents the combined effect of the weight of the backfill material and the surface pressure applied at the top of the chamber. The contact pressure distribution dramatically changed when EPS15 block was placed immediately over the buried box as shown in Figure 3-12b. The compression of the geofoam block created a reduction in contact pressure on the upper wall of the box (from an average of 149 kPa to 43 kPa) coupled with an increase in pressure within the backfill material located on both sides of the box. The pressure distribution reveals that movement of the soil column above the geofoam block resulted in not only in a contact pressure reduction on the upper wall but also a reduction in earth pressure above the box. By comparing the pressure distributions in Figure 3-12, it is clear that induced trench installation using EPS geofoam has a significant impact on the earth loads transferred to the walls of the buried structure.



(a) No EPS geofoam



(b) EPS15

Figure 3-12 In-plane principal stress distribution around the buried structure at applied surface pressure of 140 kPa

3.3.4. Parametric study

Upon the verification of the FE model, a parametric study is carried out — in this section — using the proposed model to evaluate the role of EPS density, width, thickness and location on the response of the system.

Effect of EPS density

The effect of EPS density on the load transferred to the buried structure is numerically examined in this section by comparing the calculated pressures at the investigated locations (upper, lower and side walls) for three different EPS materials, namely, EPS15, EPS22, and EPS39. The maximum surface pressure was increased in the analysis up to 300 kPa to allow for the behavior of the system to be investigated at high stress levels. For the analyzed induced trench cases, the surface pressure that allows for a maximum of 1% strain in the EPS is used in this parametric study. The results are presented in Figure 3-13a, b and c for the upper, lower and side walls, respectively. Contact pressure is also compared with the benchmark case (no EPS geofoam) to evaluate the effect of each EPS type on the load redistribution around the buried structure. The vertical axes in Figure 3-13 represent the contact pressure normalized with respect to that of the benchmark case.

For the upper wall (Figure 3-13a), the EPS density was found to have a significant impact on the earth pressure acting on the wall. Compared with the benchmark, the lowest contact pressure is calculated for the case of EPS15 with pressure reduction of about 75% at an applied pressure of 106 kPa. The pressure reduction for EPS22 and EPS39 were found to be 60% and 30% at applied surface pressures of 113 kPa and 135 kPa, respectively.

The pressure reduction ratios for the lower wall (Figure 3-13b), at 1% strain, were found to be 47%, 40% and 23% for EPS15, EPS22 and EPS39, respectively. These effects are found to be smaller compared to the reduction ratios calculated for the upper wall. Similar trends were found for the contact pressures on the side wall (Figure 3-13c) with pressure reduction ratios of 25%, 20% and 8%, respectively for the investigated EPS densities.

It is worth noting that, due to the linear nature of the calculated responses, the above reduction ratios are expected to apply for other EPS types and surface pressures as long as the maximum strain in the EPS does not exceed 1%.

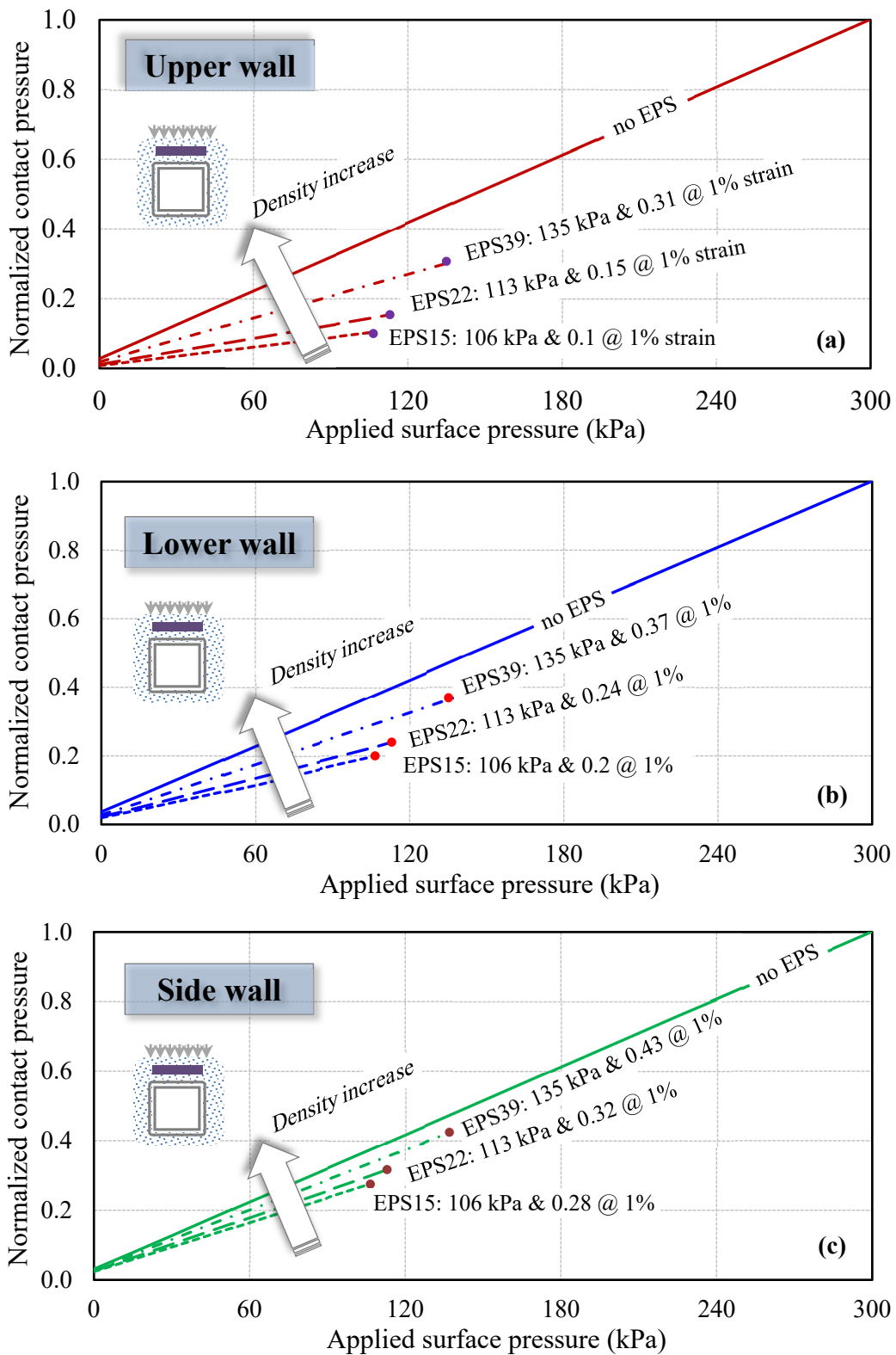


Figure 3-13 Effect of EPS density on the earth pressure acting on the walls of the structure

Effect of EPS width

To evaluate the effect of the EPS block width on the contact pressure acting on the walls of the HSS box, the EPS thickness and density are kept constant and the width is incrementally increased from one to two times the width of the HSS section, as illustrated in Figure 3-14. The results are summarized in Figure 3-15a, b and c for the upper, lower and side walls, respectively. It can be seen that increasing the width of the EPS from 1B to 2B led to 12% increase in contact pressure at the upper wall (Figure 3-15a). For the lower and side walls, however, the contact pressure decreased by about 10%. This is considered to be insignificant given that twice the geofoam volume (from 1B to 2B) was used.

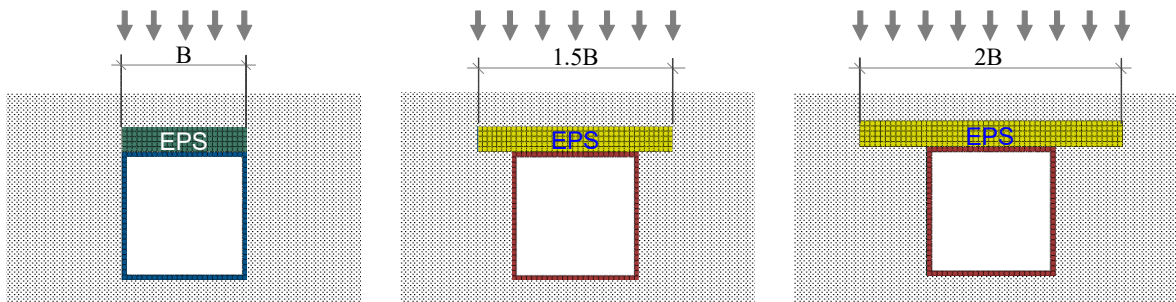


Figure 3-14 The change in EPS width

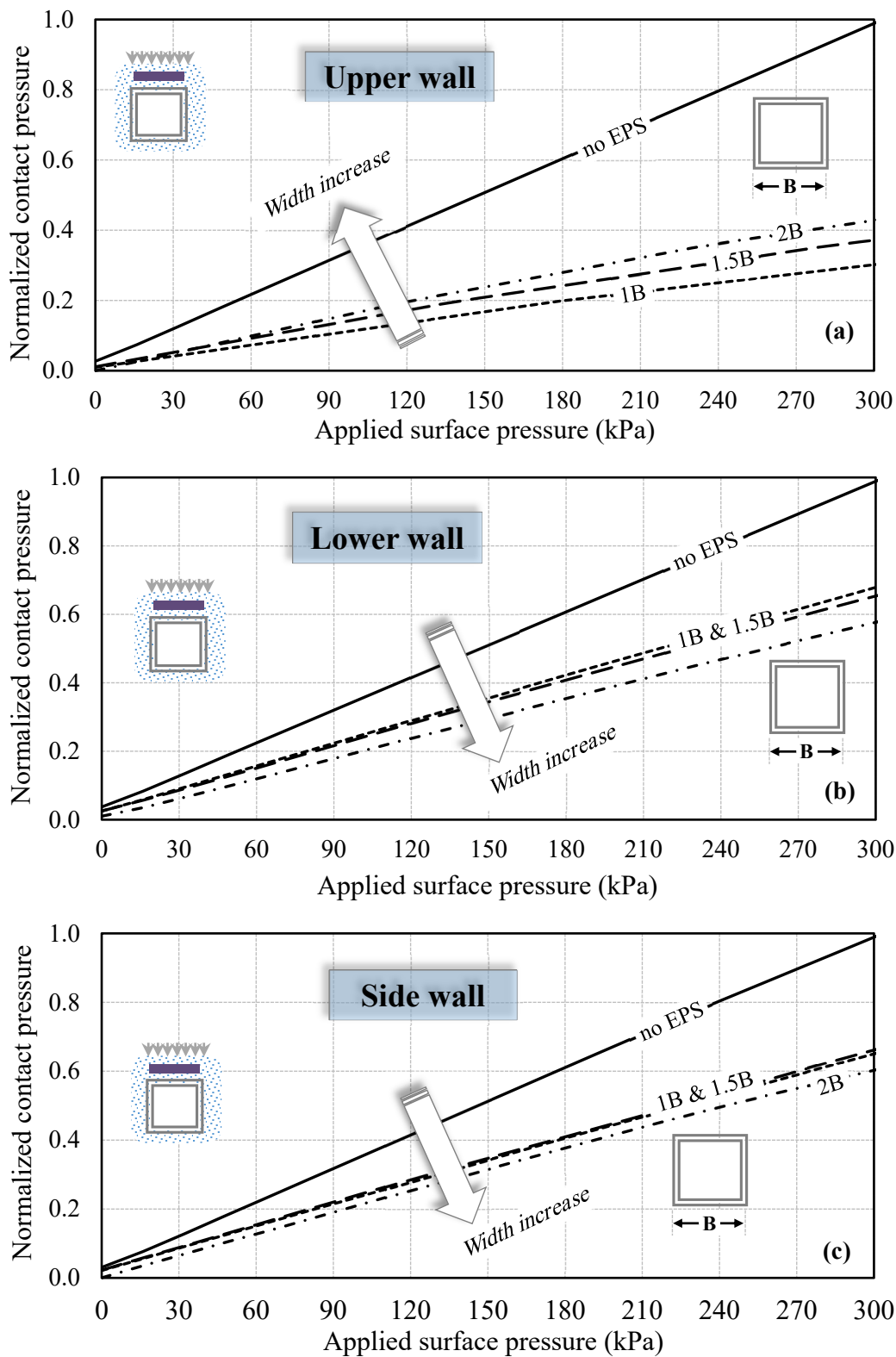


Figure 3-15 Effect of EPS width on the earth pressure acting on the walls of the structure

Effect of EPS thickness

The effect of the EPS thickness is examined for EPS15. The EPS width was chosen to be equal to that of the HSS section (width = 1B). The thickness is increased incrementally (Figure 3-166) from 2-inch to 6-inch and the contact pressure is calculated for each case around the HSS box. At the upper wall (Figure 3-17a), increasing the thickness of the EPS block from 2-inch to 6-inch resulted in pressure decrease of about 18%. No significant change was found for the lower and side walls as shown in Figures 3-17b and 3-17c.

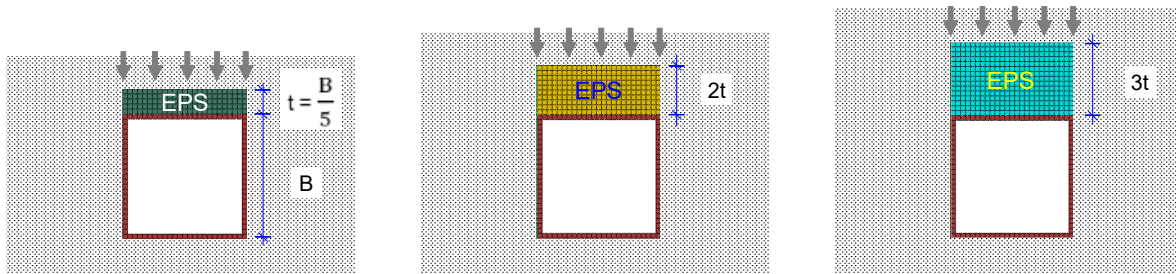


Figure 3-16 The change in EPS thickness

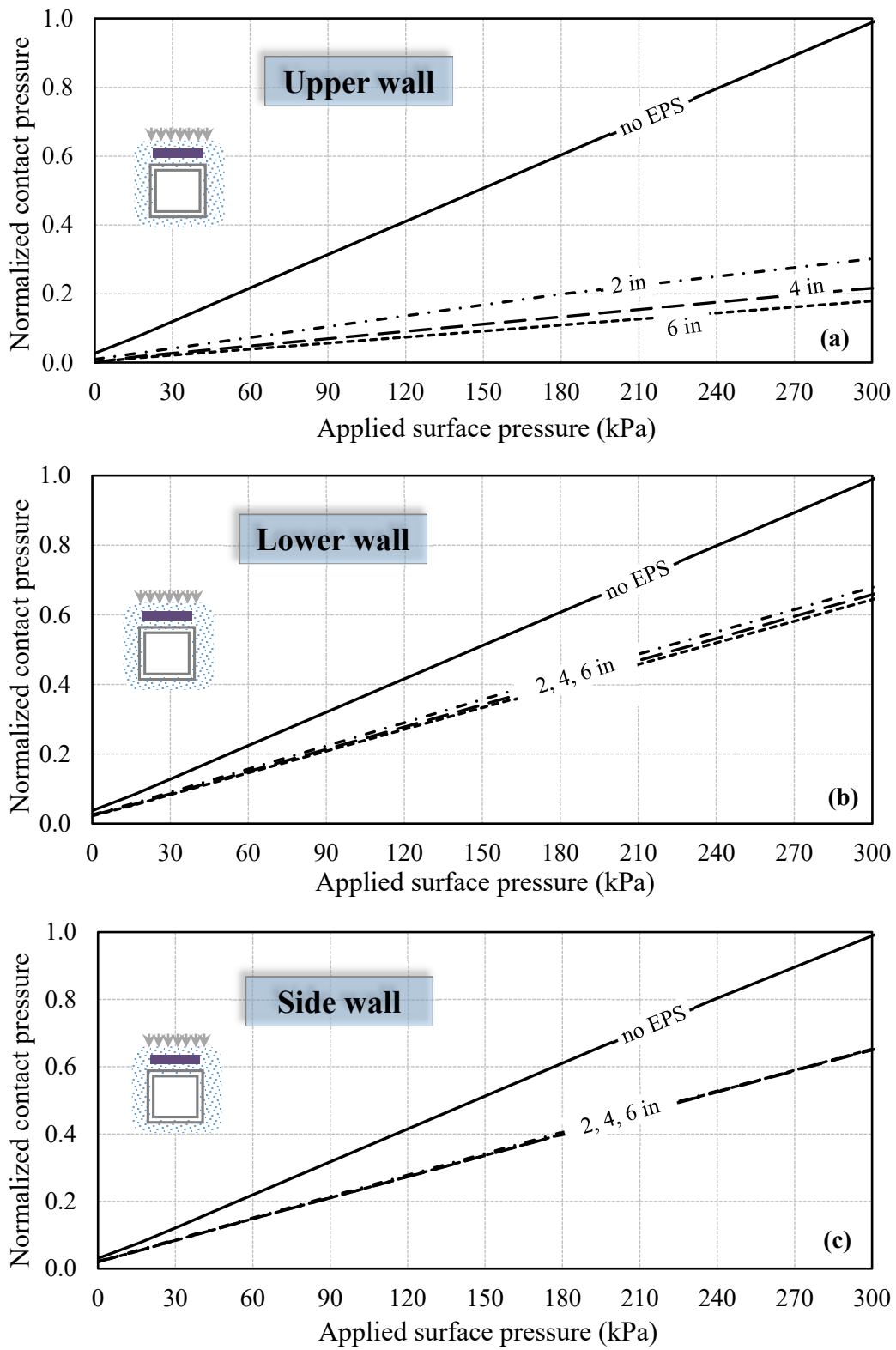


Figure 3-17 Effect of EPS thickness on the earth pressure acting on the walls of the structure

Effect of EPS location

The effect of EPS block location with respect to the upper wall on the pressure transferred to the buried structure is also evaluated. The modeled geofoam block is EPS-15 with 2-inch in thickness (t) placed at three different locations (h) above the structure such that $h/t = 0, 1$ and 2 (Figure 3-18). It can be seen (Figures 3-19a and 3-19b) that moving the EPS block by 4 inches ($2t$) led to a reduction in contact pressure at the upper and lower walls of about 10 %. No significant change in pressure was found for the side walls (Figure 3-19c) as a result of the change in EPS location.

The effect of EPS density on the load transferred to the buried structure is numerically examined in this section by comparing the calculated pressures at the investigated locations (upper, lower and side walls) for three different EPS materials, namely, EPS15, EPS22, and

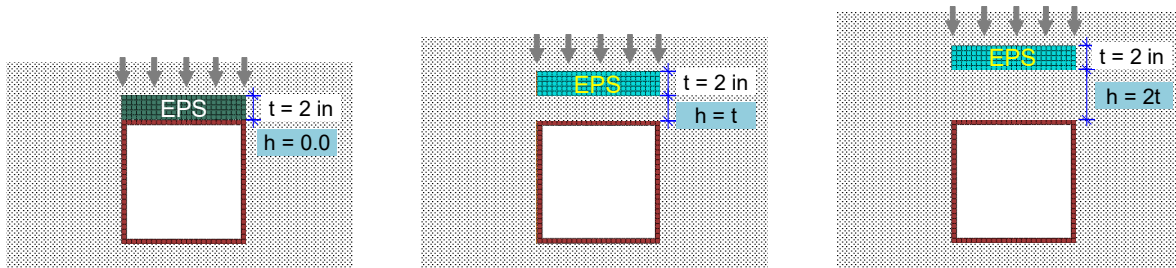


Figure 3-18 The change in EPS location

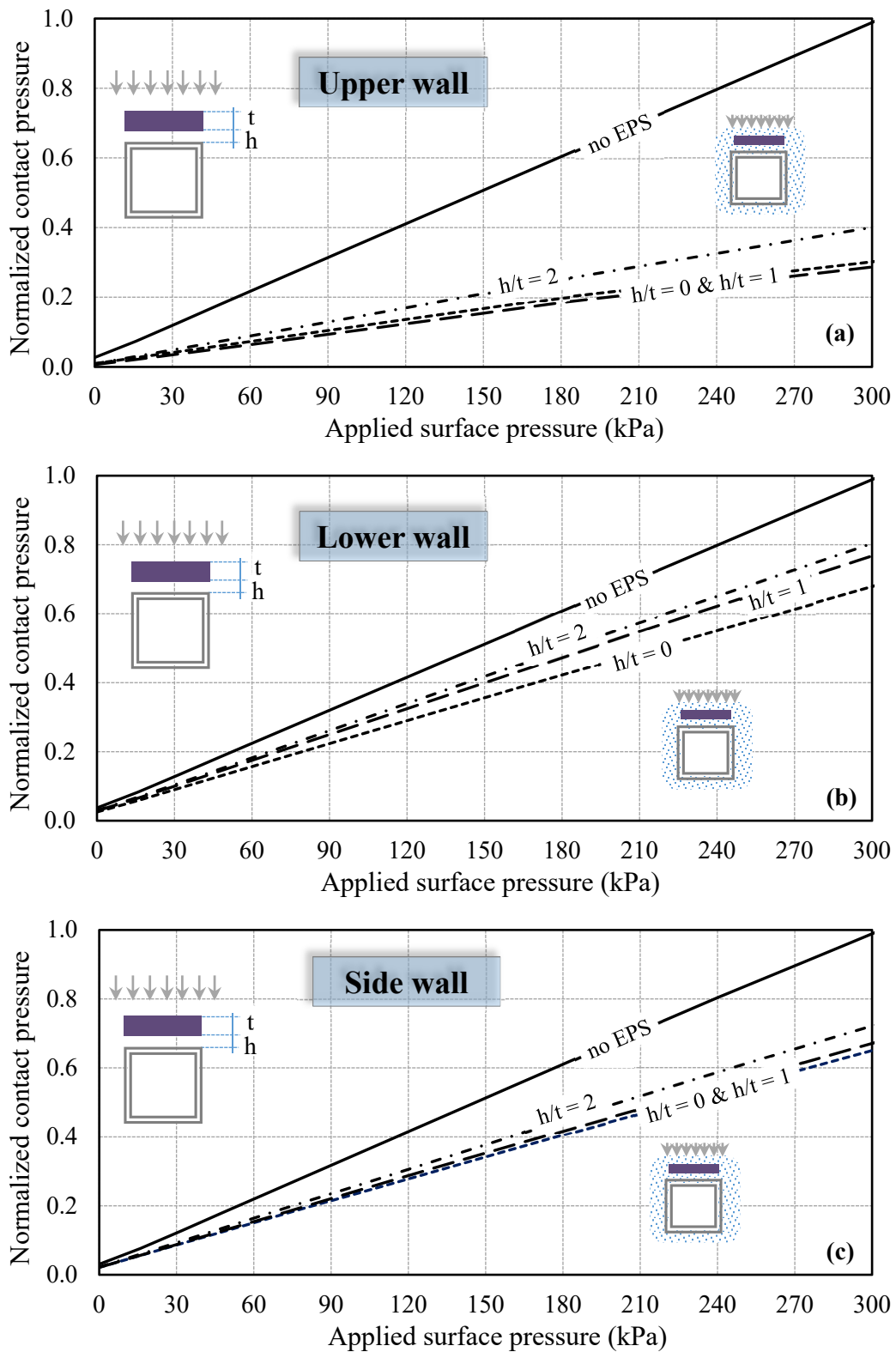


Figure 3-19 Effect of EPS location on the earth pressure acting on the walls of the structure

3.4. Summary and Conclusions

In this study, a numerical procedure for modeling the short-term response of EPS geofoam under uniaxial compression loading is developed using ABAQUS software. The model takes into account different features of the constitutive behavior responsible for the observed response in the laboratory, including material nonlinearity, plasticity and isotropic hardening. The material model is validated for three different EPS geofoam materials using index test results and the role of lateral confinement on the stress-strain response is also examined. Calibrated using the experimental data, a series of finite element analyses is performed to investigate the role of the EPS density, width, thickness and location on the earth pressure distribution acting on a rigid buried structure installed using the induced trench method.

Results showed that the introduction of EPS geofoam block immediately above the structure has a significant effect on the contact pressure distribution particularly on the upper wall covered by the geofoam inclusion. The only factor that was found to have a significant impact on the changes in earth pressure is the material density. For the investigated range of parameters, results showed that the EPS width and location did not contribute significantly to the positive arching process and, therefore, only minor pressure changes were calculated.

Finally, the proposed FE modeling approach has proven to be efficient in capturing the behavior of EPS geofoam material under complex interaction soil-structure condition and can be adopted to simulate similar soil-geofoam-structure interaction problems.

Preface to Chapter 4

The finite element approach developed in the previous chapter has demonstrated its efficiency in investigating the behavior of soil-geofoam-structure system. The model was used to study the pressure distribution around a buried structure installed using the induced trench method. An elasto-plastic constitutive model was developed to simulate the behavior of EPS geofoam inclusion. In this analysis, the EPS inclusion was embedded immediately above the upper wall of the box culvert. To continually demonstrate the applicability of the model, the same buried structure is now investigated with different EPS configuration. Comparisons are made regarding the best arrangement of the EPS inclusion that improves the earth pressure distribution around the structure. The capability of the proposed FE approach to model complex soil-structure interaction problems under different condition is verified.

CHAPTER 4

Numerical Analysis of Buried Structures Installed Using Imperfect Trench Installation*

Abstract

Expanded Polystyrene (EPS) geofoam has been successfully used as a compressible inclusion in geotechnical engineering projects to reduce earth pressure on different geotechnical structures (e.g. buried structures, retaining walls and structural slabs). Using EPS to reduce earth loads on a buried structure installed under embankment loading is known as the induced trench installation (ITI) technique. In this study, a plane strain nonlinear finite element analysis is conducted to investigate the role of embedding a layer of geofoam within the backfill soil around a buried rigid box on the earth loads reaching the box walls. This is achieved using numerical analysis that allows for the effect of several EPS parameters to be evaluated. The numerical model is first validated by comparing the calculated contact pressures acting on the walls with experimental data and then used to provide a new insight into the complex interaction between the three different elements (backfill, geofoam, and culvert) of the system. Comparisons are made regarding the effectiveness of placing EPS inclusion, with different arrangements, on the earth pressure distribution around the structure as well as the resulting soil movement near the soil surface. The calculated pressures on the buried box are compared with the theoretical overburden pressures in addition to the external surface loading. Then, preliminary design charts are provided to help engineers in selecting the proper EPS material that fits the project requirements. Finally, conclusions are made to confirm that placing EPS material above a rigid subsurface structure can result in an economic design.

Keywords: Finite element method, EPS geofoam, Buried structures, Soil-structure interaction, Soil arching.

* A version of this chapter has been submitted to *Geotextiles and Geomembranes Journal*, June 2016 (Manuscript No. G&G 3055).

4.1. Introduction

The induced trench installation (also called imperfect ditch or ITI method) has been used for several decades to reduce the vertical earth pressure on rigid culverts. It is well known that the earth pressure on deeply buried culverts is affected by soil arching. The method involves installing a compressible layer immediately above the culvert to generate positive arching in the overlying soil (Hussein et al., 2015).

The concept of induced trench was originally introduced by Marston (1930) to reduce earth pressures on buried conduits located at the bottom of an embankment of significant height (heights > 10 m). Modifications were made to the method by Spangler in 1950 to establish “Marston-Spangler” theory.

In the ITI method, a reduction in vertical pressure is achieved by inducing positive arching in the soils above the conduit. The basic idea of induced trench design compared to positive projecting box culverts is shown in Figure 4-1. As shown in this figure, for the case of positive projecting, no compressible zone above the conduit and therefore the crown of the structure experience earth loads that could exceed the overburden pressure. This pressure increase is attributed to the fact that the soil prism above the culvert deforms less compared to the adjacent soil, causing ‘negative’ arching. On the contrary, the imperfect ditch installation allows the compressible zone to induce relative settlement between the soil directly above the culvert and the adjacent backfill leading to upward shear stresses (positive arching) that reduce earth loads on the culvert.

For several years the Marston-Spangler theory was considered the basis for the design of induced trench installations in many international design standards (e.g. CSA, 2006, AASHTO, 2012) and no significant update is made since the publication of the original work. In spite of its long history, the induced trench method of design and construction is viewed with skepticism because of many simplifying assumptions used in the design method (Hansen et al., 2007). In addition, limitations of the ITI method have been reported and questions were raised regarding the long-term sustainability of the load reduction process.

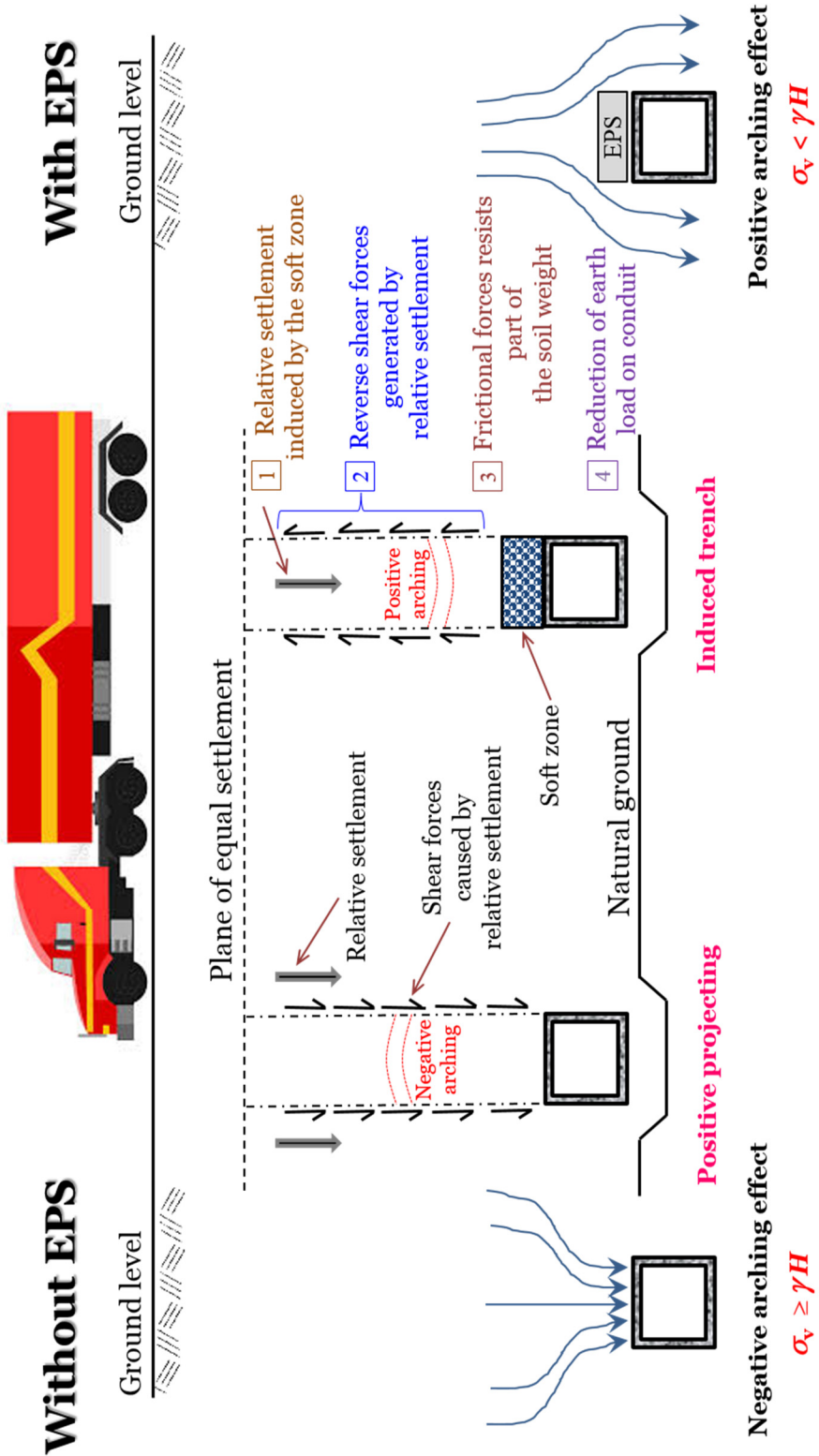


Figure 4-1 Positive projecting versus induced trench installations

As a consequence, the American Concrete Pipe Association Handbook (ACPA, 2004) has deleted the induced trench method of design. Alternatively, the method shows promising potential for stress reduction and benefits of using standard culvert sizes when embankment heights exceeds 10 m as a positive projecting type design in these instances would result in other more costly designs such as cast-in-place concrete. Generally, cost savings offered by induced trench installations are greater for larger culvert sizes.

AASHTO LRFD bridge design specifications (AASHTO, 2012) has recognized the ITI method as one of the acceptable methods of installation. However, the standards provide guidelines for estimating earth loads on positive projecting culverts, but not for culverts installed using induced trench technique. Instead of relying on the M-S theory, AASHTO suggested the use of accepted test methods, soil-structure interaction analyses, or past experience to determine the earth load on the culvert (Oshati et al., 2012).

Several researches studied the relevant soil-structure interaction using numerical modeling (e.g. Kim and Yoo, 2002, Kang et al., 2008, McAfee and Valsangkar, 2008, Sun et al., 2009, McGuigan and Valsangkar, 2010 and 2011) to help better understand the method and to address uncertainties in the design method. However, none of these studies provides technically design guides (e.g. charts or equations) that can be readily used by designers. Moreover, the constitutive model that represent the true response of the EPS material was often simplified either as a linear elastic material or an elastic-plastic which will not help to predict the stress-strain behavior of the geof foam in the short-term.

Numerical modeling of soil-structure interaction problems involving geosynthetic inclusions (e.g. EPS geof foam) is known to be challenging. This is attributed to the complicated nature of the created soil-EPS-structure system with different material models and interaction behavior. Analyzing the problem using continuum approaches (e.g. finite element method) consists of finding a unique system of displacements for each component that satisfies both force equilibrium and material continuity. Finite element method has proven to be a powerful tool in modelling boundary value problems, particularly those involving soil-structure interaction. The objective of the present study is to examine the role of geof foam properties

in reducing earth pressure on a rigid box culvert. A secondary objective is to provide technical design charts that can be readily used by designers to correlate the pressure reduction to the embankment height and EPS stiffness. This is achieved by conducting a series of numerical analyses to evaluate the effect of different EPS configurations — around the structure — on the system response. In this analysis, a material model that is able to capture the response of EPS geofoam is used.

The finite element (FE) analyses presented throughout this investigation have been performed using the general finite element software ABAQUS/Standard, version 6.13 (ABAQUS, 2013).

4.2. Description of the Numerical Analysis

A series of 2D finite element analyses is performed using ABAQUS software to confirm the experimental results of the case study that has been presented in Section 3.3 and Figure 3-9 of this thesis. For comparison purposes, the analyses that have been developed in chapter (3) is named *case-I*. In *case-I*, the EPS was placed directly above the structure. Another condition (*case-II*) is investigated in this chapter, whereas the geofoam blocks were placed above the upper wall and next to the side walls. Eventually, a comparative study is carried out to investigate the optimum EPS configuration around the buried structure. It is worth mentioned that the experimental work examined the two different cases (*case-I* and *case-II*) using two types of EPS materials (EPS15 and EPS22). The measured data will be used to calibrate the numerical models. As mentioned previously, in “section 3.3” of this thesis, the details of the experimental investigations are beyond the scope of this study.

4.2.1. Models Generation

The numerical models, for both cases (*case-I* and *case-II*) have been developed such that they follow the geometry and test procedure used in the experiments. The generation procedure used for the models, of the two cases, is typical except for the FE mesh.

FE mesh and boundary conditions

The finite element (FE) mesh that represents the geometry of the experiment, the boundary conditions, and the different soil zones around the HSS section for *case-I* is shown in Figure 3-10. Whereas, the mesh that represents the geometry of *case-II* is illustrated in Figure 4-2. In both cases, the mesh size was adjusted around the structure to provide sufficient resolution and accuracy within the studied area. The complete mesh comprises a total of 2010 quadratic plane strain elements (CPE8) and 6606 nodes for the two examined conditions.

Boundary conditions were defined such that nodes along the vertical boundaries may translate freely in the vertical direction but are fixed against displacements normal to the boundaries (smooth rigid). The nodes at the base are fixed against displacements in both directions (rough rigid).

Materials modeling

The backfill soil is modeled using elasto-plastic Mohr-Coulomb failure criteria with non-associated flow rule (Appendix-A). The input parameters as listed in Table 3-1. The dilatancy angle was determined using Bolton's equation (Bolton, 1986), which relates the mobilized frictional angle (ϕ_p) to the critical state friction angle (ϕ_{cv}).

The HSS section is treated as linear elastic material with density of 7850 kg/m³, Poisson's ratio of 0.3, and Young's modulus of 200 GPa. The EPS geofoam inclusion is modeled as nonlinear elasto-plastic strain hardening using the material model developed in "section 3.2" of this study. The elastic properties of EPS types used in the numerical study are summarized in Table 3-1 and the hardening rule is shown in Figure 3-4.

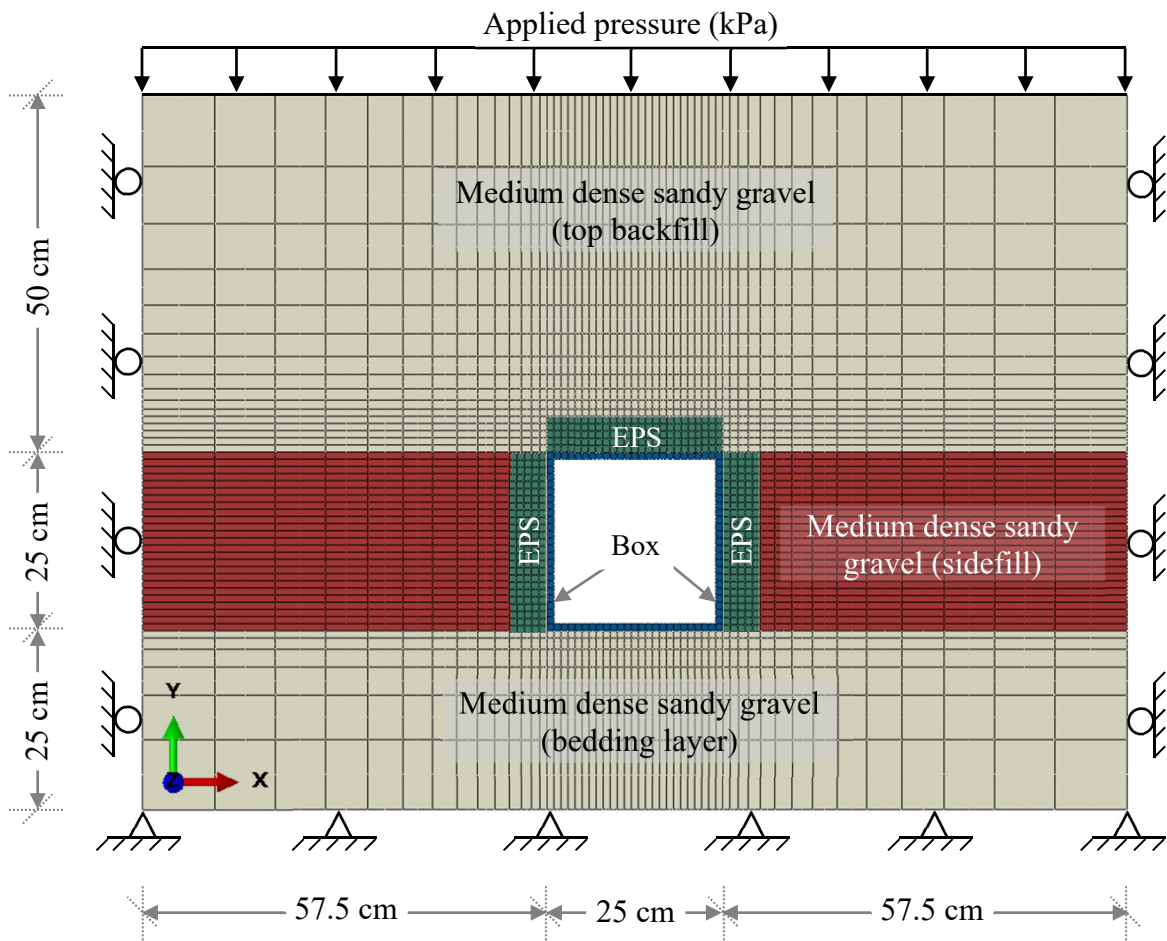


Figure 4-2 The finite element mesh used in the model of *case-II*

Interface shear strength

Three different interface conditions are modeled; namely, i) Soil-EPS interface, ii) Soil-Culvert interface and iii) EPS-Culvert interface. These interactions are simulated using the surface-to-surface, master-slave contact technique available in ABAQUS. The master-slave contact pair approach is a surface-based contact simulation in which we define surfaces for the bodies that could potentially be in contact throughout the analysis. Then, assign the mechanical contact property models that will control the relationship between the contacting bodies. In doing so, one surface in the contact pair is designated to be the slave surface and the other is the master surface. It is suggested that the body with the finer mesh be treated as the slave and the body with the coarser mesh be the master.

In the current study, the mesh was matched between the different elements of the system (Soil-EPS-Culvert system) at the interfaces and the assignment of master and slave roles was arbitrary.

Contact formulation in 2D space covers both tangential and normal directions. In the tangential direction, Coulomb friction model is used to describe the shear interface between the geofoam, the structure, and the surrounding backfill. This model involves two materials parameters- a friction coefficient (μ), and a tolerance parameter (E_{slip} - tolerance). The shearing resistance (τ) is considered as a function of the shear displacement that represents the relative movement between the two contacted parties. On the other hand, a ‘hard’ contact model with penalty stiffness is used to simulate the contact pressure in the normal direction. The parameters used to describe these interface conditions are given in Table 3-1.

4.2.2. Models validation

In this section, the numerical models used to simulate the response of the buried structure are validated by comparing the calculated pressures with the measured values for three conditions; a) the benchmark test with no geofoam, b) using EPS15 geofoam, and c) using EPS22 geofoam.

Validation of case-I: EPS over the buried box

The numerical simulation of the experiments conducted using EPS above the structure (*case-I*) is presented previously in “section 3.3” and Figure 3-11. As shown in Figure 3-11, the numerical model is able to capture the pressure changes, at the upper and lower walls for the structure, with a reasonable accuracy for the benchmark test as well as for the induced trench cases. More details are given in “section 3.3.2”.

Validation of case-II: EPS places over and around the buried box

The numerical analysis of *case-II* where the EPS blocks are placed on the upper wall and next to the side walls of the structure has been discussed in the previous section. The finite element mesh used in the analysis replicates the geometry of the experiment as shown in Figure 4-2. Figure 4-3 presents the numerical modeling results and the comparison with the experimental values of *case-II*.

General agreement was found between the calculated and measured pressures at the top wall for the investigated EPS materials. This confirms the suitability of the model in capturing the response of this complex soil-structure interaction system. In this case, the presence of the EPS at the side walls resulted in a pressure increase at the upper and lower walls compared to *case-I* where the EPS blocks are placed only above the buried structure. More details about the comparison between the effects of the two cases on the earth pressure are elaborated in the coming sections. Figure 4-4 shows the contours of the stress distribution on the soil-geofilm-structure system in *case-II* at applied surface pressure of 140 kPa using EPS15. The vertical (left hand side) and lateral (right hand side) stress components, that are translated to contact pressures on the culvert walls, are presented in Figure 4-4a. These contours confirm the calculated values of the vertical and lateral contact pressures that are presented graphically in Figure 4-3. Figure 4-4b illustrates the distribution of the in-plane principal stresses in the soil around the buried structure. By examining the contours lines, it can be seen that the vertical pressures near the upper walls decreased from -136 kPa to -54 kPa on the culvert. Similar results were found at the lower wall, where the pressures decreased from -170 to -56 on the structure. The lateral pressure on the side walls has experienced different scenario. The pressure increased in the soil from -170 kPa to -267 kPa near the structure, then decreased rapidly at the location of the EPS block to reach -15 kPa lateral pressure on the culvert side walls. This is attributed to the presence of the EPS block at the upper wall that caused a pressure increase within the backfill material located on both sides of the box.

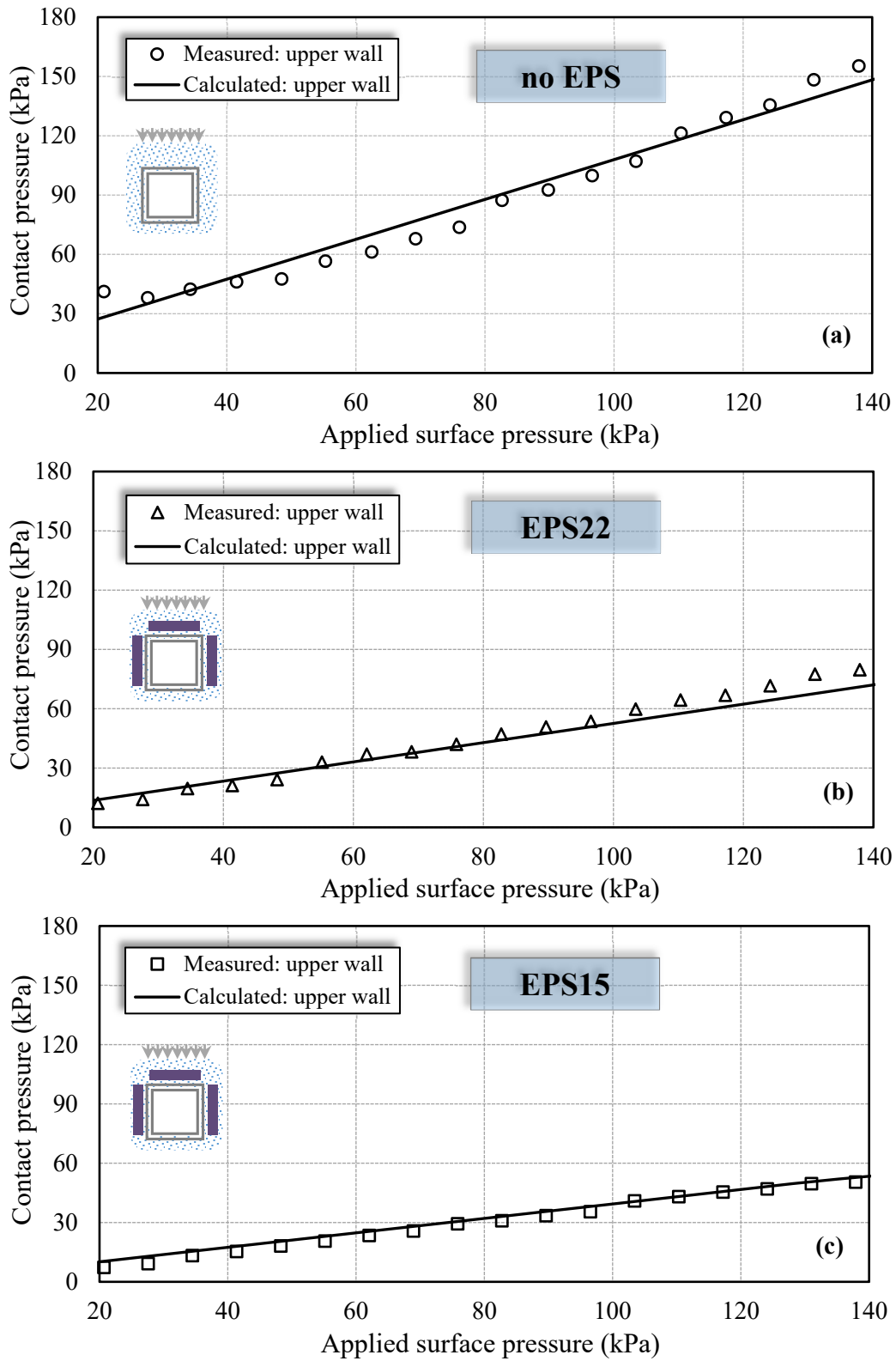
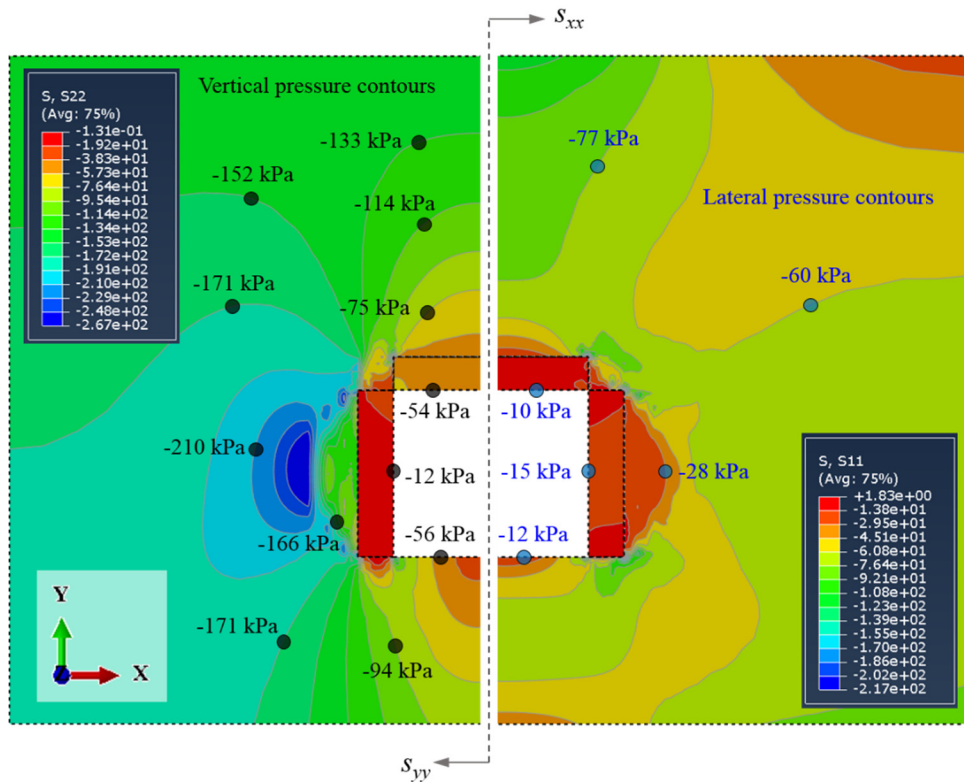
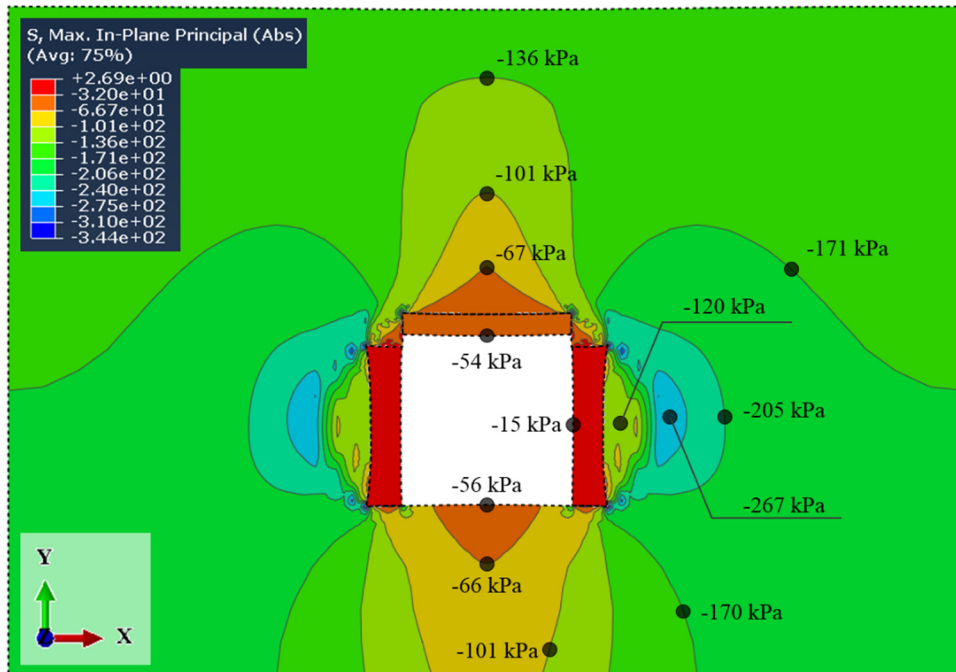


Figure 4-3 Model validation for *case-II*: a) No EPS, b) EPS22 and c) EPS15



a) Vertical (left) and lateral (right) stress distribution



b) In-plane principal stresses

Figure 4-4 Stress distribution around the buried structure for *case-II* (at 140 kPa surface pressure)

4.2.3. Effect of EPS density

The effect of EPS density is examined by comparing the calculated pressures at the walls of the buried structure (upper, lower and side) for the three given EPS materials (EPS15, EPS22, and EPS39). Similar to *case-I*, the EPS width and thickness were kept constant and the surface pressure that allows for up to 1 % EPS strain in the upper EPS block was assigned as the design limit load. Figure 4-5 presents the surface pressures corresponding to 1 % strain for EPS15, EPS22 and EPS39 were found to be 87 kPa, 97 kPa and 124 kPa, respectively. These values are generally less than those calculated for *case-I*.

For the upper wall (Figure 4-5a), the EPS density was found to have a significant impact on the earth pressure acting on the wall. Compared to the benchmark, the lowest contact pressure is calculated for the case of EPS15 with pressure reduction of about 64 % at an applied pressure of 87 kPa. The pressure reduction ratios for EPS22 and EPS39 were found to be 53 % and 27 % at applied surface pressures of 97 kPa and 124 kPa respectively. These values of pressure reduction at the upper wall are smaller compared to that of *case-I*.

The pressure reduction ratios for the lower wall (Figure 4-5b), at 1 % strain, were found to be 63 %, 54 % and 23 % for EPS15, EPS22 and EPS39, respectively. These effects are better at this location compared to the values obtained in *case-I*.

At the side walls (Figure 4-5c), the contribution of having EPS blocks next to the wall resulted in pressure reduction ratios of 81 %, 75 % and 60 % for EPS15, EPS22 and EPS39, respectively.

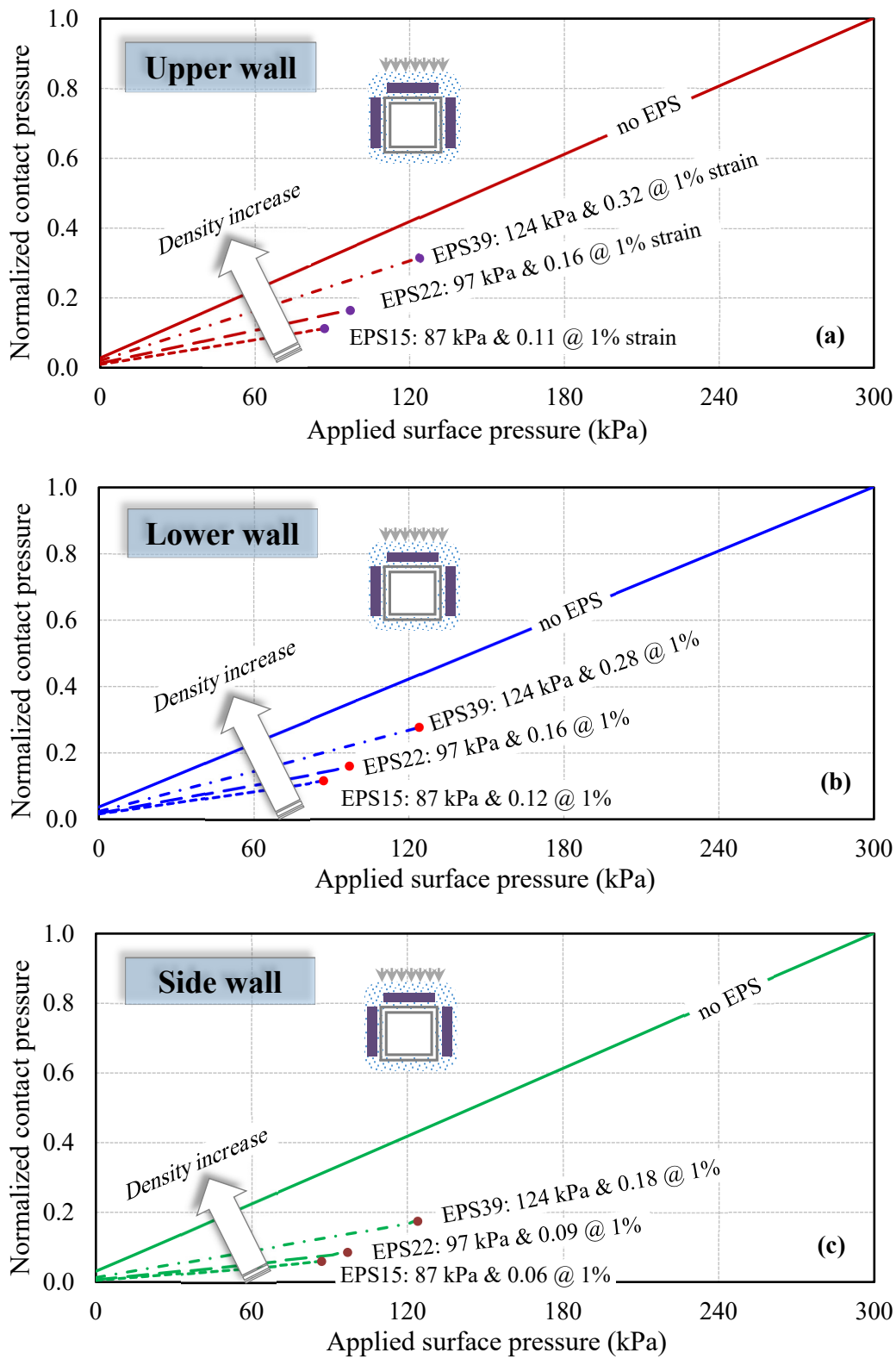


Figure 4-5 Effect of EPS density on the earth pressure acting on the structure (*case-II*)

4.3. Comparison between *case-I* and *case-II*

A comparative evaluation is performed to examine the contact pressures obtained in the two investigated cases. Figure 4-6 presents a comparison between the calculated contact pressure values for *case-I* and *case-II* at different locations on the structure for EPS15. This figure demonstrates that adding EPS geofoam at the side walls will result in an increase in contact pressure at the upper wall (Figure 4-6a). The increase in the contact pressure was found to be around 29 % at applied surface pressure of 140 kPa. At the side walls, and due to the addition of the EPS, the contact pressure significantly decreased by 74 % at 140 kPa applied surface pressure (Figure 4-6b). Similarly, the contact pressure decreased at the lower wall (Figure 4-6c) with a ratio of 32 % at the same applied pressure.

Figure 4-7 provides a relationship between the maximum fill height that is allowed above the upper wall of the culvert and the corresponding contact pressure reduction using the three EPS geofoam materials under the two investigated configurations. For example, in Figure 4-7a (*case-I*), using EPS15, 72 % reduction in pressure at the upper wall is reached for a maximum fill height of 7.05 m. Under the same condition, EPS39 will allow for a fill height of up to 8.9 m to be constructed with smaller load reduction value of about 35 %. Using the second configuration (*case-II*), EPS39 resulted in a pressure reduction of up to 27.1 % at the upper wall with a maximum fill height of 8.1 m. Load reduction ratio of 63.9 % has been achieved using EPS15 for embankment height of up to 5.85 m.

A complete summary of the vertical and lateral contact pressure distributions on the culvert for three different installations (no EPS, *case-I* and *case-II*) is illustrated in Figure 4-8 for EPS15 geofoam. It is noticed from these distributions that there are stress concentrations at the corners of the structure for all installations. These concentrations increased significantly in case of no EPS installed around the box culvert. At the upper wall, having geofoam block (*case-I* or *case-II*) helps to release the stress concentrations and produced a uniform contact pressure distribution on the upper wall of the structure. The average vertical contact pressure on the upper wall was 1, 0.28, and 0.36 times the overburden pressure for positive projecting (no EPS), *case-I* (geofoam block above the top wall), and *case-II* (geofoam blocks above the top walls and next to the side walls) respectively. The average vertical contact pressure on

the lower wall decreases from 153 kPa for positive projecting to 81 kPa in *case-I*, then 56 kPa in *case-II*. However, the pressures distribution shows an increase at the edges of the box. For side walls, the average lateral contact pressure that acting on the side walls of the culvert was 0.53, 0.39, and 0.1 times the overburden pressure (at the mid-height of the structure) for positive projecting, *case-I*, and *case-II* respectively.

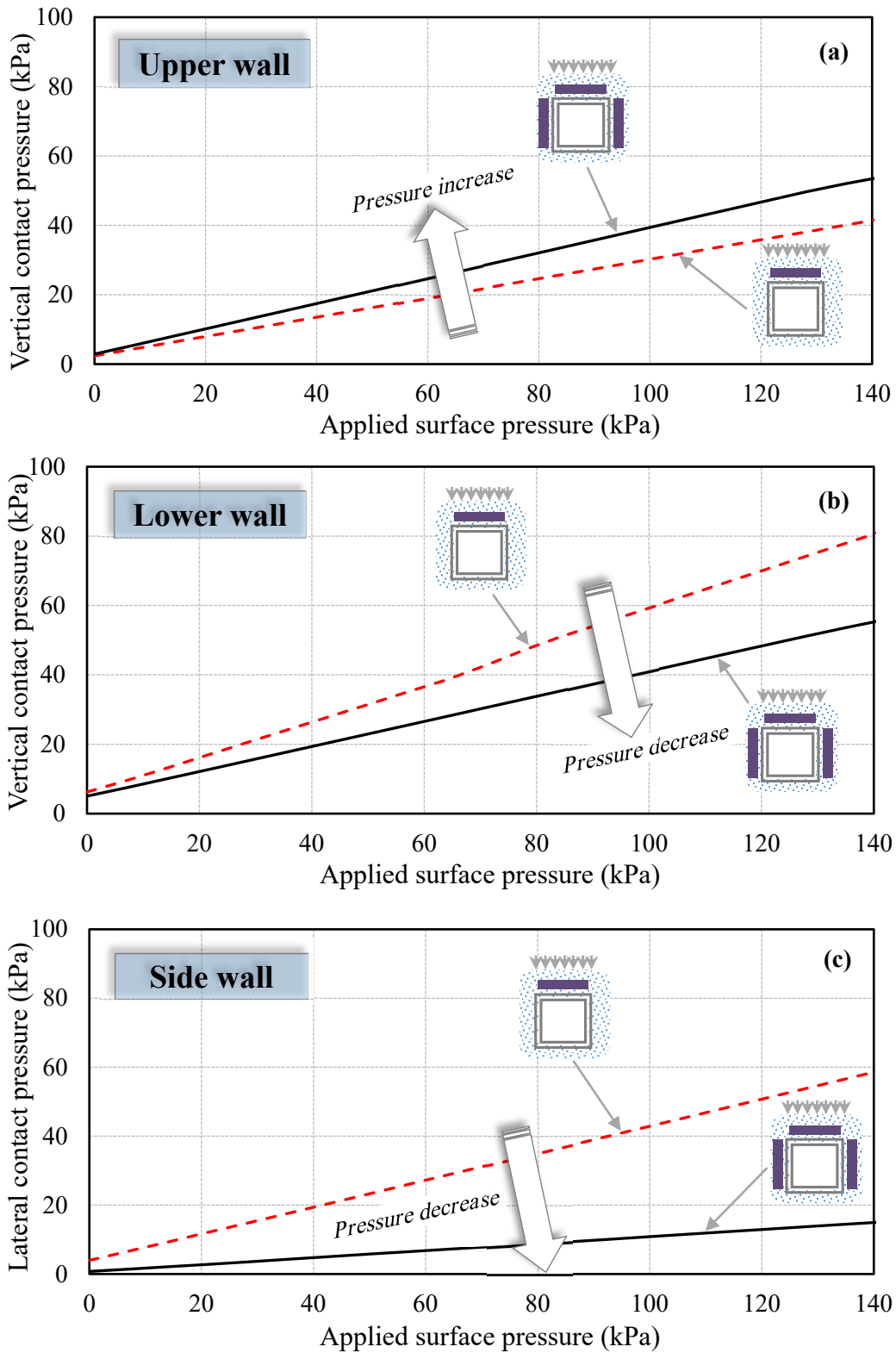


Figure 4-6 Effect of EPS geometric configuration on the change of earth pressure

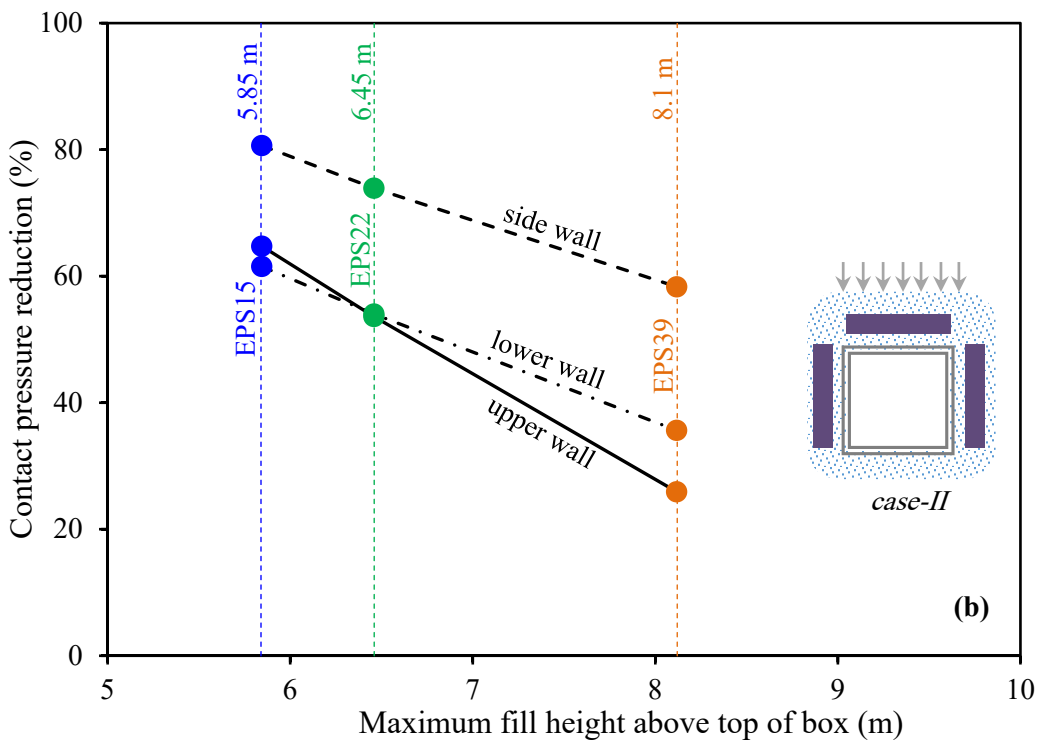
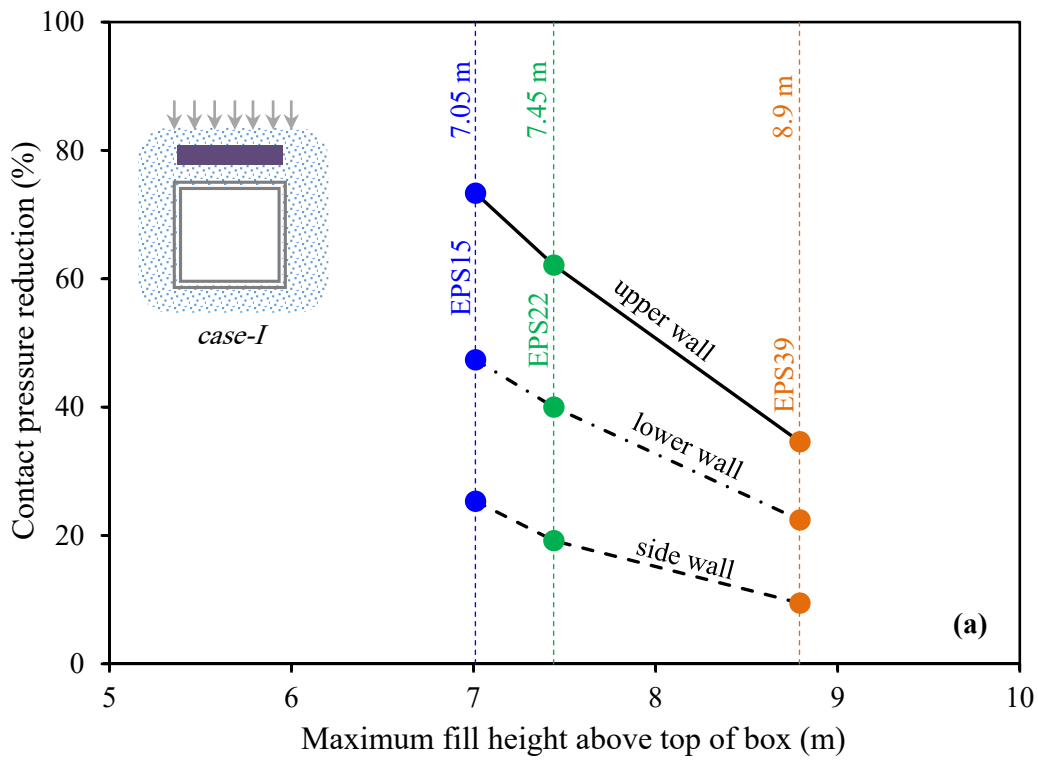


Figure 4-7 Maximum fill height versus pressure reduction (up to 1% EPS strain)

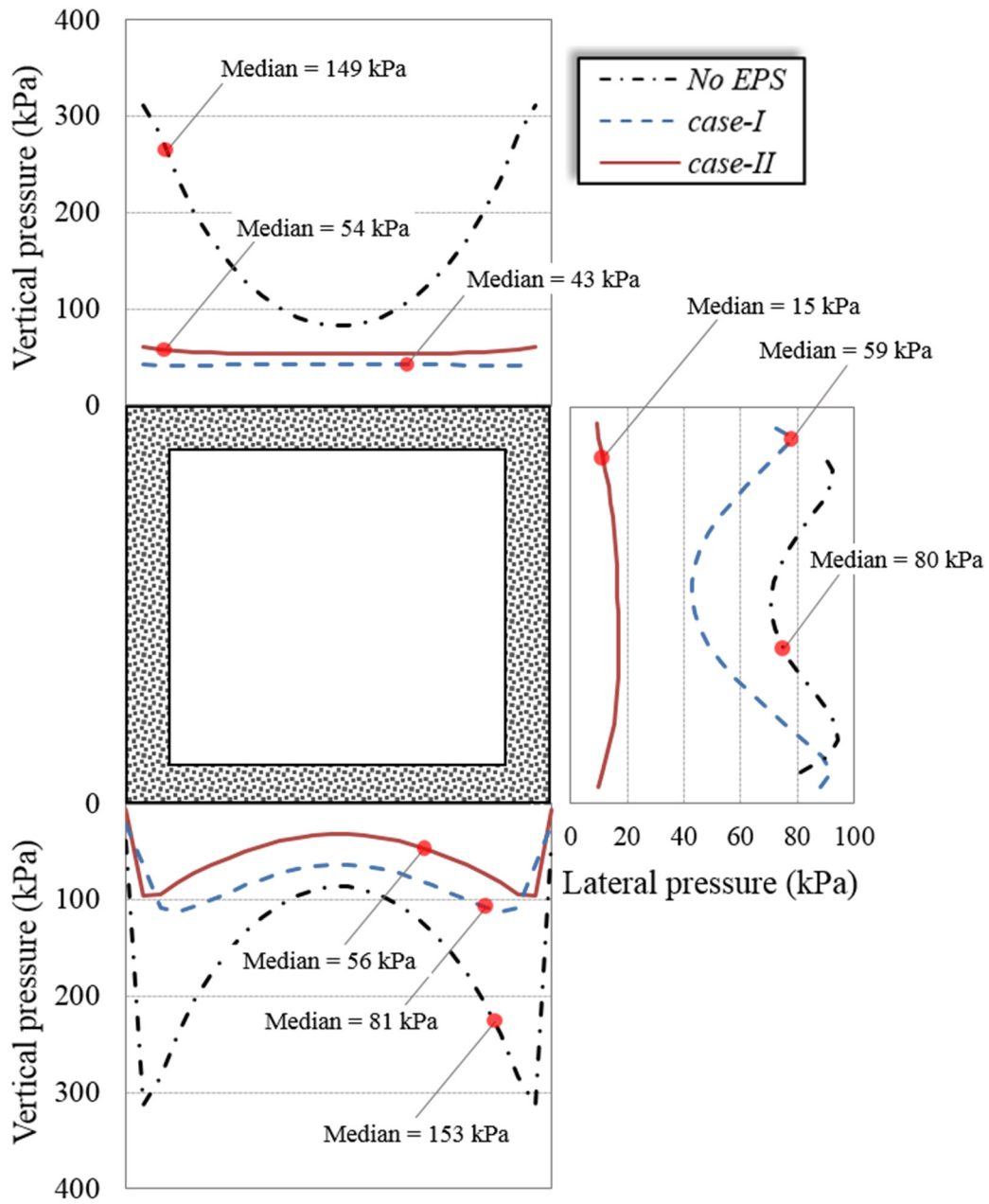


Figure 4-8 Calculated contact pressures around the culvert for three different installations (at 140 kPa surface pressure)

4.4. Comparison with Theoretical Overburden Pressure

In this section, the earth pressures calculated using the numerical model is compared with the theoretical overburden pressure at different locations on the culvert for the two examined cases. Figure 4-9 shows the results for the upper, lower and side walls for *case-I* using three different types of EPS geofoams for up to a maximum fill height that corresponds to 1% strain in the geofoam block. The horizontal axis represents the fill height above the box which includes the effect of both the backfill material and the applied surface pressure. At the upper wall (Figure 4-9a), the positive projecting case (no EPS) showed no difference from the theoretical overburden pressure γH (where H is the height of the backfill above the upper wall and γ is the unit weight of the backfill). For the induced trench condition, the calculated earth pressure values on the upper wall were found to be $0.65\gamma H$, $0.39\gamma H$ and $0.28\gamma H$ for EPS39, EPS22 and EPS15, respectively. These values correspond to pressure reductions of 35%, 61% and 72% respectively.

The comparison between the predicted contact pressure at the lower wall and the theoretical overburden pressure (γH) plus the self-weight of the box (w) is presented in Figure 4-9b. For the positive projecting case, the contact pressure at the lower wall was found to be $1.02 (\gamma H + w)$. Using EPS blocks, the calculated pressures were found to be $0.8 (\gamma H + w)$, $0.62 (\gamma H + w)$ and $0.54 (\gamma H + w)$ for EPS39, EPS22 and EPS15, respectively.

The calculated lateral contact pressures on the side walls are compared with the theoretical overburden pressure at the mid-height of the box, γH_m (where $H_m = H + L/2$ and L is the vertical height of the box) as shown in Figure 4-9c. For the positive projecting case, the calculated lateral pressure was found to be $0.53\gamma H_m$, while for the induced trench conditions the lateral pressure decreased to $0.48\gamma H_m$, $0.42\gamma H_m$, and $0.39\gamma H_m$ for EPS39, EPS22 and EPS15, respectively. These results suggest that careful selection of a suitable EPS geofoam density is important to ensure that earth pressure induced by a proposed embankment height to be built over a buried structure can be carried safely without exceeding the design strain limit of the geofoam material.

For *case-II*, the comparison between the calculated pressures on the culvert walls and the theoretical overburden pressures is illustrated in Figure 4-10. The results indicate similar trend to that calculated in *case-I* at the upper wall. However, at the lower and side walls, earth pressure significantly decreased as compared to *case-I*.

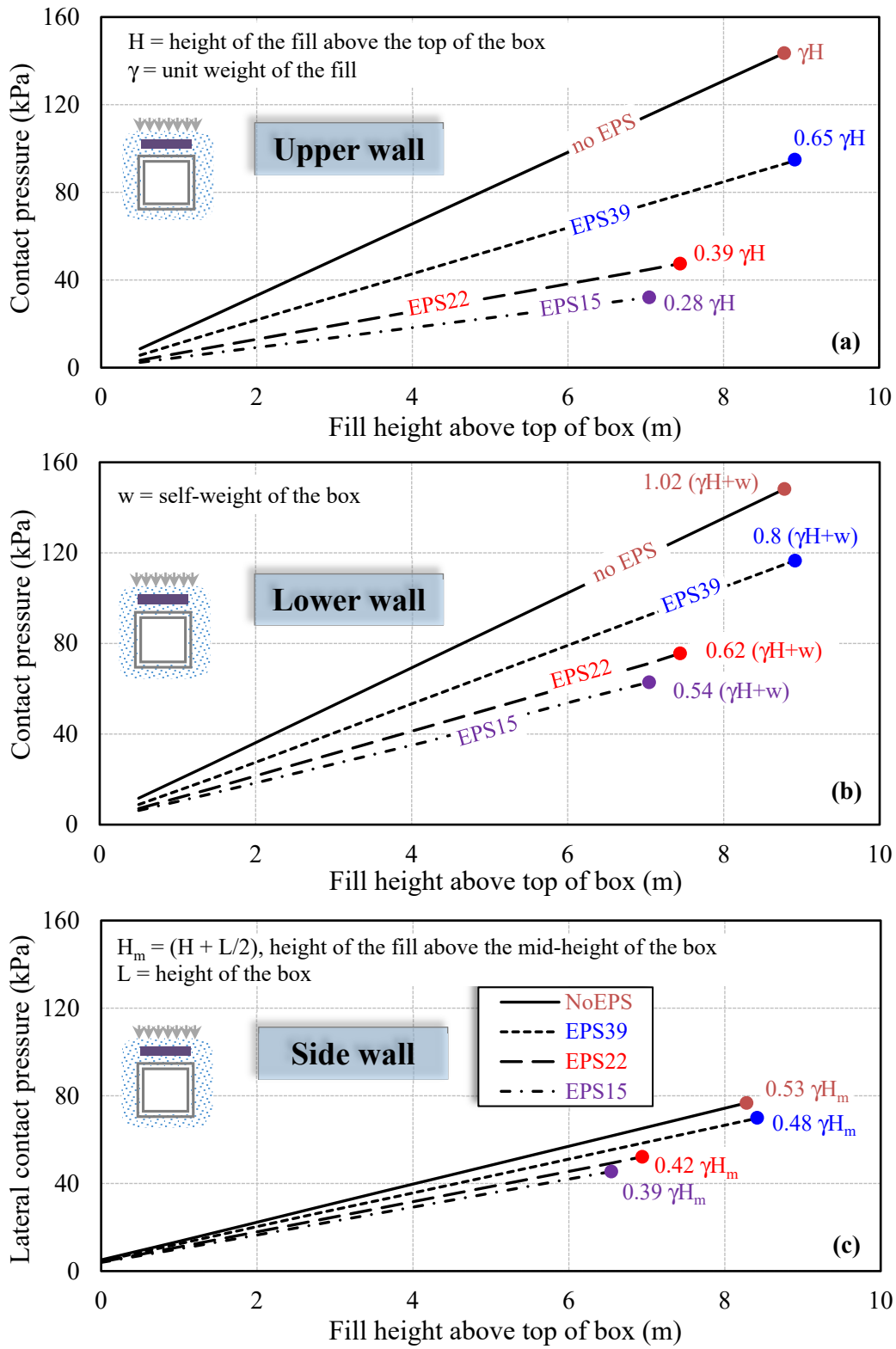


Figure 4-9 Predicted contact pressures vs theoretical overburden pressures for *case-I* (up to 1% strain)

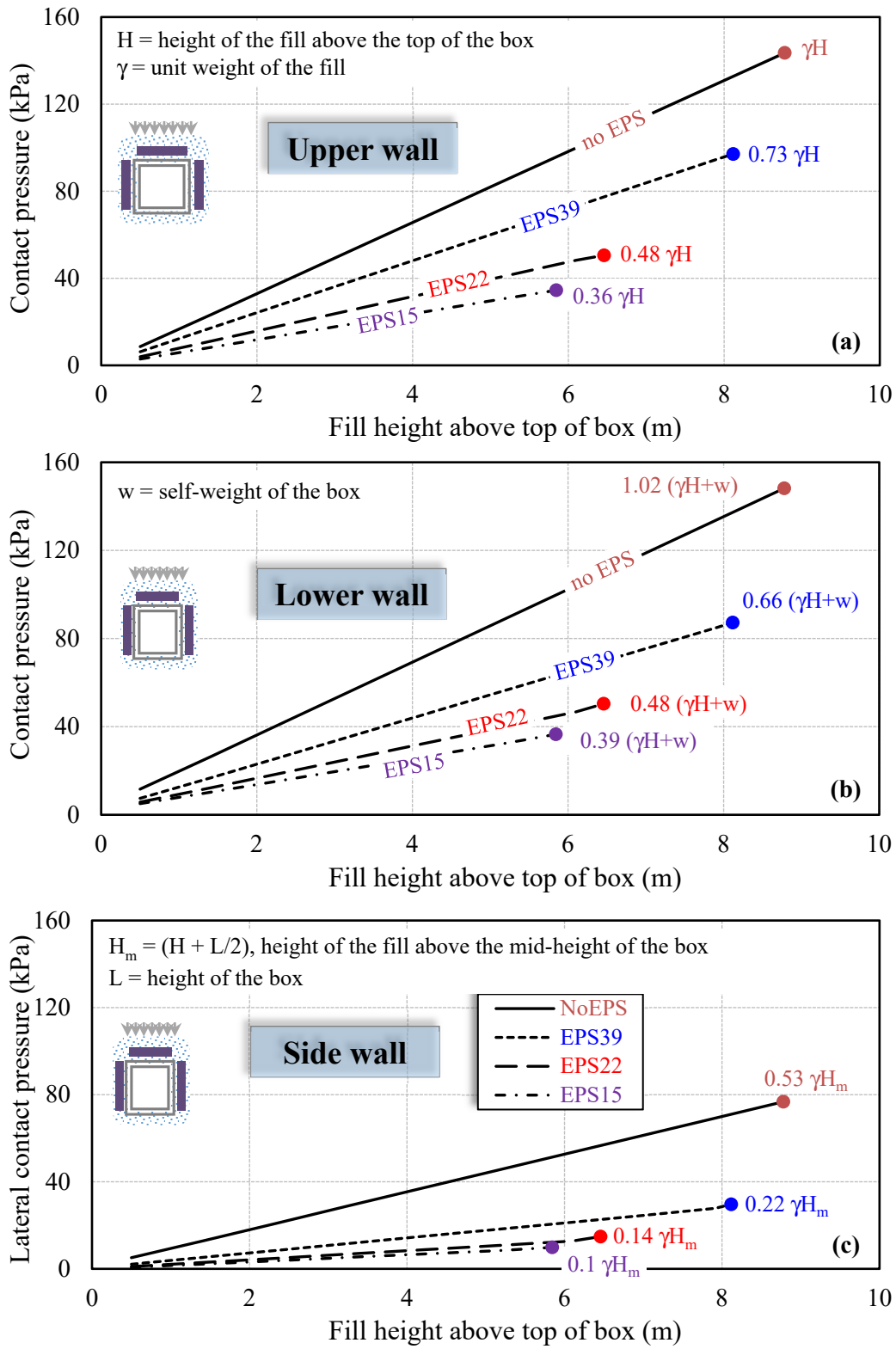


Figure 4-10 Predicted contact pressures vs theoretical overburden pressures for *case-II* (up to 1% strain)

4.5. Design Charts for *case-I* and *case-II*

Based on the previous results, preliminary design charts are proposed for the investigated cases to allow for the choice of a proper EPS material type that satisfies a specific embankment height. Figures 4-11 and 4-12 show the design charts for the two investigated cases (*case-I* and *case-II*) up to 1% allowable strain. The vertical axes represent the pressure reduction ratio that is related directly to the EPS type through the expected fill height. To better understand the use of the proposed charts, an example is provided below.

Using the design charts (Figures 4-11 & 4-12)

If it is required to construct an embankment over a buried structure with a fill height of about 6 m using the induced trench method to achieve an earth pressure reduction of up to 65% at the upper wall, Figure 4-11 shows that EPS15 is considered a reasonable choice as it will allow for up to 7.0 m of fill height with 72% pressure reduction at the upper wall.

If lateral earth pressure is an issue, configuration-II might be a good option. For example, if it is necessary to build a 7 m high embankment with a lateral pressure reduction of about 50% on the side wall, EPS should be placed over and around the buried structure. In this case, using Figure 4-12, EPS39 is suitable as it satisfies both the embankment height and the expected pressure reduction ratio.

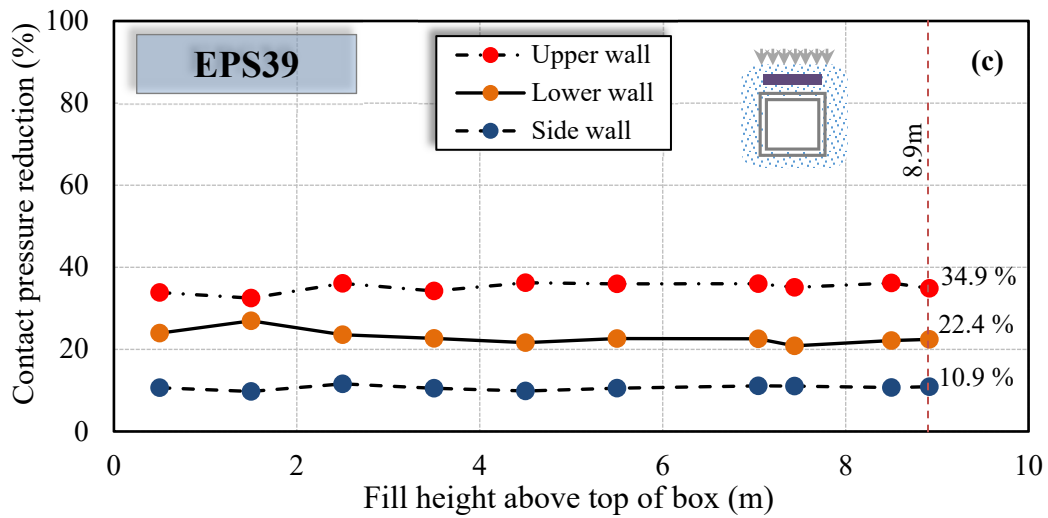
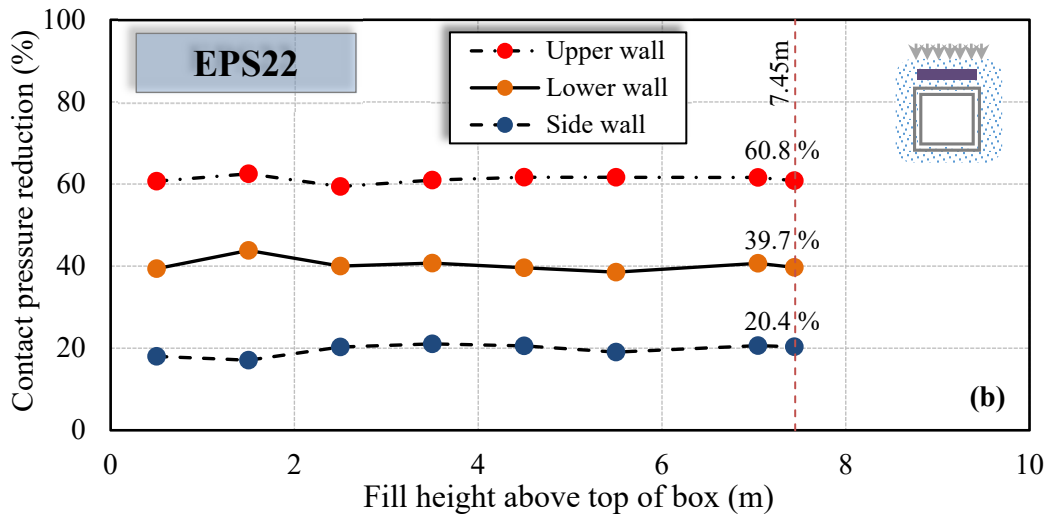
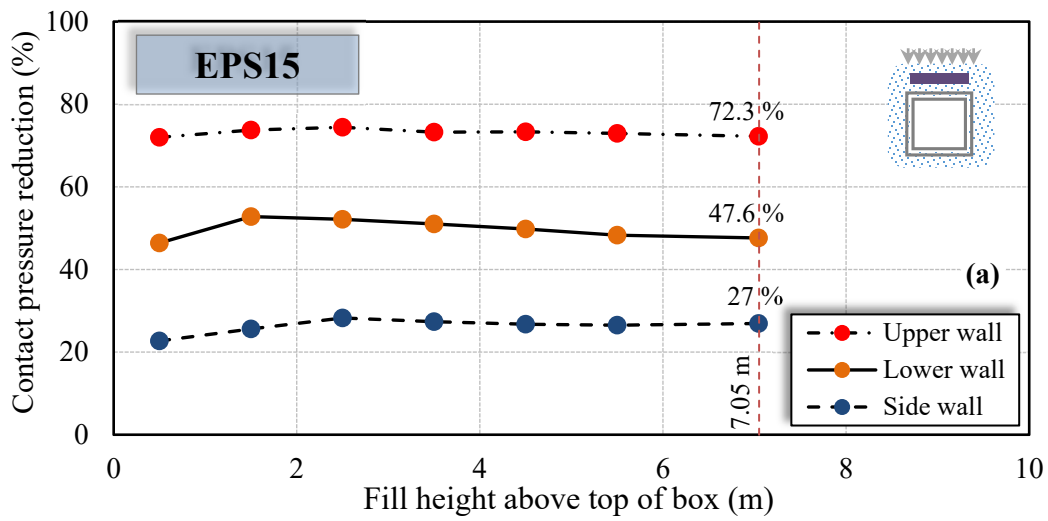


Figure 4-11 Proposed design charts for *case-I* (up to 1% strain)

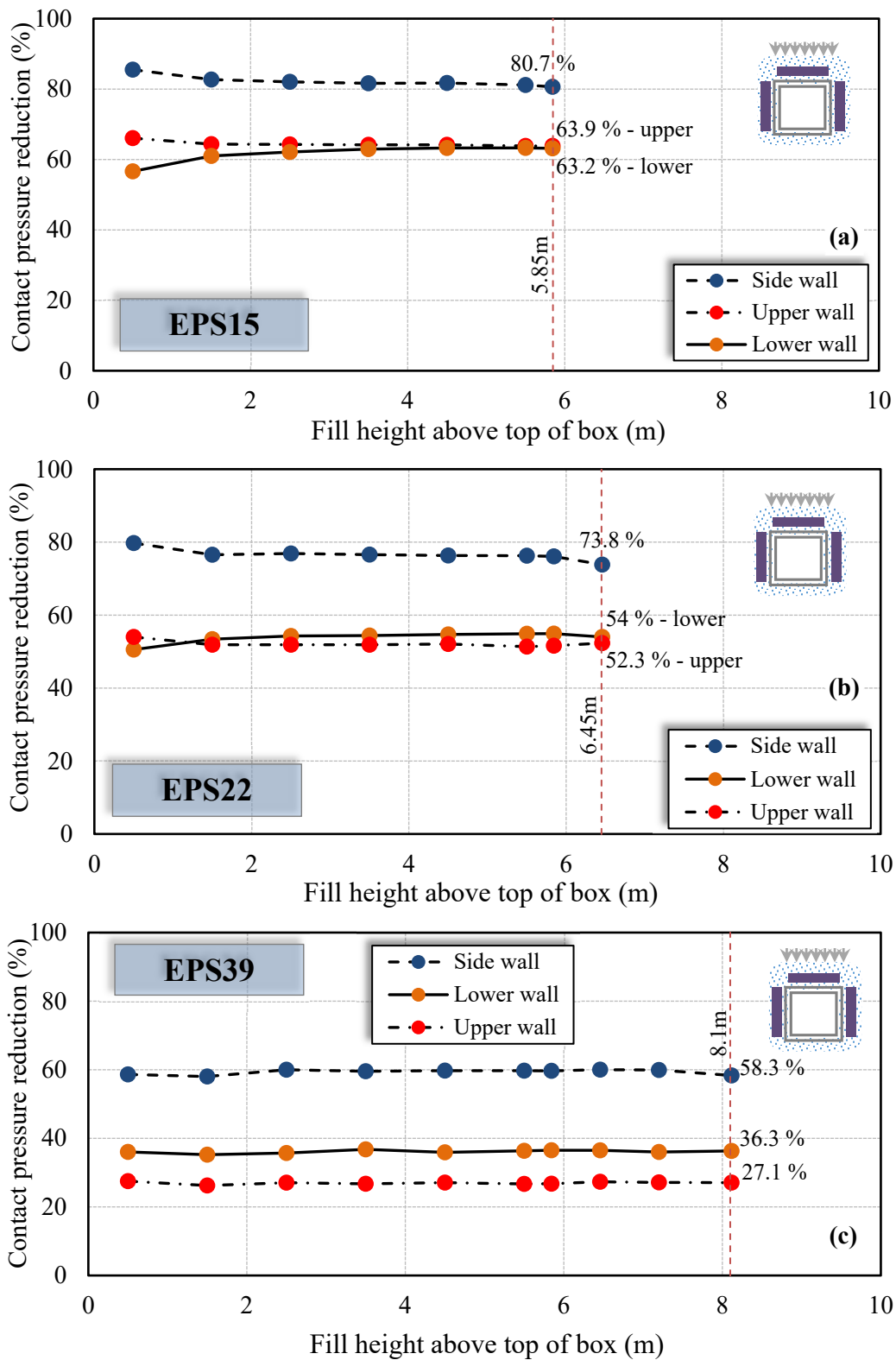


Figure 4-12 Proposed design charts for *case-II* (up to 1% strain)

4.6. Summary and Conclusions

In this study, a numerical procedure for modeling a buried box culvert installed with the induced trench installation method is developed using ABAQUS software. In this procedure, the backfill material is modeled using the Mohr-Coulomb failure criterion with associated flow rule, while the EPS material is simulated using elasto-plastic strain hardening model. Using the proposed procedure, a series of 2D plane strain finite element analyses is conducted to study the role of embedding EPS inclusion around a buried box culvert in reducing the loads on the walls of the structure. The developed model was used to investigate a case study of an instrumented HSS section (with and without EPS) that was placed within a rigid steel container backfilled with sandy gravel material and loaded incrementally with a vertical pressure using an air bag. Two different EPS configurations, that have been tested experimentally, were simulated in this study. In *case-I*, the EPS was placed directly above the structure whereas in *case-II* the geofoam blocks were placed above the upper wall and next to the side walls. In both conditions, the calculated results are compared with experimental data. Results revealed that the proposed FE model is efficient in capturing the stress distribution around the buried structure and allowed for details of the pressure reduction and EPS performance to be investigated.

A comparison between the numerical results of the two examined cases was made. This comparison showed that adding EPS blocks next to the side walls decreases the earth pressure significantly on the lower and side walls while increases the contact pressure on the upper wall of the structure.

The calculated pressures on the buried box were compared to the theoretical overburden pressures (resulting from the self-weight of the soil) in addition to the external surface loading. It was found that significant pressure reduction is achieved using EPS15 with a pressure ratio of 0.28 of the theoretical overburden pressure at the upper wall. This translates into a reduction in contact pressure of about 70 % on the upper wall.

Finally, preliminary design charts were proposed to allow for the proper choice of EPS material that satisfies a specific embankment height. These charts provide a relationship

between the pressure reduction ratio and the EPS type through the expected fill height. An example was presented to demonstrate how to use the design charts for both cases of geofoam arrangements.

The above study suggests that placing light weight EPS material above a rigid subsurface structure can result in significant reduction in vertical earth pressure and consequently an economic design. Using EPS at the side walls can be justified if reduction in lateral earth pressure on the side walls is a design requirement.

Preface to Chapter 5

The results presented in the previous chapter demonstrate the efficiency of the finite element method in investigating soil-structure interaction problems involving EPS geof foam material. To examine the applicability of the modelling method in solving more complex soil-structure interaction problems involving a different type of geosynthetic material, a 3D FE approach is developed in this chapter. Geogrid reinforcement is investigated under both unconfined and soil-confined conditions. In developing this model, the three-dimensional details of the geogrid geometry are explicitly simulated. The geogrid is investigated in-air under tensile load to examine its unconfined behavior. To study the soil-geogrid interaction in 3D analysis, a reinforced subgrade subjected to a square shaped surface loading is simulated. The proposed FE approach has proven to be efficient in capturing the 3D responses of both unconfined and soil-confined geogrids.

CHAPTER 5

A Three-Dimensional Finite Element Approach for Modeling Biaxial Geogrid with Application to Geogrid-Reinforced Soils*

Abstract

Understanding soil-geogrid interaction is essential for the analysis and design of geogrid-reinforced soil structures. A first step towards accurate modeling of this interaction is choosing a suitable material model for the geogrid that is capable of simulating tensile test results. The model must be able to capture the three-dimensional response of the geogrid considering its exact geometry. Modeling geogrid inclusion as a continuous sheet has proven to reasonably simulate the overall response of soil-geogrid systems; however, it does not explain the different sources of interaction between the geogrid layer and the surrounding soil. To understand the three-dimensional aspects of this complex interaction problem, a two-phase numerical investigation is developed in this study. The first phase focuses on the three-dimensional modeling of unconfined biaxial geogrid subjected to tensile loading. Applicability of the geogrid model in solving soil-structure interaction problems is then demonstrated, in the second phase, by investigating the response of a reinforced subgrade subjected to a square shaped surface loading. It is concluded that modeling the three-dimensional geogrid geometry is important to accurately capture the true response of geogrid under both confined and unconfined conditions. The modeling approach proposed in this study for the analysis of unconfined and soil-confined geogrid can be adapted for other reinforced soil applications.

Keywords: Geosynthetics, Soil-structure interaction, Biaxial geogrid, Numerical analysis, Index tests, Geogrid-reinforced soil, ABAQUS.

* A version of this chapter has been published in *Geotextiles and Geomembranes Journal*, 44(3): 295-307.

5.1. Introduction

Geogrid reinforcement is known to be an effective method to enhance the performance and service life of different earth structures (e.g. embankments, pavements, foundations and retaining walls). Reinforced soil structures are usually designed using limit equilibrium methods. These methods do not generally provide sufficient information on the failure load and the displacements and strains developing in the reinforcement (Rowe and Mylleville, 1994, Sugimoto and Alagiyawanna, 2003). On the other hand, finite element (FE) methods have become powerful tools to efficiently predict the pre-failure displacements, and stresses generated in the reinforcement material.

Several studies that employ finite and discrete element methods to analyze geogrid-reinforced structures have been reported in the literature (Yogarajah and Yeo, 1994, Perkins and Edens, 2003, McDowell et al., 2006, Hussein and Meguid, 2013, Tran et al., 2013a and b, Mosallanezhad et al., 2016, Wang et al., 2016). Most of these studies focused on the overall response of the reinforced structure while adopting simplifying assumptions related to either the details of the geogrid geometry or the constitutive model of the geogrid material.

The nonlinear stress-strain response of geogrid polymeric material is recognized as an important characteristic that needs to be captured in both analytical and numerical modeling of reinforced-soil applications (Bathurst and Kaliakin, 2005, Kongkitkul et al., 2014, Ezzein et al., 2015). It is therefore, necessary to develop and incorporate a nonlinear constitutive model for the geogrid material to improve the accuracy of the numerical analysis. This model should contain sufficient components to characterize the unconfined response and captures the important geometric features of the geogrid before it interacts with the backfill material. In addition, the model has to be relatively simple, with respect to the number of required parameters, to facilitate implementation into existing numerical codes. A limited number of dedicated studies have been reported, to date, focusing on geosynthetic modeling in three-dimensional (3D) space. Most notably, the work of Perkins and his coworkers between 2000 and 2003.

Perkins (2000 and 2001) presented an elastic-plastic model for geosynthetics that accounts for the creep behavior and direction dependency of the material. The model required a total of 24 input parameters to capture the material response under axial loading. The model, treated the geogrid as a planer sheet and, therefore, did not account for the discontinuous nature of the geogrid geometry. It has been demonstrated (Perkins and Edens, 2003) that the creep components have a small effect on the calculated load-displacement response of the geosynthetic material. The results did, however, show that plasticity had a significant effect on the load-displacement relationship, particularly, as the geosynthetic material approaches failure.

Another important factor to be considered in modeling geogrid is the 3D geometry of the network structure. Modelling geogrid using planer sheet does not allow for essential features to be captured, including: i) the unique deformation characteristics of each member during unconfined tensile loading condition, and ii) the effect of bearing resistance on confined geogrid ribs.

The objective of this study is to propose a 3D modeling approach to capture the details of biaxial geogrid under both unconfined and soil-confined conditions. This is achieved in two phases as follows:

i) A 3D nonlinear FE analysis has been performed to simulate the behavior of unconfined geogrid under tensile loading. The ABAQUS-based constitutive model used in the FE analysis is capable of capturing the ranges of elastic and plastic regions of the stress-strain relationship in the short-term under monotonic tensile loading. The geogrid geometry is modeled explicitly with its detailed features including the rib and junction thicknesses and the geogrid apertures.

ii) Using the geogrid model developed in the first phase, a 3D analysis of soil-confined geogrid is then performed to examine the validity of the geogrid model. An example that involves a square footing over geogrid-reinforced soil is presented and the results are compared with experimental data.

The 3D FE models presented throughout this study have been performed using the general finite element software ABAQUS/Standard, version 6.13 (ABAQUS, 2013).

5.2. Modelling Unconfined Geogrid

The details of the experiments and the 3D FE modeling of unconfined geogrid, covered in the first phase of this study, are discussed in this section.

5.2.1. Tensile tests

A series of index tests involving uniaxial-tensile loading was performed to measure the load-displacement response of the biaxial geogrid samples. The geogrid properties as provided by the manufacturer are summarized in Table 5-1. The tests are conducted according to the ASTM/D6637-11 (2011) standard on multi-rib geogrid specimens in both the machine (MD) and the cross machine (XMD) directions. The geogrid sample comprises three longitudinal ribs and six transverse bars as shown in Figure 5-1. In these index tests, one of the clamps is usually fixed while the other is allowed to move and pull the geogrid specimen. A 5 kN MTS machine with constant strain rate of 10% strain/minute was used to test five identical geogrid specimens in each direction. An extensometer with a gauge length of 25 mm was mounted at the center of the specimen to measure the elongation during the test whereas the applied load was recorded using a load cell integrated into the MTS machine. It should be noted that this test procedure allows for the overall geogrid response to be measured considering homogenized characteristics of the geogrid geometry. To take into account the solid material characteristics, the load carried by each rib is obtained by dividing the applied machine load by the number of ribs in the loading direction. The directional (axial) load-strain response of the solid material is presented in Figure 5-2. The mean values of the measurements obtained from the five index tests are shown with one standard deviation range bars. For both the MD and XMD, the measured values are tightly clustered around the mean which indicates that the test results in both directions are repeatable and the material properties are uniform for the tested specimens.

Table 5-1 Index properties of the biaxial geogrid

Direction	Aperture size (mm)	Specimen size (mm)		No. of members		Ult. Strength (kN/m)	Mass/unit area (g/m ²)	Stiffness @ 2% strain (kN/m)
		L	W	Long.	Trans.			
MD	29	149	78	3	6	12	215	204
XMD	37	185	58	3	6	20	215	292

Note: The above values are reported by the manufacturer

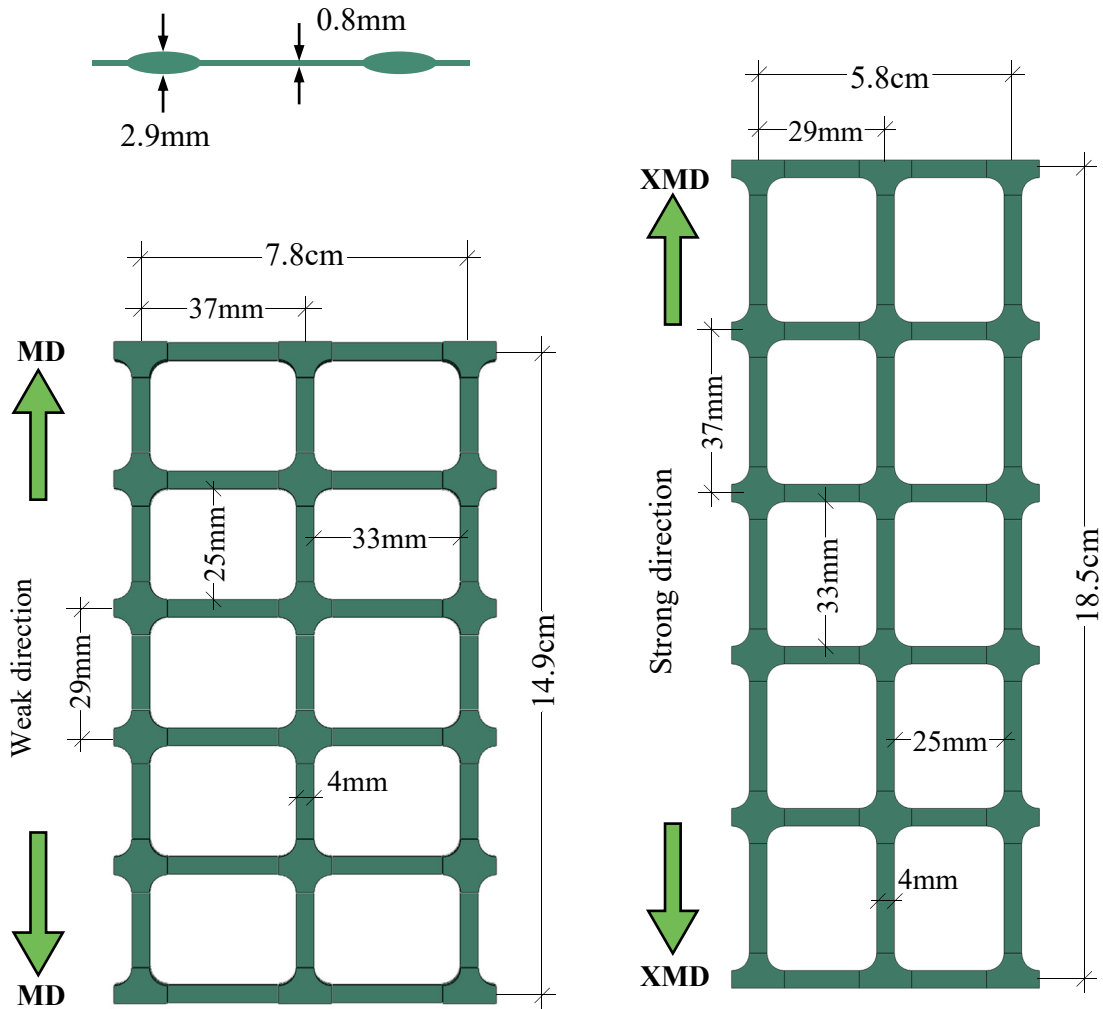


Figure 5-1 Multi-rib unconfined tensile test on biaxial geogrid

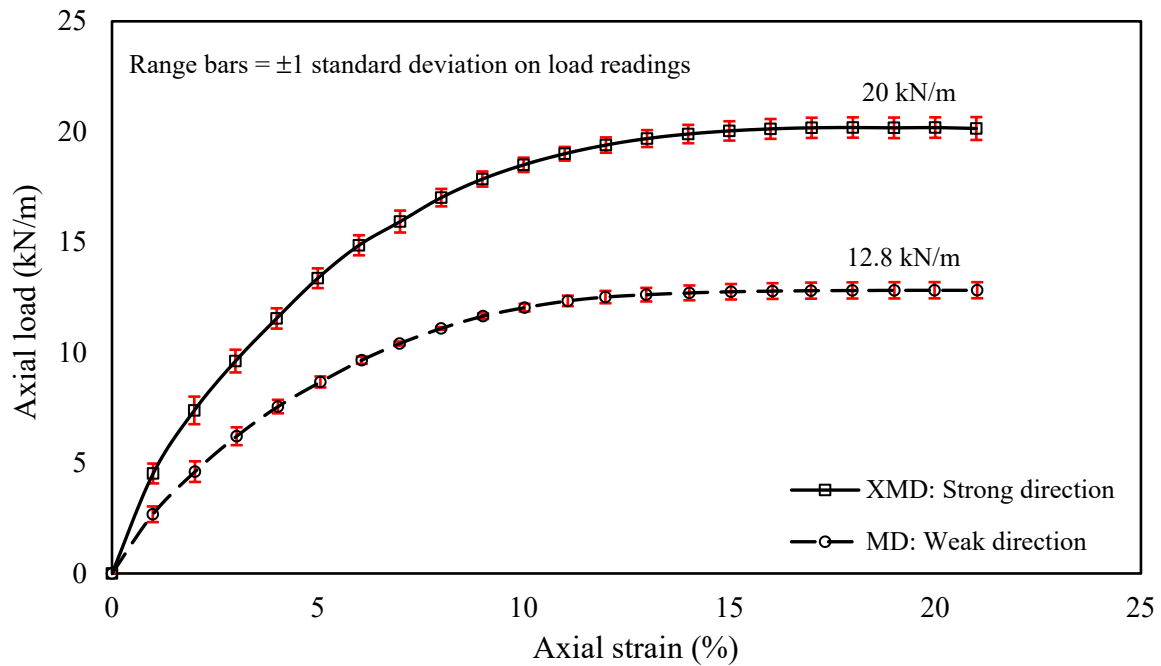


Figure 5-2 Experimental axial load-axial strain results in the MD and XMD

From Figure 5-2, the geogrid response is found to be mostly nonlinear with significant plastic deformations developing as failure is approached. The maximum strength was found to be 12.8 kN/m and 20.5 kN/m for MD and XMD, respectively. These results are consistent with the values reported by the manufacturer (given in Table 5-1). It is noted that although the response shown in Figure 5-2 represents the specific biaxial geogrid used in this study, similar approach can be used for other types of geogrid by considering the number of ribs per meter in a given direction.

5.2.2. Model development

Three-dimensional FE analyses are conducted to simulate the index tests considering the geometric features of the geogrid, including the different element thicknesses and the opening dimensions as per the geogrid specimen. An elastic-plastic constitutive model is used to explicitly simulate the measured nonlinear behavior of the geogrid. The numerical model is first validated with the test results and then used to investigate the detailed response of the geogrid under tensile loading.

Sensitivity analyses are also performed to examine the effect of the finite element size, type, shape, and interpolation function on the calculated geogrid response. The modeling details and the findings of the sensitivity analyses are discussed below.

Model components

Two main components are required for the successful development of the unconfined geogrid model: i) constitutive behavior, and ii) geometry and boundary conditions. These components are discussed in this section.

Constitutive behaviour

Experimental results (Figure 5-2) show that the biaxial geogrid sample behaves as a nonlinear elasto-plastic hardening material. Therefore, simplifying the response using linear elasticity (e.g. Liu et al., 2007, Abdi and Zandieh, 2014) may lead to incorrect response. A practical constitutive model that is capable of describing both the material nonlinearity and plasticity is needed. In addition, the geogrid exhibited different stiffness and strength responses in the MD and XMD, which implies that the geogrid's homogenized characteristics is directional dependent (anisotropic). The experimental results, however, indicated that the degree of anisotropy in both the elastic ($E_{XMD}/E_{MD} = 1.35$) and the plastic ($\sigma_{XMD}/\sigma_{MD} = 1.6$) regimes is small, and therefore the anisotropy of the biaxial geogrid is not explicitly considered in this study. Alternatively, an average stress-strain relationship that represents an isotropic state between the MD and the XMD responses is adopted to simplify the numerical analysis.

A constitutive model that is capable of simulating the nonlinear elastoplastic material with isotropic hardening is built using ABAQUS software package. The method used to combine the above model features is based on the conversion of the measured strains and stresses into the appropriate input parameters for the software. This is achieved by decomposing the total strain values into elastic and plastic strains to cover the entire range of the geogrid response. The different model components include: (i) The elasticity component is described by an elastic isotropic model where the total stress and the total strain are related using the elasticity matrix; (ii) The plasticity is modeled using von Mises yield criterion (Appendix (A)) with

isotropic hardening and associated flow rule; (iii) The isotropic yielding is defined by expressing the uniaxial yield stress as a function of the equivalent uniaxial plastic strain; (iv) The isotropic hardening rule is expressed in ABAQUS using a tabular data of yield stress as function of plastic strains.

The plasticity data has to be specified in terms of true stresses and true strains (ABAQUS, 2013) despite the fact that test data provides nominal (engineering) values of total stresses and total strains. A procedure is, therefore, needed to convert the nominal test data to its true values and then decompose the total strain values into elastic and plastic strain components to allow for direct data input into ABAQUS. A flow chart that illustrates the procedure adopted to determine the numerical input data based on the experimental results is given in Figure 5-3 and summarized in the following steps:

- (1) Converting the test data (stresses and strains) from nominal to true values using the following expressions:

$$\epsilon_{true} = \ln (1 + \epsilon_{nom}) \quad (5.1)$$

$$\sigma_{true} = \sigma_{nom} (1 + \epsilon_{nom}) \quad (5.2)$$

where ϵ_{true} is the true strain, ϵ_{nom} is the nominal strain, σ_{true} is the true stress, and σ_{nom} is the nominal stress.

Then, decompose the total true strain (ϵ_{true}) into elastic and plastic components (Figure 3-3):

$$\epsilon_{true} = \epsilon^{el} + \epsilon^{pl} \quad (5.3)$$

where ϵ^{el} is the elastic strain and ϵ^{pl} is the plastic strain.

- (2) Using the true stress (σ_{true}) and Young's modulus (E) to obtain the elastic strain component (ϵ^{el}):

$$\epsilon^{el} = \sigma_{true}/E \quad (5.4)$$

- (3) Subtract the elastic strain value from the total true strain to obtain the plastic strain.

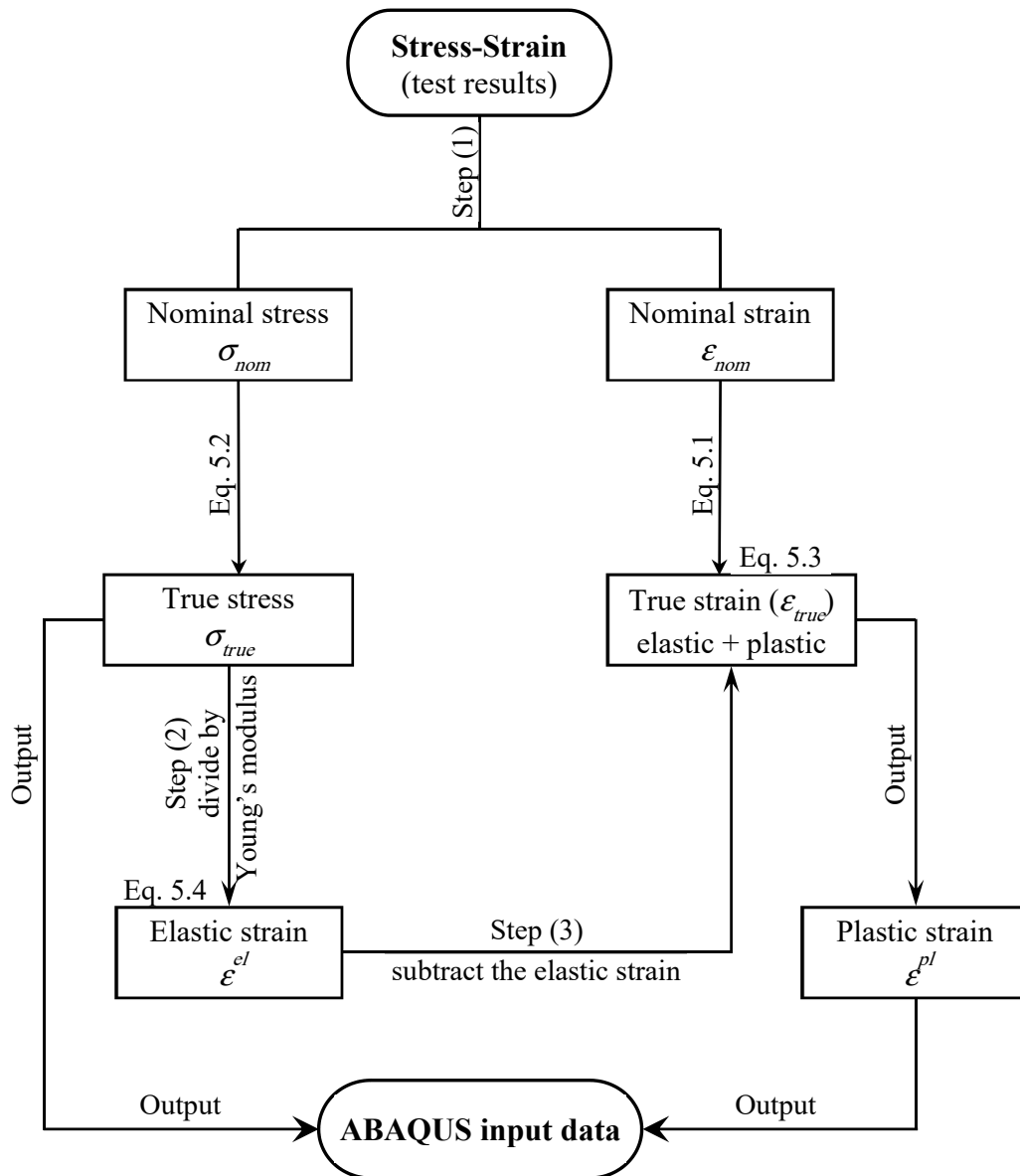


Figure 5-3 Procedure used to generate ABAQUS input parameters

The final geogrid plasticity properties are introduced into ABAQUS input module in terms of true stresses versus plastic strains.

The elastic-plastic model described above assumes that the material behavior is linear elastic at small strain levels with a relatively small elastic limit compared to the ultimate strength of the material. The elasticity is characterized by Young's modulus and Poisson's ratio and is immediately followed by a nonlinear response due to the development of large plastic deformation (Dean and Mera, 2004). Due to the fact that the elastic limit is very small, the geogrid elasticity model is described using initial tangent modulus that was calculated to be 605 MPa. A Poisson's ratio of 0.3 was used for the geogrid material, as suggested by Liu et al. (2007) and Kwon et al. (2008). The hardening rule data used to describe the geogrid plasticity model is shown in Figure 5-4.

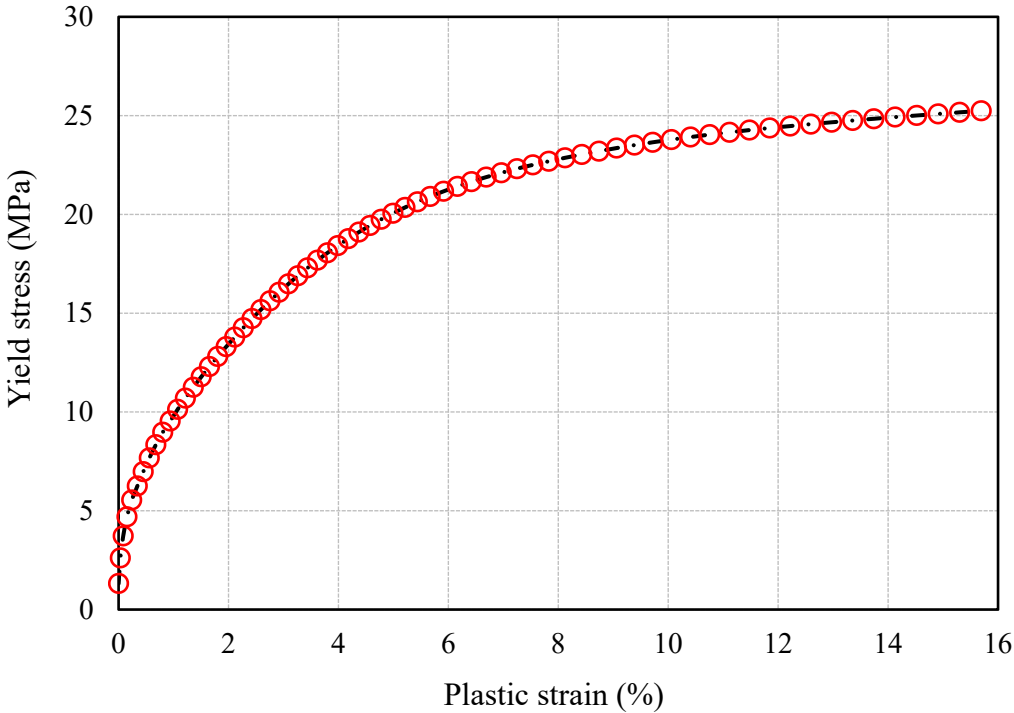


Figure 5-4 Hardening rule of the geogrid plasticity model

The von Mises yield criterion is known to provide a scalar measure of stress and strain that can generalize the 1D stress state (uniaxial test observations) into 3D state with six components. It is generally assumed that for a given stress state, there exists an equivalent uniaxial (von Mises) stress state and the material yields when the equivalent stress becomes equals to the yield stress:

$$\sigma_e = \sigma_y \quad (5.5)$$

where σ_e is equivalent (von Mises) stress and σ_y is the one-dimensional yield stress from the uniaxial tensile test.

The equivalent stress can be written in terms of principal stresses as follows:

$$\sigma_e = \sqrt{3 J_2} = \left\{ \frac{1}{2} [(\sigma_1 - \sigma_2)^2 + (\sigma_2 - \sigma_3)^2 + (\sigma_3 - \sigma_1)^2] \right\}^{\frac{1}{2}} \quad (5.6)$$

where J_2 is the second invariant of the deviatoric stress expressed as:

$$J_2 = \frac{1}{6} \{ (\sigma_1 - \sigma_2)^2 + (\sigma_2 - \sigma_3)^2 + (\sigma_3 - \sigma_1)^2 \} \quad (5.7)$$

Using the equivalent stress, the yield function can be defined as:

$$f'(\sigma) = \sigma_e^2 - \sigma_y^2 = 3J_2 - \sigma_y^2 = 0 \quad (5.8)$$

The counterpart of the equivalent stress is the von Mises effective strain (ε_e) that can be obtained by integrating the equivalent strain increment as:

$$\varepsilon_e = \int d\varepsilon_e \quad (5.9)$$

where $d\varepsilon_e$ is the strain increment that can be determined using:

$$d\varepsilon_e = \left\{ \frac{2}{9} [(d\varepsilon_1 - d\varepsilon_2)^2 + (d\varepsilon_2 - d\varepsilon_3)^2 + (d\varepsilon_3 - d\varepsilon_1)^2] \right\}^{\frac{1}{2}} \quad (5.10)$$

It should be noted that the scalar plastic strain (ϵ^p) in one-dimensional plasticity (illustrated in Figure 5-3) becomes a tensor in multidimensional plasticity analysis.

Although the above material model allows for the geogrid behavior to be closely represented, it does not consider cyclic loading or creep behavior of the polymeric material. In addition, the loading rate used in the numerical analysis is limited to that used in the experiment.

Geometry and boundary conditions

The biaxial geogrid used in this study consists of three main elements: longitudinal ribs, transverse bars and connecting junctions. These elements are combined together to form the geogrid's network structure. The details of the true geometry (Figure 5-1) are explicitly simulated considering the thicknesses of different elements and the aperture structure. To model the uniaxial tensile test, in the longitudinal ($X-X$) direction the geogrid is restrained along the right side ($U_x = 0$) and the load is applied from the opposite side using a prescribed velocity (V_x) with constant strain rate similar to that used in the experiments (10% strain/min). The geogrid movements are constrained in the transverse direction ($Y-Y$) at both ends to simulate the friction between the MTS grips and the geogrid. This loading procedure was used consistently for all analyzed geogrid models. A numerical simulation is also performed using double-sided loading to examine the difference in geogrid response compared to single-side loading. The observed difference was related to the symmetry of the stress and strain distributions, however, the overall stress-strain behavior of the geogrid remains unchanged.

Sensitivity analysis

The purpose of this section is to examine the effect of different numerical factors typically used in finite element analysis on the calculated geogrid response using the proposed numerical model. The investigated factors include the choice of membrane vs. solid elements (element type) and the role of finite element configuration (element shape, size, and interpolation function). Recommendations are then given, in section 5.3.2., for the optimal numerical configuration for use in modeling unconfined and soil-confined geogrid.

Membrane (triangular and quadrilateral) elements and solid (tetrahedron and hexahedron) elements are first examined. The reason to investigate the response of both types is that membrane elements are typically used to represent thin surfaces that offer in-plane strength but have no bending stiffness (typical response of unconfined geogrid under tensile loading condition), whereas, solid elements are used when the thickness of the structure affects the overall response (in soil, the geogrid thickness contributes toward the bearing resistance component). Both types of elements are used to model the biaxial geogrid using implicit static solver in ABAQUS/Standard. An out-of-plane thickness of 0.8 mm is assigned for membrane elements for both the longitudinal ribs and the transverse bars while the junctions were given a thickness of 2.9 mm. These thicknesses reflect the measured values for the investigated biaxial geogrid (see Figure 5-1). Figure 5-5 shows a sample of the 3D FE mesh using solid elements.

The results showed that no significant difference in response has been calculated and the two elements were found to be able to capture the unconfined geogrid response in both the axial and lateral directions.

The effect of element shape, size, and interpolation function on the response of unconfined geogrid is also examined and showed insignificant effect.

Several mesh sizes were tested in this section and reference points were used to evaluate the effect on the geogrid response for both membrane and solid elements. The element size was found to have no significant effect on the geogrid response under uniaxial loading when membrane elements are used in the analysis. The choice of a mesh size for the geogrid model using continuum elements is governed by the geogrid thickness. This is attributed to the fact that the geogrid thickness is significantly small compared to the width of the member. The effect of the mesh size is evaluated using various element sizes from $0.5t$ and up to $10t$ (where t is the geogrid rib thickness). The results showed that using geogrid mesh with a global average size of $3t$ is a reasonable choice as it provides a balance between the stress resolution and the computing time.

Model validation

To validate the proposed FE model for unconfined geogrid, the geogrid specimen is numerically simulated using 8-node continuum brick elements (C3D8).

The calculated and measured (axial) load-strain relationships are compared in Figure 6-5. Two reference points located on the longitudinal ribs are used to illustrate the geogrid response: point (I) located near the applied load where necking (maximum lateral strain) was observed in the experiment; point (II) located near the middle of the specimen. A maximum tensile load of 16.5 kN/m, that denotes the strength of the material, was reached at about 15% strain. Beyond the peak load, where necking begins at point (I), the two reference points perform differently. After necking has occurred, all further deformation was found to develop at the neck location, and as a result, point (I) experienced significant strain with a slow rate of decrease in tensile load. Due to the excessive deformation that took place at the neck location, the tensile load is released at other locations within the specimen leading to the unloading observed at point (II). It is worth noting that the calculated response at point (I) is consistent with the measured trend in the experiment.

The numerically calculated response shown in Figure 5-6 confirms the assumption of isotropic (average) state in the MD and XMD presented in Figure 5-2.

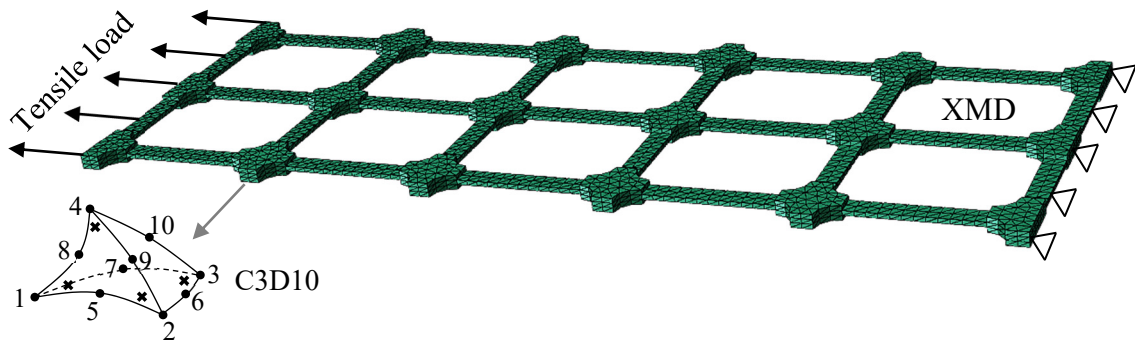


Figure 5-5 Sample of the geogrid mesh in three-dimensions

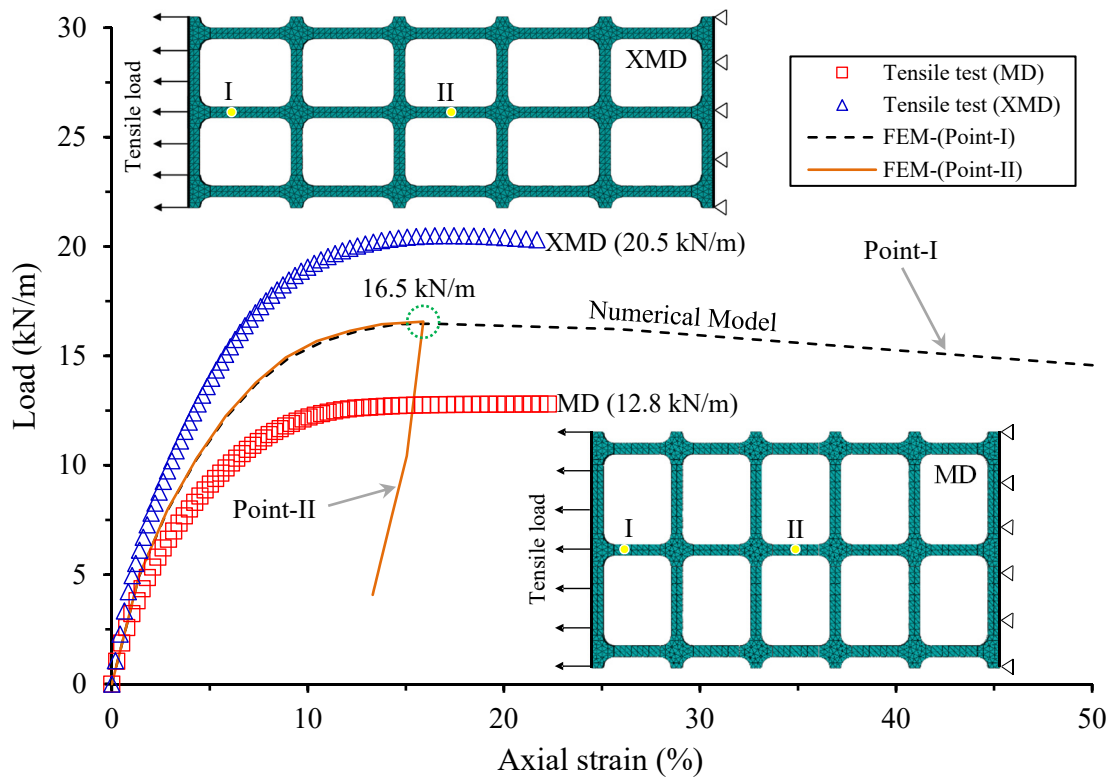


Figure 5-6 Model performance: experimental versus calculated results

5.2.3. Response to tensile loading

Although the numerical results allow for the geogrid response in both MD and XMD to be investigated, only the results of the XMD is presented in this section to keep the paper size within manageable limits.

Displacement and stresses in the geogrid

The deformed shape and displacement pattern along the geogrid are illustrated in Figure 5-7a for an applied boundary displacement (U_x) of 23 mm (onset of necking). The original geogrid geometry is also shown for comparison purpose. Displacements generally decreased with distance from the applied load (left side) and reached zero at the fixed boundary.

The stress distribution within the geogrid is shown in Figure 5-7b. In contrast with the displacement pattern, the stresses in the loading direction (S_{xx}) were found to be almost uniform along the longitudinal ribs. Much smaller stress changes were calculated in the transverse bars as well as at the connecting junctions.

Figure 5-7c shows the equivalent plastic shear strains (PEEQ) developing in the geogrid under the applied tensile loads. It is evident that plastic strains are concentrated within the necking zone located near the applied load.

The patterns observed in Figure 5-7 are confirmed by plotting the normalized displacements along the geogrid as shown in Figure 5-8a. Displacement values were found to decrease linearly with distance from the applied load. The stress distribution (Figure 5-8b) shows that the longitudinal ribs carry most of the transmitted stresses caused by the applied load with only about one fourth of the stress felt by the junctions. The stress transferred to the transverse bars was found to be negligible.

The total geogrid deformation, in both the axial and lateral directions, is evaluated. The load-displacement response calculated along the loaded geogrid boundary up to the maximum applied load is shown in Figure 5-9. The axial displacement, U_x , as the geogrid approaches failure is found to be about 20 mm whereas the lateral displacement, U_y , in the direction normal to the applied load, reached about 0.3 mm before failure.

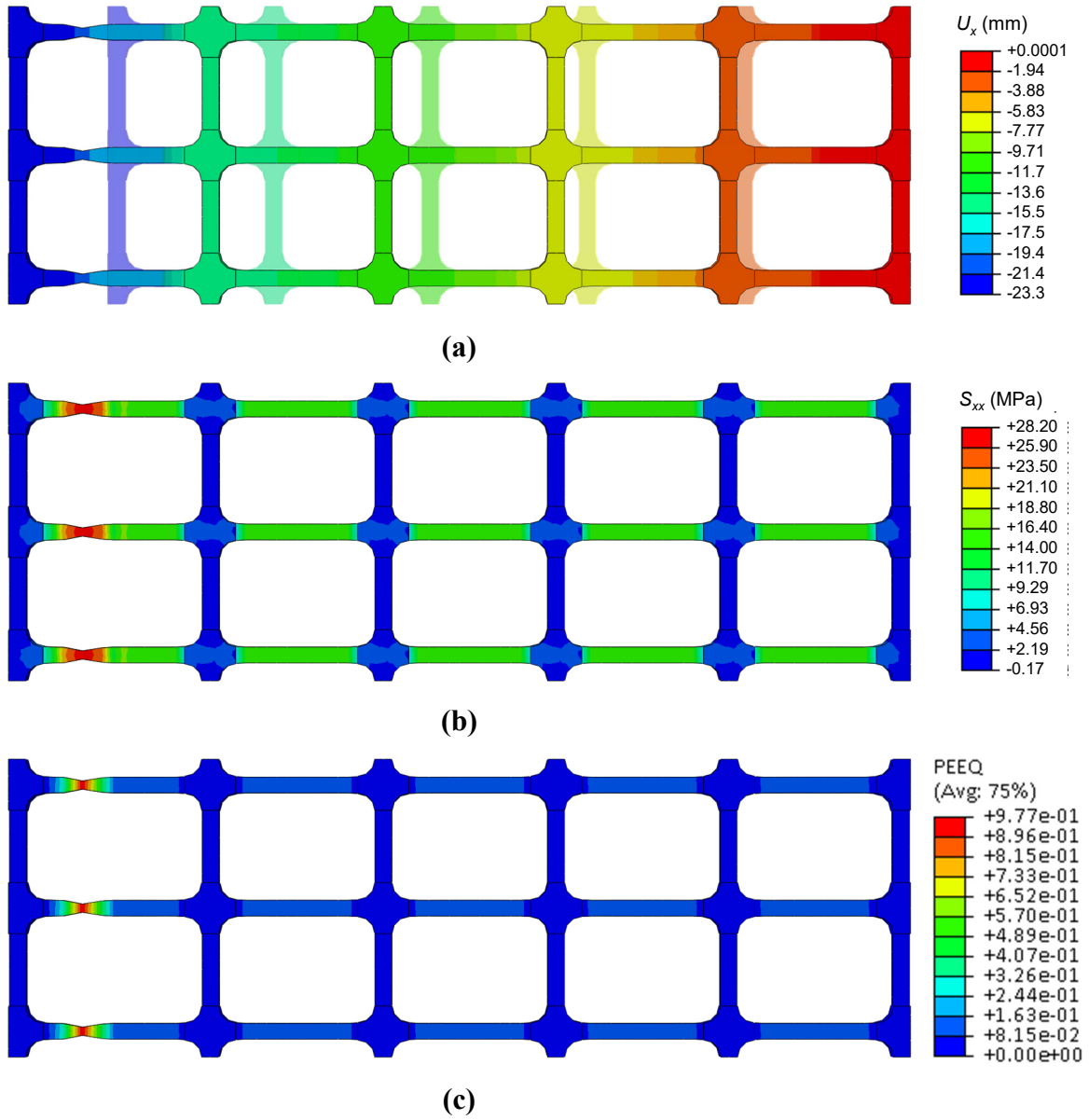
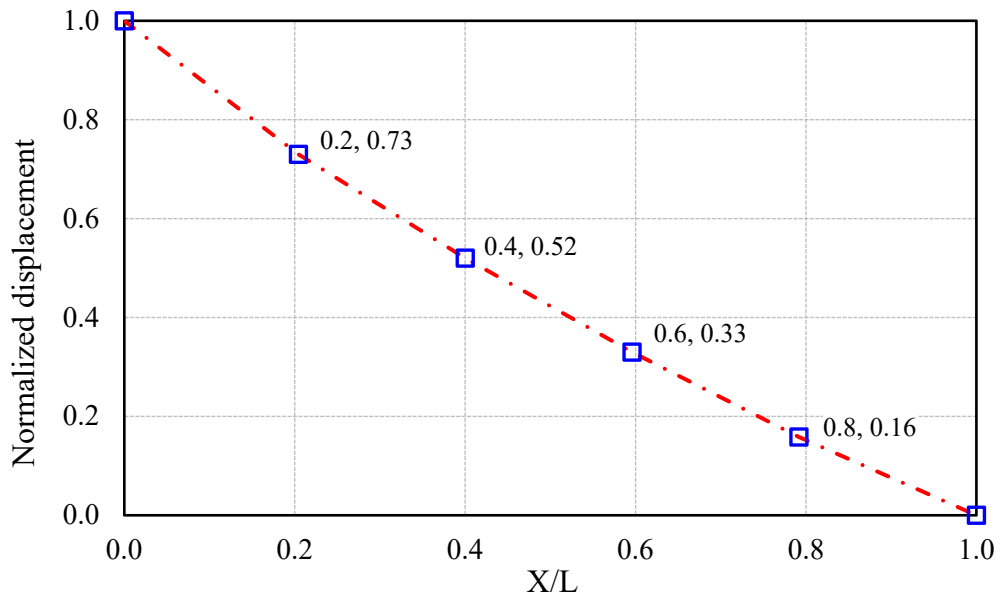
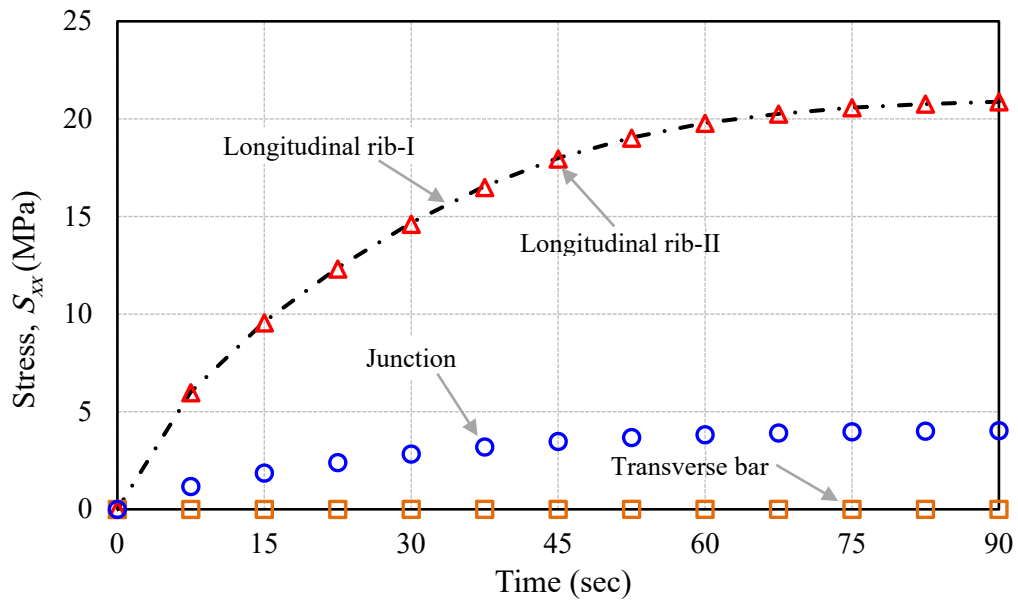


Figure 5-7 Geogrid deformation at $U_x = 23$ mm in the XMD:
a) displacements (U_x), b) stresses (S_{xx}), c) plastic strains (PEEQ)



(a)



(b)

Figure 5-8 Geogrid response at applied displacement of 23 mm: a) Displacement distribution with distance (X) from loaded boundary; b) Stress transfer along the geogrid

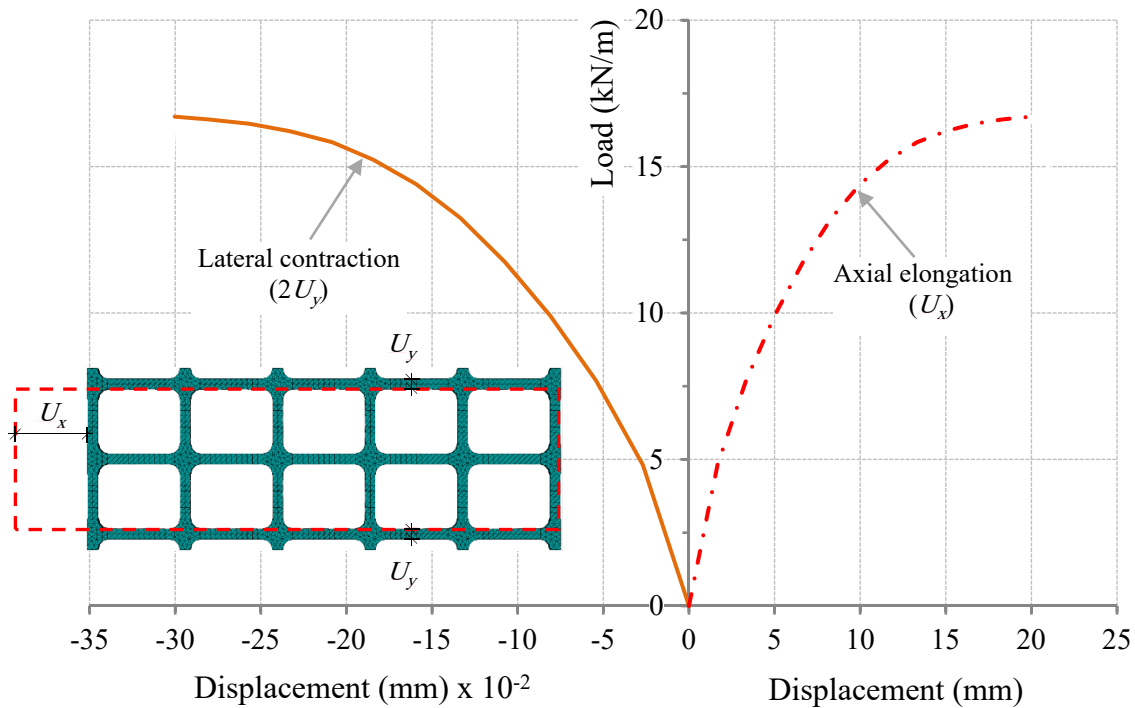
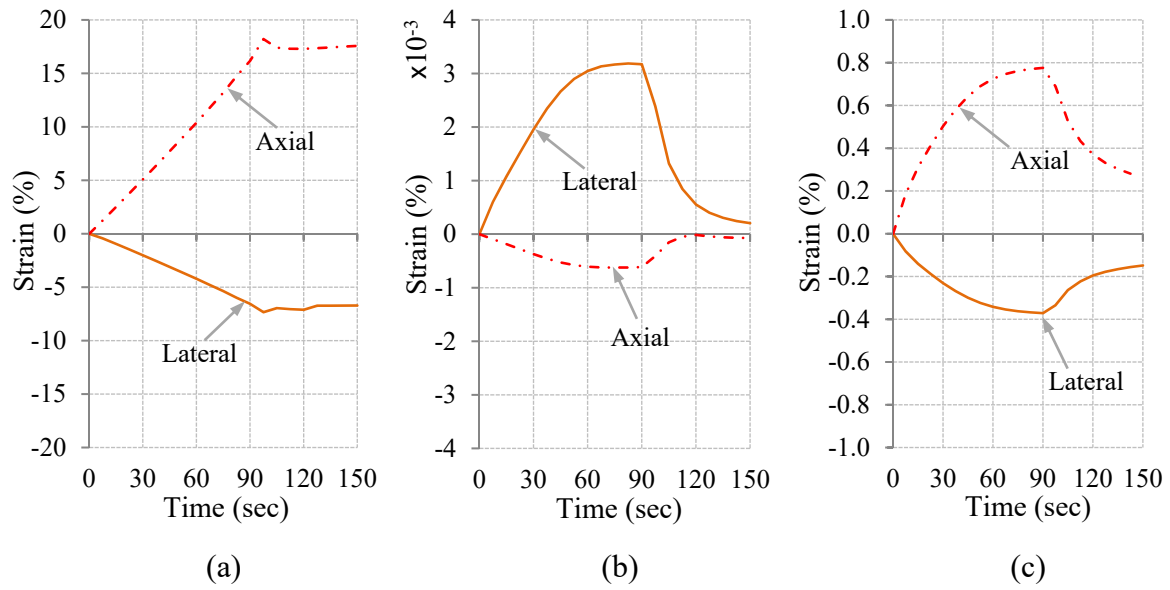


Figure 5-9 Total displacements in the axial (U_x) and lateral (U_y) directions

Axial and lateral strains

Theoretical approaches used in the geosynthetic analysis generally assume uniaxial strain and stress states (Kaliakin and Dechasakulsom, 2001). Experimental evidence, however, indicates that lateral strains manifested in the necking that develops in the longitudinal ribs can significantly affect the geogrid response (Shinoda and Bathurst, 2004). Figure 5-10 illustrates the strains calculated in the axial (X) and lateral (Y) directions at three distinct locations. The longitudinal rib (point a) exhibited positive strains (extension) in the axial direction whereas negative strains (contraction) were calculated in the lateral direction (Figure 5-10a). In contrast to the longitudinal rib, Figure 5-10b shows that transverse bar (point b) experienced extension in the lateral direction while the axial direction has slightly contracted. The magnitudes of these strains are considered to be insignificant. The junction (point c) exhibited small extension in the loading direction coupled with a smaller contraction in the lateral direction as shown in Figure 5-10c.



“Note the different vertical scales”

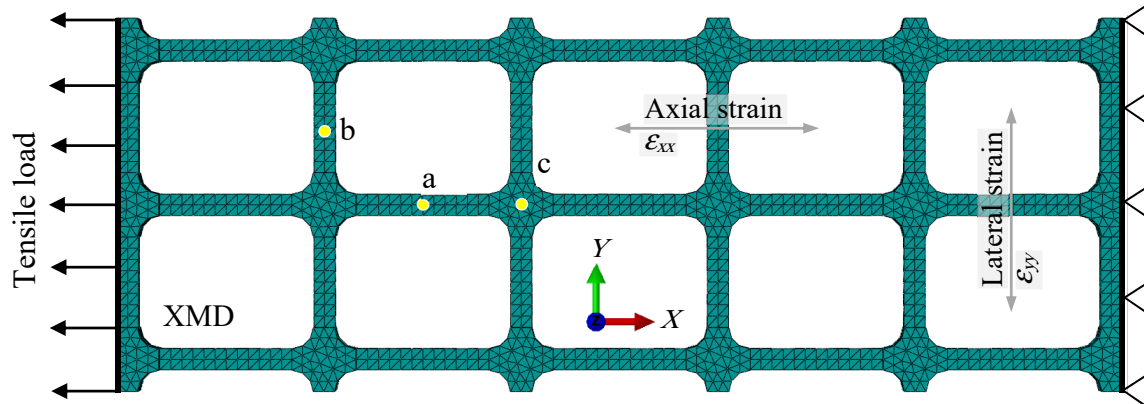


Figure 5-10 Axial and lateral strains at different locations along the geogrid:

a) longitudinal rib; b) transverse bar; c) junction

5.2.4. Exact geometry vs. planer sheet

Geogrid modeling is conventionally performed using either truss, bar, or cable elements in 2D or equivalent planer sheet in 3D analysis (Yogarajah and Yeo, 1994, Shuwang et al., 1998, Perkins and Edens, 2003, Sugimoto and Alagiyawanna, 2003, El Sawwaf, 2007, Liu et al., 2007, Dong et al., 2011, Mirmoradi and Ehrlich, 2014, El Naggat et al., 2015, Zhuang and Wang, 2015). Modelling geogrid using planer sheet requires extensive calibration to balance the increase in the geometric stiffness.

The biaxial geogrid, used in the current study, involves an open area of around 70% that will bring additional stiffness when the geogrid is modeled as a planer sheet. With the purpose of calibration of the planer sheet to represent the accurate geogrid response, it is necessarily to achieve an equivalent sheet thickness.

To determine an equivalent sheet thickness that produces a similar response to that obtained using the exact geogrid geometry, a numerical model was developed using a planer sheet (62 mm x 189 mm) and the equivalent thickness is then back calculated using the trial and error. The obtained responses are compared with those of the exact geometry as shown in Figure 5-11. It is found that using an equivalent thickness of 0.175 mm was able to capture the true behavior of the geogrid. This indicates that modeling the biaxial geogrid as a planer sheet requires a significant thickness reduction as compared to the geogrid rib thickness. This corresponds to about 80% reduction (from 0.8 mm to 0.177 mm) for the biaxial geogrid used in this study.

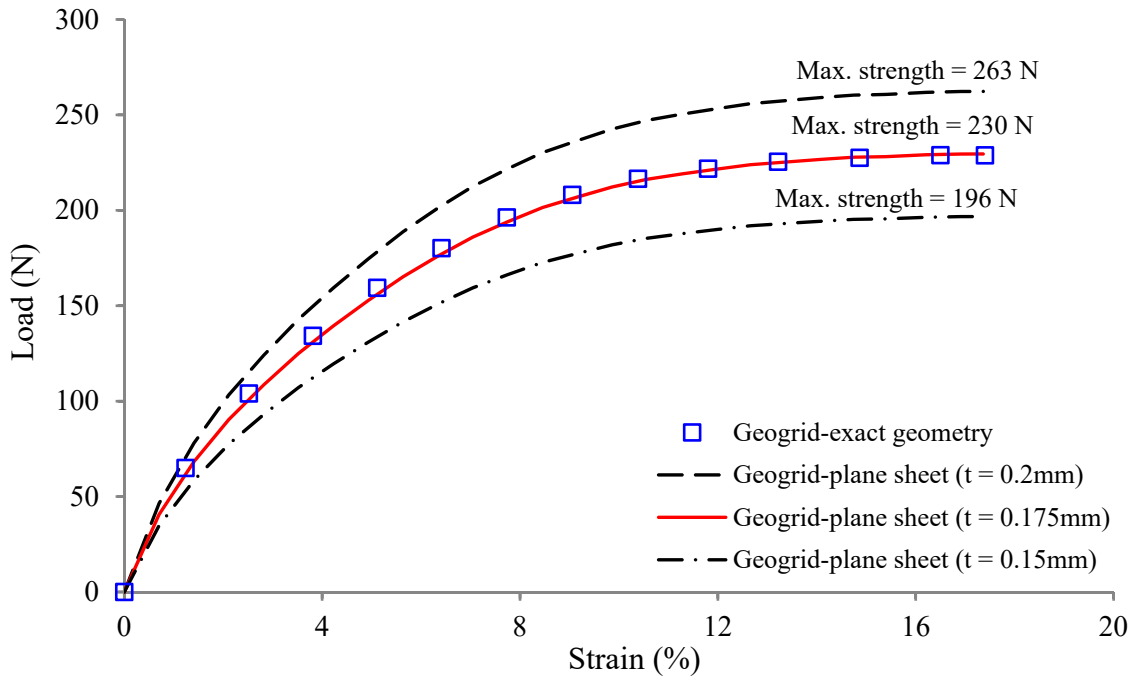


Figure 5-11 Effect of modeling geogrid as a planer sheet

5.3. Soil-Confined Geogrid

The purpose of this section is to examine the applicability of the proposed 3D unconfined geogrid model developed in phase one in modeling soil-geogrid interaction problems. A numerical example involving a square footing over geogrid-reinforced soil is presented.

5.3.1. Geogrid-reinforced foundation

Bearing capacity of reinforced soils has been studied experimentally by many researches (e.g. Guido et al., 1986, Huang and Tatsuoka, 1990, Das et al., 1994, Adams and Collin, 1997, Dash et al., 2001, Patra et al., 2006, Abu-Farsakh et al., 2008, Tafreshi and Dawson, 2010). These studies demonstrated that the overall effects of using geosynthetic material in increasing the bearing capacity of shallow foundations. The roles of different parameters such as reinforcement length, spacing between reinforcing layers, depth to the upper

geosynthetic layer, number of layers, and types of geosynthetics that contribute to the bearing capacity were also investigated in these studies.

Analytical solutions were also developed by researchers (e.g. Binquet and Lee, 1975a and b, Huang and Menq, 1997, Kumar and Saran, 2003, Sharma et al., 2009, Chakraborty and Kumar, 2014) to calculate the bearing capacity of reinforced soils.

Numerical analysis is an alternative way to study stresses and strains within a given soil-geosynthetic system. The finite element method has been proven to be effective in the analysis of reinforced foundations problems (Yetimoglu et al., 1994, Kotake et al., 2001, Basudhar et al., 2007, Ghazavi and Lavasan, 2008, Li et al., 2012, Rowe and Liu, 2015). In these studies, modeling geogrid reinforcement was often simplified either using truss elements (in 2D analysis) or a continuous sheet (in 3D analysis). In addition, the interaction between the simplified 3D geogrid models and the surrounding soil was often captured using interface layers in which the contact properties were considered while the interlocking effect was not represented. It is known that soil-geogrid interlocking plays an important role in the load-carrying capacity of foundations over geogrid-reinforced soils (Guido et al., 1986, Liu, 2015, Pinho-Lopes et al., 2015). The interlocking of soil particles through the grid apertures mobilizes the tensile strength in the reinforcing layer and generates an anchoring effect that leads to better geotechnical performance. Modeling such interactions considering the explicit geogrid geometry has been reported by Tran et al. (2013b) using the finite-discrete element method. The modeling approach presented in phase one of this study is used to simulate a geogrid-reinforced soil supporting a square footing. Using the exact geometry of geogrid allows for the interlocking effect to be explicitly simulated. The soil-geogrid interaction is ensured in this study using interface elements.

5.3.2. Numerical modeling of a square footing on geogrid-reinforced soil

The experimental results reported by Chen et al. (2009) for square footing supported by geogrid-reinforced crushed limestone is used to validate the proposed geogrid model. The experiments investigated the effect of introducing geogrid reinforcement on the stress distribution in the soil mass and the strains developing in the geogrid. The model footing was 1 in. (2.54 cm) thick steel plate with dimensions of 6 in. (15.2 cm) × 6 in. (15.2 cm) placed at the center of a rigid container (1.5 m x 0.91 m x 0.91 m). The soil used in the experiment was Kentucky crushed limestone with $D_{50} = 5.66$ mm, maximum dry unit weight of 22.68 kN/m³, and a peak friction angle of 53°. The elastic modulus of the crushed limestone was estimated from triaxial tests to be 120 MPa. Biaxial geogrids used in this experiments are similar to that used in phase one of this study (Table 5-1) with dimensions of 1.5 m in length and 0.9 m in width were used in the experiments. The upper geogrid layer was installed at a depth of 50 mm below the foundation base. The number of geogrid layers was varied keeping a distance of 50 mm between two adjacent layers. The vertical stress distribution in the soil was measured using earth pressure cells (10 cm in diameter) installed within the soil mass. The strain distribution in the geogrid reinforcement was measured using strain gauges placed at different locations along the reinforcements.

Details of the numerical model

The 3D finite element models have been developed to simulate the geometry and test procedure used in the experiments. The analysis is performed for up to two geogrid layers using ABAQUS software package. The exact geogrid geometry (16 longitudinal elements and 21 transverse elements) was modeled using 8-node linear brick elements with eight integration points (Figure 5-12). To simplify the nonlinear contact analysis in this case, the local increase in thickness of the junction is not modeled in the analysis. This approximation is expected to cause a slight reduction in the bearing resistance that would develop at these particular locations on the transverse bars.

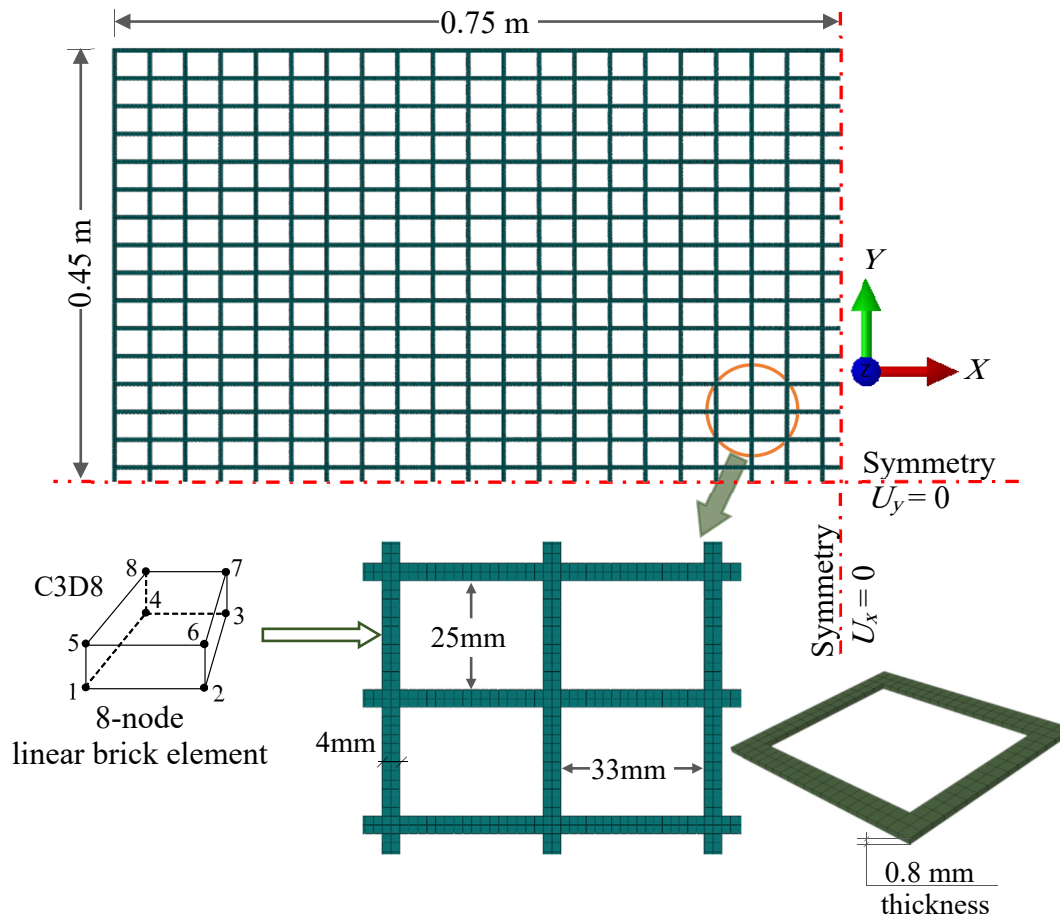


Figure 5-12 Plan view of the geogrid mesh for the in-soil model

The geogrid material model developed in phase one of this study is used throughout this analysis. The geogrid is simulated using over 15,300 finite elements as shown in Figure 5-12. Only one-quarter of the geometry has been modeled to take advantage of the problem symmetry as illustrated in Figures 5-12 and 5-13.

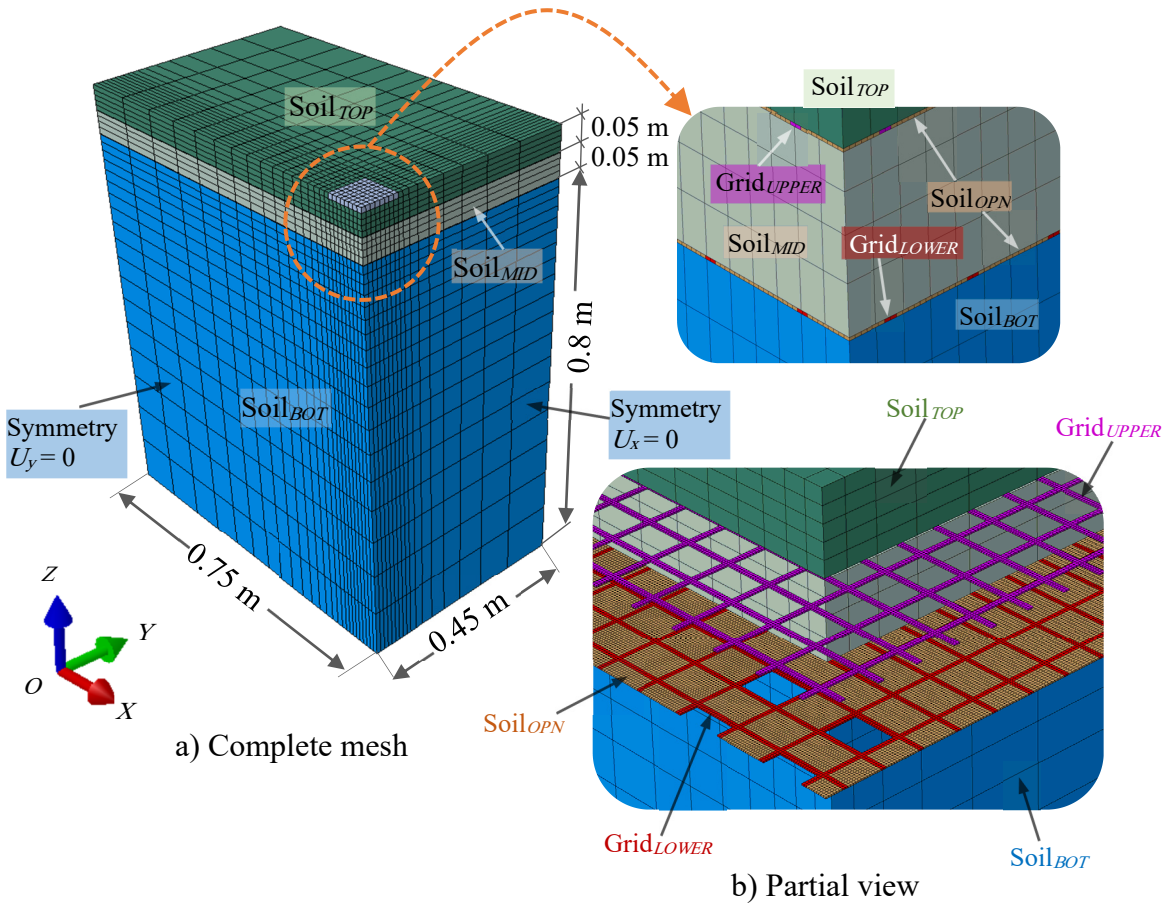


Figure 5-13 Complete and partial 3D mesh geometry of the in-soil FE model

The crushed stone backfill was modeled using elasto-plastic Mohr-Coulomb failure criteria with non-associated flow rule (Appendix (A)) and the soil domain was discretized using 8-node linear brick elements (C3D8). The input parameters used in the finite element analysis are summarized in Table 5-2.

Table 5-2 Soil input parameters used in the FE analysis of the reinforced-foundation

Elastic Modulus E (MPa)	Poisson's ratio ν	Friction angle ^a $\phi^\circ/\phi_{cv}^\circ$	Dilatancy angle ^b ψ°	Cohesion (MPa)
120	0.35	53/36	21	1E-05

^a ϕ° = peak friction angle & ϕ_{cv}° = critical state friction angle

^b Determined using Bolton's equation (1986)

Although the unconfined geogrid analysis showed no difference in the behavior of membrane and continuum elements, it was found that modeling soil-geogrid interaction using solid elements is more appropriate as it allows the contact surfaces to be fully defined as compared to the edge-to-edge contact developing when membrane elements are used.

The choice between hexahedral and tetrahedral elements was also governed by the geogrid thickness. Using tetrahedral elements can result in poor aspect ratio, whereas hexahedral elements (e.g. C3D8) are found to be suitable for modeling contact problems involving with elasto-plastic material as it allows for strain discontinuities to be captured. The backfill was divided into three layers as shown in Figure 5-13. The bottom soil layer (Soil_{BOT}) was first generated in eight stages (10 cm each) and the geostatic stress state was established for each stage. The lower geogrid layer (Grid_{LOWER}) and the soil elements needed to fill the openings (Soil_{OPN}, with t_{geogrid} 0.8 mm) are introduced in a separate step. A second soil layer (Soil_{MID}) of 5 cm in thickness was then added. Similarly, the upper geogrid layer (Grid_{UPPER}) with soil elements inside the openings was added. Finally, the third soil layer (Soil_{TOP}) of 5 cm in thickness was generated up to the soil surface.

Full interlocking between the soil and the geogrid is assumed and therefore, the soil-geogrid interaction was simulated using two fully bonded master-slave contact surfaces. This will prevent slippage from happening at the soil-geogrid interface. The surface based constraints are enforced by eliminating the degrees of freedom of the slave surface to maintain the same translational and rotational motion equal to those of the master surface. This has been achieved by assigning the soil as the master surface and the geogrid as the slave surface.

Boundary conditions were defined such that the nodes along the vertical boundaries may only translate freely in the vertical direction (smooth rigid). Nodes at the base are fixed against displacements in all directions (rough rigid). Symmetry boundary conditions were assigned at the centerlines as illustrated in Figures 5-12 and 5-13.

Sensitivity analysis was conducted using different element sizes to determine a suitable mesh reinforcement that brings a balance between accuracy and computing time. The 3D FE mesh, with over 112,875 elements, is shown in Figure 5-13a. The mesh size was adjusted in the vertical direction around the geogrid layers to provide sufficient resolution within the interaction area. The mesh was also refined in both X and Y directions around the areas where stress concentration is expected as a result of the footing pressure. A partial view of soil-geogrid interaction is shown in Figure 5-13b. It is worth noting that soil elements located above and below the geogrid can interact directly with each other leading to soil continuity through the openings which closely simulates the real behavior of soil-geogrid interaction. Figure 5-14 shows further modeling details of the soil-geogrid interaction with emphasize on the soil within the geogrid apertures. In doing so, the model incorporates three interface conditions: i) soil-to-soil; ii) soil-to-geogrid on horizontal surfaces; iii) soil-to-geogrid on vertical surfaces within the geogrid apertures.

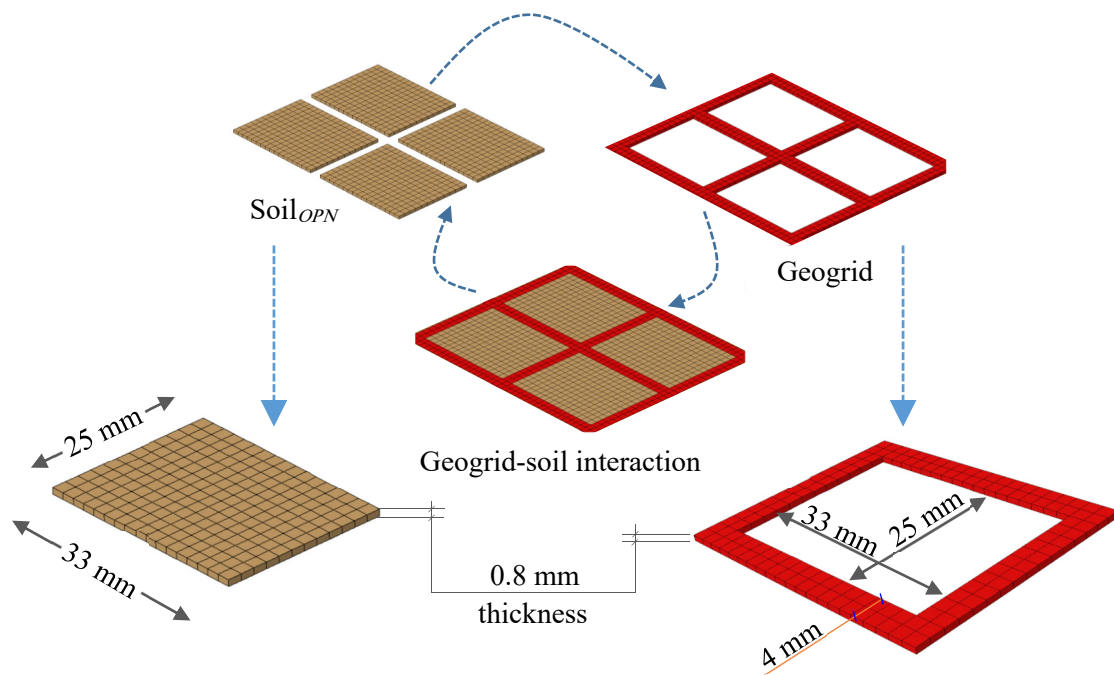


Figure 5-14 Details of geogrid-soil interaction

After the FE model was built, the square rigid footing was simulated and the surface pressure was applied in small increments using displacement control. For each load increment, the applied pressure was kept constant until the convergence condition was satisfied. The equivalent footing pressure is computed as the summation of the vertical reaction forces divided by the footing area.

Validation of the in-soil model

In this section, the effect of introducing one or two geogrid reinforcement layers into the backfill material is examined and compared with the unreinforced case. To validate the proposed model, the FE results are compared with the experimental data. Figure 5-15 shows the relationship between the equivalent footing pressure and the vertical settlement for the three investigated cases: no reinforcement ($N = 0$), one geogrid layer ($N = 1$), and two geogrid layers ($N = 2$). The load-carrying capacity generally increased when geogrid reinforcement was introduced and the ultimate bearing capacity of the footing increased with the addition of a second geogrid layer. The load-settlement results obtained using the developed numerical model agreed reasonably well with the experiment data reported by Chen et al. (2009) up to a footing displacement of about 25mm. As failure is approached for the reinforced cases, the model slightly underestimated the bearing capacity of the footing.

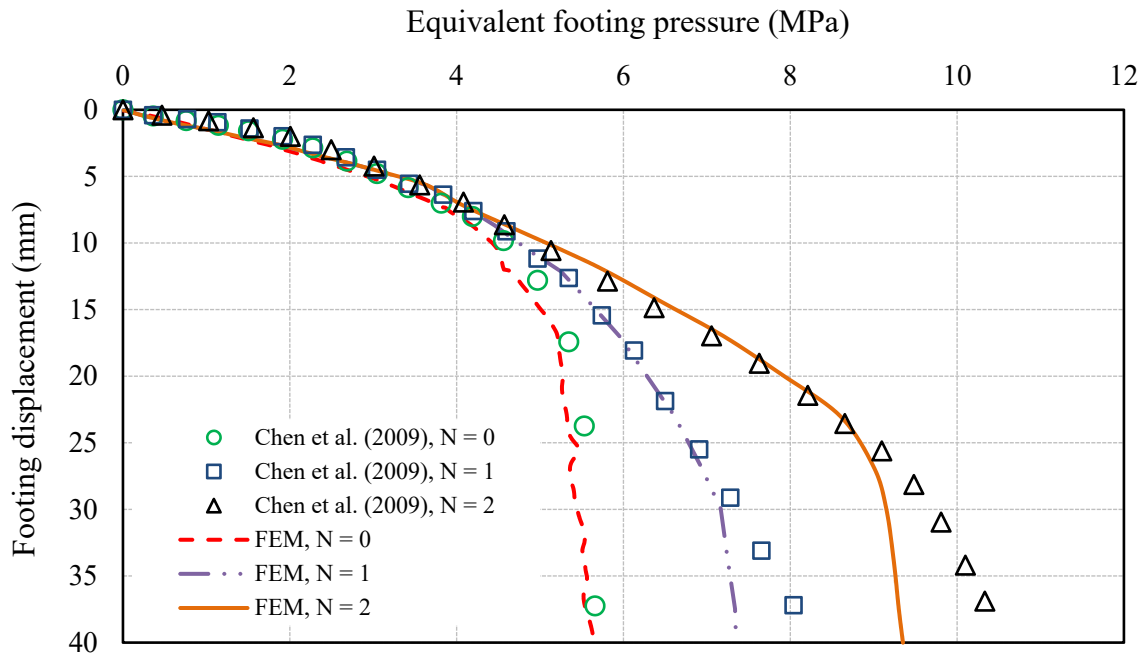
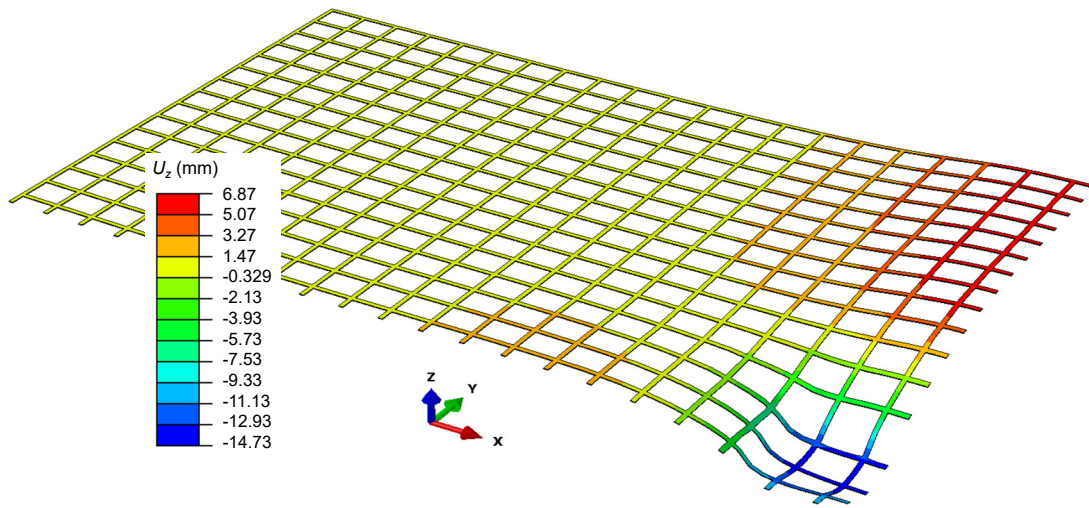


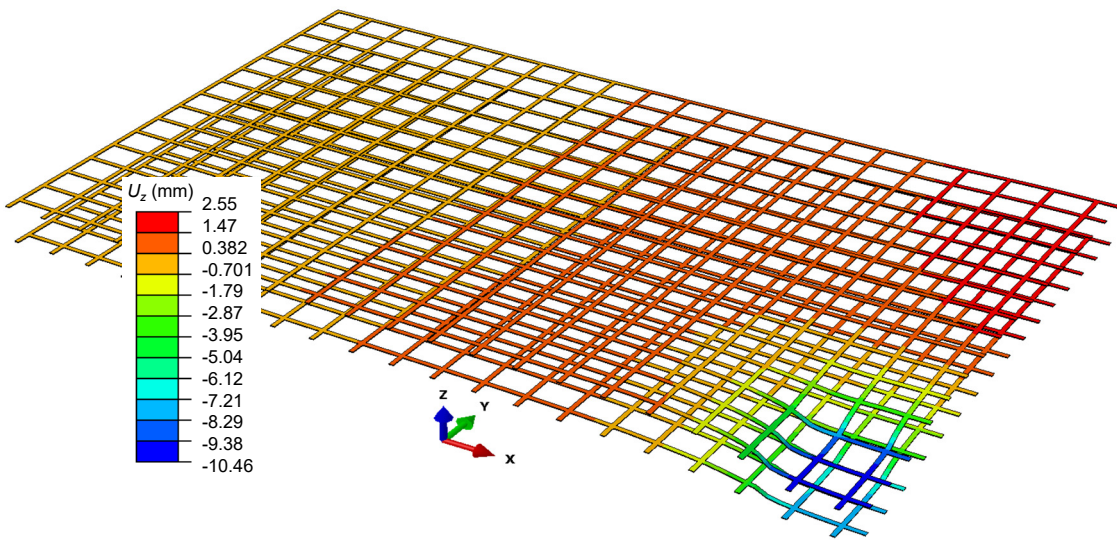
Figure 5-15 Load-settlement relationships for geogrid-reinforced crushed limestone

5.3.3. Response of the geogrid

The deformed shapes of the geogrid layers for a given footing pressure are shown in Figure 5-16. A reference pressure value of 6 MPa (smaller than the ultimate capacity for $N = 1$) was chosen to allow for the displacements of the reinforced foundation to be examined. The vertical displacements developing in the geogrid for the reinforced cases are shown in Figure 5-16. The maximum displacement was found to decrease with the addition of a second geogrid layer. For $N = 2$ (Figure 5-16b), the vertical displacement of the upper layer (located closer to the footing) is larger than that of the lower one. Similarly, the tensile stresses, S_{xx} and S_{yy} , developing in the geogrid decreased when two geogrid layers were installed under the footing, as shown in Figure 5-17, with the upper geogrid layer carrying more tensile stresses compared to the lower layer. In both cases, most of the geogrid deformations and stresses occurred mainly in the area immediately below the footing with very small deformation away from the loaded area.



a) $N = 1$



b) $N = 2$

Figure 5-16 Geogrid deformation at a given footing load (6MPa):

a) one layer of geogrid; b) two layers of geogrid

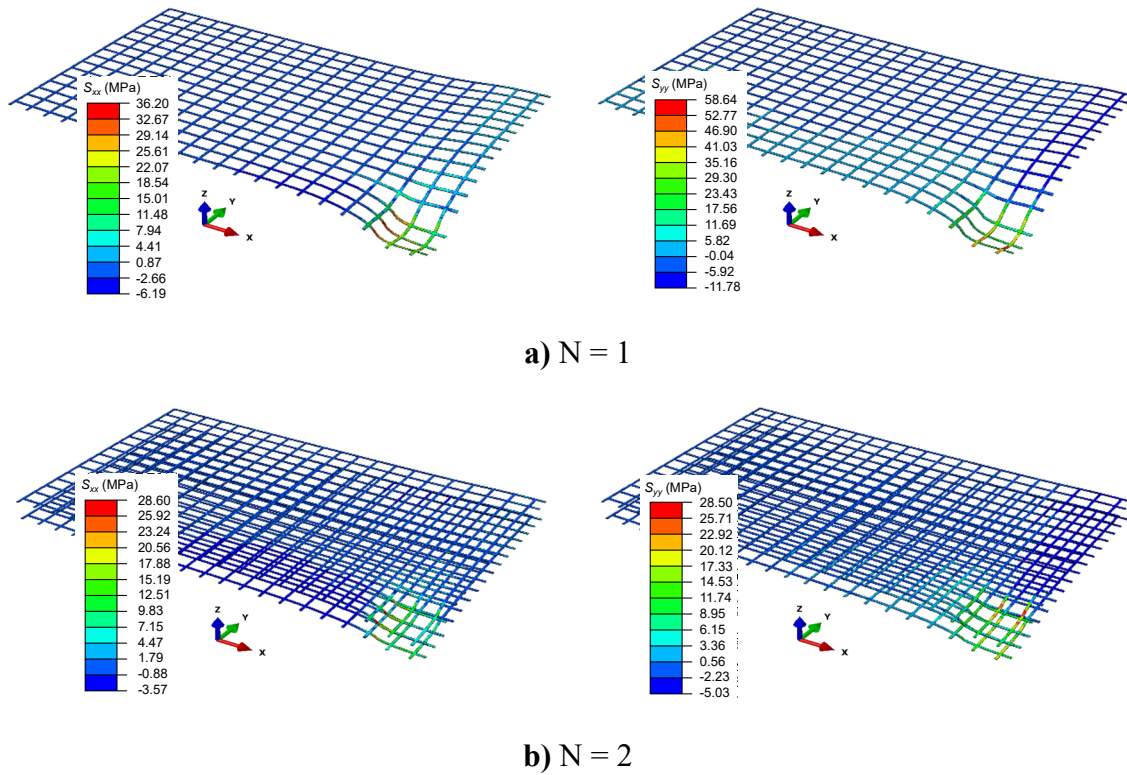


Figure 5-17 Tensile stresses (S_{xx} & S_{yy}) at footing pressure of 6MPa:
a) one layer of geogrid; b) two layers of geogrid

The above example demonstrates that the proposed approach for modeling unconfined geogrid in 3D is suitable for solving geogrid-reinforced soil systems. The results showed that the model can capture the essential interlocking and friction mechanisms that allow for the response of these systems to be evaluated.

5.4. Summary and Conclusions

In this study, a procedure for the 3D finite element analysis of unconfined and soil-confined geogrid is developed using ABAQUS software. A numerical model that is capable of simulating the response of the unconfined biaxial geogrid under tensile loading is first introduced and validated using index test results. In developing this model, the details of the geometrical features are explicitly simulated. Sensitivity analysis was performed to evaluate the role of different numerical parameters on the predicted geogrid response. The difference between modelling the exact geogrid geometry as opposed to an equivalent sheet is also examined.

Tensile load applied to a geogrid specimen causes stresses that are carried mostly by the longitudinal ribs in the direction of the applied load and the portion transmitted to the junctions and transvers bars are insignificant. The displacement is found to decrease linearly with distance from the loaded boundary. Using equivalent plane sheet without proper calibration with exact geometry to model geogrid may lead to a much stiffer response resulting in an overestimation in the design load.

To confirm the validity of the unconfined geogrid model, a 3D analysis is conducted to investigate the geogrid performance as it interacts with the backfill material. A case study involving a square footing supported by a geogrid-reinforced material is investigated. The 3D geometry of the geogrid, its deformation, and stress distribution were presented. The model was able to capture the 3D response of the soil-geogrid system with one or more geogrid layers installed under the footing. Increasing the number of geogrid layers resulted in an increase in the ultimate bearing capacity of the system. The geogrid deformations and tensile stresses for the case of $N = 1$ were found to be generally larger than those calculated for $N = 2$.

Finally, the proposed FE approach has proven to be efficient in capturing the 3D responses of both unconfined and soil-confined geogrid and can be adopted by researchers for soil-geogrid interaction analysis.

Preface to Chapter 6

The efficiency of the FE approach proposed in the previous chapter in analyzing soil-geogrid interaction problems has been demonstrated. To examine the capability of this technique in solving problems involving large strains, a three-dimensional analysis is developed to investigate the pullout behavior of biaxial geogrid embedded in granular backfill. Modeling the 3D soil-geogrid interaction under pullout loading is a challenging problem that requires a special consideration to simulate the different modes of resistance that contribute to the pullout capacity of the geogrid layer in addition to the large deformations associated with the pullout process. The detailed behavior of the geogrid and the surrounding backfill is investigated. The suitability of the proposed numerical technique to solve this class of problems is therefore demonstrated.

CHAPTER 6

Three-Dimensional Modeling of Soil-Geogrid Interaction under Pullout Loading Condition*

Abstract

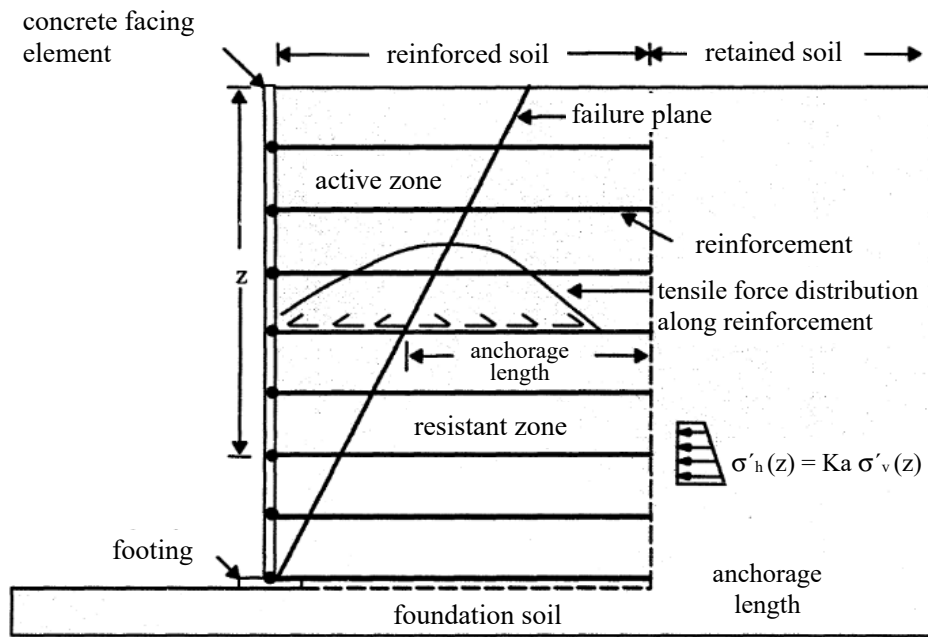
Soil reinforcement has rapidly become one of the most common soil improvement techniques used in geotechnical engineering applications. Understanding the behavior of a geogrid layer subjected to pullout loading condition is considered to be crucial to any successful design. This behavior is dependent on the properties of the geogrid material, the backfill soil and the interface condition. Modeling the 3D soil-geogrid interaction under pullout is a challenging numerical problem that requires a special consideration to simulate the different modes of resistance that contribute to the pullout capacity of the geogrid layer. This paper describes the results of a three-dimensional finite-element analysis that has been developed to investigate the behavior of biaxial geogrid embedded in granular backfill and subjected to pullout loading. The model is performed to simulate a laboratory size pullout test using an innovative numerical approach that has been introduced in a previous publication. This approach considers the non-continuous nature of the geogrid geometry and using an elasto-plastic constitutive model to describe the behavior of the geogrid material. Validation is performed by comparing experimental data and numerically calculated results using the proposed model. The detailed behavior of the geogrid and the surrounding backfill is then investigated. In addition, the effect of different numerical parameters that contribute to the soil-geogrid interaction, including the contact modeling of different parts of the geogrid, is examined. Finally, the advantages of the proposed numerical approach are discussed and conclusions are extracted to highlight the suitability of the proposed technique to solve this class of soil-structure interaction problems.

Keywords: Geosynthetics, Biaxial geogrid, Pullout, Soil-geogrid interaction, Friction resistance, Bearing resistance, Numerical analysis, Nonlinear contact.

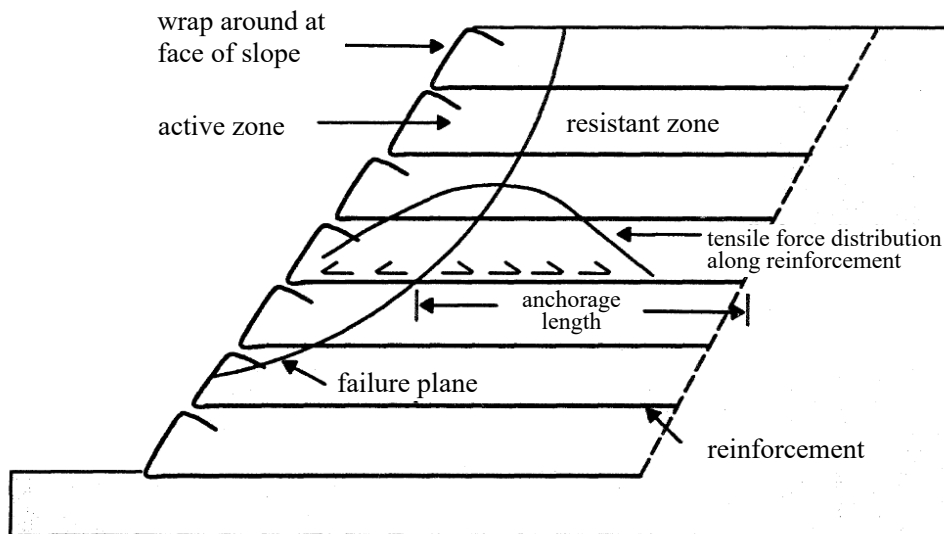
* A version of this chapter will be submitted to *Geotechnical and Geoenvironmental Engineering*, an ASCE Journal.

6.1. Introduction

Geosynthetic reinforcements are used for different applications in geotechnical engineering such as reinforced earth fills, retaining walls, embankments, road pavement and foundations. The use of geosynthetics is known to improve soil performance, increase the safety factor against shear failure while reducing the construction cost of the project (Koerner, 2012). In general, the evaluation of soil-geosynthetics interaction is very complex as it is affected by: i) the geometrical, and mechanical characteristics of the geosynthetic material, ii) mechanical properties of soil, and iii) the boundaries and loading conditions. When using continuous geotextile (sheet) to reinforce soils, skin friction is the only mechanism that develops at the soil-geotextile interface, while for geogrids and due to its open structure, the interaction becomes more complex (Moraci et al., 2014). The interaction between granular soils and extensible geogrids in reinforced-soil systems has been the subject of much research since these reinforcement materials were introduced more than three decades ago (e.g. McGown et al., 1984). The soil-geogrid interaction involves three basic load transfer mechanisms, namely: i) tangential/skin friction, which is a three-dimensional friction between the geogrids elements (friction on the solid surface areas of the longitudinal ribs and the transversal bars) and the surrounding backfill, ii) passive earth pressure (bearing resistance) on the transversal bars of the geogrid, and iii) the interlocking of grain particles in grid openings (soil-to-soil friction). Depending on the load condition and the geosynthetics geometry, one or more of these interaction mechanisms can be mobilized at the soil-geosynthetics interface. Two design criteria are generally used for most reinforced-soil structures; i) the reinforcement must not fail in tension (by rapture or excessive deformation), and ii) the reinforcement must not pull out of the soil resistant zone (Lentz and Pyatt, 1988). Designing against tensile failure requires that tensile stresses in the reinforcement be less than the ultimate strength of the material. In pullout failure, however, it is also required to determine the reinforcement anchorage capacity. The second criterion (pullout) dominates in the design of both reinforced walls and slopes as illustrated in Figure 6-1. Therefore, it is important in this case to select an appropriate reinforcement spacing and length to prevent pullout failure.



(a)



(b)

Figure 6-1 Pullout failure mechanism: a) reinforced retaining wall and b) reinforced slope (After McLay, 1993)

6.1.1. Soil-geogrid interface

The shear stress-strain relationship along a given soil-geogrid interface, which is used to determine the required anchorage length, is commonly characterized using direct shear and/or pullout tests (Farrag et al., 1993). These two methods evaluate the soil-geogrid bond in different ways. The direct shear test is applicable to potential failure mechanisms where the failure plane propagates mainly along the reinforcement (direct sliding mechanism) and is used to find the frictional bond between the soil and the solid surface area of the geogrid (Figure 6-2). Pullout test, on the other hand, is used to study the anchorage capacity of the geogrid reinforcement and to model the load transfer mechanism within the anchorage zone.

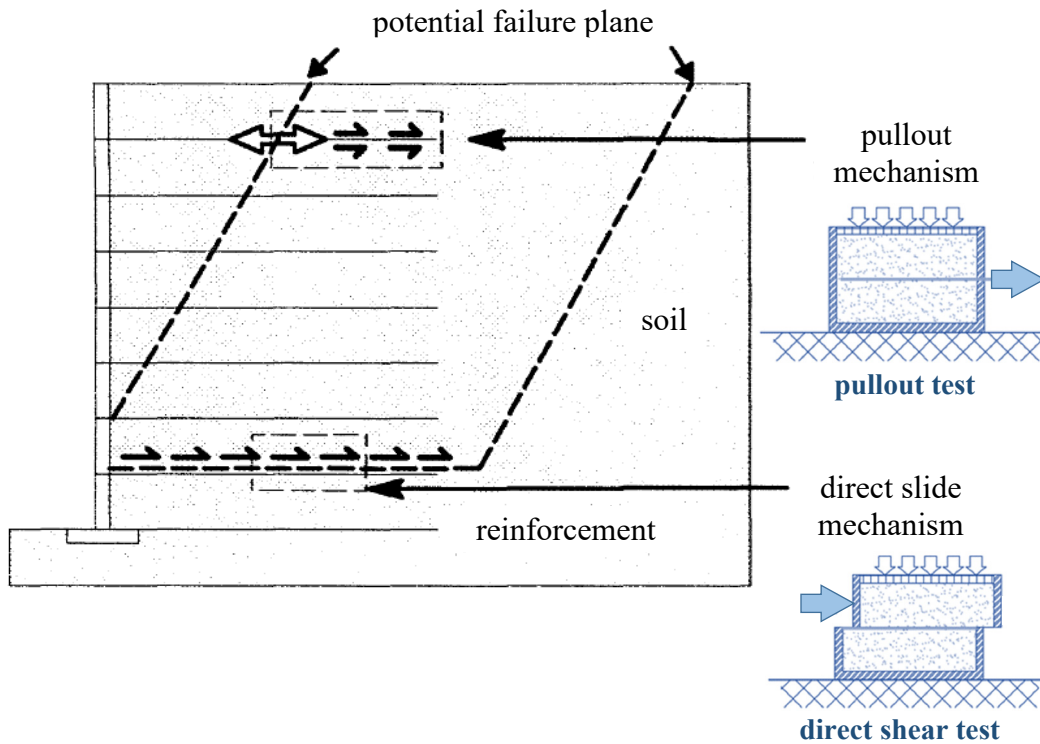


Figure 6-2 Pullout and direct sliding mechanisms

Another distinction between the two tests relate to how strains mobilize along the surface of the reinforcement. In direct shear test, the mobilized shear strain is postulated to be uniformly distributed along the soil-geogrid interface. While in pullout tests, mobilized strain is a combination of the interface shear strain and geogrid extension. This coupled mechanism results in a non-uniform shear strain-stress distribution along the geogrid. In addition, pullout boxes are often designed with fixed boundaries that increased the soil confinement. This increase in confining pressure reduces soil tendency to dilate (restrained dilatancy) leading to an increase in passive resistance on the transversal ribs and consequently an increase in pullout resistance.

6.1.2. Soil-geogrid interaction under pullout loading

Pullout test provides pullout capacity values for specific reinforcement, soil and load conditions and can be used to determine the coefficient of interaction which is of primary interest in design. According to AASHTO (2012), the coefficient of interaction is a mass parameter that combines the effect of all interaction mechanisms. This section examines the current available soil-geogrid pullout models.

Several Limit equilibrium-based models that estimate geogrid pullout capacity have been developed by researchers (e.g. Jewell et al., 1984, Koerner et al., 1989, Palmeira and Milligan, 1989, Gurung and Iwao, 1999, Perkins and Cuelho, 1999, Moraci and Gioffrè, 2006). Some of these models have been reviewed in section 2.1.3 of Chapter 2 of the thesis. In summary, most of these theoretical models calculate the pullout capacity of geogrid as the cumulative contribution of bearing resistance mobilized at the transversal bars and frictional resistance mobilized along the solid surface area of the geogrid (friction on the longitudinal and transversal elements). The details of these models are expressed in equations 2.8 to 2.17, and a schematic representation of the pullout capacity components is given in Figure 6-3.

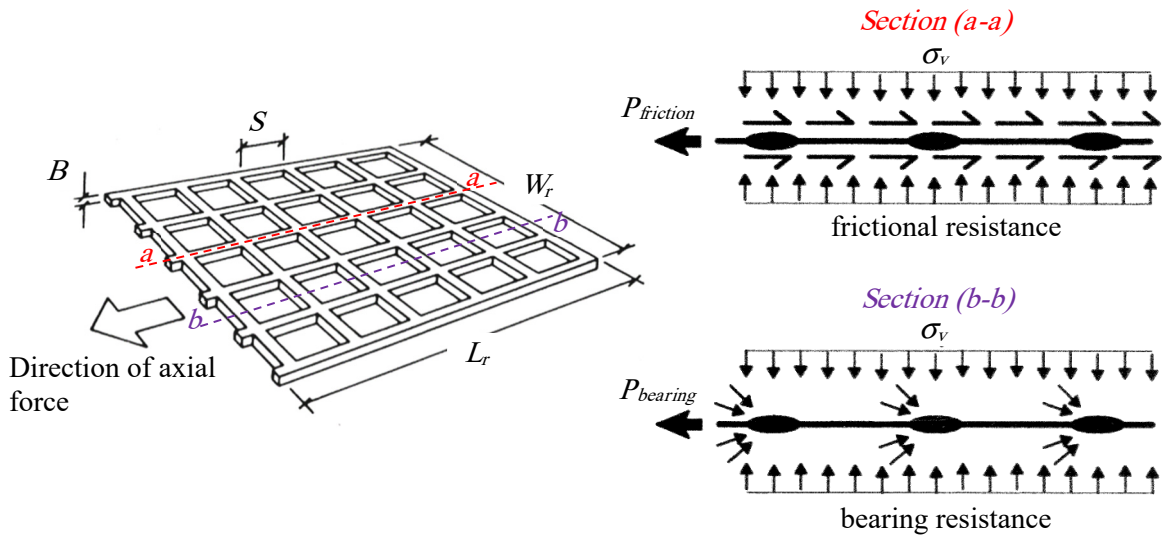


Figure 6-3 Schematic representation of geogrid pullout components

Besides the previously discussed models, this section describes the commonly used pullout capacity models of geogrid in North America based on both the AASHTO and the FHWA design specifications.

AASHTO and FHWA model for geogrid pullout capacity

The AASHTO (2012) and the FHWA (Berg et al., 2009) procedure lumps the contributions of frictional and bearing resistance into a single non dimensional parameter called *the pullout resistance factor, F^** , also called *the coefficient of interaction parameter* or *the friction-bearing-interaction factor* according to FHWA (2009).

In this method, the pullout capacity is estimated as:

$$P = 2 L_e \sigma_v F^* \alpha \tag{6.1}$$

where P is the pullout resistance per unit width of the geogrid, L_e is the length of reinforcement in the resisting zone (anchorage length), σ_v is the normal stress at the reinforcement level, F^* is the pullout resistance factor (coefficient of interaction), and α is a scale effect correction factor.

The extensibility of the reinforcement influences the load transfer mechanism, thereby affecting the pullout response of the soil-reinforcement system (Juran et al., 1988). With inextensible reinforcement (e.g. metal grids), finding the pullout resistance and coefficient of interaction is relatively simple (stresses and displacements are uniformly distributed and the reinforcement moves as a rigid member). However, extensible reinforcements (e.g. synthetics geogrids) develop a nonuniform shear stress-shear displacement distribution due to the reinforcement elongation during pullout loading. This nonuniform load transfer mobilization can significantly cause a nonlinear increase in the pullout response with increasing the reinforcement length. The FHWA method incorporated the scale effect correction factor (α) to account for the extensibility of the geosynthetic reinforcement. Hence, for inextensible reinforcement, α is approximately 1, and can be substantially smaller than 1 for extensible reinforcements.

According to AASHTO and FHWA, F^* and α can be obtained from product-specific pullout tests in the project backfill material or they can be estimated using analytical or numerical load transfer models which have been calibrated through numerical test simulations. In the absence of test data, the following values are recommended by AASHTO and FHWA:

$$\begin{aligned}\alpha &= 0.8 \text{ for geogrids} \\ &= 0.6 \text{ for geotextiles (sheet geosynthetics)}\end{aligned}$$

F^* value can conservatively be taken as:

$$F^* = \frac{2}{3} \tan \phi \quad \text{where } \phi \text{ is peak friction angle of the soil.}$$

6.1.3. Background on soil-geogrid pullout modeling

In North America, ASTM/D6706-01 (2013) is used to quantify pullout capacity in the laboratory. A large amount of literature related to the results and interpretation of pullout laboratory tests is available (Palmeira and Milligan, 1989, Farrag et al., 1993, Bakeer et al., 1998, Alagiyawanna et al., 2001, Moraci and Recalcati, 2006, Lopes and Silvano, 2010, Hatami et al., 2013, Ferreira et al., 2015, Bathurst and Ezzein, 2016, Cardile et al., 2016). The influence of several factors, such as the pullout box size, front and side wall conditions, sleeve length, soil and reinforcement properties, test speed and applied normal stress on the

pullout test results has been evaluated and discussed. In most of these investigations, the focus has been on understanding the mechanisms of soil-structure interaction, development of pullout models of varying complexity, and refinement of test methodology to ensure a consistent and reliable estimate of the pullout capacity. However, the number of tests performed has been limited and often restricted to one class of geosynthetic product or one manufacturer product line.

Several attempts have been made to develop analytical models to estimate the soil-geosynthetic interaction under pullout loading conditions (e.g. Jewell et al., 1984, Koerner et al., 1989, Palmeira and Milligan, 1989, Gurung and Iwao, 1999, Perkins and Cuelho, 1999, Moraci and Giofrè, 2006). The theoretical expressions used in these models to evaluate the pullout resistance and the associated soil-geogrid interaction coefficient show some limitations. In particular, these models do not take into account the true reinforcement geometry and extensibility, and the soil dilatancy that strongly affect the pullout behavior.

While it is possible to track the load-displacement response of a geogrid layer in pullout experiments, the behavior of the backfill soil as it interacts with the geogrid material is hard to evaluate experimentally (Meguid, 2014). Numerical methods are, therefore, considered more suitable for that purpose. The discrete element (DE) method has been used by several researchers to model soil-geogrid interaction (McDowell et al., 2006, Zhang et al., 2008, Bhandari and Han, 2010, Chen et al., 2012, Wang et al., 2016). In this approach, the geogrid is simulated using a set of spherical particles bonded together to form the geogrid shape. The interaction between the geogrid and the surrounding soil is obtained through the contact between discrete particles. Although microscopic parameters of the bonded geogrid particles are determined using index tests, the complex geogrid deformation may not be accurately captured due to the inflexibility of the used particles. Moreover, since a set of bonded particles are used to capture the continuous nature of the geogrid, the strains and stresses within the geogrid may not be accurately obtained.

Tran et al. (2013b) introduced an approach to simulate the pullout test by coupling both the FE and DE methods. In this procedure, the reinforcement layer is modeled using FE whereas

the backfill soil can be modeled using the DE method. The coupling of the two methods can efficiently model the geogrid behavior as well as the backfill material. Although the model was able to capture the important features of the problem, the method was limited in considering the geogrid as linear elastic material.

Finite element method (FE) is widely used as a numerical tool to model pullout procedure (e.g. Yuan and Chua, 1990, Wilson-Fahmy and Koerner, 1993, Shuwang et al., 1998, Perkins and Edens, 2003, Sugimoto and Alagiyawanna, 2003, Siriwardane et al., 2008, Rong et al., 2011, Abdi and Zandieh, 2014). Throughout these studies, the geogrid geometry is often simplified either as a truss structure (in 2D analysis) or a continuous sheet (in 3D analysis). Using these simplified approaches makes it difficult to separate the contributions of the frictional and bearing resistances with respect to the overall pullout capacity of a geogrid-reinforced system. In addition, it would be challenging to determine the stress and strain distributions in the geogrid members as well as in the surrounding soil material.

In an attempts to capture the detailed geometry of an embedded geogrid, Hussein and Meguid (2009 and 2013) modelled geogrid pullout test using 3D FE analysis. The geogrid was simulated using a nonlinear elasto-plastic constitutive model that separates the elastic and plastic strains. The analysis was performed using 6-noded solid elements for the soil and 3-noded triangular membrane elements for the geogrid. It should be noted that the details of the grid apertures were taken into account in this study to capture the discontinuous nature of the geogrid sheet. Although the finite element analysis conducted using explicit 3D geogrid geometry has reasonably captured the pullout response and predicted a load-displacement relationship that is consistent with the experimental data, the response of the model was only reliable at the front face of the box as finding stresses and displacements within the composite system was found to be challenging.

6.1.4. Objective of the current study

The objective of this paper is to introduce a finite element framework that can be used to investigate the soil-geogrid interaction under pullout loading condition. This numerical framework aims at simulating the detailed geometry and material of the geogrid and the

surrounding backfill in three-dimensional. The model is capable of capturing the severe nonlinearity of the system caused by not only the constitutive models adopted but also from the contact properties and the large relative movements at the soil-geogrid interface. Although emphasis is placed in this study on evaluating the contributions of the frictional and bearing components of the pullout resistance, displacements, stresses, and strain fields in the vicinity of the geogrid layer are also highlighted. The results of the numerical simulation including the detailed response of the geogrid and the surrounding soil are presented and compared with experimental data. The approach used in this study aims at helping researchers gain new insights into soil-structure interaction problems involving geosynthetic inclusions.

The 3D FE analyses presented throughout this study have been performed using the general finite element software ABAQUS/Standard, version 6.13 (ABAQUS, 2013).

6.2. Numerical Modeling of Pullout Test

The current numerical framework is an extension of that presented in the previous chapter. To take advantage of the developed geogrid material model, a case study involving an experiment performed on a geogrid material similar to that used in Chapter 5 is carefully selected and used throughout the analysis reported in this chapter.

6.2.1. Characterization of the simulated pullout setup

In this study, the pullout test performed on a biaxial geogrid by Alagiyawanna et al. (2001) and Sugimoto and Alagiyawanna (2003) is adopted and analysed using the proposed FE framework that has been introduced in Chapter 5. Details of the laboratory setup are summarized as follows:

The soil container was reported to be 0.52 m in length, 0.3 m in width and 0.625 m in height. The front wall composed of six acrylic plates each of 0.3 m wide and 0.1 m height to reduce the soil-wall friction. The soil used in the experiment was Silica Sand No. 5 with $D_{50} = 0.34$ mm, dry unit weight of 16.32 kN/m^3 , and a peak friction angle of 29.9° ($D_r = 70\%$) as obtained from laboratory triaxial tests. A biaxial geogrid specimen (with material and geometry similar

to that presented in Chapter 5) of 500 mm in length and 300 mm in width was used throughout the experiments. The sand was placed in layers using the raining technique and the pullout load was applied through a clamp attached to the front end of the geogrid sheet. Vertical stresses 49 kPa and 93 kPa were applied above and below the box using air bags to prevent vertical movement of the geogrid during the test. The geogrid was pulled out at a constant rate of 1.0 mm/min and both the load and lateral movement were measured using load cells and displacement gauges, respectively.

6.2.2. FE-model generation

The numerical model has been developed, using ABAQUS, such that it follows the geometry and test procedure used in the experiment. The dimensions and properties of the different components (e.g. box, clamp, and geogrid) were chosen to represent those of the experiment.

Geogrid modeling

The exact geogrid geometry (8 longitudinal ribs and 18 transverse bars) was modeled using 8-noded linear brick elements with 8 integration points as recommended in Chapter 5 (Figure 6-4). The elasto-plastic material model developed for the biaxial geogrid is used throughout this analysis. A non-deformable clamp is introduced at the front end of the geogrid. The clamp is treated as linear elastic material with density of 7850 kg/m³, Poisson's ratio of 0.3, and Young's modulus of 200 GPa. The geogrid is simulated using over 6,430 finite elements as shown in Figure 6-4. It should be noted that the local increase in joint thickness is not considered in the geogrid model in order to simplify the nonlinear contact analysis. This approximation is expected to cause a slight reduction in bearing resistance that would develop at these particular locations.

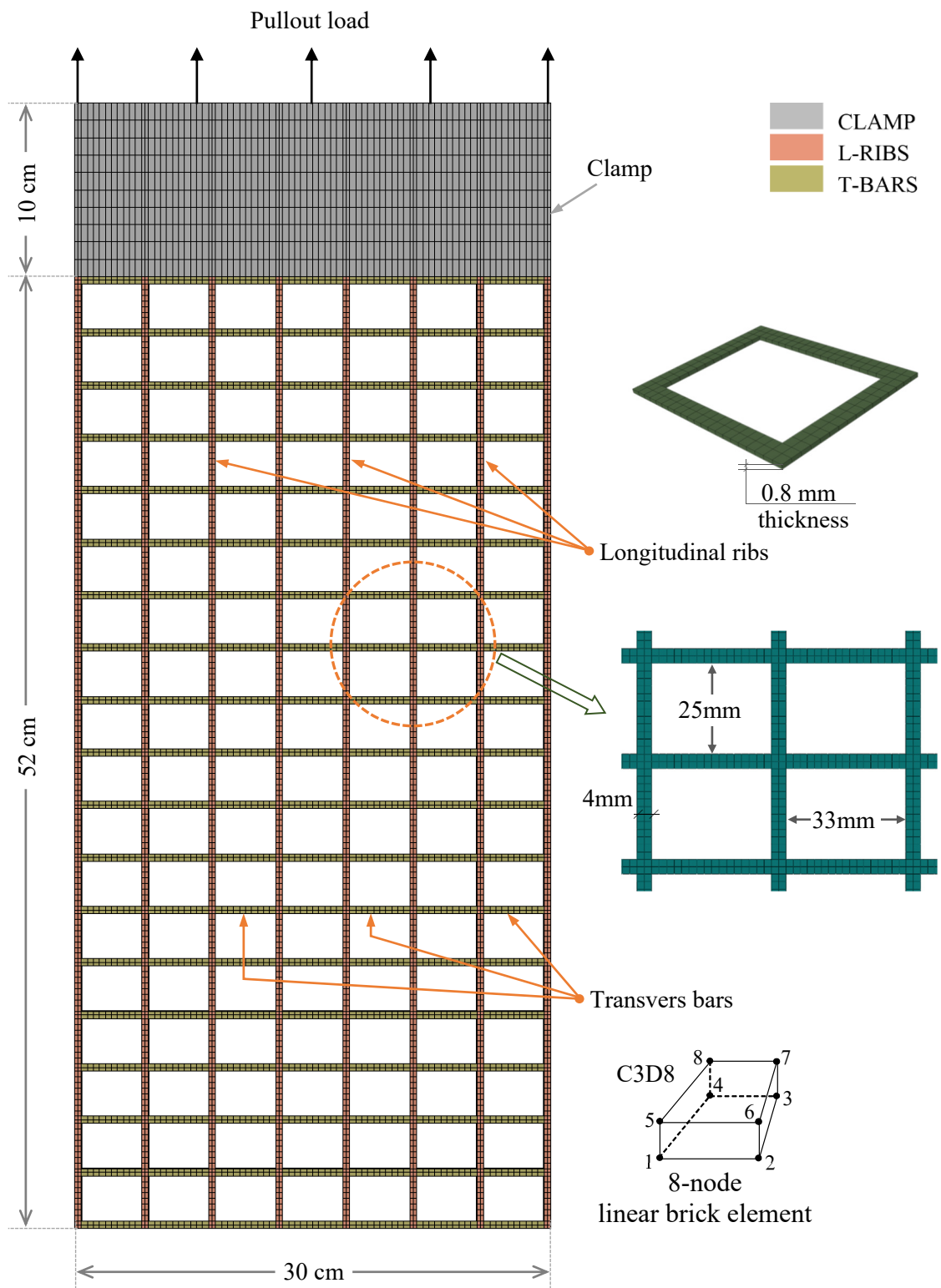


Figure 6-4 Plan view of the geogrid mesh and geometry for the pullout model

Backfill modeling

The sand used in the experiment is modeled using elasto-plastic Mohr-Coulomb failure criteria with none-associated flow rule (Appendix-A) and the soil domain was discretized using 8-nodded linear brick elements (C3D8). The input parameters used in the finite element analysis are summarised in Table (6-1).

Table 6-1 Soil input parameters used in the FE analysis of pullout test

Elastic Modulus E (MPa)	Poisson's ratio ν	Friction angle ^a $\phi^\circ/\phi_{cv}^\circ$	Dilatancy angle ^b ψ°	Cohesion (MPa)
50	0.3	29.9/28	3	1E-05

^a ϕ° = peak friction angle & ϕ_{cv}° = critical state friction angle

^b Determined using Bolton's equation (1986)

Modeling procedure

The model was divided into four main domains as shown in Figure 6-5. The bottom soil domain (BS) was first generated in three stages (around 10 cm each) and the geostatic stress state was established for each stage. Then, the geogrid layer (GEO) was added and the soil elements needed to fill the openings (Soil_{OPN}, with a thickness of 0.8 mm) are introduced in a separate step. Finally, the top soil domain (TS) of around 30 cm in thickness was generated in stages (around 10 cm each) up to the soil surface. The partial view of the 3D mesh is presented in Figure 6-5 with half of the top soil (TS) removed for illustration purposes. It is worth noting that soil elements located above (TS) and below (BS) the geogrid layer can interact directly with each other through the soil elements in the openings (Soil_{OPN}) leading to soil continuity which closely simulates the real behavior of soil-geogrid interaction. This is achieved numerically by merging the three soils domains together, using the meshing *merge* tool in ABAQUS, to form one soil part.

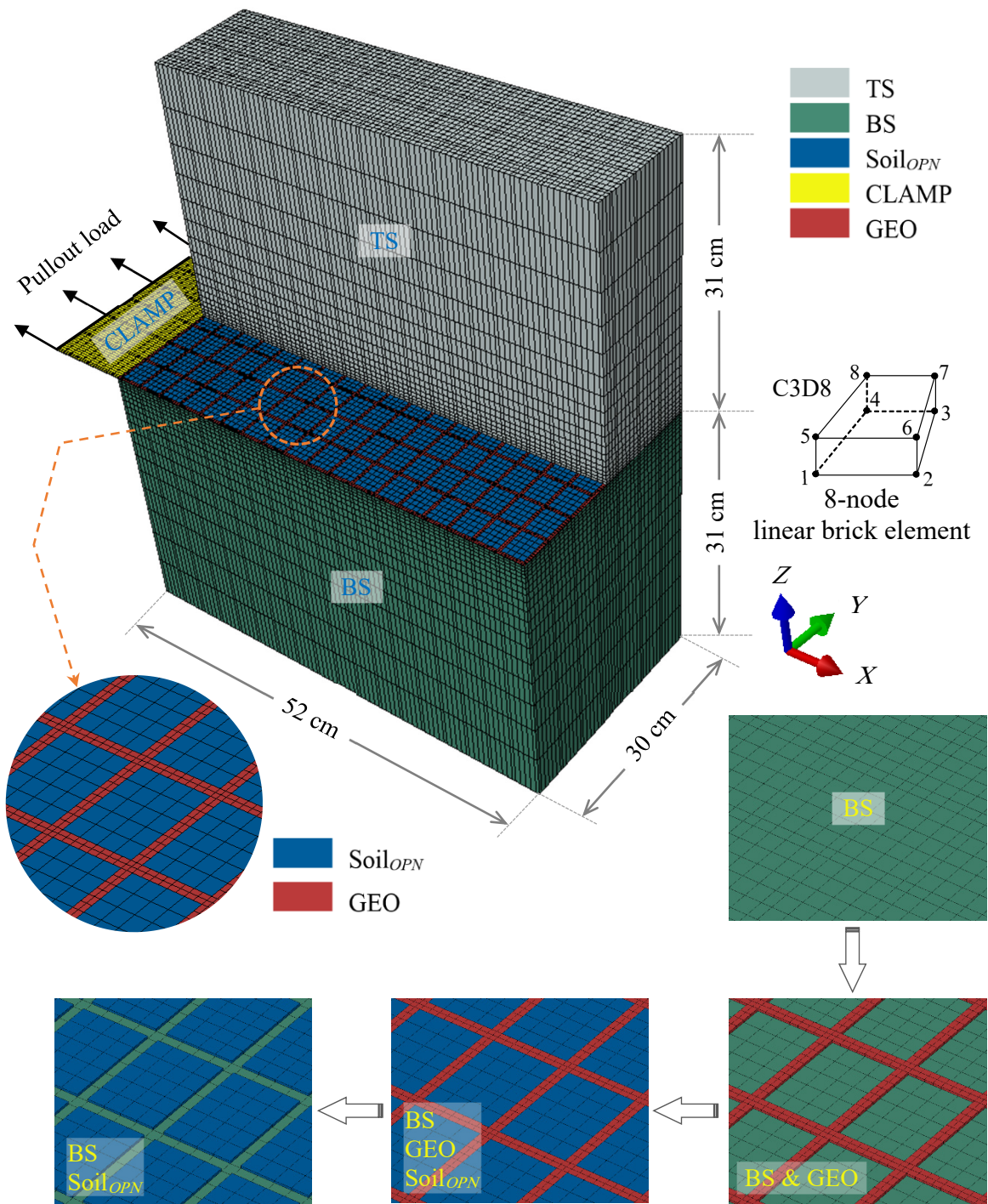


Figure 6-5 Details of the 3D mesh geometry for pullout modeling

Sensitivity analysis was first conducted using different element sizes to determine a suitable mesh refinement that brings a balance between accuracy and computing time. The 3D FE mesh, with over 153,170 elements, is shown in Figure 6-5. The mesh size was adjusted in the vertical direction around the geogrid layer to provide sufficient resolution within the interaction area. Boundary conditions were defined such that the nodes along the vertical boundaries may only translate freely in the vertical direction but are fixed against displacements normal to the boundaries (smooth rigid). Nodes at the base are fixed against displacements in all directions (rough rigid).

6.2.3. Technical details of soil-geogrid interface

The simulation of the soil-geogrid interaction is considered one of the most difficult tasks in this analysis. The test involves large deformations that lead to relative movements between the geogrid and the surrounding backfill. This results in a severe nonlinearity at the contact in addition to the other sources of nonlinearity from the geogrid and soil materials. Moreover, modeling the contact interface in three-dimensional analysis requires special experience and tools to be implemented in the right approach within an acceptable computing time. Figure 6-6 shows the modeling details of the soil-geogrid interaction technique that is used throughout this study. This contact interaction is enforced through the master-slave contact pair technique available in ABAQUS. Additional details are provided in the next section.

Master-slave contact pair

The master-slave contact pair approach is a surface-based contact simulation in which we define surfaces for the bodies that could potentially be in contact throughout the analysis. Then, assign the mechanical contact property models that will control the relationship between the contacting bodies. In doing so, one surface in the contact pair is designated to be the slave surface and the other is the master surface. It is suggested that the body with the finer mesh be treated as the slave and the body with coarser mesh be the master. In the current study, the soil domain above and below the geogrid layer and inside the apertures was the coarser and therefore, the soil is to be taken as the master surface and the geogrid as the slave surface.

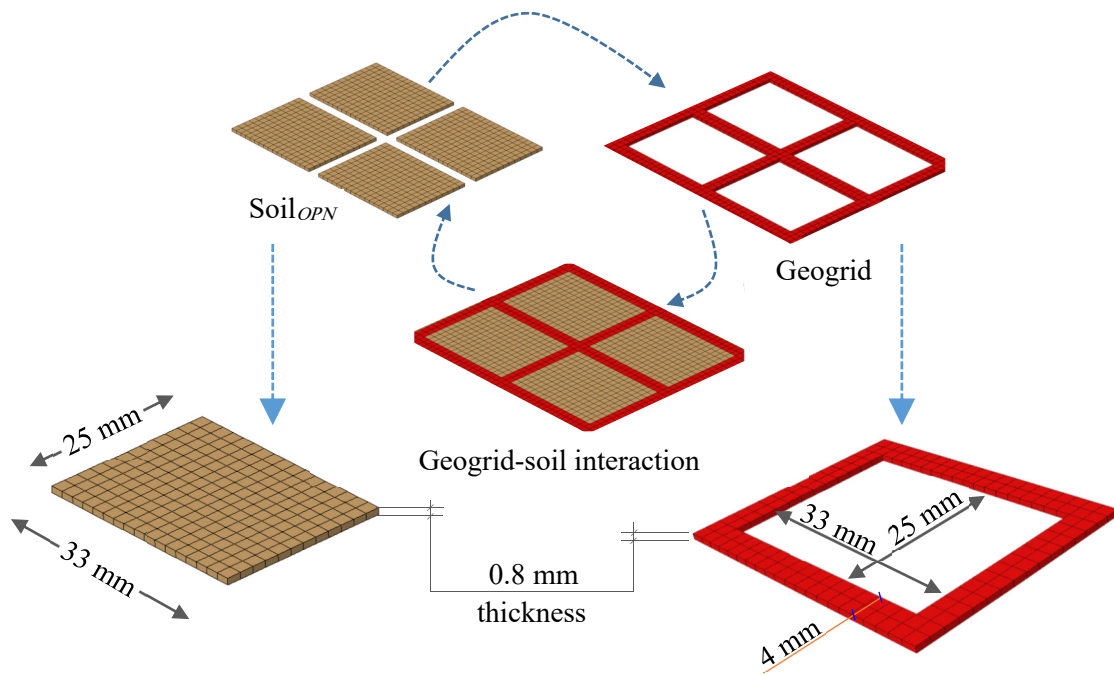


Figure 6-6 Details of soil-geogrid interaction

Contact formulation aspects

To define contact between any pair of surfaces, three main aspects need to be addressed. First, how the contact constraints are formed (discretized); then, how are constraints enforced; and third, how do constraints evolve upon sliding.

a) Contact discretization

ABAQUS offers two types of contact discretization, namely: i) surface-to-surface, and ii) node-to-surface. Figure 6-7 shows a schematic of the difference between the two approaches. In surface-to-surface formulation, the contact condition is enforced in an average sense over regions nearby slave nodes rather than only at individual slave nodes. The averaging regions are approximately centered on slave nodes, so each contact constraint will predominantly consider one slave node but will also consider adjacent slave nodes. This means, each contact constraint is formulated based on an integral over the region surrounding a slave node. On the other hand, in node-to-surface discretization method, each contact condition involves a single slave node and a group of nearby master nodes (master facet).

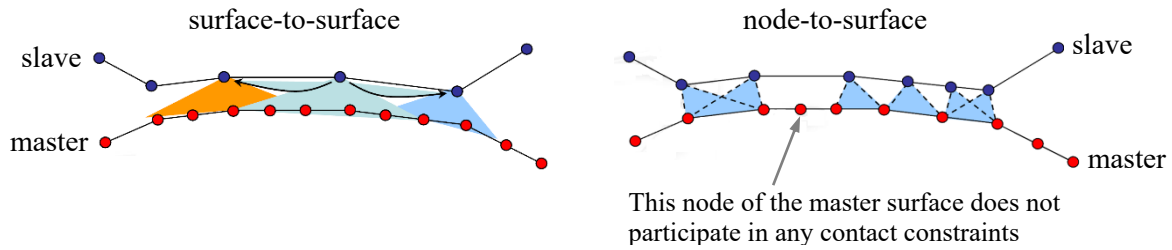


Figure 6-7 surface-to-surface discretization versus node-to-surface discretization

In the current study we chose to simulate soil-geogrid interaction using surface-to-surface contact discretization. The advantage of this approach over the node-to-surface one is that the contact is enforced in an average sense over a region surrounding each slave node. This procedure produced more accurate contact stresses, and resulted in a better convergence of the analysis.

b) Constraints enforcement (contact constitutive models)

When surfaces are in contact they usually transmit shear (tangential) as well as normal forces across their interface. There is generally a relationship between these two force components. In a mechanical contact simulation, the interaction between contacting bodies is defined by assigning a contact property model to a contact interaction. In this study two types of constitutive models are used; namely: i) friction model, and ii) a model for the contact pressure-overclosure (penetration/clearance). The friction model is used to induce frictional stresses to resist sliding, while the contact pressure-overclosure model controls the contact pressure that resists penetration in the normal direction. Both models are used simultaneously for any contact pair involved in the analysis.

Friction model

The friction model defines the force resisting the relative tangential motions of the contacting surfaces. In ABAQUS, there are many options available to describe the stick/slip discontinuity (frictional behavior) condition in the tangential direction. Among these options is the Coulomb friction model with normal stress dependent friction coefficient. The current

study employed this model to simulate the frictional resistance between the soil and the geogrid.

Coulomb friction model

The basic concept of the Coulomb friction model is that every two contacting surfaces can carry shear stresses up to a certain magnitude ($\tau_{critical}$) across their interface before they start sliding relative to one another; this state is known as sticking (Figure 6-8). This model obeys the Mohr-Coulomb failure criterion:

$$\tau_{critical} = c + \sigma_n \tan \delta \quad (6.2)$$

where $\tau_{critical}$ is the shear strength at which the slip occurs for the first time, c is the apparent cohesion, σ_n is the normal stress, and δ is the interface friction angle at the yield/critical state.

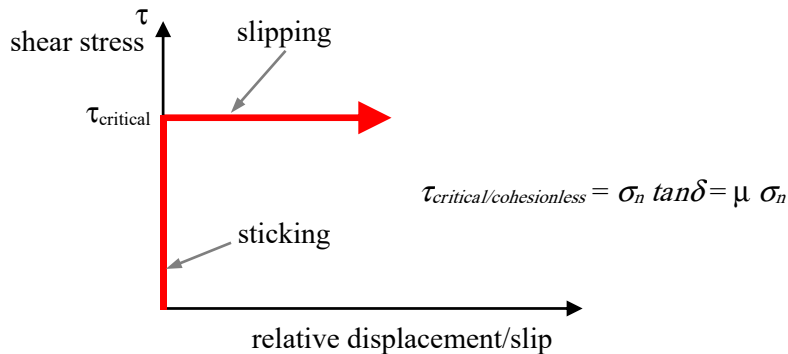


Figure 6-8 Coulomb friction model in its basic form

The interface friction angle (δ) between the sand and the geogrid can be obtained through a direct shear test as shown in Figure 6-9. Hence, the friction interface coefficient ($f_{ds} = \frac{\tan \delta}{\tan \phi}$) can be calculated knowing the values of δ and the sand friction angle (ϕ). Also, the value of the coefficient of friction can be determined ($\mu_{sand/geogrid} = \tan \delta$).

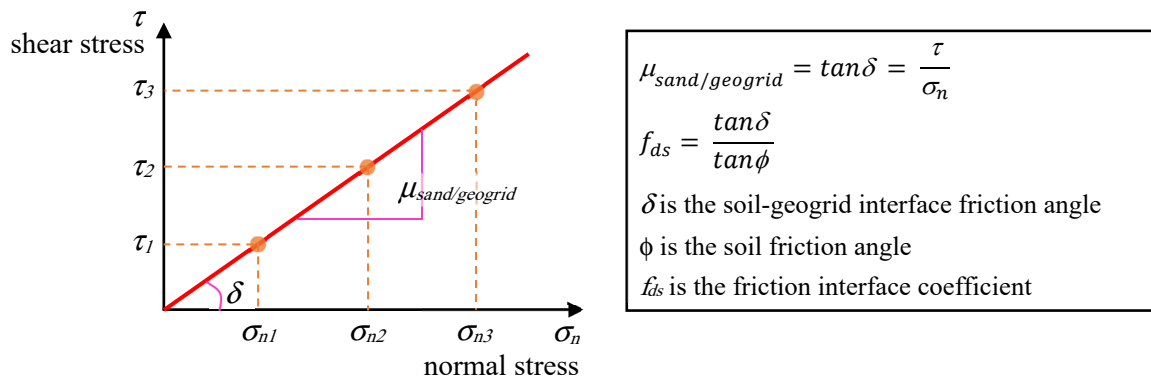


Figure 6-9 Parameters of direct shear test on soil-geogrid interface

In ABAQUS Coulomb friction model, the sticking constraints at an interface (Figure 6-8) can be enforced by using the Lagrange multiplier contact algorithm. With this method there is no relative motion between two closed surfaces until ($\tau = \tau_{critical}$). However, the Lagrange multipliers increase the computational cost of the analysis by adding more degrees of freedom to the model and often by increasing the number of iterations required to obtain a converged solution. On the other hand, the penalty function method (stiffness method) is also available in the Coulomb friction model and is used in the current study. As shown in Figure 6-10, the penalty contact algorithm introduces a softer constraint through a penalty parameter (tangential/shear stiffness, k_s) that relates the frictional forces to slip displacement. The method permits some relative motion of the surfaces (an elastic slip) when they should be sticking. While the surfaces are sticking (i.e., $\tau < \tau_{critical}$), the magnitude of sliding is limited to this elastic slip (E_{slip}). Within this elastic stick condition, if the tangential load is removed, the body returns to its original state. The advantage of using the penalty function method is that it is easy to implement, and does not require solving a nonlinear system of equations in every time step.

The Coulomb friction model used in the current study, in its simplest form, contains two material properties, a friction coefficient (μ), and a tolerance parameter to calculate the elastic slip (E_{slip}). Previous research recommends a 0.9 to 1.0 frictional interface coefficient (f_{ds}) between the geogrid and the sandy soil (Lopes et al., 2001, Liu et al., 2009). In the current

analysis we chose a value of 0.9 that corresponds to a coefficient of friction (μ) equal to 0.51, knowing that the friction angle (ϕ) of the modeling backfill is 29.9°.

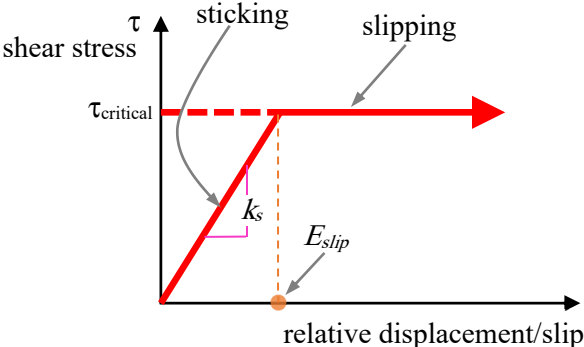
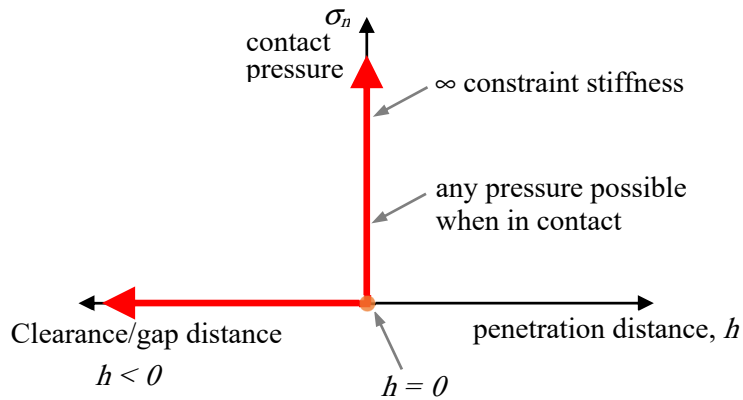


Figure 6-10 Coulomb friction model using the penalty contact algorithm

Contact pressure-overclosure model

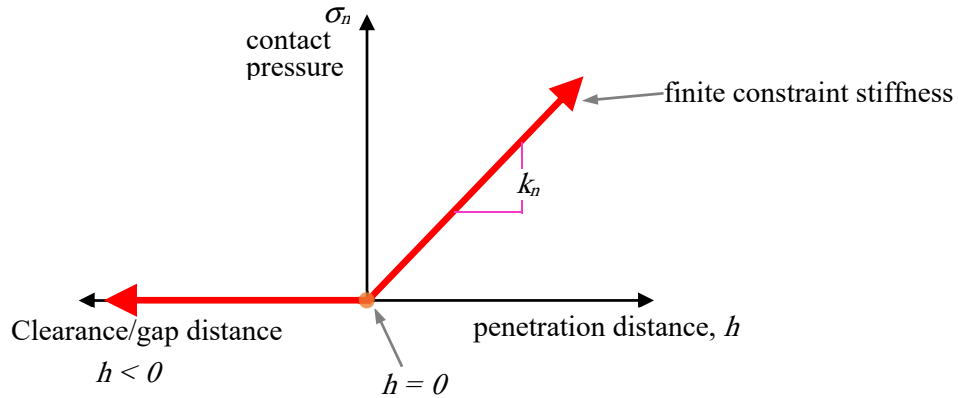
The contact pressure-overclosure model is used to control the contact pressure that resists penetration. Open/closed discontinuity in the normal direction is similar to the stick/slip discontinuity in the friction model. In ABAQUS there are several models available to describe the contact behavior in the normal direction (contact-pressure overclosure) of two contacting surfaces. Figure 6-11 illustrates the most common models used to simulate the contact pressure-overclosure relationship; the hard contact and the softened contact models.

In the current study both models were simultaneously used at several locations on the soil-geogrid interface, this will be explained in the sections to come. Constraints in the hard contact model that is described in Figure 6-11 a and used in the numerical analysis is enforced using the augmented Lagrange method. In this model, no contact pressure occurs until nodes are in contact ($h = 0$), and once the contact has been established between the contacting surfaces, unlimited contact pressure can be transmitted between them. The surfaces start to separate ($h < 0$) if the contact pressure reduces to zero (or if the normal stress becomes tensile) and they can come into contact again when the clearance between them reduces to zero.



a) Hard contact model

(constraints enforced with Lagrange multiplier method in the normal direction)



b) Linear softened contact model

(constraints enforced with the penalty method in the normal direction)

Figure 6-11 Contact behavior in the normal direction

Linear softened contact model is also used in the current analysis to enforce the contact in the normal direction using the penalty stiffness method. This model describes a contact pressure-overclosure relationship in which the contact pressure is a linear function of the penetration between the surfaces. The surfaces transmit contact pressure when the overclosure/penetration between them, measured in the contact (normal direction), is greater than zero. As seen in Figure 6-11b, the slope of this contact pressure-overclosure relationship describes a constant penalty stiffness parameter (normal/contact stiffness, k_n) in the normal direction. The surfaces start to separate ($h < 0$) if the contact pressure reduces to zero or if the normal stress is tensile. The softened contact model is preferred in cases of large

penetration as it makes it easier to resolve the contact condition. In addition, the numerical softening associated with the penalty method can mitigate the overconstraint issues, reduce the number of iterations required in the analysis, and improve convergence.

Following the above discussion, it is evident that the hard contact model will be used in the analysis at particular locations on the soil-geogrid interface where the penetration in the normal direction is prevented, whereas the linear softened contact model with a specific contact stiffness value is being used when the penetration is allowed in the normal direction (e.g. the contact pressure developed on the transverse bars during the pullout step while penetration of the geogrid into the soil is allowed in the direction of the pullout load). This will be further described in the next section.

a) Evolution of surface contact

There are two tracking approaches available in ABAQUS to account for the relative motion of two interacting surfaces in mechanical contact simulations. The first is a rigorous, nonlinear evolution, (finite-sliding), while the other is an approximate formulation (small-sliding).

Small-sliding contact assumes that there will be relatively *little* sliding of one surface along the other and is based on linearized approximations of the master surface per constraint. Although the approach contains less nonlinearity, and is intended to reduce the solution cost per iteration and finding a converged solution in fewer iterations, the method has a very limited applicability. This is due to the assumption that the relative tangential motion should remain small.

Finite-sliding contact, on the other hand, is the most general tracking approach and allows for arbitrary relative separation, sliding, and rotation of the contacting surfaces. It includes nonlinear geometric effects that can help in simulations that involve large deformations and large rotations. The problem investigated in the current study involves large deformation and therefore the finite-sliding tracking formulation is more suitable for the analysis.

Assignment of contact models in the numerical analysis

When two bodies are in contact, normal as well as shear forces develop on the interface between the contacting bodies. The formulation used to describe the tangential and normal behavior at this interface should include separate constitutive models to simulate the two behaviors simultaneously. This means that the contact formulation is detecting any two bodies that may come into contact at any time during the course of the analysis and apply the constitutive models in the normal and the tangential directions on each interface. Based on this hypothesis, the current model incorporates two interface conditions (Figure 6-12):

HZ soil-to-geogrid interface; this interface condition defines the contact between the horizontal geogrid surfaces — on the longitudinal ribs and transverse bars — and the horizontal surfaces of the top and bottom soils that will be in direct contact with geogrid plane surfaces (Figure 6-12a). During pullout loading, the applied vertical stresses ($\sigma_v = 49$ kPa) will cause normal/contact pressure along the horizontal interfaces. At the same time, the pullout loading creates shear stresses along the same interface. Coulomb friction model with a penalty contact algorithm (Figure 6-10) will be used to simulate the frictional behavior along the interface using a friction coefficient (μ) value of 0.51. In addition, and on the same interface, a *hard* contact model (Figure 6-11a) is imposed to simulate the contact pressure on the normal direction. The *hard* contact is selected on this interface to prevent any penetration between the soil and the geogrid surface area and maintain the geogrid in its vertical place during the pullout loading step.

The frictional resistance on this HZ soil-geogrid interface, which is dependent on the contact pressure on the same interface, is considered the frictional component of the total pullout capacity of the analyzed model.

VL soil-to-geogrid interface; this interface condition defines the contact between the vertical surfaces within the geogrid apertures — on the longitudinal ribs and transverse bars — and the vertical sides of the soil (Soil_{OPN}) elements that are used to fill the geogrid apertures (Figure 6-12b).

As mentioned previously, the contact formulation on each interface will be simulated with frictional and normal contact constitutive models. Within the geogrid apertures there are two vertical interface conditions (Figure 6-12b) namely: i) VL interface on the surfaces of the longitudinal ribs, and ii) VL interface on the surfaces of the transverse bars.

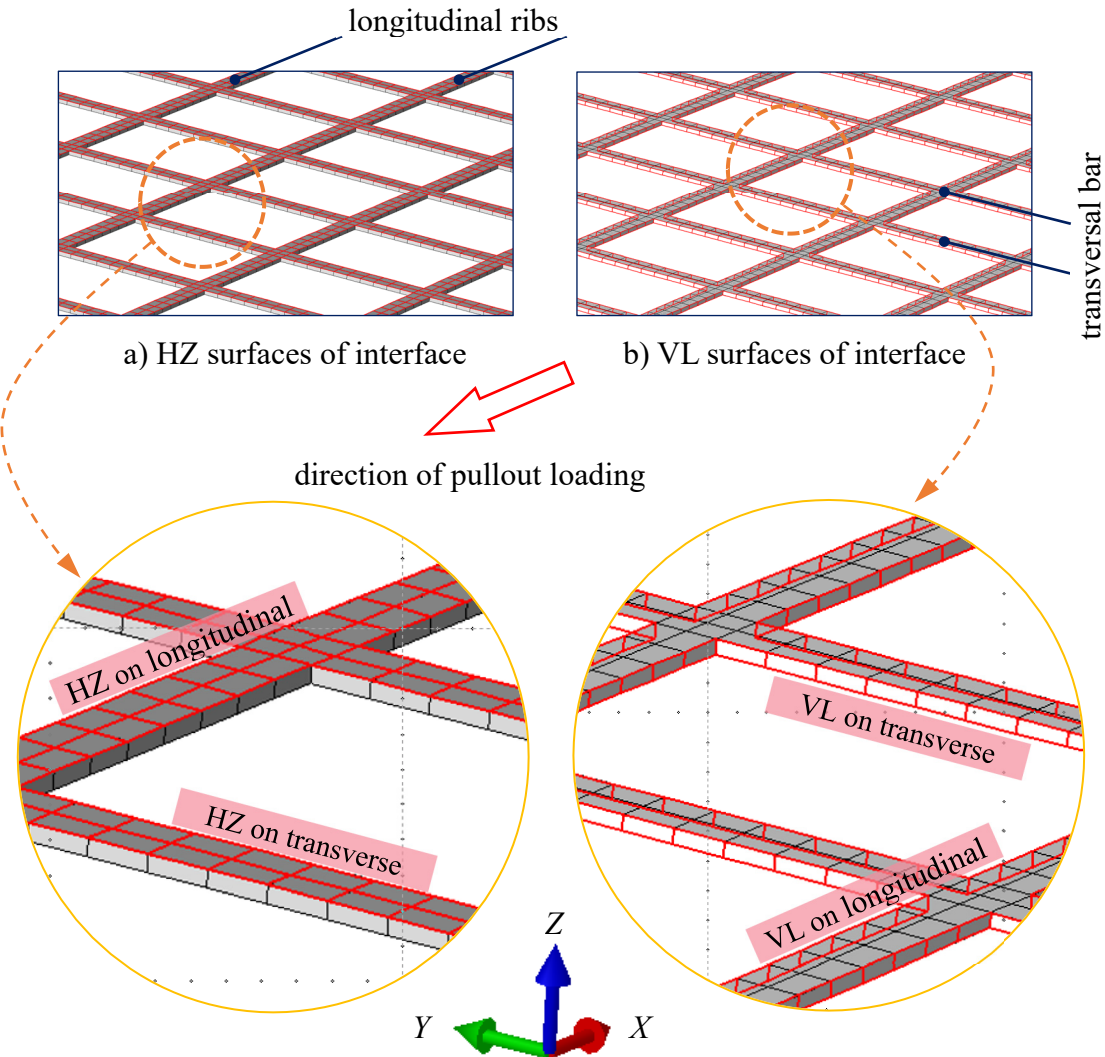


Figure 6-12 Horizontal and vertical interface conditions

For the vertical interface on the longitudinal ribs, the frictional resistance is the dominating contact interaction that will contribute to the pullout loading resistance. This friction is simulated using the Coulomb friction model similar to the friction on the horizontal surfaces of the same longitudinal elements ($\mu = 0.51$). However, contact pressure on the same longitudinal vertical surfaces is modeled using the hard contact model to describe the confinement of the geogrid in the Y - Y direction that develops due to the soil interlocking within the geogrid aperture.

The vertical interface on the transverse bars is very important resistance component. Similar to the previous surfaces, the tangential behavior on these elements will be described using the Coulomb friction model with 0.51 coefficient of friction and penalty stiffness method. On the other hand, the contact pressure developing on this VL soil-geogrid interfaces is important and should be accurately predicted as it is considered the bearing resistance component of the total pullout capacity of the analyzed model. The details of the description of this contact pressures on the transverse bars are discussed below.

The contact pressure developing on the transverse bars is the only normal behavior in this analysis that is described using the softened contact pressure-overclosure model. As explained before, when the pullout load is applied, frictional resistance as well as bearing resistance will be mobilized along the interface between the soil and the geogrid. During pullout loading, the geogrid slides on the horizontal interfaces between the soil and the geogrid and frictional stresses are mobilized through the Coulomb friction model to resist such slippage. In addition, under pullout loading condition, the geogrid penetrates the soil and as a result, contact pressures develop on the vertical surfaces of the transverse bars to resist such penetration. Since the test includes large deformation (around 25mm applied displacement at the geogrid front end), the soft contact pressure-overclosure model is considered suitable and used to simulate the contact pressure on the transverse bars. Using this model requires the definition of the contact stiffness (k_n) value which relates the contact pressure on the transverse bar to the penetration distance into the soil. This parameter has to be calculated using the relative stiffness between the two contacting bodies. A large value of contact stiffness can reduce penetration but can also cause convergence problems. Therefore,

a proper value of contact stiffness must be determined based on the allowable penetration, which requires user's experience. Most of the FE programs recommend to start with a small initial k_n value that can be gradually increased until a reasonable penetration is achieved.

In the current study, the propagation of the geogrid penetration into the soil is carefully investigated considering the experimental results. Understanding the geogrid penetration during pullout will help in selecting a proper k_n value that can be used to simulate the behavior of the transverse bars in the normal direction. More details are provided in the validation section (6.3.1).

The current analysis involves a total of 1,012 surfaces that are in contact with each other. This forms 506 contact pairs to be defined in the 3D model. They are generated using the *automatic contact detection* tool available in ABAQUS, and optimized according to the required configurations.

6.2.4. Pullout test modeling

After the FE model was built, the vertical stress ($\sigma_v = 49$ kPa) is applied above and below the soil sample at the same time to maintain the geogrid layer at its place in the vertical direction. This procedure is achieved numerically by applying a surface pressure using an instantaneous loading amplitude. Figure 6-13 shows the displacement field of the model after the application of vertical stress ($\sigma_v = 49$ kPa) at the top and bottom surfaces of the soil. It could be seen that the deformations values are decreased from the top and the bottom to reach zero value at the mid height of the box where the geogrid layer is located. It should be highlighted that the vertical stress is kept constant and propagated through the next steps of the analysis.

Following the above step, the pullout load is introduced using a velocity control approach. Lateral velocity was applied to the clamp in 10 steps (2.5 mm each), using the same rate used in the experiment (1 mm/min), to achieve a total frontal displacement (U_x) of 25 mm. Based on past experience, the velocity control scheme improves the convergence of the analysis. It is worth noting that each pullout increment (step) was applied in 150 seconds with a velocity

of 1.66×10^{-5} m/sec (1mm/min loading rate) to complete a total of 2.5 mm/step ($U_x = V_x * \text{time} = 1.66 \times 10^{-5} * 150 = 0.0025\text{m}$ or 2.5mm).

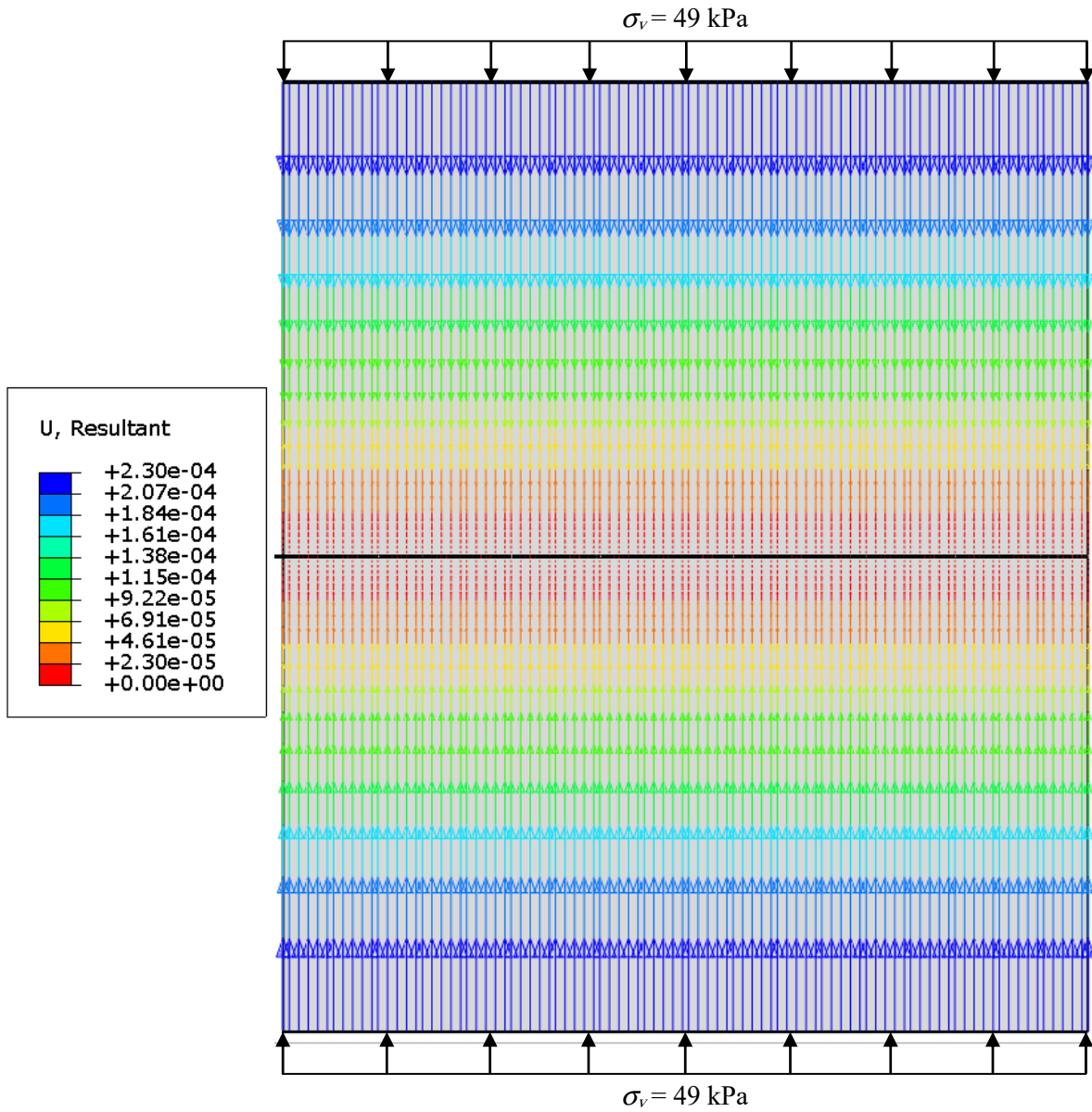


Figure 6-13 Displacement field of the soil and the geogrid layer at ($\sigma_v = 49 \text{ kPa}$)

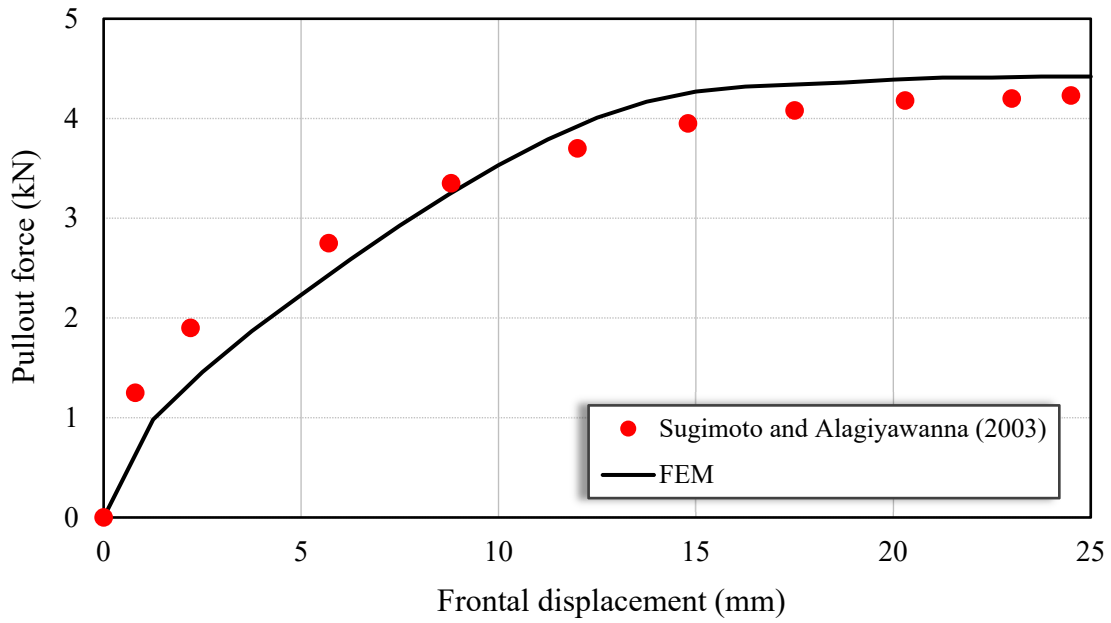
6.3. Results and Discussions

6.3.1. Validation of the numerical model

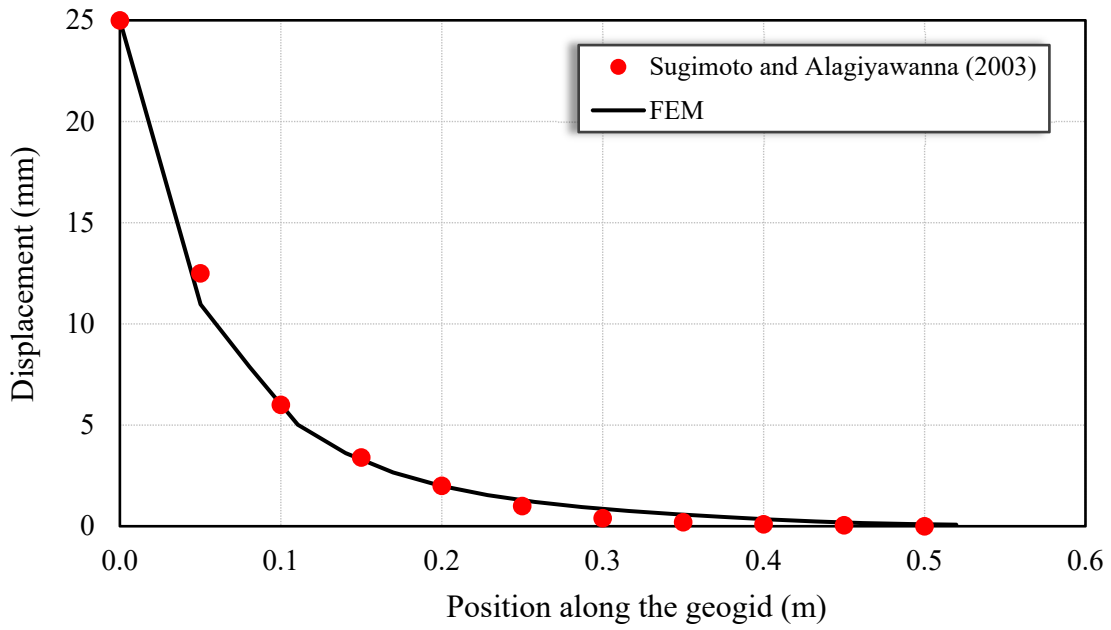
To validate the proposed model, the FE results are compared with the experimental data (Figure 6-14). Figure 6-14a shows the relationship between the pullout force and the frontal displacement obtained from both the experimental and numerical models. The numerical results generally agreed with the experimental data except for low displacement values of less than 5 mm. This is expected because of the simplification made in modeling the geogrid junction's thickness that may lead to underestimating the interaction between soil and the geogrid particularly at the early stages of the test.

To ensure that the numerical model performs well at the frontal face as well as at any other location along the geogrid length, Figure 6.14b shows a comparison between the calculated and measured displacements along the geogrid. Geogrid displacements generally decrease with distance from the face up to about the middle of the geogrid. Then, very small displacements were calculated outside this region. The figure also confirms the agreement between the experimental and numerical results calculated using the proposed modeling approach.

By examining the displacement reduction along the geogrid (Fig. 6-14b), it can be seen that the rate of change in displacement is not constant. To match the experimental results, a series of finite element analyses was conducted using variable k_n value with distance along the geogrid. The results shown in Figure 6-15 illustrates the different k_n values that control the penetration at each transverse bar on the geogrid. It could be seen from the figure that five contact stiffness values have been used at different locations. In contrast to the displacement distributions, the contact stiffness increases with distance from the face (where the pullout load is applied) indicating a stiffer response of the soil-geogrid system inside the box.



a) Pullout load-frontal displacement relationship



b) Horizontal displacement along the geogrid

Figure 6-14 Pullout response of the geogrid ($\sigma_v = 49$ kPa)

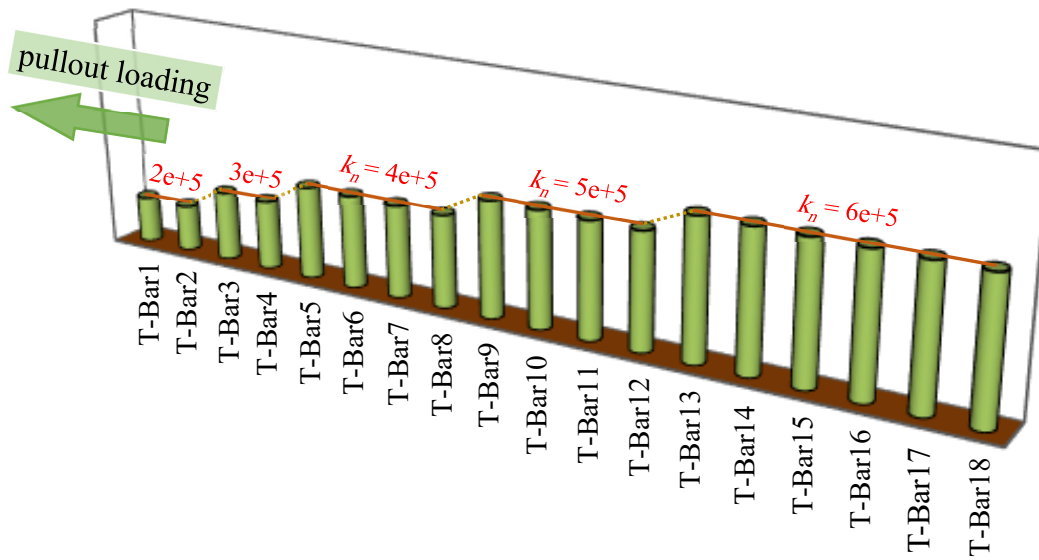
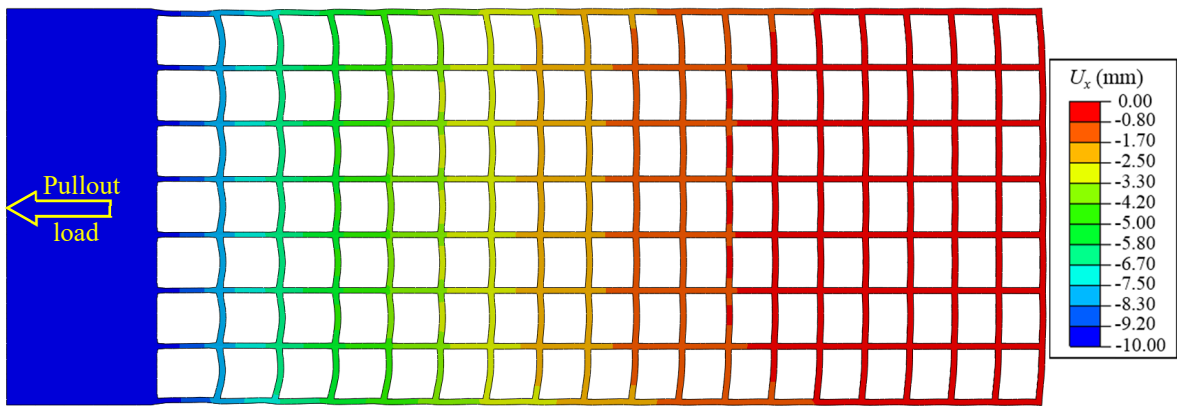


Figure 6-15 Changes of k_n values on the transverse bars along the geogrid

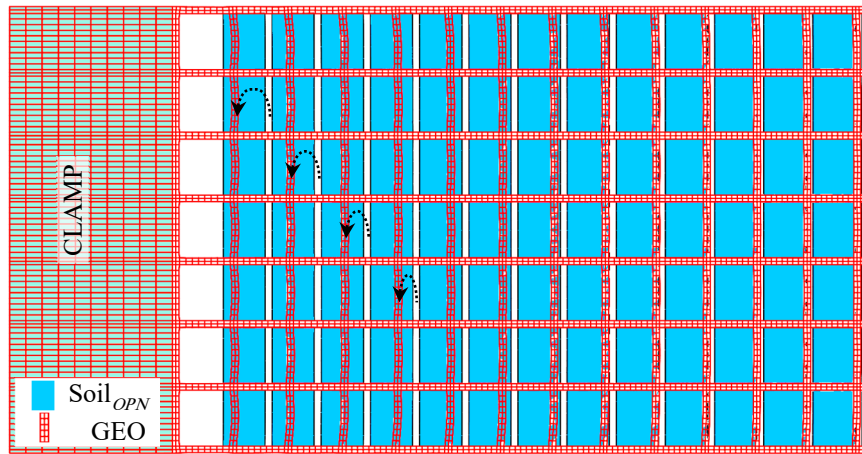
6.3.2. Response of the geogrid

The deformed shape of the geogrid for a frontal displacement (U_x) of 10 mm and a vertical pressure (σ_v) of 49 kPa is shown in Figure 6-16a. The largest deformation of the geogrid is found to occur in the vicinity of the applied load and rapidly decreases with distance toward the rear side of the box. The longitudinal elements of the geogrid experienced deformation in its axial direction with the largest elongation occurring near the loading side. It should be noted that part of the geogrid that is connected to the loading clamp becomes unconfined right after the load application which results in a softer behavior and larger elongation in that region. Transverse members, on the other hand, showed a considerable bending deformation particularly near the loaded side. This bending behavior originates from the frictional forces acting at the upper and lower surfaces of the transverse bars as well as the bearing forces acting to resist the geogrid penetration into the soil. Figure 6-16b shows two more patterns that describe the geogrid penetration into the soil within the apertures ($Soil_{OPN}$). The transverse bars left its original locations and moved in the pullout loading direction. The stress distribution within the geogrid is shown in Figure 6-17. In consistency with the displacement pattern, the stresses S_{xx} were highest near the front side and decreases with distance along the geogrid length. It can be also realized that stresses in the longitudinal

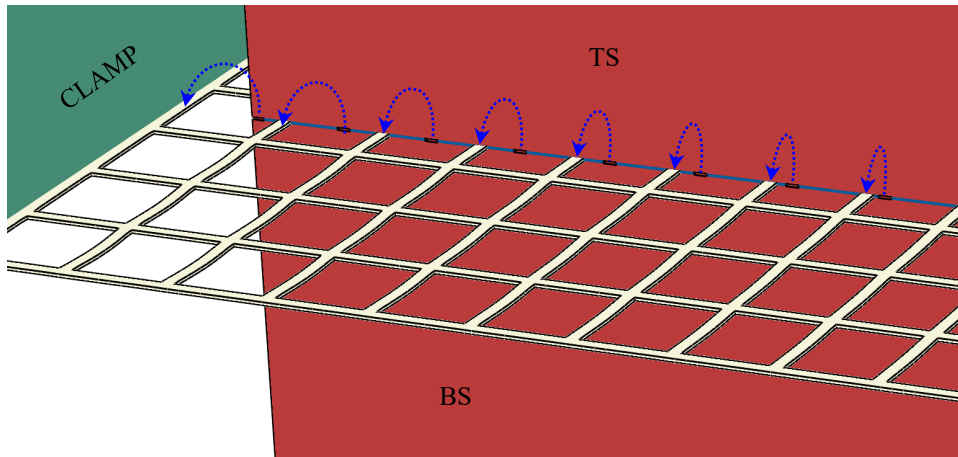
members are much larger compared to the transverse ones. The same behavior has been noticed in previous research by the authors when testing this biaxial geogrid under unconfined tensile loading.



a) Geogrid deformed shape and displacement at $U_x = 10$ mm and $\sigma_v = 49$ kPa



Geogrid versus Soil_{OPN}



Geogrid versus TS and BS

b) Relative movements between geogrid and the backfill soil

Figure 6-16 Geogrid deformation and relative movements

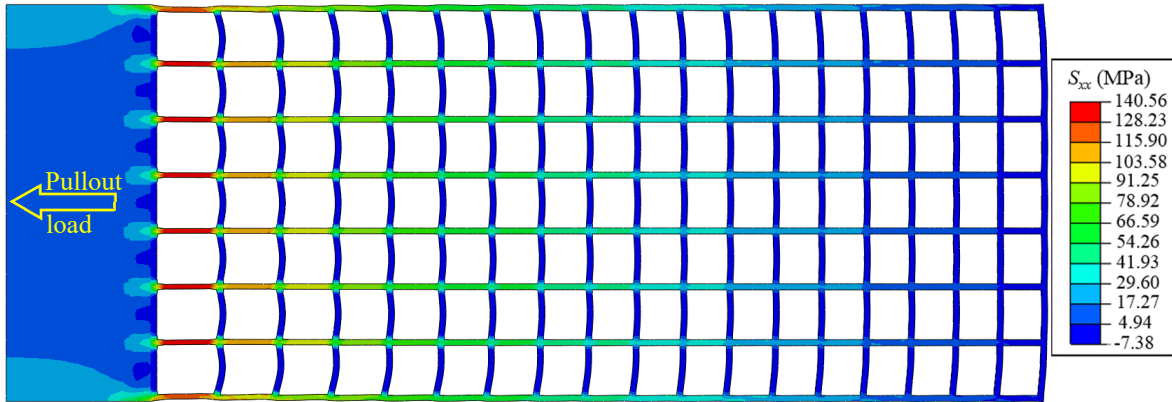


Figure 6-17 Geogrid stresses S_{xx} at $U_x = 10$ mm and $\sigma_v = 49$ kPa

The tensile force distributions in the longitudinal members for different frontal displacements are illustrated in Figure 6-18. At a given location along the geogrid, the average tensile force (T_{xx}) in all longitudinal members was found to increase with the increase in frontal displacements. For the illustrated range of frontal displacements, the force T_{xx} was large near the front side and rapidly decreased toward the middle of the geogrid. Beyond the middle zone, T_{xx} became negligible due to the insignificant displacement experienced by the rest of the geogrid.

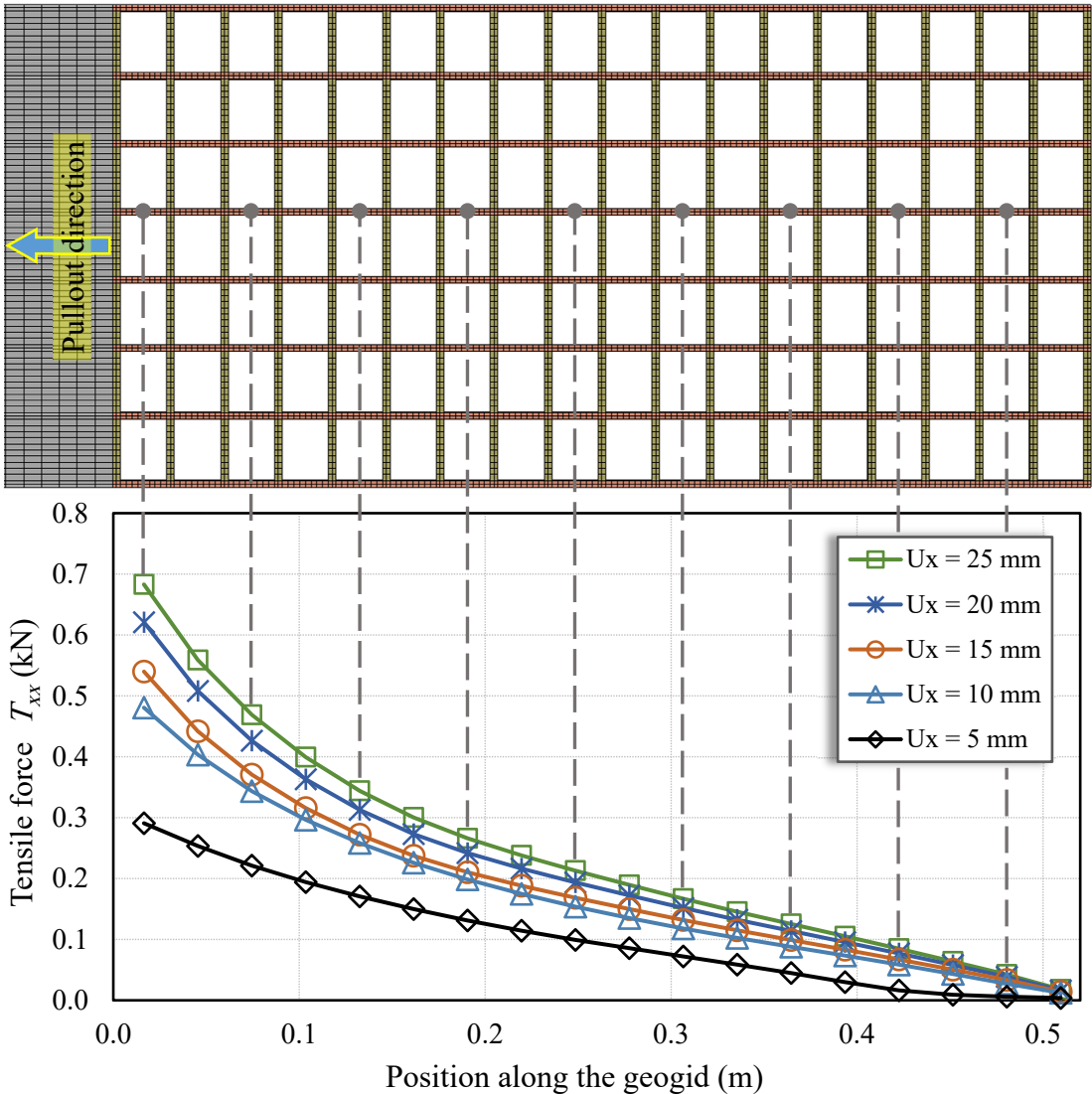


Figure 6-18 Average tensile force T_{xx} in the longitudinal members ($\sigma_v = 49$ kPa)

6.3.3. Contributions of bearing and frictional resistances

The used geogrid comprises longitudinal and transverse members as well as junctions connecting these members. Each of these components contributes to the total pullout force. Since the resistance of the junctions in this study is numerically included in the frictional resistance of the geogrid, the total pullout resistance F_{pull} can be written as:

$$F_{pull} = F_{friction} + F_{bearing} \quad (6.3)$$

where: $F_{friction}$ is the frictional resistance component arising on the geogrid surface, $F_{bearing}$ is the bearing resistance of the transverse members.

To understand the contribution of the bearing and frictional resistances individually, researchers usually test the geogrid in the laboratory with and without the transverse bars by removing the bars that are responsible to develop the bearing components (e.g. Alagiyawanna et al., 2001). Similarly, other researchers followed the same procedure in the numerical analysis (e.g. Wang et al., 2016). This technique is not recommended by the authors as removing the transverse bars will result in both the frictional and passive bearing resistances being eliminated.

To assess the contribution of the bearing component in the current study, the transverse bars are kept with its frictional resistance as in the original geometry, however, k_n (contact stiffness) parameter that controls the bearing resistance is reduced. By reducing the k_n value, in the normal direction (on the VL surfaces of the transverse bars) to a value of zero, the bearing resistance developing on this member will diminish. This technique will eliminate the bearing resistance only from the transverse bars however the effect of the frictional resistance on the HZ surfaces of the transverse bars remains the same. Since a value of $k_n = 0.00$ is not accepted for numerical stabilities, a value of $k_n = 0.0001$ was selected in the current study.

To understand the cumulative contributions of the 18 transverse bars toward the total pullout resistance, a specific procedure was carried out to achieve this objective. This procedure includes 6 steps that have been implemented using 6 separate analyses. In each step, the

bearing resistance component is removed (k_n is set to 0.0001) for a group of three transverse bars along the geogrid. This procedure is illustrated in Figure 6-19.

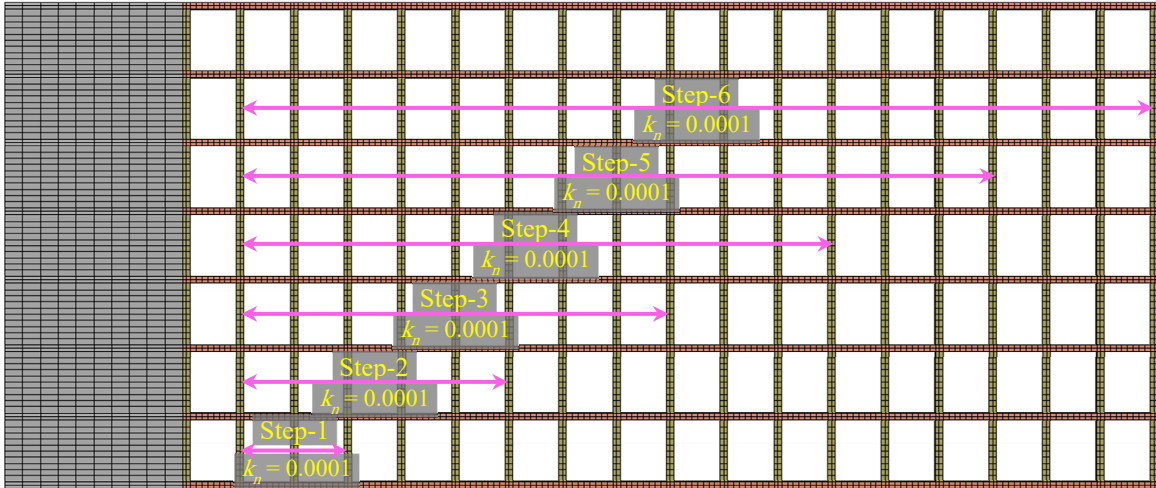
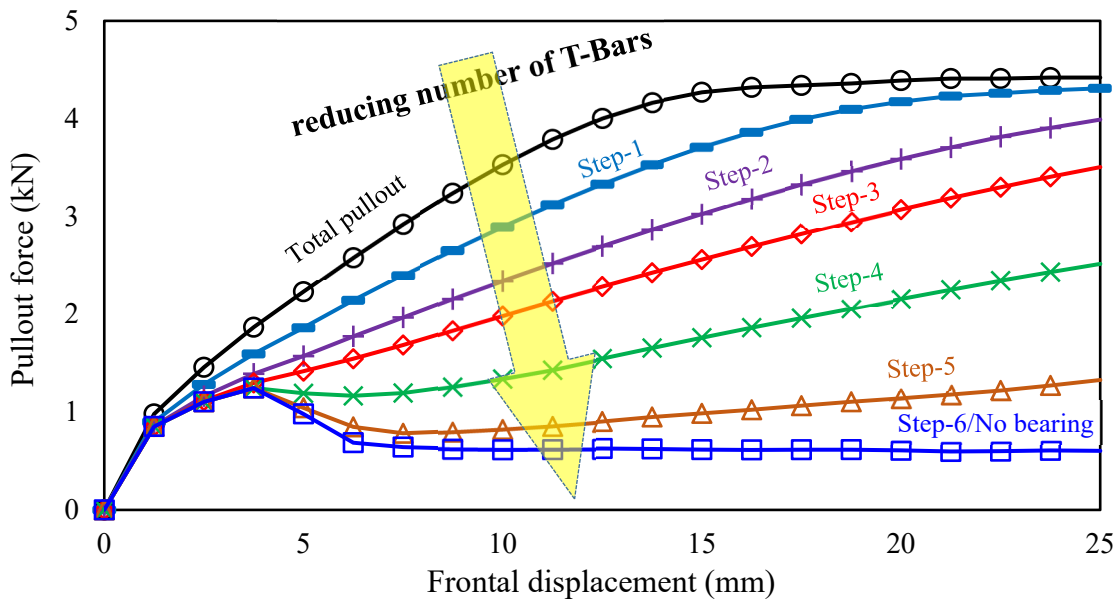


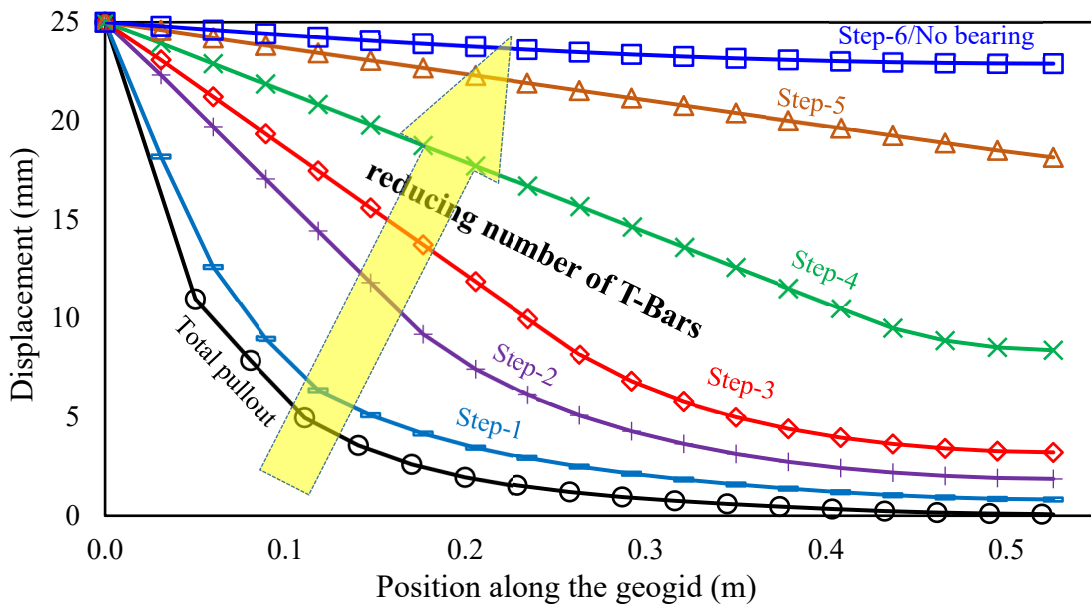
Figure 6-19 Procedure to assess the accumulative contributions of the bearing members

The bearing resistances on the transverse bars are determined numerically using the previous procedure and the cumulative contribution to the total pullout force is presented in Figure 6-20. It is evident that increasing the numbers of transverse members incrementally in 6 equal steps (from 0 at step-1 to 18 members at step-6) increases the total pullout load and decreases the relative movement of the geogrid.

Comparing the results of the original condition and the results of step-6 where no bearing members contribute to the total pullout force allows one to calculate the frictional resistance component. The separate contributions to the total pullout resistance is shown in Figure 6-21. It can be seen that the contribution of the frictional resistance is less than that of the bearing resistance leading to bearing component ($F_{bearing}$) dominating the pullout resistance F_{pull} . The frictional component contributed about 28 % of the total pullout load. Similar observations were made by previous researchers confirming that, in this class of problems, bearing resistance component is larger than frictional component (e.g. Milligan and Palmeira, 1987, Bergado and Jin-Chun, 1994, Lopes and Lopes, 1999).



(a)



(b)

Figure 6-20 Cumulative contribution of the bearing members to the total pullout resistance

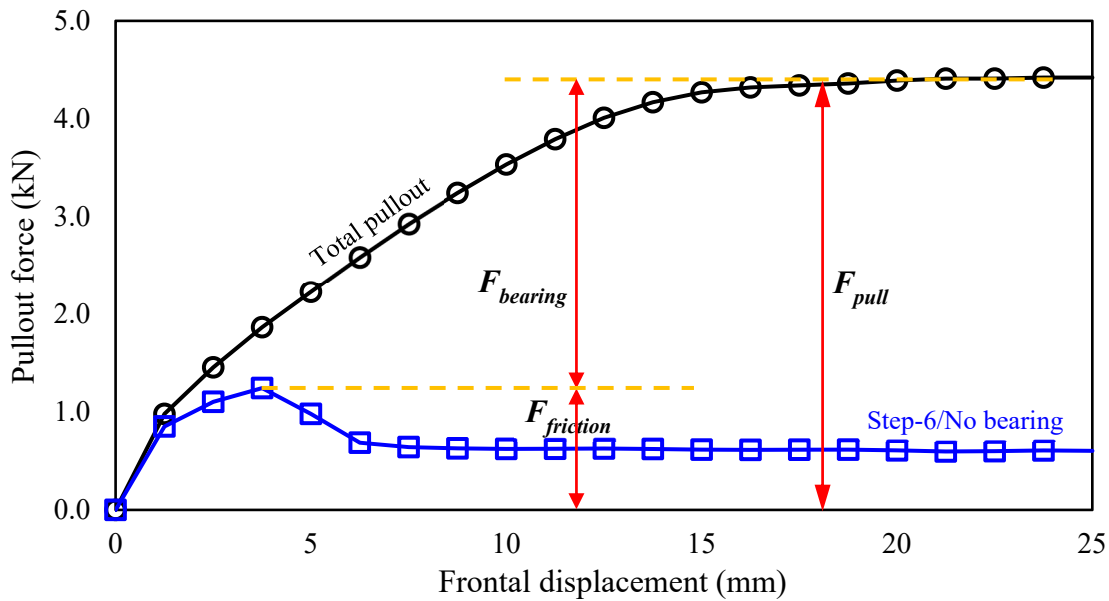


Figure 6-21 Components of the pullout resistance ($\sigma_v = 49\text{kPa}$)

Figure 6-22 shows the relationship between the bearing resistance and the frontal displacement up to $U_x = 10\text{mm}$ at different locations along the geogrid. Contact pressure on the transverse bars is found to increase with increasing the applied displacement. Also, contact pressure is found to be maximum near the location of the applied load and decreases gradually with distance at different transverse members. It should be highlighted that only selected bars are presented in this figure however the same trend applies to all the transverse members.

The accumulated contribution of different transverse members ($T_{bearing/member}$) with respect to the total bearing resistance ($T_{bearing}$) is shown in Figure 6-23. In the original condition (Figure 6-23a), transverse members contribute to the bearing resistance and the members located within the middle of the geogrid (at about 0.27m) measured from the front side contribute about 90% of the total bearing resistance. In general, the first transverse member (counted from the loaded end) contributes the largest bearing resistance and the contributions of transverse members decrease with distance from the loaded side. When bearing members are progressively eliminated with distances along the geogrid (Figures 6-23b, c, and d), the

remaining transverse members will start resisting the penetration from the first effective transverse bar which has been found to carry around 20% of the total bearing resistance.

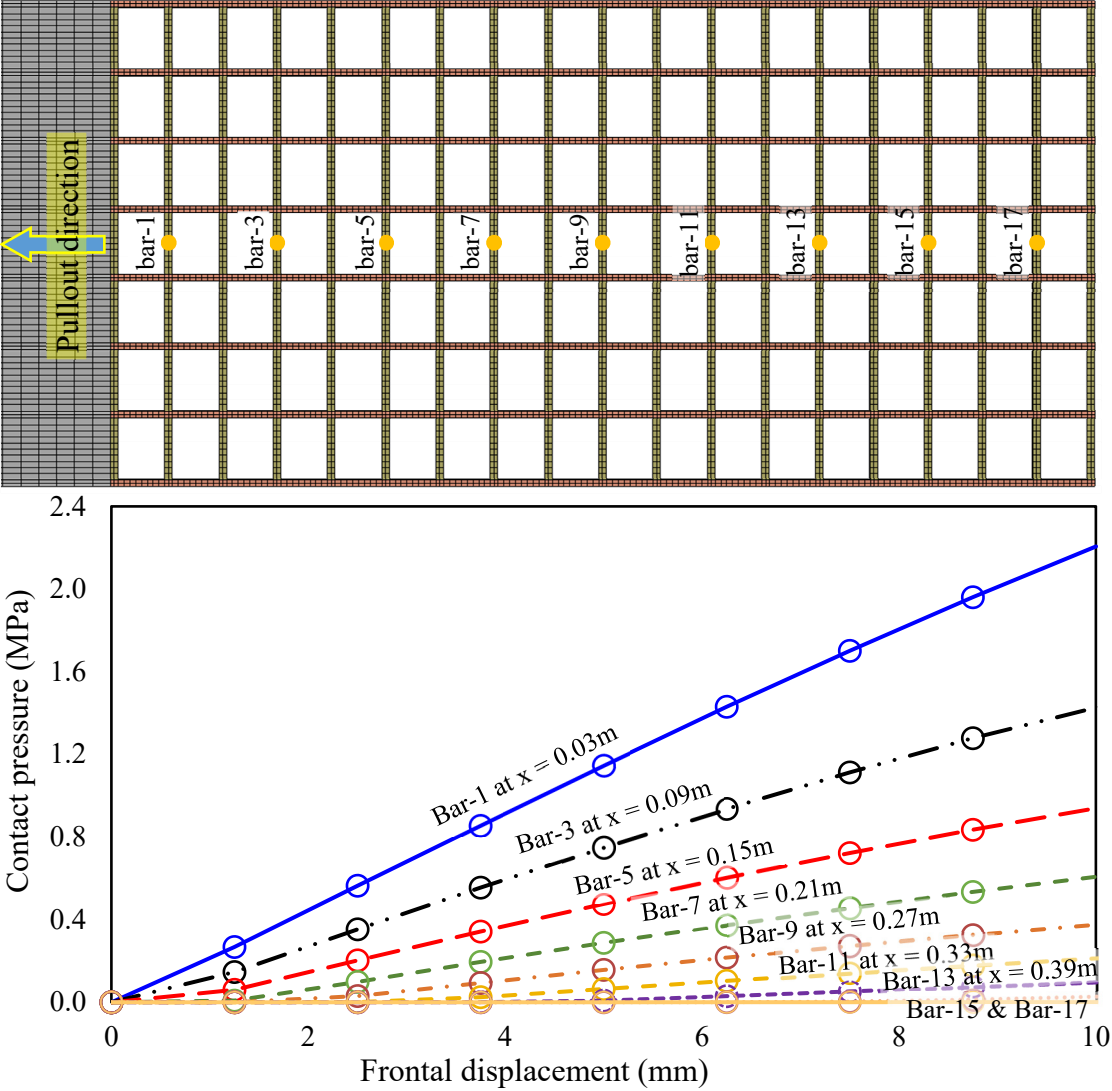


Figure 6-22 Contact pressure developed on T-bars versus frontal displacement

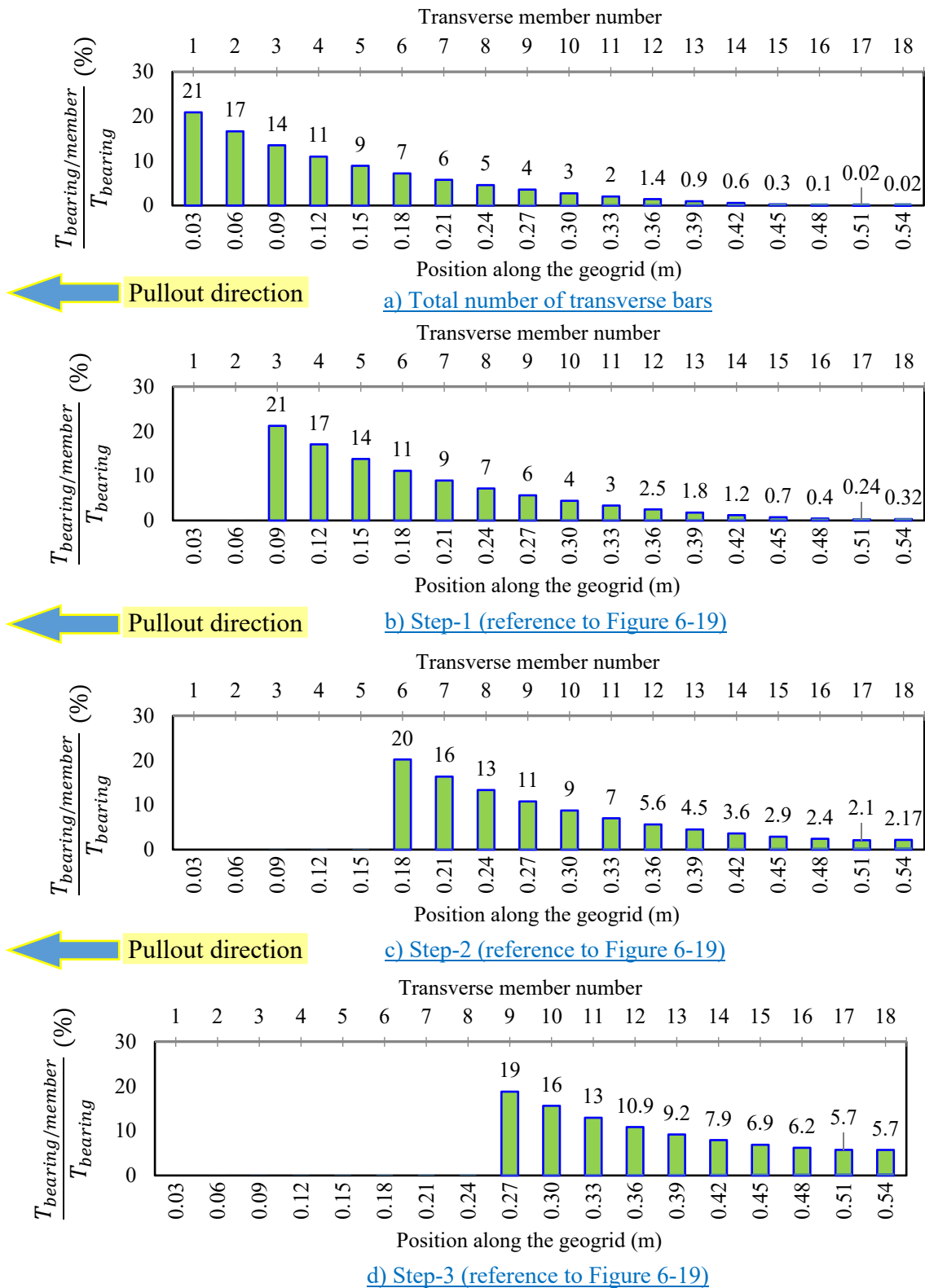


Figure 6-23 Contribution of the transverse members to the total bearing resistance ($U_x = 10\text{mm}$)

A normalized comparison between the original geogrid geometry (contains 18 transverse bars) and the investigated cases with removed members is illustrated in Figure 6-24. Removing half of the transverse members (step-3) resulted in a reduction of the bearing resistance by about 50% and hence only half of the pullout capacity becomes available in the system.

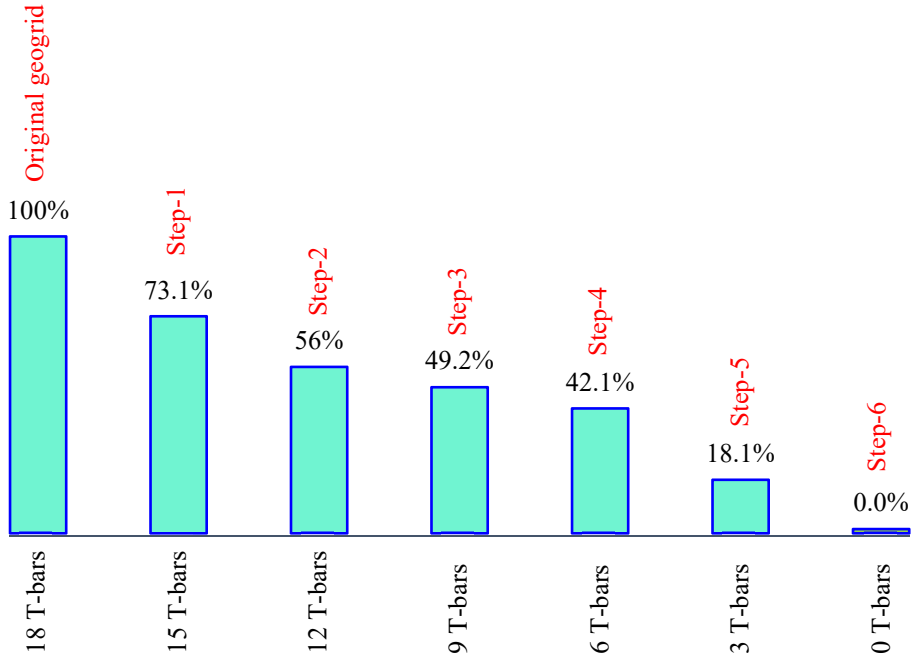


Figure 6-24 Effect of removing transverse bars (reference to Figure 6-19)

The change in tensile forces under different conditions, with references to Figure 6-19, is further examined by plotting the change in tensile force for the different investigated scenarios as illustrated in Figure 6-25. It can be seen that, for the original geometry, the tensile forces in the longitudinal ribs decreased with distance along the geogrid. Removing transverse bars causes the tensile forces to become constant for the distance where no transverse bars existed and then started to decrease with distance towards the free end. This is attributed to the absence of confinement in this area. For example, in step-4 where the transverse bars were removed for a distance of about 0.34m, the tensile force was constant at a value of 0.2 kN up to that location then decreases to zero at the free end. This constant load is similar to that of the tensile stresses for the geogrid tested in air, whereas no confinement

existed and the role of the transverse ribs in carrying tensile load was very minimum (See Figure 5-7b).

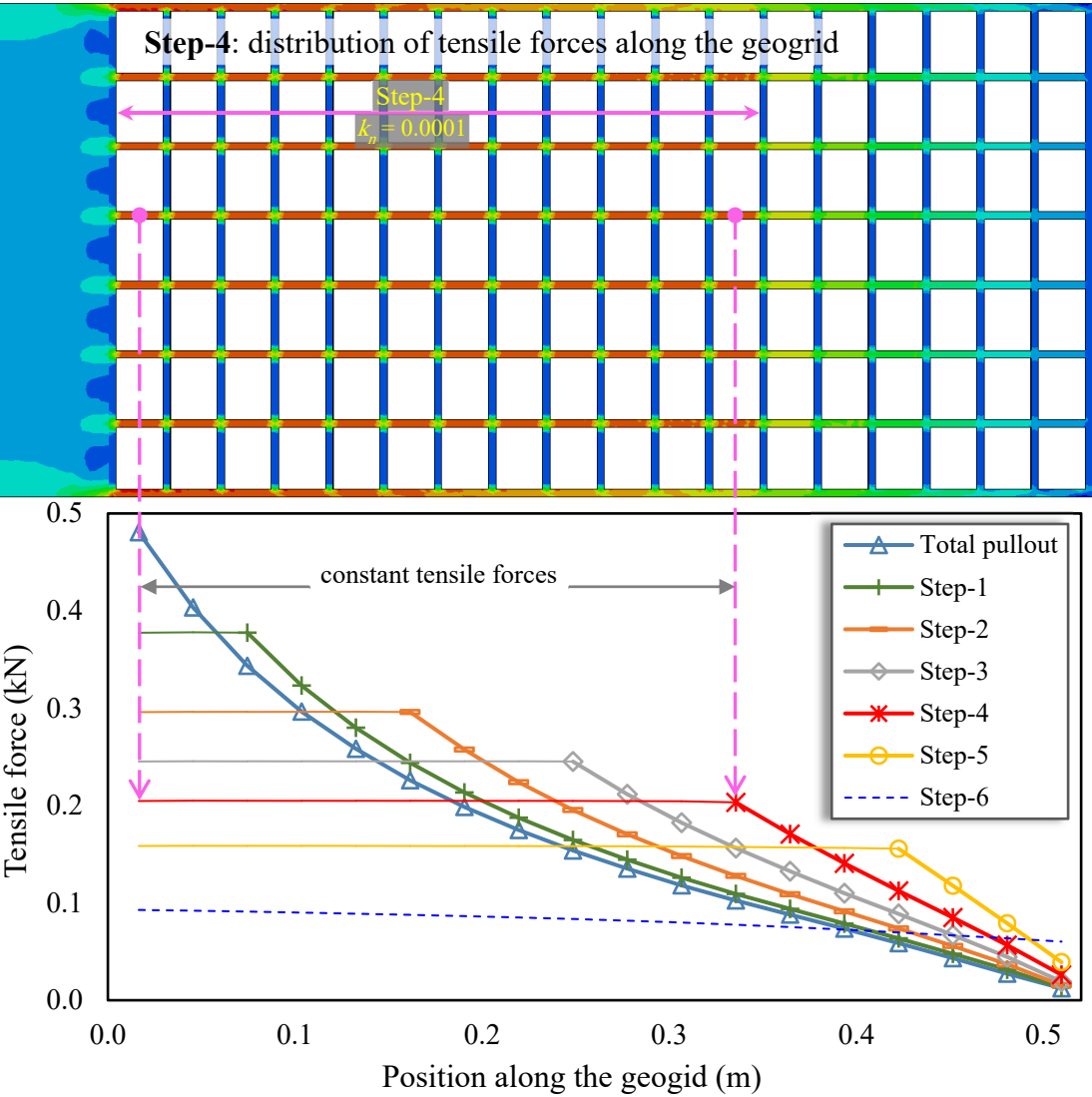


Figure 6-25 Change in tensile forces under different conditions at $U_x = 10\text{mm}$ (reference to Figure 6-19)

6.3.4. Response of the backfill soil

The vertical stress distribution is calculated on a horizontal plane located 50 mm above the geogrid and the results are presented in Figure 6-26. This location was chosen to avoid stress concentration zones located at the geogrid location. Before the pullout starts ($U_x = 0$ mm/initial condition), the vertical stress distribution was approximately constant and equal to the applied vertical stress ($\sigma_v = 49$ kPa). With increasing the frontal displacements, an increase in the vertical stress is calculated with a maximum increase at the front facing. Similar observations were made by (Tran et al., 2013b, Wang et al., 2016). This increase in pressure is attributed to the fact that geogrid movement towards the front wall generates more horizontal forces that restrain the soil dilatancy near the front boundary. This behavior continues up to approximately half of the geogrid length (the effective zone of geogrid lateral displacements) and the stresses go back to their initial values. Based on the results of this study, the extent of the pullout load is generally limited to about 50% of the geogrid length.

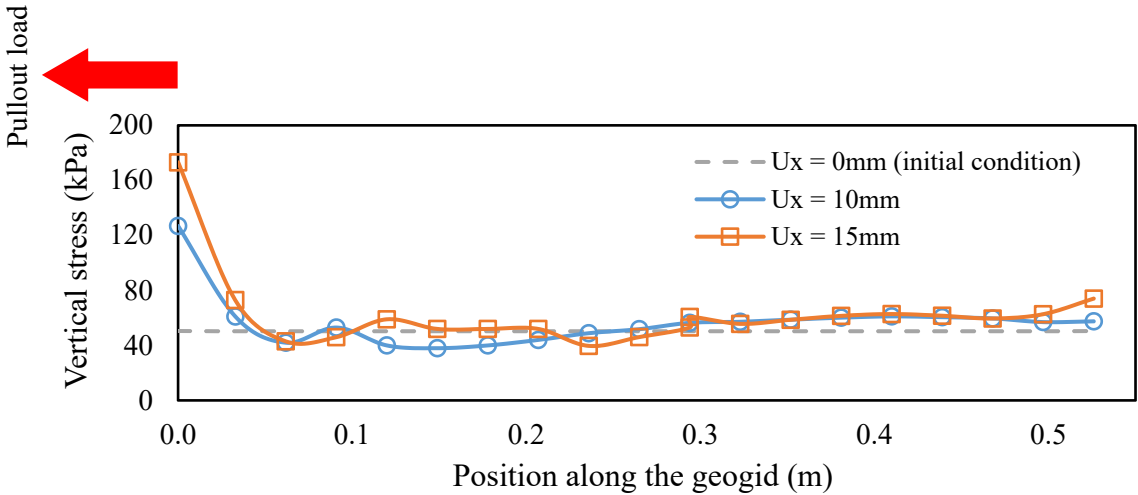


Figure 6-26 Distribution of the vertical stresses (S_{zz}) in the soil specimen

Figure 6-27 shows the displacement field in the soil domain at a frontal displacement of 10 mm. It can be seen that most of the soil movement is concentrated near the front face of the box leading to soil densification in that area. Soil movements started vertically from the top and bottom towards the geogrid and then shifted horizontally toward the front face. As the front wall is approached, soil starts to gradually move in the vertical direction away from the

geogrid. These observations agree well with the results of the X-ray radiographs reported by (Sugimoto et al., 2001). Similar soil movement pattern in pullout tests has also been reported by Jewell (1980) and Dyer (1985).

Figure 6-28 illustrates a plot of AC YIELD (ACtively yielding) zone, which is a scalar quantity denoting the onset of soil yielding. A value of 0 indicates that the soil has not yielded, and a value of 1.0 indicates that the soil has yielded and plastic strains changed during that increment. The shape of the plastic strain in this figure represents the plasticity developing immediately in front of bearing members which is consistent with the theoretical bearing resistance mechanism described by Jewell et al. (1984) and Dyer (1985). It should be noted also that the zone of plasticity further increases with the increase in applied frontal displacement.

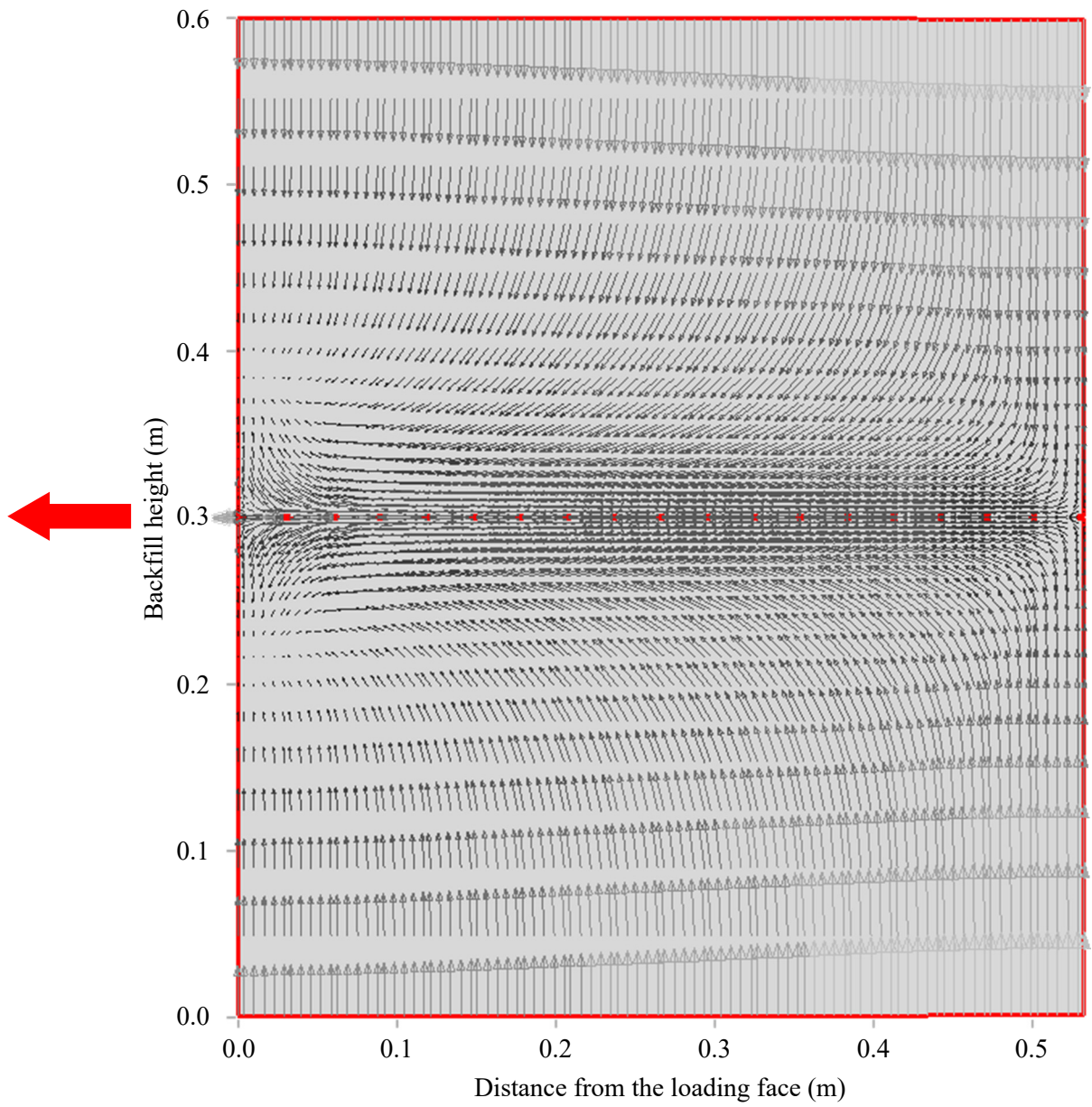


Figure 6-27 Displacement field of the soil specimen at $U_x = 10$ mm

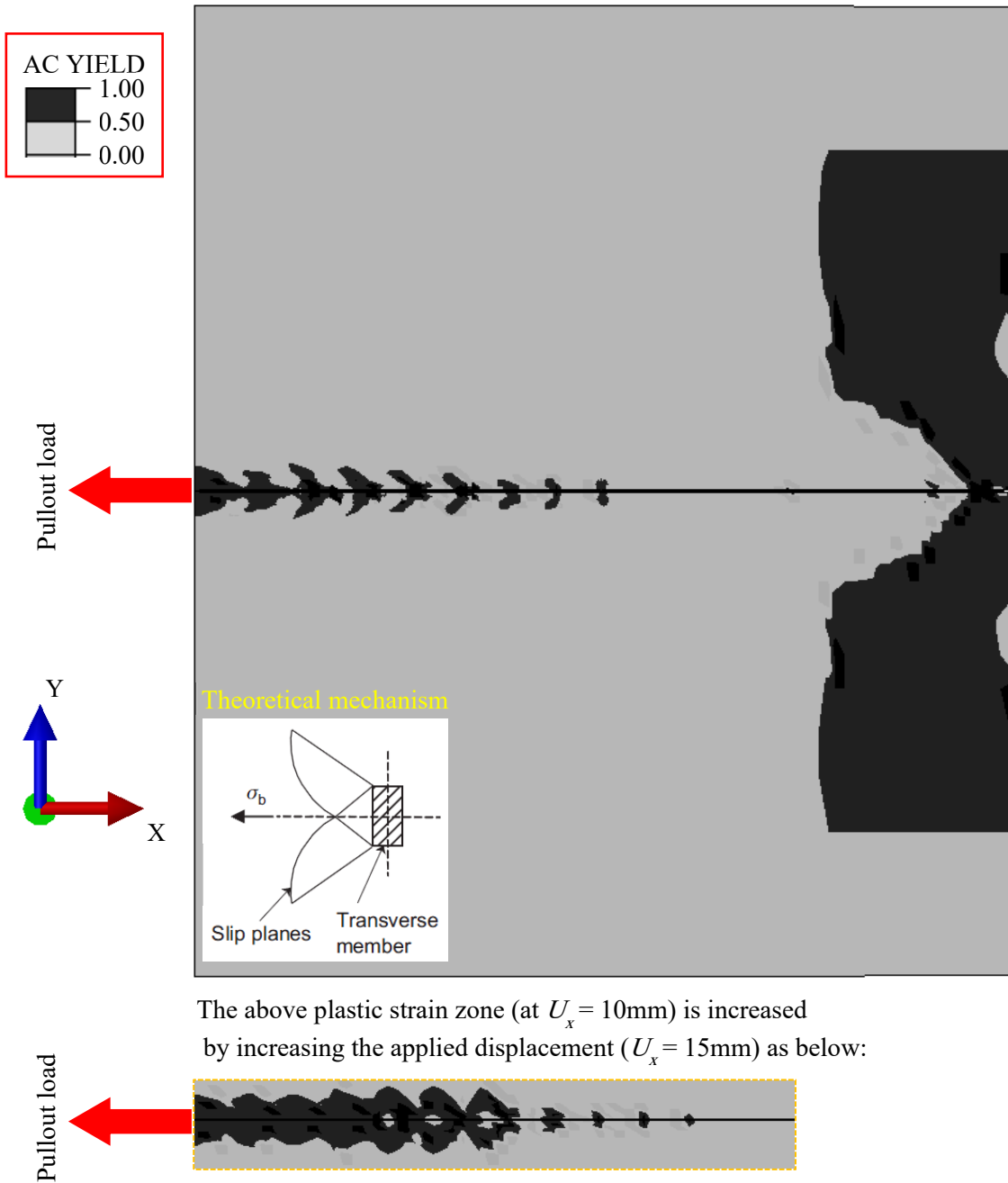


Figure 6-28 Contour plot of AC YIELD in soil at $U_x = 10\text{ mm}$

6.4. Summary and Conclusions

This study investigated the pullout behavior of biaxial geogrid embedded in granular soil using an innovative 3D FE approach. In developing this model, the details of the geometrical features are explicitly simulated. The geogrid was modeled using an elasto-plastic constitutive model that has been developed and validated by the writers in a previous study. The backfill material was simulated using Mohr-Coulomb failure criterion. Both, the geogrid and the backfill were discretized using continuum elements. A detailed procedure of the contact technique used throughout the analysis is described. This includes the contact constitutive models in both the tangential and the normal direction, the contact discretization, and the constraints evolution. A softened contact pressure-overclosure model is used to simulate the behavior of the transverse members. This model is governed by a penalty stiffness parameter that has been calibrated in the present study using the actual displacement distributions of the geogrid from the experimental data. The developed 3D model was validated using experimental results. The displacements and stresses developing in the geogrid were calculated and the backfill movements and plastic strains developing in the soil were investigated.

Most of the geogrid stresses and displacements occurred near the front side of the box with rapid decrease with distance reaching insignificant values around the middle of the geogrid. The load transfer mechanism has been investigated by examining the distribution of the tensile forces, contact pressures, and the displacements along the geogrid by progressively removing transverse members. This was achieved in six separate steps and the contributions of the frictional and bearing resistance components to the total pullout load is then evaluated. For the investigated geogrid and soil conditions, the contribution of the bearing resistance to the total pullout capacity was found to be larger than the frictional resistance. The contribution of the bearing resistance was found to increase as the geogrid displacement increased and the total capacity decreased with reduction in the number of bearing members. The accumulated contribution of the different transverse members to the total bearing resistance was also evaluated. The transverse members located within the middle third of the geogrid was found to contribute significantly to the total bearing resistance. The first

transverse member contributes the largest bearing resistance and the contributions of transverse members decrease with distance from the loaded side.

In the original condition, tensile forces in the longitudinal ribs were found to decrease with distance along the geogrid. When transverse members are removed, the tensile forces become constant along the unconfined distance and then decreased with distance towards the free end of the geogrid.

Soil movement and stresses agreed reasonably well with experimental observations. An increase in soil stresses was found near the front face. The plastic strain patterns confirm the theoretical approaches for the bearing resistance developing against the transverse members.

Finally, the proposed FE approach has proven efficient in modeling the pullout experiment in three-dimensional space and capturing the response of both the geogrid and the surrounding backfill material.

CHAPTER 7

Conclusions and Recommendations

7.1. Conclusions

In this thesis, the finite element method is used to analyze different classes of soil-structure interaction problems involving two types of geosynthetics; EPS geofoam and geogrid reinforcement. Numerical results were compared with experimental measurements to validate the proposed FE simulations. The efficiency of the finite element method in analyzing this class of soil-geosynthetic interaction problems was demonstrated.

A FE approach is introduced to simulate the soil-geosynthetic interaction systems and used to analyze selected problems including uniaxial compression test on EPS geofoam cubes, EPS inclusion above a rigid buried box culvert, unconfined geogrid uniaxial tensile test, a square footing supported by a geogrid-reinforced granular soil, and a biaxial geogrid layer embedded in granular backfill and subjected to pullout loading. The following conclusions can be drawn from the thesis:

- 1) In chapter 3, a numerical procedure for modeling the short-term response of EPS geofoam under uniaxial compression is developed and validated for three different EPS materials. The developed constitutive behavior is able to capture the material nonlinearity and plasticity. The role of lateral confinement on the stress-strain response of the EPS material is also examined. A series of plane strain finite element analyses is then performed to investigate the role of the EPS density, width, thickness and location on the earth pressure distribution acting on a rigid buried structure installed using the induced trench method. Results showed that the introduction of EPS geofoam block immediately above the structure has a significant effect on the contact pressure distribution particularly on the upper wall covered by the geofoam inclusion. The only factor that was found to have a significant impact on the changes in earth pressure is the material density. For the investigated range of parameters, results showed that the EPS width and location did not contribute significantly to the

positive arching process and, therefore, only minor pressure changes were calculated. This study suggests that placing light weight EPS block above a rigid subsurface structure can result in a significant reduction in vertical earth pressure resulting in economic design.

- 2) In chapter 4, the developed FE model that has previously demonstrated its efficiency in investigating the behavior of soil-geofoam-structure system in chapter 3 is used in another analysis to examine the optimum EPS geometrical configuration around the buried structure. In this analysis (*case-II*) the EPS geofoam inclusion is placed above the upper wall and next to the side walls of the buried box culvert. The calculated results are validated using experimental data. Results revealed that the proposed modeling approach is efficient in capturing the stress distribution around the buried structure and allowed for the details of the pressure reduction and EPS performance to be investigated. A comparative study is carried out to evaluate the optimum EPS arrangement around the buried structure by examining the numerical results of the two simulated cases (*case-I* in chapter 3 and *case-II* in chapter 4). This comparison showed that adding EPS blocks next to the side walls decreases the earth pressure significantly on the lower and side walls while increases the contact pressure on the upper wall of the structure. The calculated pressures on the buried box were compared to the theoretical earth pressures. It was found that significant pressure reduction is achieved using EPS15 with a pressure ratio of 0.28 of the theoretical overburden pressure at the upper wall. This translates into a reduction in contact pressure of about 70 % on the upper wall. Finally, preliminary design charts were proposed to allow for the proper choice of EPS material that satisfies a specific embankment height. These charts provide a relationship between the pressure reduction ratio and the EPS type through the expected fill height. Using EPS at the side walls can be justified if reduction in lateral earth pressure on the side walls is a design requirement.
- 3) In chapter 5, the capability of the finite element method to investigate a more complex soil-geosynthetics system is evaluated. A 3D FE approach is developed to investigate the geogrid reinforcement behavior under unconfined and soil-confined conditions.

A numerical model that is capable of simulating the response of the unconfined biaxial geogrid under tensile loading is first introduced and validated using index test results. In developing this model, the details of the geogrid geometrical features are explicitly simulated. Sensitivity analysis was performed to evaluate the role of different numerical parameters on the predicted geogrid response. The difference between modelling the exact geogrid geometry as opposed to an equivalent sheet is also examined. Tensile load applied to a geogrid specimen causes stresses that are carried mostly by the longitudinal ribs in the direction of the applied load and the portion transmitted to the junctions and transvers bars are insignificant. The displacement is found to decrease linearly with distance from the loaded boundary. Using equivalent plane sheet without proper calibration with exact geometry to model geogrid may lead to a much stiffer response resulting in an overestimation in the design load. To confirm the validity of the unconfined geogrid model, a 3D analysis is conducted to investigate the geogrid performance as it interacts with the backfill material. A case study involving a square footing supported by a geogrid-reinforced material is investigated. The 3D geometry of the geogrid, its deformation, and stress distribution were presented. The model was able to capture the 3D response of the soil-geogrid system with one or more geogrid layers installed under the footing. Increasing the number of geogrid layers resulted in an increase in the ultimate bearing capacity of the system. The geogrid deformations and tensile stresses for the case of having one geogrid layer were found to be generally larger than those calculated for the two-layer case. Finally, the proposed FE approach has proven to be efficient in capturing the 3D responses of both unconfined and soil-confined geogrid and can be adopted by researchers for soil-geogrid interaction analysis.

- 4) In chapter 6, the efficiency of the 3D FE approach that was proposed in chapter 5 in analyzing soil-geogrid interaction problems has been demonstrated. In this chapter, the pullout behavior of biaxial geogrid embedded in granular soil is investigated using an innovative 3D FE procedure. The geogrid was modeled using an elasto-plastic constitutive model that has been developed and validated in chapter 5. A detailed

procedure of the contact technique used throughout the analysis is described. This includes the contact constitutive models in both the tangential and the normal direction, the contact discretization, and the constraints evolution. A softened contact pressure-overclosure model is used to simulate the behavior of the transverse members. The results of the analysis were compared with experimental data. The displacements and stresses developing in the geogrid were analyzed and the backfill movements and plastic strains were investigated. Most of the geogrid stresses and displacements occurred near the front side of the box with rapid decrease with distance and reached very small values around the middle of the geogrid. The soil-geogrid load transfer mechanism has been investigated by examining the distribution of the tensile forces, contact pressures, and the displacements along the geogrid with different number of transverse members. For the investigated geogrid and soil conditions, the contribution of the bearing resistance to the total pullout resistance was found to be larger than the frictional resistance. The accumulated contribution of the different transverse members to the total bearing resistance was also evaluated. The tensile force of the geogrid longitudinal ribs was found to decrease with distance along the geogrid. In case of removing the contributions of some transverse members, the tensile forces tend to remain constant along the unconfined distance then reduces with distance to the free end of the geogrid. The soil movement and stresses within the soil domain agreed with experimental observations. An increase in soil stresses was observed near the front face. The plastic strain patterns confirm the theoretical approaches for the soil bearing resistance developed against the transverse members. The proposed FE approach has proven efficient in modeling the pullout experiment in three-dimensional space and capturing the response of both the geogrid and the surrounding backfill material.

7.2. Recommendations for Future Work

Various soil-structure interaction problems can be studied following the methodology that has been developed in this thesis including:

- Mitigation of Earthquake load on retaining walls using EPS seismic buffer.
- Cyclic loading of geogrid-reinforced ballast.
- Large scale geofoam embankments.

APPENDIX (A)

Finite Element Constitutive Models

A.1. Introduction

This appendix presents more details on the formulations of the constitutive material models used in this thesis. Mohr-Coulomb failure criterion is used throughout the analysis of the developed models to describe the behavior of the backfill soils. Von Mises plasticity model, on the other hand, is adapted to simulate the short-term response of the geosynthetics materials.

A.2. ABAQUS/Extended Mohr-Coulomb Model (EMC)

The ABAQUS extended Mohr-Coulomb model is used to simulate the soil behavior throughout this study. It is an advanced elasto-plastic model that is developed by considering a yield surface similar to the classical Mohr-Coulomb (MC) line in addition to a flow rule and a hardening law.

Classical Mohr-Coulomb Model (MC)

The MC criterion is one of the most widely used theories for describing the failure of soil materials. This is due to a number of reasons, one of which is its mathematical simplicity. Another reason is the physical meaning of the material parameters, and lastly, there is a general level of acceptance for the criterion. The MC theory can be thought of as a set of linear equations in principal stress space that represent a shear failure surface for an isotropic material, with no effect from the intermediate principal stress (σ_{II}). It assumes that failure occurs when shear stress on any point in a material reaches a limit value that depends linearly on the normal stress in the same plane. The classical formulation of the MC model can be written as follows:

$$\tau = c + \sigma_n \tan \phi \quad \text{A.1}$$

where τ and σ_n are the shear and normal stresses on the failure plan respectively, c is the cohesion, ϕ is the angle of internal friction. A representation of the MC failure criterion on a Mohr diagram is shown in Figure A-1. From this figure the criterion states that the larger the pressure σ_n , the more shear the material can sustain.

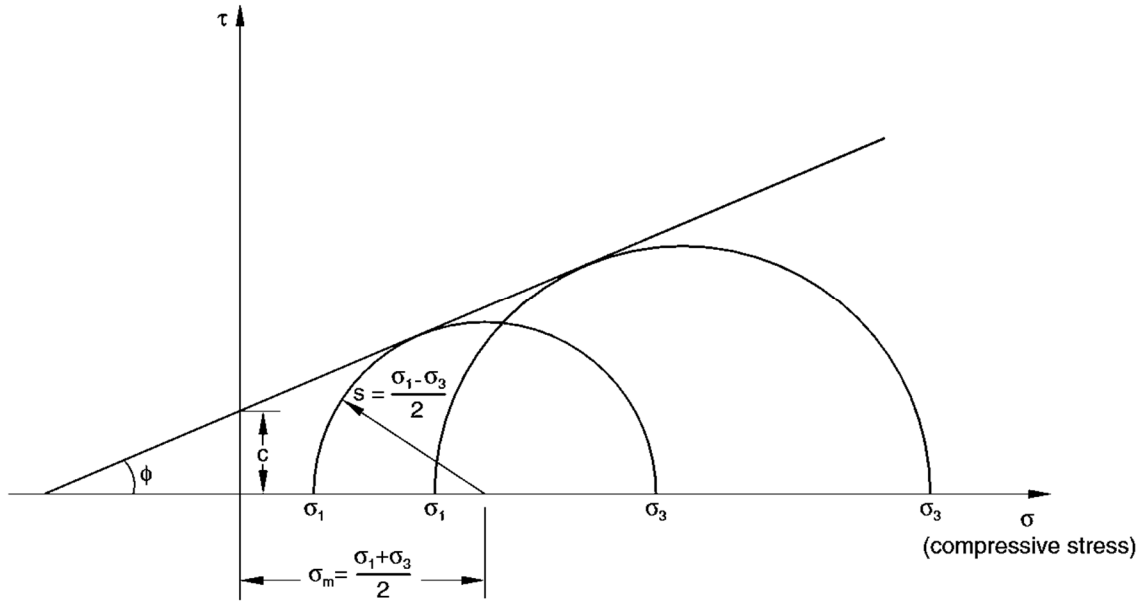


Figure A-1 Mohr-Coulomb failure criterion

According to Figure A-1, the MC model is a two-parameter model (the friction angle, ϕ and cohesion, c) with criterion of shear failure. From Figure A-1, and noting that the large Mohr circle has centre $(\sigma_m = \frac{1}{2}(\sigma_1 + \sigma_3), 0)$ and radius $(S = \frac{1}{2}(\sigma_1 - \sigma_3))$, one has:

$$\tau = S \cos \phi = \frac{\sigma_1 - \sigma_3}{2} \cos \phi \quad \text{A.2}$$

$$\sigma_n = \sigma_m + S \sin \phi = \frac{\sigma_1 + \sigma_3}{2} + \frac{\sigma_1 - \sigma_3}{2} \sin \phi \quad \text{A.3}$$

Thus the MC criterion in terms of principal stresses can be written as:

$$\sigma_1 - \sigma_3 = 2c \cos\phi - (\sigma_1 + \sigma_3) \sin\phi \tag{A.4}$$

where σ_1 and σ_3 are the major (maximum) and minor (minimum) principal stresses respectively, σ_m is the mean (average) principal stress, and S is the maximum shear stress.

Soil is a complicated material that behaves non-linearly and often shows anisotropic and time dependent behavior when subjected to stresses. In general stress state, the MC model simplifies the soil behavior as elastic-perfectly plastic material that behaves linearly in the elastic range, with two defining parameters from Hook’s law (Young’s modulus, E and Poisson’s ration, ν) as shown in Figure A-2.

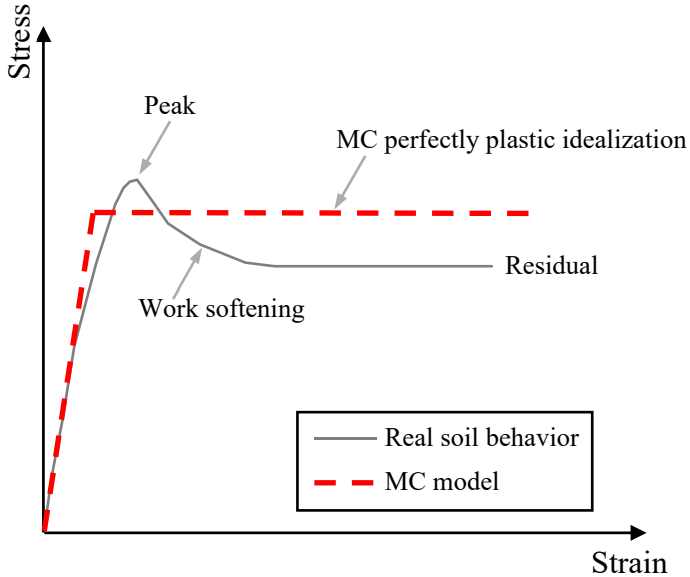


Figure A-2 Elastic-perfectly plastic assumption of Mohr-Coulomb model

The Mohr-Coulomb yield surface in the meridional and deviatoric (Π -plan) planes is illustrated in Figure A-3. In the deviatoric plane, the MC model has an irregular hexagonal shape which can be constructed from two lengths:

- 1) The magnitude of the deviatoric stress in uniaxial tension (S_t) at yield

$$S_t = \frac{\sqrt{6}f_{Yt}(1 - \sin\phi)}{3 + \sin\phi} \quad \text{A.5}$$

where f_{Yt} is the strength of the MC material in uniaxial tension, $f_{Yt} = \frac{2c \cos\phi}{1 + \sin\phi}$

- 2) The corresponding value of S_t in compression, S_c

$$S_c = \frac{\sqrt{6}f_{Yc}(1 - \sin\phi)}{3 + \sin\phi} \quad \text{A.6}$$

where f_{Yc} is the strength of the MC material in uniaxial compression, $f_{Yc} = \frac{2c \cos\phi}{1 - \sin\phi}$

In the meridional stress plane, the failure surface cuts the $q = 0$ axis at $p = \sqrt{3}c \cot\phi$.

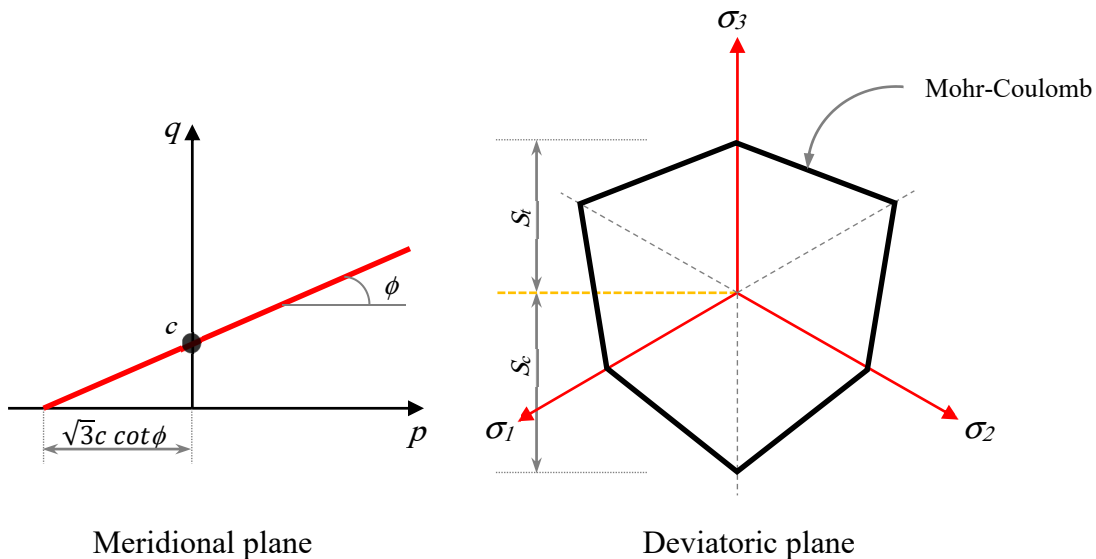


Figure A-3 Classical Mohr-Coulomb yield surface in meridional and deviatoric planes

The MC failure surface in the principal stress space appears as hexagonal pyramid (six edged cone), as the criterion is independent of the intermediate principal stress (Figure A-4).

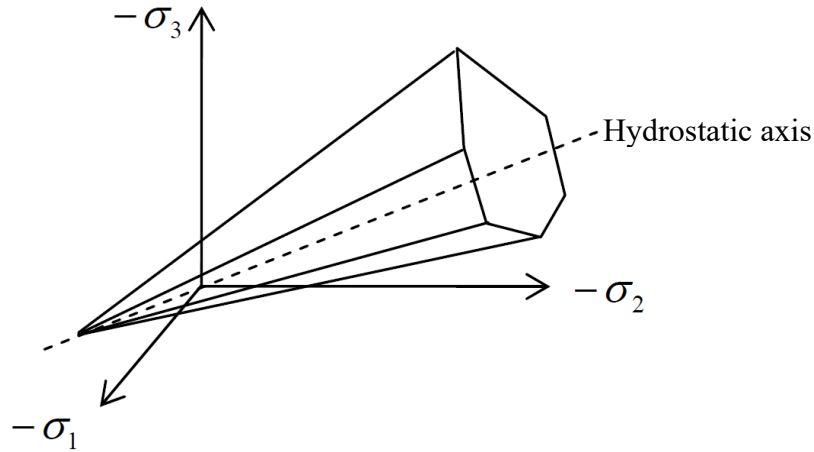


Figure A-4 Mohr-Coulomb yield surface in principal stress space

Yet, MC is the most prevalent failure criterion for soil that includes a hydrostatic pressure effect (predicting a linear increase in strength with increasing the confining pressure).

Extended Mohr-Coulomb Model (EMC)

The ABAQUS Mohr-Coulomb (EMC) is an extension of the classical MC failure criterion. It is an elastoplastic model that uses the yield function of the Mohr-Coulomb form in addition to a hardening law and a flow rule. The yield function includes isotropic cohesion hardening/softening. However, the model uses a flow potential that has a hyperbolic shape in the meridional stress plane and a piecewise elliptic shape (with no corners) in the deviatoric stress space.

To describe the EMC, one has to define two main aspects, namely: i) the yield function, and ii) the flow potentials (flow rule)

a) Yield function with isotropic hardening

For general state of stress, the yield function of the EMC is conveniently written in terms of three stress invariants:

1) Equivalent pressure stress

$$p = -\frac{1}{3} \text{trace} (\boldsymbol{\sigma}) \quad \text{A.7}$$

2) The Mises equivalent stress

$$q = \sqrt{\frac{2}{3} (\boldsymbol{S} : \boldsymbol{S})} \quad \text{A.8}$$

where \boldsymbol{S} is the deviatoric stress, defined as $\boldsymbol{S} = \boldsymbol{\sigma} + p\boldsymbol{I}$

3) The third invariant of deviatoric stress

$$r = \left(\frac{9}{2} \boldsymbol{S} : \boldsymbol{S} : \boldsymbol{S}\right)^{\frac{1}{3}} \quad \text{A.9}$$

The variables q and p are commonly defined in soil mechanics as the stress deviator and the effective mean stress, respectively.

Then, the yield surface is written as:

$$F = R_{mc}q - p \tan\phi - c = 0 \quad \text{A.10}$$

where:

ϕ is the slope of Mohr-Coulomb yield surface in the meridional stress plane (p - $R_{mc}q$), which is commonly referred to as the classical friction angle of the material, $0^\circ \leq \phi \leq 90^\circ$.

c is the evolution of the cohesion of the material in the form of isotropic hardening (or softening) and it is a function of the equivalent plastic strain $\bar{\epsilon}^{pl}$.

R_{mc} is a measure of the shape of the yield surface in the deviatoric stress that is defined as:

$$R_{mc}(\Theta, \phi) = \frac{1}{\sqrt{3} \cos\phi} \sin\left(\Theta + \frac{\pi}{3}\right) + \frac{1}{3} \cos\left(\Theta + \frac{\pi}{3}\right) \tan\phi \quad \text{A.11}$$

where Θ is the deviatoric polar angle (Chen and Han, 1988) defined as:

$$\cos(3\theta) = \left(\frac{r}{q}\right)^3 \quad \text{A.12}$$

The extended Mohr-Coulomb yield surface in meridional and deviatoric planes is shown in Figure A-5. The friction angle (ϕ) controls the shape of the yield surface in the deviatoric plane as shown in Figure A-5. The friction angle range is $0^\circ \leq \phi \leq 90^\circ$. In case of $\phi = 0^\circ$, the Mohr-Coulomb reduces to the pressure independent Tresca model with a perfectly hexagonal deviatoric section. However, when $\phi = 90^\circ$, the Mohr-Coulomb reduces to the “tension cutoff” Rankine model with a triangular deviatoric section and $R_{mc} = \infty$ (this limiting case is not permitted within the Mohr-Coulomb model described here).

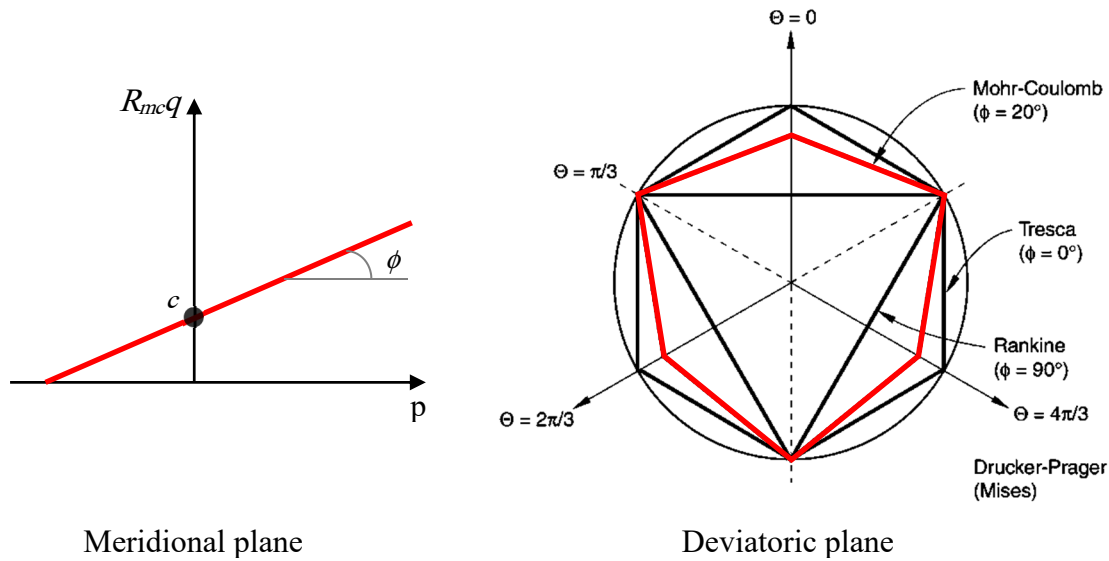


Figure A-5 ABAQUS Mohr-Coulomb yield surface in meridional and deviatoric planes

Isotropic cohesion hardening is assumed for the hardening behavior of the Mohr-Coulomb yield surface. The hardening curve must describe yield stress as a function of plastic strain. The hardening law has to be provided by the user as tabular data in the input file, and the unique hardening parameter is the cohesion yield stress, which is assumed to be dependent only on the equivalent plastic strain, defined as:

$$\bar{\epsilon}^{pl} = \int \frac{1}{c} \boldsymbol{\sigma} : d\boldsymbol{\epsilon}_{pl} \quad \text{A.13}$$

b) Flow potentials (flow rule)

The flow potential, G , used for the EMC model has a hyperbolic function in the meridional stress plane and is described by the smooth elliptic function proposed by Menétrey and Willam (1995) in the deviatoric stress plan:

$$G = \sqrt{(\epsilon c|_0 \tan \psi)^2 + (R_{mw} q)^2} - p \tan \psi \quad \text{A.14}$$

where:

R_{mw} is the polar radius and it is a function in Θ (the deviatoric polar angle defined previously) and e as described below. It controls the shape of G in the deviatoric plane.

ψ is the dilatancy angle measured in the p - $R_{mw}q$ plane at high confining pressure.

$c|_0$ is the initial cohesion yield stress that is corresponding to zero plastic strain, $c|_0 = c(\bar{\epsilon}^{pl} = 0.0)$.

ϵ is a parameter referred to as the meridional eccentricity (with default value of 0.1), which controls the shape of G in the meridional plane. It defines the rate at which the hyperbolic function approaches the asymptote (the flow potential tends to a straight line in the meridional stress plane as the meridional eccentricity tends to zero).

e is a parameter referred to as the deviatoric eccentricity, that describes the “out-of-roundness” of the deviatoric section ($0 \leq \Theta \leq \frac{\pi}{3}$). The default value of the deviatoric eccentricity is calculated by $= \frac{3-\sin\phi}{3+\sin\phi}$, and allows the ABAQUS Mohr-Coulomb model to match the behavior of the classical Mohr-Coulomb model in triaxial compression and tension. It may have a range of $\frac{1}{2} < e \leq 1.0$.

This flow potential, which is continuous and smooth in the deviatoric and meridional stress planes, ensures that the flow direction is always uniquely defined in this plane. A family of hyperbolic potentials in the meridional stress plane is shown in Figure A-6, and the flow potential in the deviatoric Π -plan is shown in Figure A-7. In the meridional plane, the function asymptotically approaches a linear flow potential at high confining pressure and intersects the hydrostatic pressure axis at 90° .

Flow in the meridional stress can be close to associated (the plastic potential function is the same as the yield function) when the angle of friction (ϕ) and the angle of dilation (ψ) are equal and the meridional eccentricity parameter, ϵ is very small; however, flow in this plan is, in general, nonassociated (used to describe the behavior of sands). Flow in the deviatoric stress plan is always nonassociated. Therefore, the use of Mohr-Coulomb model generally requires the solution of nonsymmetric equations, which is imposed in the current study.

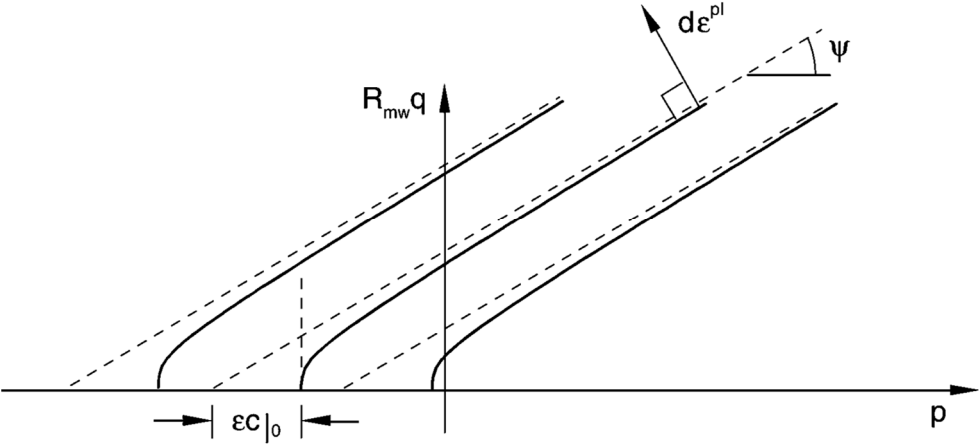


Figure A-6 Family of hyperbolic flow potentials in the meridional plane

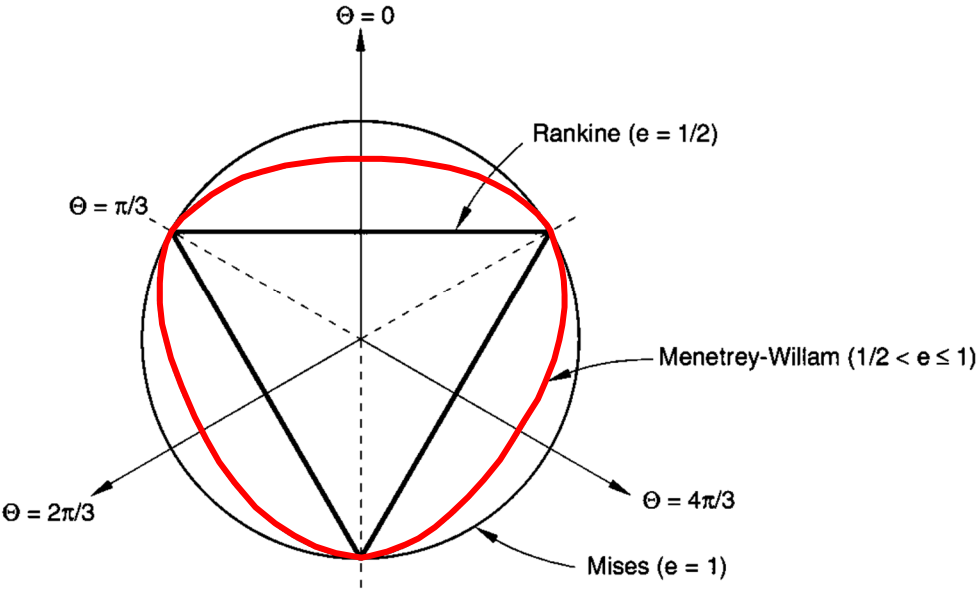


Figure A-7 Menétrey-Willam flow potential in the deviatoric plane

Summary of the ABAQUS/Extended Mohr-Coulomb Model (EMC)

The ABAQUS Mohr-Coulomb plasticity model has the following characteristics:

- is used in combination with the linear elastic material model;
- is used to model materials with the classical Mohr-Coulomb yield criterion;
- the yield behavior depends on the hydrostatic pressure. One of the consequences of this is that the material becomes stronger as the confining pressure increases;
- allows the material to harden and/or soften isotropically;
- The plastic behavior will generally be accompanied by some volume change; the flow rule may include inelastic dilation as well as inelastic shearing;
- uses a smooth flow potential that has a hyperbolic shape in the meridional stress plane and a piecewise elliptic shape in the deviatoric stress plane; this flow potential is generally nonassociated.

The use of the EMC model to describe the soil backfill in the current study requires the identification of five parameters:

ϕ	slope of the failure curve in p - $R_{mc}q$ plane (classical soil friction angle)
ψ	soil dilation angle
$c _0$	initial cohesion stress, corresponding to zero plastic strain (soil cohesion)
E	Young's modulus
ν	Poisson's ratio

Some other constitutive parameters (e.g. ϵ and e) are not calibrated due to their minor influence and difficulties in their identification without carrying out specific tests. The default values proposed by ABAQUS are accepted and used.

Although the failure of typical geotechnical materials generally includes some small dependence on the intermediate principal stress, which is not included in the Mohr-Coulomb model, the model is generally considered to be sufficiently accurate for most applications. Consequently, a large number of the routine design calculations in the geotechnical area are performed using the Mohr-Coulomb criterion.

A.3. The Von Mises Isotropic Elasto-Plasticity Model

Plasticity models are used to simulate problems in which the elastic response must always be very small. In practice this is the case for metals, polymers, soil, and concrete. In each of these materials, it is very unlikely that the elastic strain would ever be larger than a few percent. The Von Mises plasticity model is used throughout this study to simulate the nonlinear short-term response of the geosynthetic materials; geofoam and geogrids. This isotropic yield surface is defined in ABAQUS with isotropic hardening and associated flow rule. In doing so, three main aspects, namely: i) the Von Mises yield function, ii) isotropic hardening rule, and iii) flow rule, are addressed.

a) *Von Mises yield function*

The Von Mises criterion states that yield occurs when the principal stresses satisfy the relation:

$$\sigma_e = \sigma_y \quad \text{A.15}$$

where σ_e is equivalent (Von Mises) stress and σ_y is the one-dimensional yield stress. This Von Mises stress (σ_e) sometimes denoted as (σ_{vm}).

The equivalent stress can be written in terms of principal stresses as follows:

$$\sigma_e = \sqrt{3 J_2} = \left\{ \frac{1}{2} [(\sigma_1 - \sigma_2)^2 + (\sigma_2 - \sigma_3)^2 + (\sigma_3 - \sigma_1)^2] \right\}^{\frac{1}{2}} \quad \text{A.16}$$

where J_2 is the second invariant of the deviatoric stress expressed as:

$$J_2 = \frac{1}{6} \{ (\sigma_1 - \sigma_2)^2 + (\sigma_2 - \sigma_3)^2 + (\sigma_3 - \sigma_1)^2 \} \quad \text{A.17}$$

Using the equivalent stress, the yield function can be defined as:

$$f(\sigma) = \sigma_e^2 - \sigma_y^2 = 3J_2 - \sigma_y^2 = 0 \quad \text{A.18}$$

This potential is a circle in the plane normal to the hydrostatic axis (Π -plane) in principal space with a radius of $\sqrt{\frac{2}{3}} \sigma_e$, as shown in Figure A-8. The yield surface is a circular cylinder with axis along the space diagonal, as shown in Figure A-9.

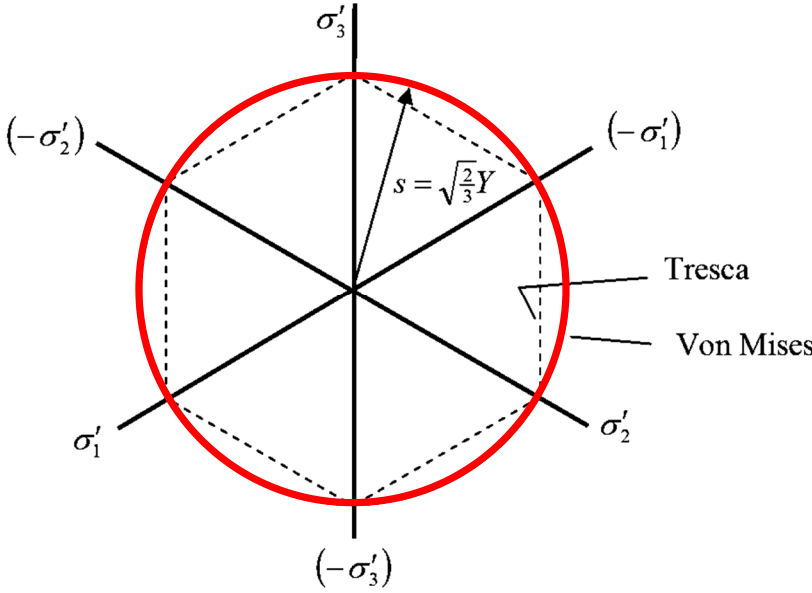


Figure A-8 The Von Mises yield criterion in the Π -plane

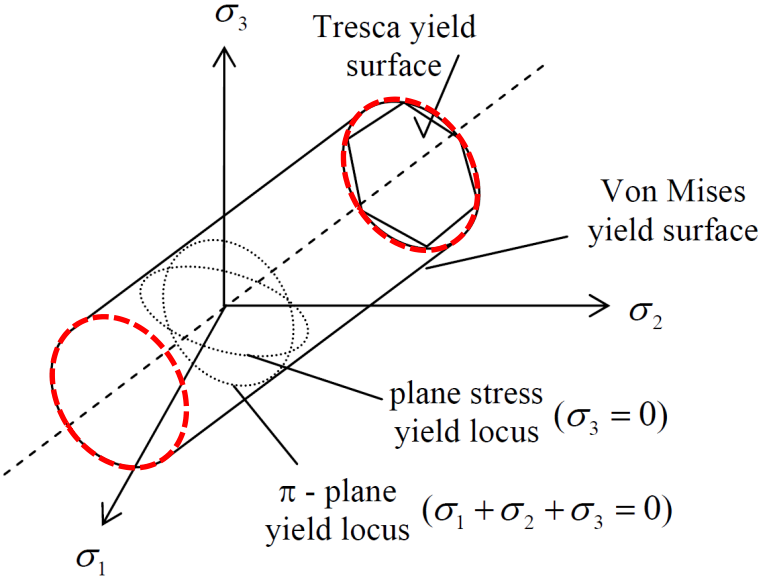


Figure A-9 The Von Mises yield surface

The counterpart of the equivalent stress is the Von Mises effective strain (ε_e) that can be obtained by integrating the equivalent strain increment as:

$$\varepsilon_e = \int d\varepsilon_e \quad \text{A.19}$$

where $d\varepsilon_e$ is the strain increment that can be determined using:

$$d\varepsilon_e = \left\{ \frac{2}{9} [(d\varepsilon_1 - d\varepsilon_2)^2 + (d\varepsilon_2 - d\varepsilon_3)^2 + (d\varepsilon_3 - d\varepsilon_1)^2] \right\}^{\frac{1}{2}} \quad \text{A.20}$$

It should be noted that the scalar plastic strain (ε^p) in one-dimensional plasticity, that is usually predicted from a one dimensional uniaxial test, becomes a tensor in multidimensional plasticity analysis.

b) Isotropic hardening rule

Plastic strain hardening (ε^p) is characterized by a specific rule (hardening curve) describing the variation of the yield stress with equivalent plastic strain.

The hardening curve is then defined with the following function:

$$\sigma_y = f(\bar{\varepsilon}^p) \quad \text{A.21}$$

After defining this function, it becomes evident that equation (A.15) describing a state of yielding characterised by the yield stress and the associated level of plastic strain.

This hardening rule is an isotropic. Isotropic hardening means that the yield surface changes size uniformly in all directions such that the yield stress increases (or decreases) in all stress directions as plastic straining occurs. Although the model is referred to as a “hardening” model, strain softening or hardening followed by softening can be defined.

c) Flow rule

In combination with the Von Mises yield criterion, ABAQUS uses associated plastic flow. Therefore, as the material yield, the inelastic deformation rate is in the direction of the normal to the yield surface (no volumetric plastic strain).

Assignment of Von Mises elasto-plastic model in ABAQUS

The Von Mises elasto-plastic model is defined in ABAQUS by giving the value of the uniaxial yield stress as a function of uniaxial equivalent plastic strain. This is achieved by decomposing the total strain values into elastic and plastic strains to cover the entire range of the geosynthetic material response. The different model components include:

- i) The elasticity component is described by an elastic isotropic model where the total stress and the total strain are related using the elasticity matrix. This requires two defining parameters; Young's modulus (E) and the Poisson's ratio (ν);
- ii) The plasticity is modeled using Von Mises yield criterion (described previously) with isotropic hardening and associated flow rule;
- iii) The isotropic yielding is defined by expressing the uniaxial yield stress as a function of the equivalent uniaxial plastic strain;
- iv) The isotropic hardening rule is expressed in ABAQUS using a tabular data of yield stress as function of plastic strains.

The plasticity data has to be specified in terms of true stresses and true strains (ABAQUS, 2013) despite the fact that test data provides nominal (engineering) values of total stresses and total strains. A procedure is, therefore, needed to convert the nominal test data to its true values and then decompose the total strain values into elastic and plastic strain components to allow for direct data input into ABAQUS.

A flow chart that illustrates the procedure adopted to determine the numerical input data based on the experimental results is given in Figure A-10. This procedure is developed for two different cases. In the first case, the Von Mises elasto-plastic model is used to describe the compressive stress behavior of the EPS geofoam, whereas, in the other case the model is used to simulate the response of the geogrid material under tensile stresses. The steps to accomplish the proposed procedure for both cases are identical, except for converting the nominal stresses to true values, as summarised below:

- 1) Converting the test data (stresses and strains) from nominal to true values using the following expressions:

$$\varepsilon_{true} = \ln(1 + \varepsilon_{nom}) \quad A.22$$

For tensile stresses
$$\sigma_{true} = \sigma_{nom} (1 + \varepsilon_{nom}) \quad A.23$$

For compressive stresses
$$\sigma_{c-true} = \frac{\sigma_{c-nom}}{(1 - \nu \cdot \varepsilon_{c-nom})^2} \quad A.24$$

where ε_{true} is the true strain, ε_{nom} is the nominal strain, σ_{true} is the true tensile stress, σ_{nom} is the nominal stress, and σ_{c-true} is the true compressive stress.

Then, decompose the total true strain (ε_{true}) into elastic and plastic components:

$$\varepsilon_{true} = \varepsilon^{el} + \varepsilon^{pl} \quad A.25$$

where ε^{el} is the elastic strain and ε^{pl} is the plastic strain.

- 2) Using the true stress (σ_{true}) and Young's modulus (E) to obtain the elastic strain component (ε^{el}):

$$\varepsilon^{el} = \frac{\sigma_{true}}{E} = \frac{\sigma_{c-true}}{E} \quad A.26$$

- 3) Subtract the elastic strain value (ε^{el}) from the total true strain (ε_{true}) to obtain the plastic strain (ε^{pl}).

The final plasticity properties are introduced into ABAQUS input module in terms of true stresses versus plastic strains.

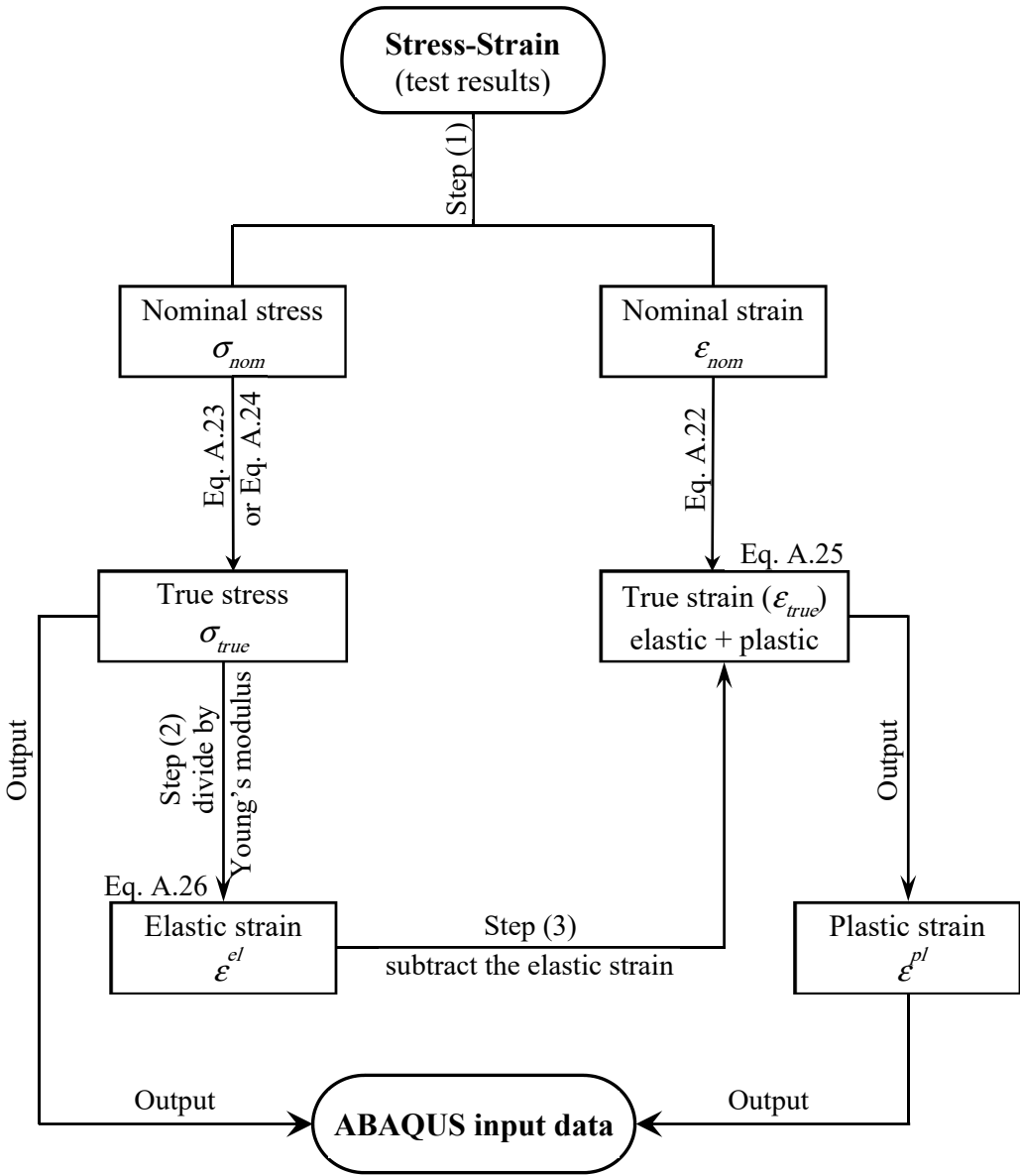


Figure A-10 Procedure used to generate ABAQUS input parameters

REFERENCES

- AASHTO, American Association of State Highway and Transportation Officials, (2007). LRFD Bridge Design Specifications. 4th ed. Washington, D.C., USA.
- AASHTO, American Association of State Highway and Transportation Officials, (2012). LRFD Bridge Design Specifications. 6th ed. Washington, D.C., USA, p. 1661.
- ABAQUS, Version 6.13, (2013). ABAQUS User's Manuals. Dassault Systems Simulia Corp. Providence, USA.
- Abdi, M.R., and Zandieh, A.R., (2014). Experimental and Numerical Analysis of Large Scale Pull Out Tests Conducted on Clays Reinforced with Geogrids Encapsulated with Coarse Material. *Geotextiles and Geomembranes* 42(5), pp. 494-504.
- Abu-Farsakh, M., Chen, Q., and Yoon, S., (2008). Use of Reinforced Soil Foundation (RSF) to Support Shallow Foundation. *Louisiana Transportation Research Center (LTRC)*, Report No. FHWA/LA.07/424. Louisiana Department of Transportation and Development, Baton Rouge, LA, USA, p. 195.
- ACPA, (1994). Concrete Pipe Technology Handbook: A Presentation of Historical and Current State-of-the-art Design and Installation Methodology, *Americam Concrete Pipe Association*, Vienna, VA, USA.
- ACPA, (2004). Concrete Pipe Handbook, *Americam Concrete Pipe Association*, Vienna, VA, USA, p. 440.
- Adams, M.T., and Collin, J.G., (1997). Large Model Spread Footing Load Tests on Geosynthetic Reinforced Soil Foundations. *Geotechnical and Geoenvironmental Engineering* 123(1), pp. 66-72.
- Alagiyawanna, A.M.N., Sugimoto, M., Sato, S., and Toyota, H., (2001). Influence of Longitudinal and Transverse Members on Geogrid Pullout Behavior During Deformation. *Geotextiles and Geomembranes* 19(8), pp. 483-507.
- Arellano, D., (2005). Guidelines for the Use of Expanded Polystyrene (EPS)-Block Geofoam for the Function of Lightweight Fill in Road Embankment Projects. A Ph.D. thesis, Department of Civil and Environmental Engineering, *University of Illinois at Urbana-Champaign*, Urbana, Illinois, USA, p. 1006.
- ASTM/D1388-14e1, (2014). Standard Test Method for Stiffness of Fabrics. *ASTM International*. West Conshohocken, PA, USA.

- ASTM/D1621-10, (2010). Standard Test Method for Compressive Properties of Rigid Cellular Plastics. *ASTM International*. West Conshohocken, PA, USA.
- ASTM/D1622-14, (2014). Standard Test Method for Apparent Density of Rigid Cellular Plastics. *ASTM International*. West Conshohocken, PA, USA.
- ASTM/D5321-14, (2014). Standard Test Method for Determining the Shear Strength of Soil-Geosynthetic and Geosynthetic-Geosynthetic Interfaces by Direct Shear Method. *ASTM International*. West Conshohocken, PA, USA.
- ASTM/D6637-11, (2011). Standard Test Method for Determining Tensile Properties of Geogrids by the Single or Multi-Rib Tensile Method. *ASTM International*. West Conshohocken, PA, USA.
- ASTM/D6637M-15, (2015). Standard Test Method for Determining Tensile Properties of Geogrids by the Single or Multi-Rib Tensile Method. *ASTM International*. West Conshohocken, PA, USA.
- ASTM/D6706-01, (2013). Standard Test Method for Measuring Geosynthetic Pullout Resistance in Soil. *ASTM International*. West Conshohocken, PA, USA.
- ASTM/D6817-15, (2015). Standard Specification for Rigid Cellular Polystyrene Geofoam. *ASTM International*. West Conshohocken, PA, USA.
- Bakeer, R.M., Sayed, S.M., Cates, P., and Subramanian, R., (1998). Pullout and Shear Tests on Geogrid Reinforced Lightweight Aggregate. *Geotextiles and Geomembranes* 16(2), pp. 119-133.
- Bartlett, S., Negussey, D., Kimble, M., and Sheeley, M., (2000). Use of Geofoam as Super-Lightweight Fill for I-15 Reconstruction. in: *The 79th Annual Meeting for the Transportation Research Board* Transportation Research Board Washington, DC, p. 21.
- Basudhar, P.K., Saha, S., and Deb, K., (2007). Circular Footings Resting on Geotextile-Reinforced Sand Bed. *Geotextiles and Geomembranes* 25(6), pp. 377-384.
- Bathurst, R.J., and Ezzein, F.M., (2016). Geogrid Pullout Load-Strain Behaviour and Modelling using a Transparent Granular Soil. *Geosynthetics International*-(online, ahead of print issue), p. 16.
- Bathurst, R.J., and Kaliakin, V.N., (2005). Review of Numerical Models for Geosynthetics in Reinforcement Applications. in: *The 11th International Conference on Computer Methods and Advances in Geomechanics*. Torino, Italy, pp. 407-416.
- Berg, R.R., Christopher, B.R., and Samtani, N.C., (2009). Design of Mechanically Stabilized Earth Walls and Reinforced Soil Slopes - Volume I. *U.S. Department of Transportation*

- FHWA, Report No. FHWA-NHI-10-024. NHI - National Highway Institute, Woodbury, Minnesota, USA, p. 332.
- Bergado, D.T., and Jin-Chun, C., (1994). Pullout Force/Displacement Relationship of Extensible Grid Reinforcements. *Geotextiles and Geomembranes* 13(5), pp. 295-316.
- Bhandari, A., and Han, J., (2010). Investigation of Geotextile-Soil Interaction under a Cyclic Vertical Load using the Discrete Element Method. *Geotextiles and Geomembranes* 28(1), pp. 33-43.
- Binquet, J., and Lee, K.L., (1975a). Bearing Capacity Analysis of Reinforced Earth Slabs. *Geotechnical Engineering Division* 101(12), pp.1257-1276.
- Binquet, J., and Lee, K.L., (1975b). Bearing Capacity Tests on Reinforced Earth Slabs. *Geotechnical Engineering Division* 101(12), pp.1241-1255.
- Bolton, M.D., (1986). The Strength and Dilatancy of Sands. *Géotechnique* 36(1), pp. 65-78.
- Bourque, S.W., (2002). Centrifuge and Numerical Modeling of Induced Trench Twin Conduits. An M.Sc. thesis, Department of Civil Engineering, *The University of New Brunswick*, New Brunswick, Canada, p. 224.
- Cardile, G., Moraci, N., and Calvarano, L.S., (2016). Geogrid Pullout Behaviour According to the Experimental Evaluation of the Active Length. *Geosynthetics International*-(online, ahead of print issue), p. 12.
- CFEM, (2006). Canadian Foundation Engineering Manual, 4th ed. *Canadian Geotechnical Society, BiTech*, Richmond, Canada, p. 488.
- Chakraborty, D., and Kumar, J., (2014). Bearing Capacity of Strip Foundations in Reinforced Soils. *International Journal of Geomechanics* 14(1), pp. 45-58.
- Chang, J.C., Hannon, J.B., and Forsyth, R.A., (1977). Pull Resistance and Interaction of Earthwork Reinforcement and Soil. *Transportation Research Record*-(640), pp. 1-6.
- Chen, C., McDowell, G.R., and Thom, N.H., (2012). Discrete Element Modelling of Cyclic Loads of Geogrid-Reinforced Ballast under Confined and Unconfined Conditions. *Geotextiles and Geomembranes* 35, pp. 76-86.
- Chen, Q., Abu-Farsakh, M., and Sharma, R., (2009). Experimental and Analytical studies of reinforced crushed limestone. *Geotextiles and Geomembranes* 27(5), 357-367.
- Chen, W.F., and Han, D.J., (1988). Plasticity for Structural Engineers, *J. Ross Publishing*, p. 606.

- Chun, B.S., Lim, H., Sagong, M., and Kim, K., (2004). Development of a Hyperbolic Constitutive Model for Expanded Polystyrene (EPS) Geofoam under Triaxial Compression Tests. *Geotextiles and Geomembranes* 22(4), pp. 223-237.
- CSA, (2006). Canadian Highway Bridge Design Code - CHBDC. *Canadian Standards Association*. Mississauga, Canada, p. 930.
- Das, B.M., Shin, E.C., and Omar, M.T., (1994). The Bearing Capacity of Surface Strip Foundations on Geogrid-Reinforced Sand and Clay - A Comparative Study. *Geotechnical & Geological Engineering* 12(1), p. 1-14.
- Dash, S.K., Krishnaswamy, N.R., and Rajagopal, K., (2001). Bearing Capacity of Strip Footings Supported on Geocell-Reinforced Sand. *Geotextiles and Geomembranes* 19(4), pp. 235-256.
- Dean, G., and Mera, R., (2004). Determination of Material Properties and Parameters Required for the Simulation of Impact Performance of Plastics Using Finite Element Analysis. *National Physical Laboratory (NPL)*, Report No. DEPC-MPR 007. Middlesex, UK, p. 55.
- Dong, Y.L., Han, J., and Bai, X.H., (2011). Numerical Analysis of Tensile Behavior of Geogrids with Rectangular and Triangular Apertures. *Geotextiles and Geomembranes* 29(2), pp. 83-91.
- Dyer, M.R., (1985). Observation of the Stress Distribution in Crushed Glass with Applications to Soil Reinforcement. A Ph.D. thesis, Department of Engineering Science, *University of Oxford*, Oxford, UK, p. 222.
- Ekanayake, S.D., Liyanapathirana, D.S., and Leo, C.J., (2015). Numerical Simulation of EPS Geofoam Behaviour in Triaxial Tests. *Engineering Computations* 32(5), pp. 1372-1390.
- El Naggar, H., Turan, A., and Valsangkar, A.J., (2015). Earth Pressure Reduction System Using Geogrid-Reinforced Platform Bridging for Buried Utilities. *Geotechnical and Geoenvironmental Engineering* 141(6), 04015024-1:10.
- El Sawwaf, M.A., (2007). Behavior of Strip Footing on Geogrid-Reinforced Sand Over a Soft Clay slope. *Geotextiles and Geomembranes* 25(1), pp. 50-60.
- Elragi, A.F., (2000). Selected Engineering Properties and Applications of EPS Geofoam. A Ph.D. thesis, Faculty of Construction Management and Wood Products Engineering, *State University of New York College of Environmental Science and Forestry*, Syracuse, New York, USA, p. 296.
- Ezzein, F.M., Bathurst, R.J., and Kongkitkul, W., (2015). Nonlinear Load–Strain Modeling of Polypropylene Geogrids During Constant Rate-of-Strain Loading. *Polymer Engineering and Science* 55(7), pp. 1617-1627.

- Farrag, K., Acar, Y.B., and Juran, I., (1993). Pull-Out Resistance of Geogrid Reinforcements. *Geotextiles and Geomembranes* 12(2), pp. 133-159.
- Ferreira, F.B., Vieira, C.S., Lopes, M.L., and Carlos, D.M., (2015). Experimental Investigation on the Pullout Behaviour of Geosynthetics Embedded in a Granite Residual Soil. *European Journal of Environmental and Civil Engineering*-(ahead of print issue), pp. 1-34.
- Ghazavi, M., and Lavasan, A.A., (2008). Interference Effect of Shallow Foundations Constructed on Sand Reinforced with Geosynthetics. *Geotextiles and Geomembranes* 26(5), pp. 404-415.
- Gnip, I.J., Kersulis, V.I., and Vaitkus, S.I., (2005). Predicting the Deformability of Expanded Polystyrene in Long-Term Compression. *Mechanics of Composite Materials* 41(5), pp. 407-414.
- Guido, V.A., Chang, D.K., and Sweeney, M.A., (1986). Comparison of Geogrid and Geotextile Reinforced Earth Slabs. *Canadian Geotechnical Journal* 23(4), pp. 435-440.
- Gurung, N., and Iwao, Y., (1999). Comparative Model Study of Geosynthetic Pull-Out Response. *Geosynthetics International* 6(1), pp. 53-68.
- Handy, R.L., (2004). Anatomy of an Error. *Geotechnical and Geoenvironmental Engineering* 130(7), pp. 768-771.
- Hansen, P., Miller, L., Valsangkar, A.J., Bourque, S., and MacLeod, T., (2007). Performance of Induced Trench Culverts in New Brunswick. in: *The Annual Conference of the Transportation Association of Canada*. Transportation Association of Canada (TAC), Saskatoon, Canada,
- Hatami, K., and Bathurst, R.J., (2005). Development and Verification of a Numerical Model for the Analysis of Geosynthetic-Reinforced Soil Segmental Walls under Working Stress Conditions. *Canadian Geotechnical Journal* 42(4), pp. 1066-1085.
- Hatami, K., Mahmood, T., Ghabchi, R., and Zaman, M., (2013). Influence of In-Isolation Properties of Geogrids on Their Pullout Performance in a Dense Graded Aggregate. *Indian Geotechnical Journal* 43(4), pp. 303-320.
- Hazarika, H., (2006). Stress-Strain Modeling of EPS Geofoam for Large-Strain Applications. *Geotextiles and Geomembranes* 24(2), pp. 79-90.
- Horvath, J.S., (1995). Geofoam Geosynthetic, *Horvath Engineering*, New York, USA, p. 217.
- Horvath, J.S., (1997). The Compressible Inclusion Function of EPS Geofoam. *Geotextiles and Geomembranes* 15(1-3), pp. 77-120.

- Horvath, J.S., (2001). Concepts for Cellular Geosynthetics Standards with Example for EPS-Block Geofoam as Lightweight Fill for Roads. *Center for Geotechnology*, Research Report No. CGT-2001-4. Manhattan College, New York, USA, p. 92.
- Huang, C., and Menq, F., (1997). Deep-Footing and Wide-Slab Effects in Reinforced Sandy Ground. *Geotechnical and Geoenvironmental Engineering* 123(1), pp. 30-36.
- Huang, C.C., and Tatsuoka, F., (1990). Bearing Capacity of Reinforced Horizontal Sandy Ground. *Geotextiles and Geomembranes* 9(1), pp. 51-82.
- Hussein, M.G., and Meguid, M.A., (2009). On the 3D Modelling of Soil-Geogrid Interaction. in: *GeoHalifax 2009, the 62nd Canadian Geotechnical Conference*. Canadian Geotechnical Society, Halifax, Canada, Paper No. 138 (pp. 986-991).
- Hussein, M.G., and Meguid, M.A., (2013). Three-Dimensional Finite Element Analysis of Soil-Geogrid Interaction under Pull-out Loading Condition. in: *GeoMontreal 2013, the 66th Canadian Geotechnical Conference*. Canadian Geotechnical Society, Montreal, Canada, Paper No. 260 (pp. 452-458).
- Hussein, M.G., and Meguid, M.A., (2015). Numerical Modeling of Soil-Structure Interaction with Applications to Geosynthetics. in: *The 14th International Conference on Structural and Geotechnical Engineering (ICSGE 14) - Sustainable Infrastructure: From Research to Practice*. Ain Shams University, Cairo, Egypt, Paper No. 155 (p. 12).
- Hussein, M.G., Meguid, M.A., and Whalen, J., (2015). On the Numerical Modeling of Buried Structures with Compressible Inclusion. in: *GeoQuebec 2015, the 68th Canadian Geotechnical Conference*. Canadian Geotechnical Society, Quebec City, Canada, Paper No. 577 (p. 8).
- Ingold, T.S., (1982). Reinforced Earth, *Telford*, London, p. 141.
- Janbu, N., (1976). Static Bearing Capacity of Friction Piles. in: *The 6th European Conference on Soil Mechanics and Foundation Engineering*. Vienna, Austria, Vol. 3, pp. 479-488.
- Jewell, R.A., (1980). Some Effects of Reinforcement on the Mechanical Behaviour of Soils. A Ph.D. thesis, Department of Engineering: Civil Engineering Division, *University of Cambridge*, Cambridge, England, p. 309.
- Jewell, R.A., Milligan, G.W.E., Sarsby, R.W., and Dubois, D., (1984). Interaction Between Soil and Geogrid. in: *Polymer Grid Reinforcement*. Thomas Telford, London, UK, pp. 18-30.
- Juran, I., Knochenmus, G., Acar, Y.B., and Arman, A., (1988). Pull-Out Response of Geotextiles and Geogrids (synthesis of available experimental data). in: *Geosynthetics for Soil Improvement, Symposium at the ASCE National Convention*. American Society of Civil Engineers, Nashville, Tennessee, USA, pp. 92-111.

- Jutkofsky, W., Sung, J., and Negussey, D., (2000). Stabilization of Embankment Slope with Geofam. *Transportation Research Record*-(1736), pp. 94-102.
- Kaliakin, V.N., and Dechasakulsom, M., (2001). Time-Dependent Behavior of Geosynthetic Reinforcement – A Review of Mathematical Models. *Department of Civil and Environmental Engineering*, Report No. 01-2. University of Delaware, Newark, Delaware, USA, p. 14.
- Kang, J., (2007). Soil–Structure Interaction and Imperfect Trench Installations as Applied to Deeply Buried Conduits. A Ph.D. thesis, Department of Civil Engineering, *Auburn University*, Auburn, Alabama, USA, p. 228.
- Kang, J., Parker, F., Kang, Y.J., and Yoo, C.H., (2008). Effects of Frictional Forces Acting on Sidewalls of Buried Box Culverts. *International Journal for Numerical and Analytical Methods in Geomechanics* 32(3), pp. 289-306.
- Katona, M.G., Smith, J.M., Odello, R.S., and Allgood, J.R., (1976). CANDE - A Modern Approach for the Structural Design and Analysis of Buried Culverts. Report No. FHWA-RD-77-5. Civil Engineering Laboratory, Naval Construction Battalion Center, California, USA, p. 480.
- Kim, K., and Yoo, C., (2005). Design Loading on Deeply Buried Box Culverts. *Geotechnical and Geoenvironmental Engineering* 131(1), pp. 20-27.
- Kim, K., and Yoo, C.H., (2002). Design Loading for Deeply Buried Box Culverts. *Highway Research Center*, Report No. IR-02-03. Auburn University, Alabama, USA, p. 215.
- Koerner, R.M., (2012). Designing with Geosynthetics, 6th ed. *Xlibris Corporation*, USA, Vol. 1 & Vol. 2.
- Koerner, R.M., Wayne, M.H., and Carroll, R.G., (1989). Analytic Behavior of Geogrid Anchorage. in: *Geosynthetics '89*. IFAI San Diego, San Diego, California, USA, pp. 525-536.
- Kongkitkul, W., Chantachot, T., and Tatsuoka, F., (2014). Simulation of Geosynthetic Load–Strain–Time Behaviour by the Non-Linear Three-Component Model. *Geosynthetics International* 21(4), pp. 244-255.
- Kotake, N., Tatsuoka, F., Tanaka, T., Siddiquee, M.S.A., and Huang, C.C., (2001). FEM Simulation of the Bearing Capacity of Level Reinforced Sand Ground Subjected to Footing Load. *Geosynthetics International* 8(6), pp. 501-549.
- Kumar, A., and Saran, S., (2003). Bearing Capacity of Rectangular Footing on Reinforced Soil. *Geotechnical & Geological Engineering* 21(3), pp. 201-224.

- Kwon, J., Tutumluer, E., and Konietzky, H., (2008). Aggregate Base Residual Stresses Affecting Geogrid Reinforced Flexible Pavement Response. *International Journal of Pavement Engineering* 9(4), pp. 275-285.
- Lentz, R.W., and Pyatt, J.N., (1988). Pull-Out Resistance of Geogrids in Sand. *Transportation Research Record*-(1188), pp. 48-55.
- Leo, C.J., Kumruzzaman, M., Wong, H., and Yin, J.H., (2008). Behavior of EPS Geofom in True Triaxial Compression Tests. *Geotextiles and Geomembranes* 26(2), pp. 175-180.
- Li, F.L., Peng, F.L., Tan, Y., Kongkitkul, W., and Siddiquee, M.S.A., (2012). FE Simulation of Viscous Behavior of Geogrid-Reinforced Sand Under Laboratory-Scale Plane-Strain-Compression Testing. *Geotextiles and Geomembranes* 31, pp. 72-80.
- Li, J., and Qubain, B.S., (2004). Soil Pressure Distribution on Culverts with Various Foundation Yielding Conditions. in: *EM2004, the 17th ASCE Conference on Engineering Mechanics*. The American Society of Civil Engineers, The University of Delaware, Newark, Delaware, USA, USA.
- Liedberg, N.S.D., (1997). Load Reduction on a Rigid Pipe: Pilot Study of a Soft Cushion Installation. *Transportation Research Record*-(1594), pp. 217-223.
- Liu, C., Zornberg, J., Chen, T., Ho, Y., and Lin, B., (2009). Behavior of Geogrid-Sand Interface in Direct Shear Mode. *Geotechnical and Geoenvironmental Engineering* 135(12), pp. 1863-1871.
- Liu, H., (2015). Reinforcement Load and Compression of Reinforced Soil Mass under Surcharge Loading. *Geotechnical and Geoenvironmental Engineering* 141(6), 04015017-1:10.
- Liu, H.L., Charles, W.W.N., and Fei, K., (2007). Performance of a Geogrid-Reinforced and Pile-Supported Highway Embankment over Soft Clay: Case Study. *Geotechnical and Geoenvironmental Engineering* 133(12), pp. 1483-1493.
- Lopes, M.J., and Lopes, M.L., (1999). Soil-Geosynthetic Interaction-Influence of Soil Particle Size and Geosynthetic Structure. *Geosynthetics International* 6(4), pp. 261-282.
- Lopes, M.L. (2002). Soil-Geosynthetic Interaction. A book chapter in *Geosynthetics and their Applications*. Edited by S. K. Shukla. Thomas Telford, London, UK, pp. 55-78.
- Lopes, M.L., and Ladeira, M., (1996). Influence of the Confinement, Soil Density and Displacement Rate on Soil-Geogrid Interaction. *Geotextiles and Geomembranes* 14(10), pp. 543-554.
- Lopes, M.L., and Silvano, R., (2010). Soil/Geotextile Interface Behaviour in Direct Shear and Pullout Movements. *Geotechnical & Geological Engineering* 28(6), pp. 791-804.

- Lopes, P.C., Lopes, M.L., and Lopes, M.P., (2001). Shear Behaviour of Geosynthetics in the Inclined Plane Test – Influence of Soil Particle Size and Geosynthetic Structure. *Geosynthetics International* 8(4), pp. 327-342.
- MacLeod, T., (2003). Earth Pressures on Induced Trench Conduits. An M.Sc. thesis, Department of Civil Engineering, *The University of New Brunswick*, New Brunswick, Canada, p. 219.
- Marston, A., (1922). Second Progress Report to the Joint Concrete Culvert Pipe Committee. Iowa Engineering Experimental Station, Ames, IA, USA.
- Marston, A., (1930). The Theory of External Loads on Closed Conduits in the Light of the Latest Experiments. in: *The 9th Annual Meeting of the Highway Research Board*. Highway Research Board, Washington, D.C., USA, pp. 138-170.
- Marston, A., and Anderson, A., (1913). The Theory of Loads on Pipes in Ditches, and Tests of Cement and Clay Drain Tile and Sewer Pipe, Bulletin No. 31. *Iowa Engineering Experiment Station*, Ames, Iowa, USA, p. 185.
- McAfee, R.P., and Valsangkar, A.J., (2008). Field Performance, Centrifuge Testing, and Numerical Modelling of an Induced Trench Installation. *Canadian Geotechnical Journal* 45(1), pp. 85-101.
- McDowell, G.R., Harireche, O., Konietzky, H., Brown, S.F., and Thom, N.H., (2006). Discrete Element Modelling of Geogrid-Reinforced Aggregates. *Proceedings of the ICE-Geotechnical Engineering* 159(1), pp. 35-48.
- McGown, A., Andrawes, K.Z., Yeo, K.C., and DuBois, D., (1984). The Load-Strain-Time Behaviour of Tensar Geogrids. in: *Polymer Grid Reinforcement*. Thomas Telford, London, UK, pp. 11-17.
- McGuigan, B.L., and Valsangkar, A.J., (2010). Centrifuge Testing and Numerical Analysis of Box Culverts Installed in Induced Trenches. *Canadian Geotechnical Journal* 47(2), pp. 147-163.
- McGuigan, B.L., and Valsangkar, A.J., (2011). Earth Pressures on Twin Positive Projecting and Induced Trench Box Culverts under High Embankments. *Canadian Geotechnical Journal* 48(2), pp. 173-185.
- McLay, M.J., (1993). Pullout Testing of Geogrid Reinforcement. An M.Sc. thesis, Department of Civil Engineering, *Royal Military College of Canada*, Kingston, Ontario, Canada, p. 143.
- Meguid, M.A., (2014). Recent Developments in Numerical Modelling of Composite Systems with Geogrid Inclusions. in: *The International Workshop on Advanced Composites for*

- Engineering Applications (ACEA 2014)*. The German University in Cairo, Cairo, Egypt, pp. 13-26.
- Menétrey, P., and Willam, K.J., (1995). Triaxial Failure Criterion for Concrete and its Generalization. *ACI Structural Journal* 92(3), pp. 311-318.
- Milligan, G.W.E., and Palmeira, E.P., (1987). Prediction of Bond Between Soil and Reinforcement. in: *International Symposium on Prediction and Performance in Geotechnical Engineering*. Calgary, Canada, pp. 147–153.
- Mirmoradi, S., and Ehrlich, M., (2014). Numerical Evaluation of the Behavior of GRS Walls with Segmental Block Facing under Working Stress Conditions. *Geotechnical and Geoenvironmental Engineering* 141(3), 04014109-1:8.
- Moraci, N., Cardile, G., Gioffrè, D., Mandaglio, M., Calvarano, L., and Carbone, L., (2014). Soil Geosynthetic Interaction: Design Parameters from Experimental and Theoretical Analysis. *Transportation Infrastructure Geotechnology* 1(2), 165-227.
- Moraci, N., and Gioffrè, D., (2006). A Simple Method to Evaluate the Pullout Resistance of Extruded Geogrids Embedded in a Compacted Granular Soil. *Geotextiles and Geomembranes* 24(2), pp. 116-128.
- Moraci, N., and Recalcati, P., (2006). Factors Affecting the Pullout Behaviour of Extruded Geogrids Embedded in a Compacted Granular Soil. *Geotextiles and Geomembranes* 24(4), pp. 220-242.
- Mosallanezhad, M., Taghavi, S.H.S., Hataf, N., and Alfaro, M.C., (2016). Experimental and Numerical Studies of the Performance of the New Reinforcement System Under Pull-Out Conditions. *Geotextiles and Geomembranes* 44(1), pp. 70-80.
- Musser, S.C., (1989). User Manual of CANDE-89, Culvert Analysis and Design Computer Program. *Federal Highway Administration, FHWA-RD-89-169*. U.S. Department of Transportation, Washington D.C., USA, p. 236.
- Negussey, D., (2007). Design Parameters for EPS Geofoam. *Soils and Foundations* 47(1), pp. 161-170.
- Negussey, D., and Elragi, A., (2000). Strain Rate Effect on the Uniaxial Compression Behavior of EPS Geofoam. *Geofoam Research Center, Report No. AE2-00*. Syracuse University, Syracuse, New York, USA.
- Oshati, O.S., Valsangkar, A.J., and Schriver, A.B., (2012). Earth Pressures Exerted on an Induced Trench Cast-in-Place Double-Cell Rectangular Box Culvert. *Canadian Geotechnical Journal* 49(11), pp. 1267-1284.

- Palmeira, E.M., and Milligan, G.W.E., (1989). Scale and Other Factors Affecting the Results of Pull-out Tests of Grids Buried in Sand. *Géotechnique* 39(3), pp. 511-524.
- Patra, C.R., Das, B.M., Bhoi, M., and Shin, E.C., (2006). Eccentrically Loaded Strip Foundation on Geogrid-Reinforced Sand. *Geotextiles and Geomembranes* 24(4), pp. 254-259.
- Perkins, S.W., (2000). Constitutive Modeling of Geosynthetics. *Geotextiles and Geomembranes* 18(5), pp. 273-292.
- Perkins, S.W., (2001). Numerical Modeling of Geosynthetic Reinforced Flexible Pavements. *Montana Department of Transportation*, Report No. FHWA/MT-01/003/99160-2. Department of Civil Engineering, Montana State University, Helena, Montana, USA, p. 97.
- Perkins, S.W., and Cuelho, E.V., (1999). Soil-Geosynthetic Interface Strength and Stiffness Relationships From Pullout Tests. *Geosynthetics International* 6(5), pp. 321-346.
- Perkins, S.W., and Edens, M.Q., (2003). Finite Element Modeling of a Geosynthetic Pullout Test. *Geotechnical & Geological Engineering* 21(4), pp. 357-375.
- Peterson, L.M., and Anderson, L.R., (1980). Pullout Resistance of Welded Wire Mesh Embedded in Soil. *Research Report Submitted to Hilfiker Pipe Co.* . Department of Civil Engineering at Utah State University, Logan, Utah, USA.
- Pinho-Lopes, M., Paula, A.M., and Lopes, M.L., (2015). Pullout Response of Geogrids after Installation. *Geosynthetics International* 22(5), pp. 339-354.
- Prozzi, J.A., and R., L., (2007). Using Geogrids to Minimize Reflective Longitudinal Cracking on Pavements over Shrinking Subgrades. *Transportation Research Record-* (2004), pp. 99-110.
- Rong, C., Maotian, L., and Dongxue, H., (2011). Improved Simulation Method for Soil-Geogrid Interaction of Reinforced Earth Structure in FEM. *Transactions of Tianjin University* 17(3), pp. 220-228.
- Rowe, R.K., and Liu, K.W., (2015). Three-Dimensional Finite Element Modelling of a Full-Scale Geosynthetic-Reinforced, Pile-Supported Embankment. *Canadian Geotechnical Journal* 52(12), pp. 2041-2054.
- Rowe, R.K., and Mylleville, B.L.J. (1994). Analysis and Design of Reinforced Embankments on Soft or Weak Foundations. A book chapter in *Soil-Structure Interaction: Numerical Analysis and Modelling*. Edited by J. W. Bull. Chapman & Hall, pp. 231-260.
- Scarino, J., (2003). Reappraisal of Marston's Formula. *Journal of Transportation Engineering* 129(6), pp. 703-712.

- Sharma, R., Chen, Q., Abu-Farsakh, M., and Yoon, S., (2009). Analytical Modeling of Geogrid Reinforced Soil Foundation. *Geotextiles and Geomembranes* 27(1), pp. 63-72.
- Shinoda, M., and Bathurst, R.J., (2004). Lateral and Axial Deformation of PP, HDPE and PET Geogrids Under Tensile Load. *Geotextiles and Geomembranes* 22(4), pp. 205-222.
- Shukla, S.K., (2002). Geosynthetics and their Applications, 1st ed. *Thomas Telford*, London, UK, p. 421.
- Shuwang, Y., Shouzhong, F., and Barr, B., (1998). Finite-Element Modelling of Soil-Geogrid Interaction Dealing with the Pullout Behaviour of Geogrids. *Acta Mechanica Sinica* 14(4), pp. 371-382.
- Siriwardane, H., Gondle, R., Kutuk, B., and Ingram, R., (2008). Experimental Investigation and Numerical Analysis of Reinforced Geologic Media. in: *The 12th International Conference of International Association for Computer Methods and Advances in Geomechanics (IACMAG)*. Goa, India, pp. 4369-4376.
- Sladen, J.A., and Oswell, J.M., (1988). The Induced Trench Method - A Critical Review and Case History. *Canadian Geotechnical Journal* 25(3), pp. 541-549.
- Sobhi, S., and Wu, J.T.H., (1996). An Interface Pullout Formula for Extensible Sheet Reinforcement. *Geosynthetics International* 3(5), pp. 565-582.
- Spangler, M.G., (1950). Field Measurements of the Settlement Ratios of Various Highway Culverts, Bulletin No. 170. *Iowa Engineering Experiment Station*, Ames, Iowa, USA, p. 99.
- Spangler, M.G., (1951). A Theory on Loads on Negative Projecting Conduits. in: *The 13th Annual Meeting of the Highway Research Board*. Washington, D.C., USA, pp. 153-161.
- Spangler, M.G., and Handy, R.L., (1982). Soil Engineering, 4th ed. *Harper & Row*, New York, USA, p. 819.
- Stark, T.D., Arellano, D., Horvath, J.S., and Leshchinsky, D., (2004a). Geofoam Applications in the Design and Construction of Highway Embankments. *National Cooperative Highway Research Program (NCHRP)*, Report No. 65 (Project 24-11). Transportation Research Board, Washington, D.C., USA, p. 792.
- Stark, T.D., Arellano, D., Horvath, J.S., and Leshchinsky, D., (2004b). Guideline and recommended standard for geofoam applications in highway embankments. *National Cooperative Highway Research Program (NCHRP)*, Report No. 529. Transportation Research Board, Washington, D.C., USA, p. 71.

- Sugimoto, M., and Alagiyawanna, A., (2003). Pullout Behavior of Geogrid by Test and Numerical Analysis. *Geotechnical and Geoenvironmental Engineering* 129(4), pp. 361-371.
- Sugimoto, M., Alagiyawanna, A.M.N., and Kadoguchi, K., (2001). Influence of Rigid and Flexible Face on Geogrid Pullout Tests. *Geotextiles and Geomembranes* 19(5), pp. 257-277.
- Sun, C., Hopkins, T.C., and Benkham, T.L., (2009). Reduction of Stresses on Buried Rigid Highway Structures using the Imperfect Ditch Method and Expanded Polysterene (Geofoam). *Kentucky Transportation Center*, Report No. KTC-07-14-SPR-228-01-1F. University of Kentucky, Kentucky, USA, p. 49.
- Sun, L., Hopkins, T., and Beckham, T., (2011). Long-Term Monitoring of Culvert Load Reduction Using an Imperfect Ditch Backfilled with Geofoam. *Transportation Research Record*-(2212), pp. 56-64.
- Tafreshi, S.N.M., and Dawson, A.R., (2010). Behaviour of Footings on Reinforced Sand Subjected to Repeated Loading – Comparing Use of 3D and Planar Geotextile. *Geotextiles and Geomembranes* 28(5), pp. 434-447.
- Takahara, T., and Miura, K., (1998). Mechanical Characteristics of EPS Block Fill and its Simulation by DEM and FEM. *Soils and Foundations* 38(1), pp. 97-110.
- Terzaghi, K., (1943). Theoretical Soil Mechanics, *John Wiley & Sons, Inc.*, New York, p. 503.
- Tran, V., (2013). A Coupled Finite-Discrete Element Framework for Soil-Structure Interaction Analysis. A Ph.D. thesis, Department of Civil Engineering and Applied Mechanics, *McGill University*, Montreal, Canada, p. 243.
- Tran, V.D.H., Meguid, M.A., and Chouinard, L.E., (2013a). The Application of Coupled Finite-Discrete Element Method in Analyzing Soil-Structure Interaction Problems. in: *Particles 2013, The 3rd International Conference on Particle-Based Methods - Fundamentals and Applications*. Stuttgart, Germany, pp. 200-211.
- Tran, V.D.H., Meguid, M.A., and Chouinard, L.E., (2013b). A Finite-Discrete Element Framework for the 3D Modeling of Geogrid-Soil Interaction Under Pullout Loading Conditions. *Geotextiles and Geomembranes* 37, pp. 1-9.
- Vaslestad, J., (1991). Load Reduction on Buried Rigid Pipes Below High Embankments. in: *Pipeline Crossings Conference*. American Society of Civil Engineers, Denver, Colorado, USA, pp. 47-58.

- Vaslestad, J., Johansen, T.H., and Holm, W., (1993). Load Reduction on Rigid Culverts Beneath High Fills: Long-Term Behavior. *Transportation Research Record*-(1415), pp. 58-68.
- Wang, Z., Jacobs, F., and Ziegler, M., (2016). Experimental and DEM Investigation of Geogrid-Soil Interaction under Pullout Loads. *Geotextiles and Geomembranes* 44(3), pp. 230-246.
- Wilson-Fahmy, R.F., and Koerner, R.M., (1993). Finite Element Modelling of Soil-Geogrid Interaction with Application to the Behavior of Geogrids in a Pullout Loading Condition. *Geotextiles and Geomembranes* 12(5), pp. 479-501.
- Yetimoglu, T., Wu, J., and Saglamer, A., (1994). Bearing Capacity of Rectangular Footings on Geogrid-Reinforced Sand. *Journal of Geotechnical Engineering* 120(12), pp. 2083-2099.
- Yogarajah, I., and Yeo, K.C., (1994). Finite Element Modelling of Pull-Out Tests with Load and Strain Measurements. *Geotextiles and Geomembranes* 13(1), pp. 43-54.
- Yuan, Z., and Chua, K.M., (1990). Numerical Evaluation of the Pullout Box Method for Studying Soil-Reinforcement Interaction. *Transportation Research Record*-(1278), p. 116-124.
- Zhang, J., Yasufuku, N., and Ochiai, H., (2008). Discrete Element Modelling of Geogrid Pullout Test. in: *The 4th Asian Regional Conference on Geosynthetics*. Shanghai, China, pp. 11-14.
- Zhuang, Y., and Wang, K.Y., (2015). Three-Dimensional Behavior of Biaxial Geogrid in a Piled Embankment: Numerical Investigation. *Canadian Geotechnical Journal* 52(10), pp. 1629-1635.